Bulletin No. 36
May 1977

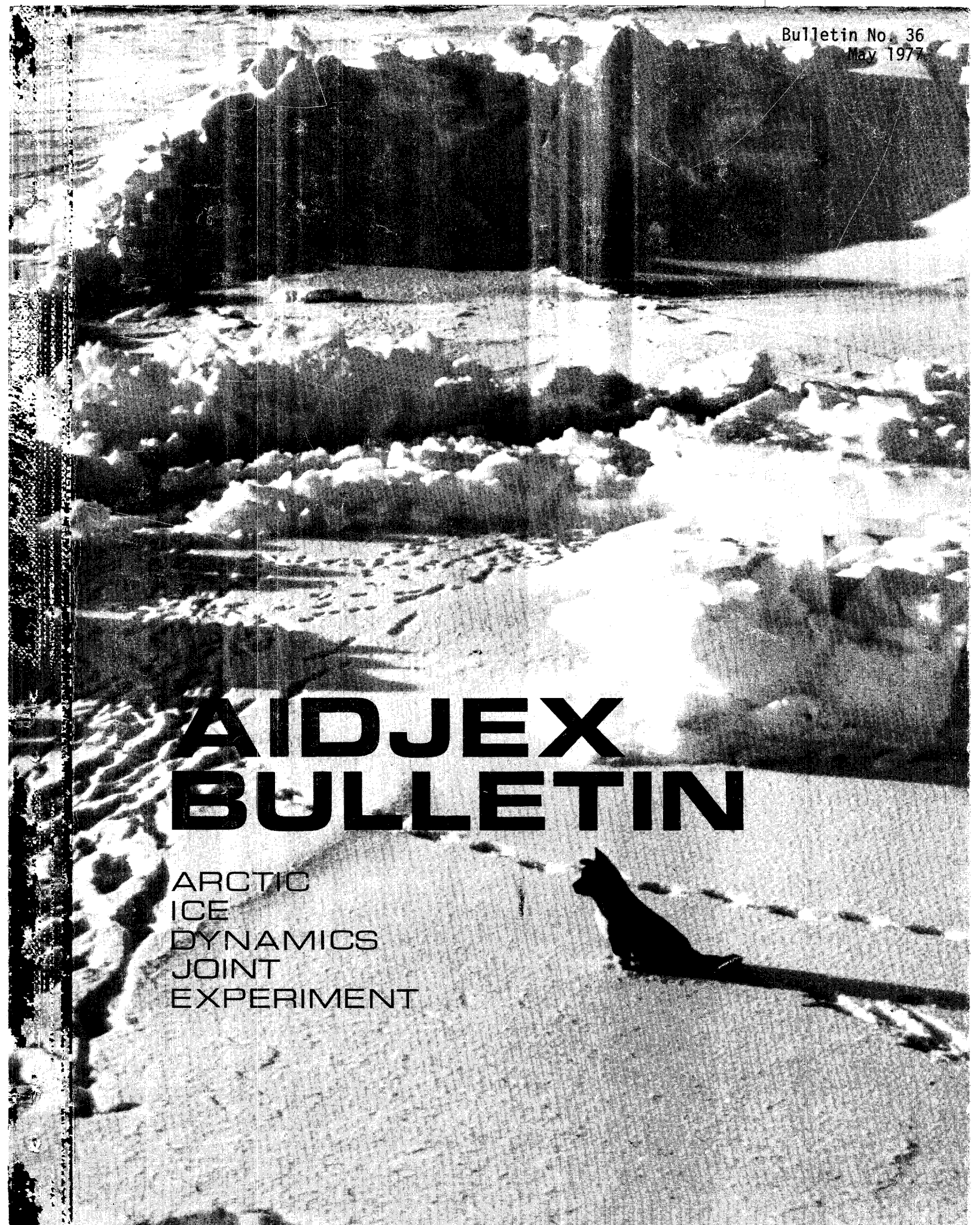

AIDJEX BULLETIN

ARCTIC
ICE
DYNAMICS
JOINT
EXPERIMENT

AIDJEX BULLETIN No. 36

May 1977

ICE FORECASTING LIMITATIONS IMPOSED BY THE ACCURACY OF ATMOSPHERIC PREDICTION MODELS
--John E. Walsh 1

ARCTIC CONTINENTAL SHELF PROCESSES AND MORPHOLOGY RELATED TO SEA ICE ZONATION, BEAUFORT SEA, ALASKA
--E. Reimnitz, L. Toimil, and P. Barnes 15

A SIMULATION OF INERTIAL OSCILLATIONS OBSERVED IN THE DRIFT OF MANNED ICE STATIONS
--M. G. McPhee 65

PIBAL/ACOUSTIC RADAR DATA IN MEASUREMENT AND COMPUTATION OF AIR STRESS OVER PACK ICE
--Frank Carsey and Eric Leavitt 87

FIELD CALIBRATION REPORT, AIDJEX METEOROLOGY PROGRAM, APRIL 1975-APRIL 1976
--M. Clarke, D. Bell, and E. Leavitt 129

COMPUTATION OF AIR STRESS AND SENSIBLE HEAT FLUXES FROM SURFACE LAYER PROFILE DATA, AIDJEX, 1975
--E. Leavitt, D. Bell, M. Clarke, R. Andersen, and C. Paulson . . 157

NCAR ELECTRA PLANETARY BOUNDARY LAYER FLIGHTS DURING AIDJEX
--R. A. Brown 175

CONTENTS OF PAST BULLETINS 187

DATA AVAILABLE FROM THE ARCTIC ICE DYNAMICS JOINT EXPERIMENT AS OF 1 MAY 1977
--Murray J. Stateman 203

* * * * * * * * * * * * * * *

Front cover: Alone at last in the solitude of the evening, Madge recalled, with a thrill that caught her breath, the wild ecstasy of Ernest's kisses, those mad, heedless moments in his arms, when the earth stood still as the inner planets spun in golden frenzies. "Ernie!" the passionate cry rose unbidden from her anguished bosom and

Back cover: The Nansen Drift Station, after several budget cuts, finally gets under way.

AIDJEX BULLETIN No. 36

May 1977

Financial support for AIDJEX is provided by the National Science Foundation, the Office of Naval Research, and other U.S. and Canadian agencies.

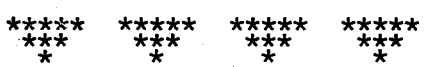

Arctic Ice Dynamics Joint Experiment
Division of Marine Resources
University of Washington
Seattle, Washington 98105

UNIVERSITY OF WASHINGTON

Division of Marine Resources

The AIDJEX Bulletin aims to provide both a forum for discussing AIDJEX problems and a source of information pertinent to all AIDJEX participants. Issues--numbered, dated, and sometimes subtitled--contain technical material closely related to AIDJEX, informal reports on theoretical and field work, translations of relevant scientific reports, and discussions of interim AIDJEX results.

Bulletin No. 36 contains reports from the 1975-76 field work and from the modeling group, as well as a cautionary note from John Walsh, now at NCAR, on ice forecasting limitations imposed by the accuracy of atmospheric prediction models. At the end of Bulletin 36 can be found a listing of Bulletin reports since their printing began. Most issues from No. 25 on are still available in their entirety.

"Hooray, hooray, the first of May, outdoor funning begins today!" A better cartoon or any correspondence concerning the Bulletin should be addressed to Alma Johnson, Editor, AIDJEX Bulletin, 4059 Roosevelt Way N.E., Seattle, WA 98105.

"I really shouldn't be here. I should be out trying to get funded."

ICE FORECASTING LIMITATIONS IMPOSED BY THE ACCURACY OF ATMOSPHERIC PREDICTION MODELS

by

John E. Walsh*
National Center for Atmospheric Research
Boulder, Colorado 80303

ABSTRACT

Forecasts produced by the operational prediction model of the National Meteorological Center are examined for errors that may limit the accuracy of sea ice model predictions. Errors in the predicted low-level height gradients and geostrophic winds are found to be no worse in the Arctic than in most mid-latitude land areas. However, the forecast skill approaches zero by 72 hours when the errors in the predicted geostrophic winds typically become as large as the geostrophic winds themselves. It is concluded that the application of the AIDJEX model to sea ice forecasting will be limited much more severely by the accuracy of atmospheric pressure forecasts than by the formulation of the ice dynamics.

INTRODUCTION

One of the motivating factors in the development of the AIDJEX model is the need for better predictions of the presence and movement of pack ice.

---

*On leave from the Laboratory for Atmospheric Research, University of Illinois, Urbana.

The AIDJEX model has been described in considerable detail by Coon et al. [1974], and the results of some early tests of the model have been reported by Coon et al. [1976]. Encouraging agreement between computed and observed ice parameters was obtained from a simulation in which the air stress was determined from observed surface pressures and derived geostrophic winds.

The use of such a model for ice prediction purposes will require forecasts of the quantities used in computing the external forces acting on the ice. The principal motive force for sea ice is the surface air stress. The AIDJEX model uses a boundary layer subprogram to compute the surface air stress from the surface geostrophic winds. It follows that the accuracy of ice forecasts obtained from the AIDJEX model will be limited by the accuracy with which the atmospheric pressure gradients or geostrophic winds can be forecast.

Unfortunately, the high-latitude performance of atmospheric prediction models has received little attention from forecasting centers, which are understandably more concerned with forecasts for the heavily populated land areas of the middle latitudes. This is one reason for the recommendation by the U.S. POLEX Panel [National Academy of Sciences, 1974] that the high-latitude performance of atmospheric models be reviewed.

This paper will examine the accuracy of high-latitude forecasts produced by the operational numerical model of the National Meteorological Center (NMC). Since the primary concern here is the limitation imposed by the atmospheric prediction model on the ice prediction model to which it may be coupled, the focus will be on the forecasts of the low-level horizontal gradients of pressure or, alternatively, geopotential height. It should be noted that the NMC model has compared favorably with other atmospheric prediction models in case studies by Houghton and Irvine [1976] and by Baumhefner and Downey [1976].

THE MODEL AND THE DATA

The operational NMC model is a 6-layer primitive equation model. A polar stereographic coordinate system is used on an octagonal grid covering the northern hemisphere from approximately 15°N to the pole. The grid

contains 47 × 51 points at each level. The grid spacing is 381 km at 60°N. Details of the model formulation are given by Shuman and Hovermale [1968].

The model is run twice daily beginning at 00Z and 12Z. The results to be shown here are for the 24-, 48-, and 72-hour forecasts made at 00Z during the period 1 July 1974 - 30 June 1975. The files of NMC data stored on tape at the National Center for Atmospheric Research provided 360 sets of the three forecasts and verifications.

Of the forecast parameters that are routinely output and saved from the operational model runs, the most appropriate for this study is the 1000 mb height field. The geostrophic wind is a linear function of the height gradient along a constant-pressure surface:

$$u_g = -\frac{g}{f}\left(\frac{\Delta z}{\Delta y}\right)_p \qquad v_g = +\frac{g}{f}\left(\frac{\Delta z}{\Delta x}\right)_p \tag{1}$$

where u_g and v_g are the geostrophic wind components in the x and y directions, z is the height of the p-surface, g is the gravitational constant, and f is the Coriolis parameter. The proximity of the 1000 mb surface to mean sea level implies that u_g and v_g computed from (1) with p = 1000 mb will closely approximate the surface geostrophic wind components.

RESULTS OF THE FORECAST ANALYSIS

Before the forecasts of the height gradients are examined, the accuracy of the forecasts of the height fields themselves will be illustrated. Attention will be focused on the sector of the Arctic Ocean shown in Figure 1. This sector contains 16 NMC grid points and includes the region of the AIDJEX main experiment. The lines labeled "M_A" in Figure 2 show the mean magnitudes of the errors in the height forecasts for the 16 grid points of the Arctic sector. The errors are plotted for four seasons of approximately 90 days each: Summer (July-September), Autumn (October-December), Winter (January-March), and Spring (April-June). The forecast errors in Figure 2 range from 15-25 m at 24 hours to 40-50 m at 72 hours. The forecast errors are largest in the winter and smallest in the summer.

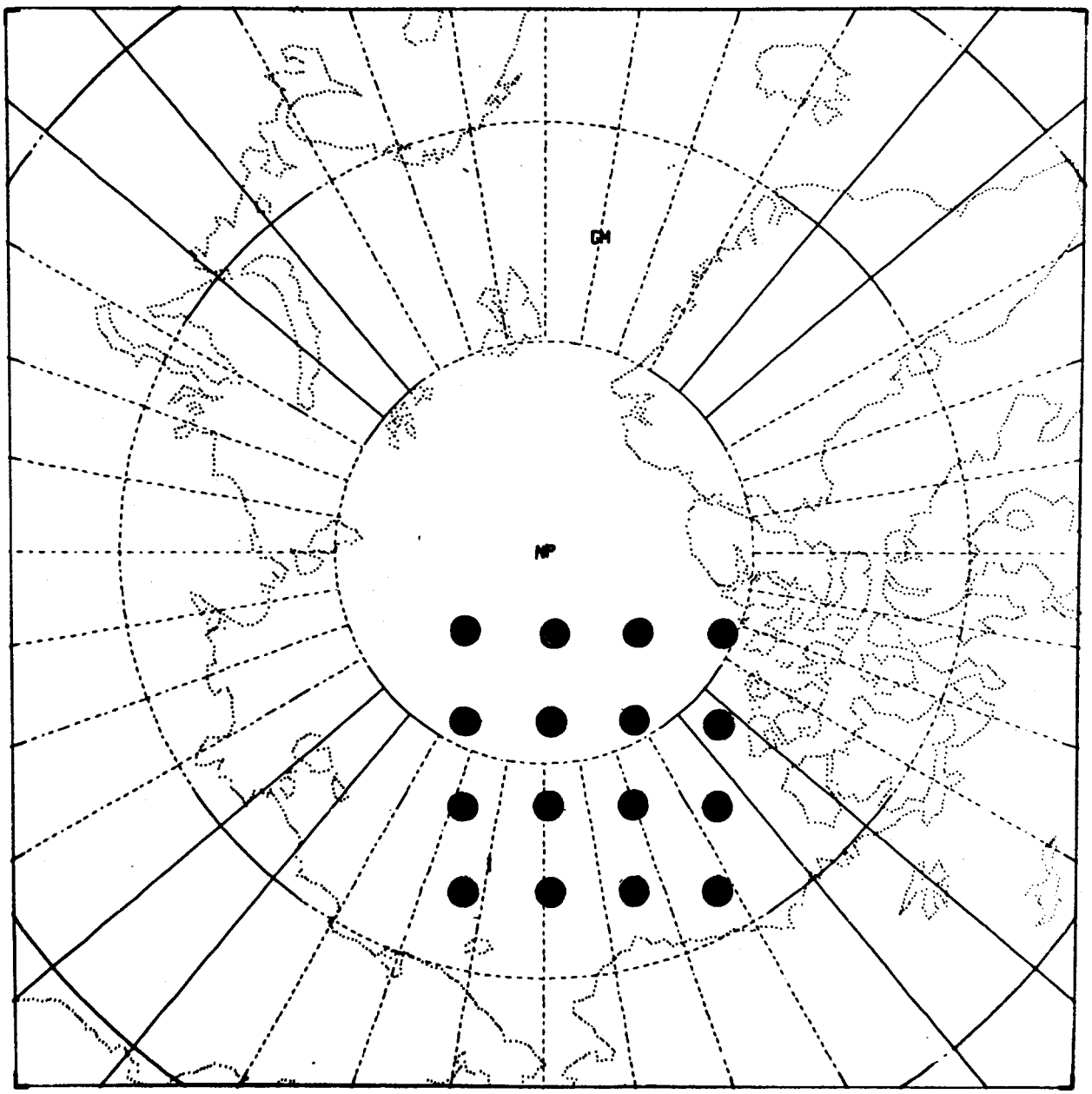

Fig. 1. NMC grid points for which the errors in the Arctic height and height gradient forecasts were computed.

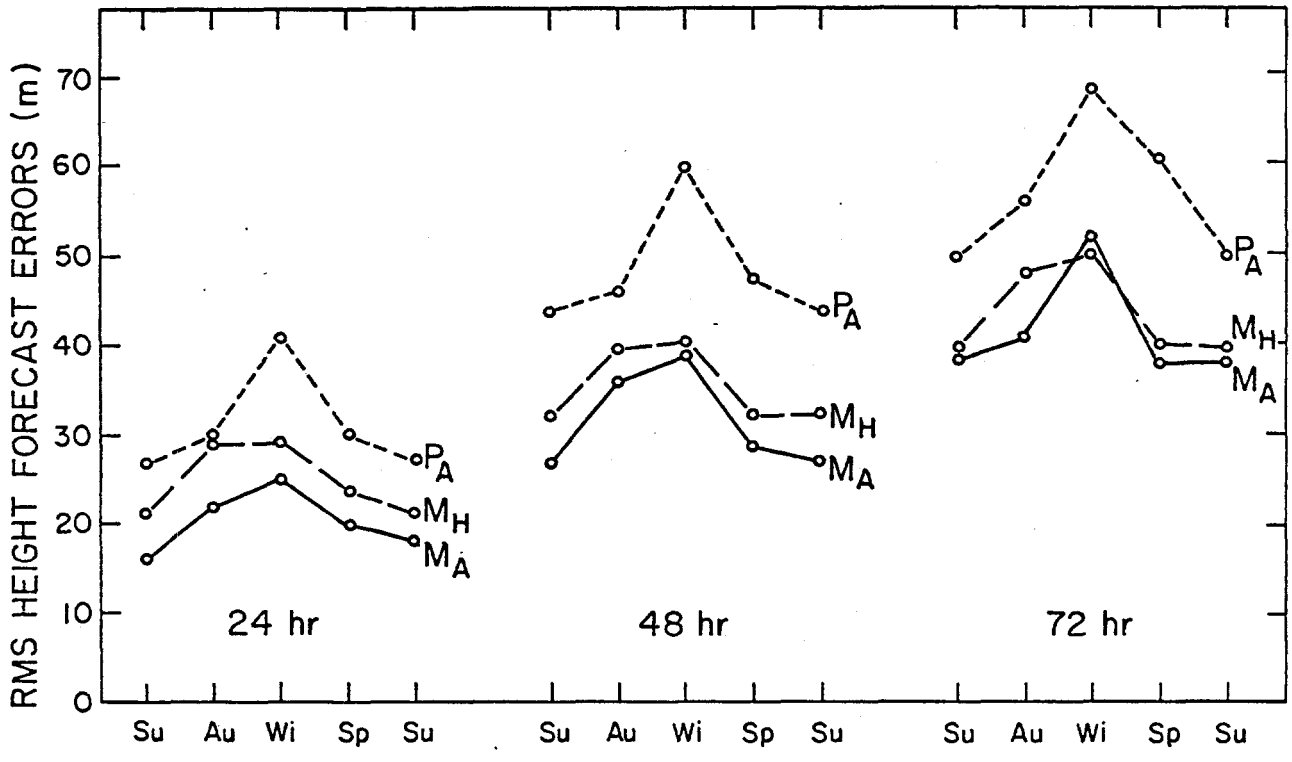

Fig. 2. Mean magnitude (in meters) of the errors in the 1000 mb height forecasts of the NMC model (M) and persistence (P). Each dot represents an average over the 90 forecast days in the season (Su = Summer, Au = Autumn, Wi = Winter, Sp = Spring) and over either the 16 Arctic grid points (subscript A) or the entire hemispheric cap north of 30°N (subscript H).

Figure 2 also shows the corresponding errors for persistence, which was used as the control forecast. (A persistence forecast assumes that the forecast quantities do not change from their initial values.) The NCM forecasts are clearly superior to the persistence forecasts in all seasons and at all three forecast intervals.

Finally, Figure 2 shows that the root mean square (rms) errors in the Arctic height forecasts are generally smaller than the rms height errors averaged over all grid points north of 30°N. While the sparseness of the data network in the central Arctic might have been expected to contribute to more serious errors in high latitudes, the Arctic's position at the center of the NMC grid may render it less susceptible than lower latitudes to errors introduced by the artificial lateral boundaries. On the other hand, the

smaller errors in the Arctic may simply be due to a generally weaker level of synoptic activity in the Arctic. The geographical distribution of the persistence errors (Figure 3) implies that transient synoptic activity is considerably stronger in middle latitudes, especially in the northern ocean areas. A report by the U.S. National Academy of Sciences [1974] describes a similar distribution of synoptic activity at 500 mb.

It should be mentioned that errors in the NMC high-latitude analyses have been noted by Brown et al. [1974]. It is unlikely, however, that the verification errors would correlate significantly with the forecast errors, since the verification data are obtained from an objective analysis performed independently of the forecast data. It is therefore assumed that the forecast errors in Figure 2 are not biased by systematic verification errors.

The relation (1) between the height gradient and the geostrophic wind enables one to express the percentage error, E, in a geostrophic wind prediction for the grid point (i,j) as

$$E \equiv \frac{|\delta(\vec{V}_g)_{ij}|}{|(\vec{V}_g)_{ij}|} = \frac{|\delta(\Delta z)_{ij}|}{|(\Delta z)_{ij}|} \tag{2}$$

where the symbol $|\ |$ indicates a magnitude, $\vec{V}_g$ is the geostrophic wind vector, $\delta(x) = x_{obs} - x_{fcst}$ is the error in the forecast of the quantity x, and

$$\Delta z = \sqrt{(z_{ij+1} - z_{ij-1})^2 + (z_{i+1j} - z_{i-1j})^2}$$

When an observed geostrophic wind vector is expressed as the sum of a forecast vector and an error vector, the quantity (E) in (2) is the ratio of the magnitude of the error vector to the magnitude of the observed vector.

Figure 4 contains several plots of $\overline{E} = \overline{|\delta(\vec{V}_g)_{ij}|} / \overline{|(\vec{V}_g)_{ij}|}$, where the overbar denotes the average over a season (approximately 90 days) for the grid points within a particular region. The region consists of either the 16 NMC grid points of the Arctic sector (subscript A) of Figure 1 or all

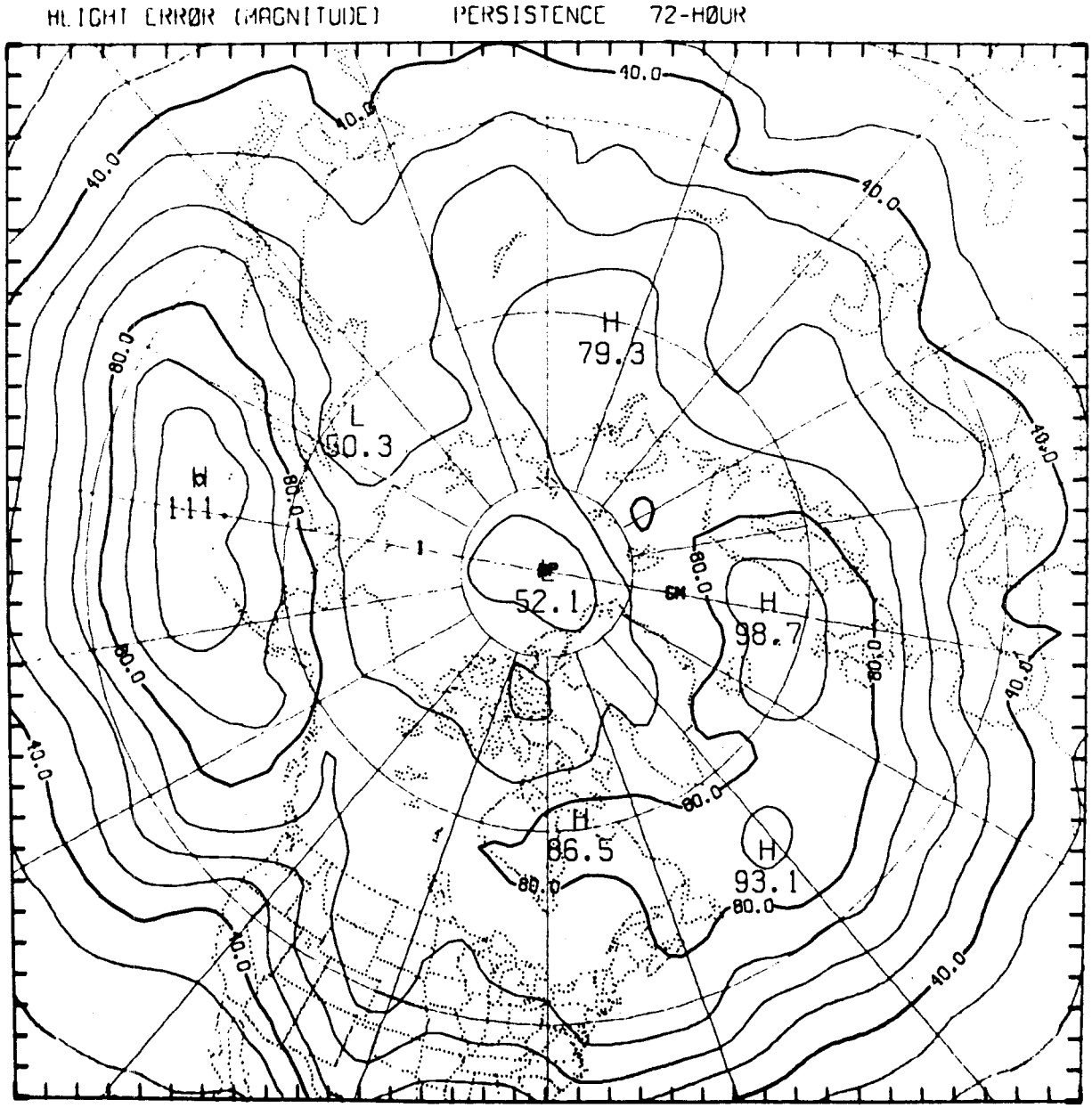

Fig. 3. Mean magnitude (in meters) of the errors in the 72-hour persistence forecasts of 1000 mb height. Errors are averaged over the 360 forecast days.

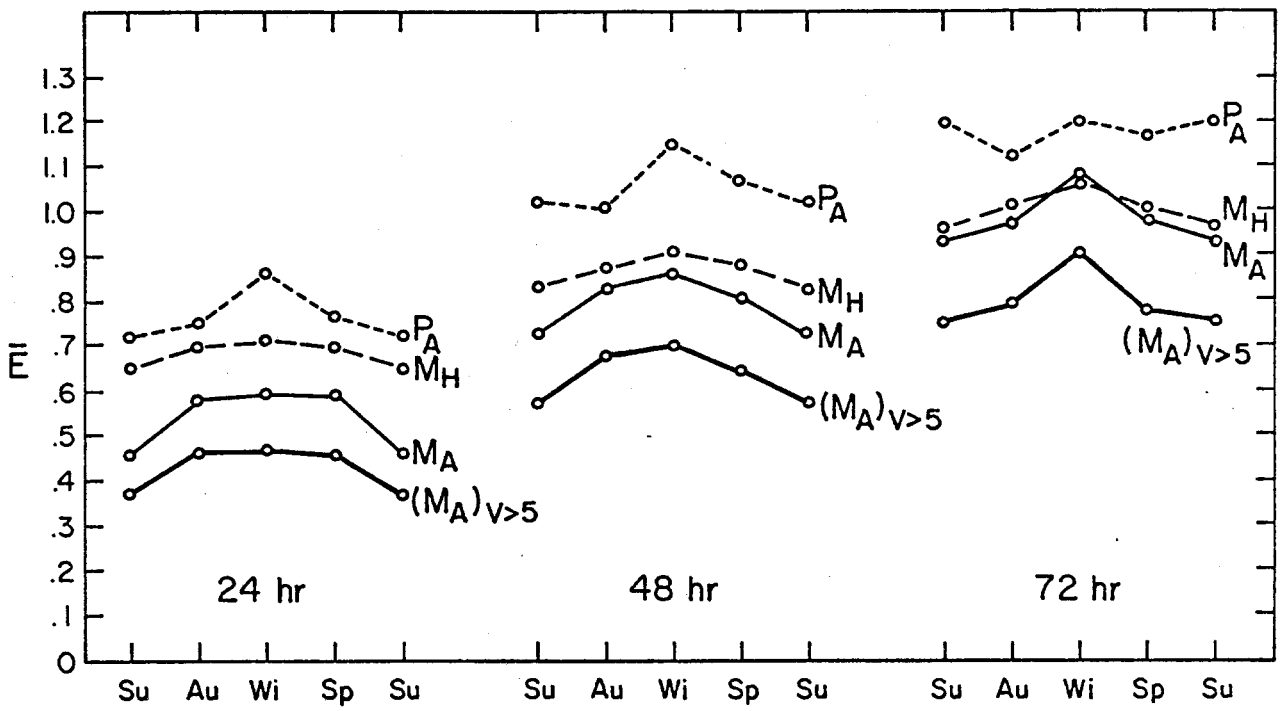

Fig. 4. Mean error, $\bar{E} \equiv |\delta\vec{V}_g|/|\vec{V}_g|$, in the geostrophic wind forecasts of the NMC model (M) and persistence (P). Each dot represents an average over the 90 forecast days in the season and over either the 16 Arctic grid points (subscript A) or the entire hemispheric cap north of 30°N (subscript H). Results labeled "$V > 5$" include only those cases where the verifying geostrophic wind exceeded 5 m sec^{-1}.

grid points in the hemispheric cap north of 30°N (subscript H). Results are shown for the 24-, 48-, and 72-hour forecasts of the NMC model (M) and persistence (P). The values of $\bar{E}$ for the NMC Arctic forecasts (M_A) range from 45%-60% at 24 hours to 90%-110% at 72 hours. The errors are largest in winter and smallest in summer, although the seasonal variation is not as large as in the height errors of Figure 2. The errors in the NMC Arctic forecasts are smaller than the mean NMC errors (M_H) for the region north of 30°N. The NMC Arctic forecasts are again superior to the Arctic forecasts of persistence (P_A), but the NMC improvement over persistence is only on the order of 20% at 72 hours. An examination of the 96- and 120-hour (4- and 5-day) forecasts indicates that the mean errors ($\bar{E}$) of the NMC and persistence forecasts approach each other at $\bar{E} \approx 1.3$-1.4 by day 5 in both the Arctic and in middle latitudes.

As noted by Coon et al. [1976], the major part of pack ice motion and deformation occurs under conditions of strong winds. Figure 4 shows the $\overline{E}$ values of the NMC Arctic forecasts for cases in which the verifying geostrophic winds exceeded 5 m sec^{-1}. (The frequency of such winds at the Arctic grid points ranged from 31% to 58% of the total cases, depending on the season and the grid point.) The percentage errors ($\overline{E}$) are smaller for the strong wind situations, increasing from approximately 45% at 24 hours to approximately 80% at 72 hours. Although they are not plotted in Figure 4, the $(M_A)_{V<5}$ points tend to be about as far above the M_A points as the $(M_A)_{V>5}$ points are below the M_A points.

The geographical distribution of the quantity $\overline{E}$ at 24 and 72 hours is shown in Figure 5 (a,b) for the spring forecasts of the NMC model. The relatively uniform errors in the central Arctic are comparable to the errors over the northern land areas (excluding the elevated Greenland ice sheet, where 1000 mb heights are rather meaningless). Somewhat smaller values of $\overline{E}$ are seen over the northern ocean areas where the geostrophic wind speeds are generally stronger.

The values of $\overline{E}$ shown in Figures 4 and 5 are to be compared with the corresponding values obtained from the results of the early tests of the AIDJEX model. The error parameter for the ice model results is $E_i \equiv |\delta(\vec{V}_i)|/|\vec{V}_i|$, where $\vec{V}_i$ is the observed ice drift vector and $\delta(\vec{V}_i)$ is the vector difference between the computed and observed drift vectors. The 10 sets of mid-day drift velocities from Coon et al. [1976, Fig. 11] give $\overline{E}_i = 0.36$ for $|\vec{V}_i| > 5$ cm sec^{-1} and $\overline{E}_i = 0.75$ for all cases. These percentage errors in the ice drift vectors computed from observed geostrophic winds are comparable to the percentage errors in the geostrophic wind forecasts for 24 hours and are generally less than the percentage errors in the geostrophic wind forecasts for 48 and 72 hours. Since the AIDJEX model results used here are from preliminary tests of the "untuned" model, it is reasonable to assume that the values of $\overline{E}_i$ will eventually be reduced even further below the corresponding values for the geostrophic wind forecasts.

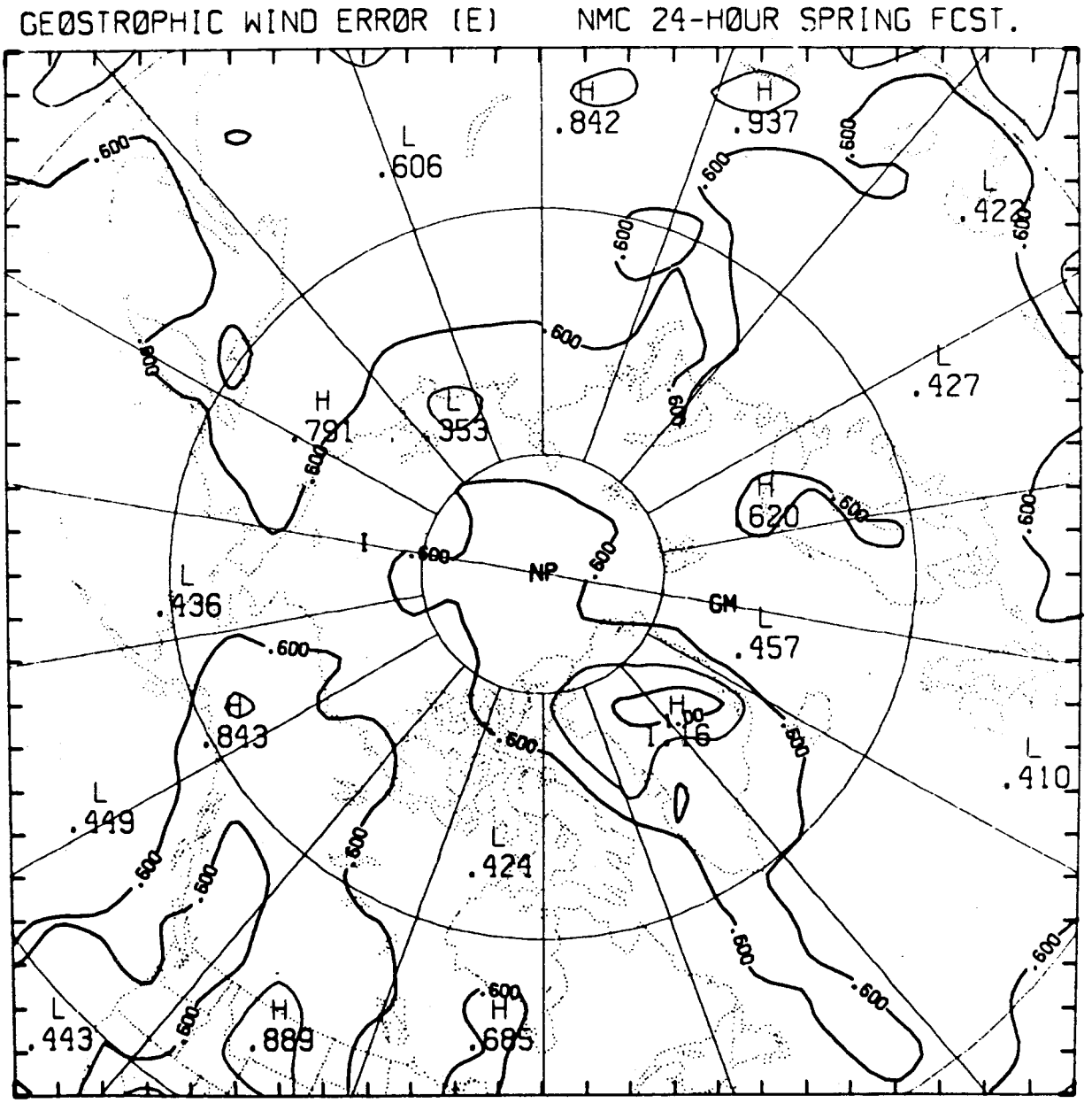

Fig. 5a. Mean error, $\overline{E}$, in the NMC 24-hour geostrophic wind forecasts for the spring season.

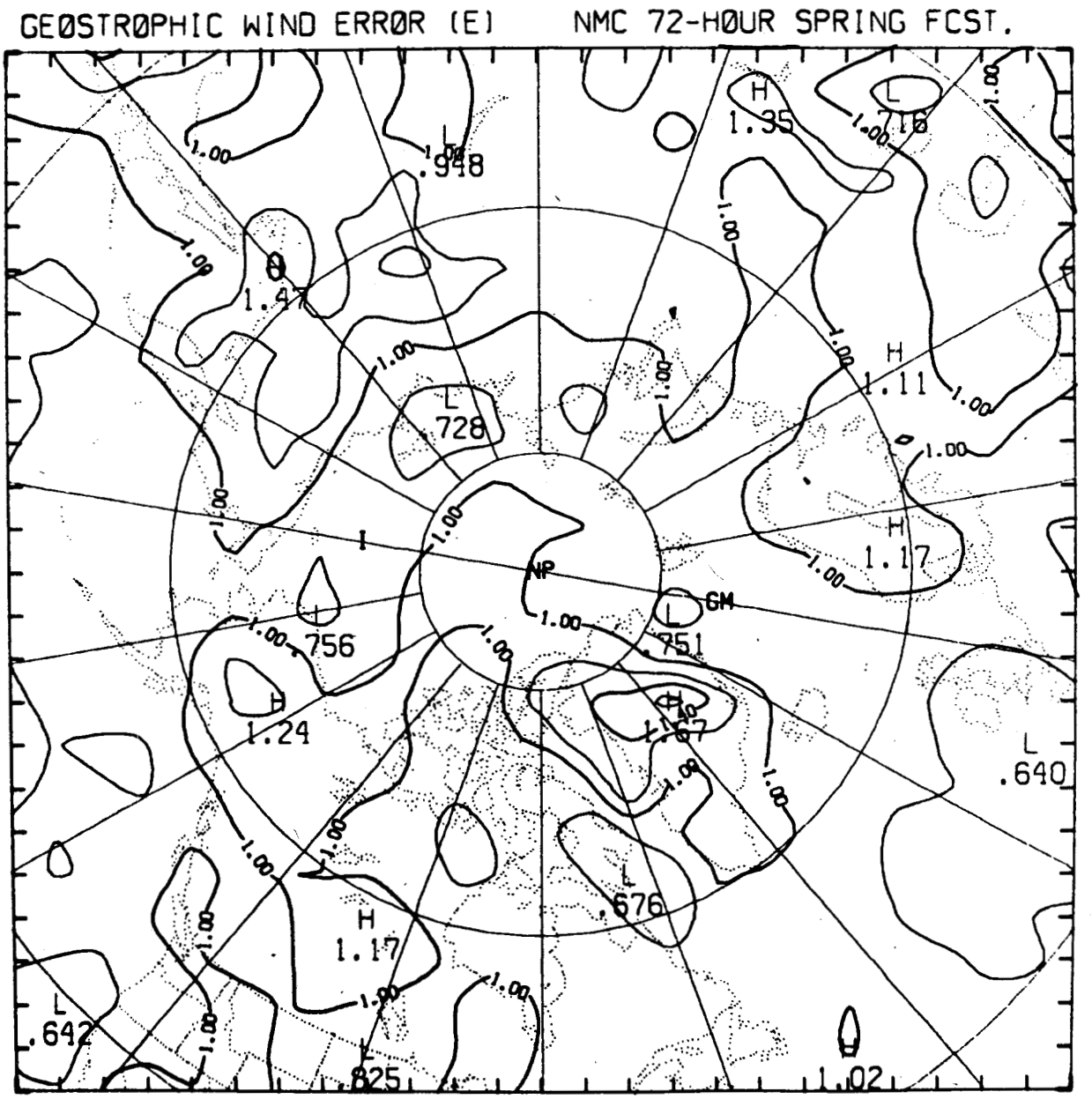

Fig. 5b. As in Figure 5a, but for the 72-hour geostrophic wind forecasts.

CONCLUSIONS

The results described in the previous section show that the skill in the high-latitude geostrophic wind forecasts approaches zero by 72 hours. The results imply that the errors in forecasts of ice motion for periods exceeding 24 hours will be dominated by errors in the geostrophic wind forecasts. It follows that the predictive value of the AIDJEX model or any other ice model will be limited not so much by the formulation of the ice dynamics but by the accuracy of the atmospheric pressure forecasts. More specifically, detailed forecasts of ice motion for periods exceeding 72 hours will show little skill without an improvement in the performance of atmospheric prediction models.

ACKNOWLEDGMENTS

This work was supported in part by the National Science Foundation, Office of Polar Programs, through Grant DPP 76-15352. The data were provided by the National Meteorological Center through the Computing Facility of the National Center for Atmospheric Research. The author wishes to thank Drs. W. Kellog and D. Baumhefner for their constructive reviews of the manuscript.

REFERENCES

Baumhefner, D., and P. Downey. 1976. Forecast intercomparisons between large-scale numerical weather prediction models. In *Proceedings of the Joint DMG/AMS International Conference on Simulation of Large-Scale Atmospheric Processes*, Hamburg, F. R. Germany.

Brown, R. A., P. Maier, and T. Fox. 1974. Surface atmospheric pressure fields and derived geostrophic winds, AIDJEX 1972. *AIDJEX Bulletin, 26,* 173-203.

Coon, M. D., R. Colony, R. S. Pritchard, and D. A. Rothrock. 1976. Calculations to test a pack ice model. In *Proceedings of the Second International Conference on Numerical Methods in Geomechanics.* (Also in *AIDJEX Bulletin, 31,* 170-187.)

Coon, M. D., G. A. Maykut, R. S. Pritchard, D. A. Rothrock, and A. S. Thorndike, 1974. Modeling the pack ice as an elastic-plastic material. *AIDJEX Bulletin, 24,* 1-105.

Houghton, D. D., and W. S. Irvine, Jr. 1976. A case study comparison of the performance of operational prediction models used in the United States. *Monthly Weather Review, 104,* 817-827.

Shuman, F. G., and J. B. Hovermale. 1968. An operational six-layer primitive equation model. *Journal of Applied Meteorology, 7,* 525-547.

U. S. National Academy of Sciences. 1974. *U. S. Contribution to the Polar Experiment. Part 1, POLEX-GARP (North),* Washington, D.C., 119 pp.

ARCTIC CONTINENTAL SHELF PROCESSES AND MORPHOLOGY RELATED TO SEA ICE ZONATION, BEAUFORT SEA, ALASKA

by

E. Reimnitz, L. Toimil, and P. Barnes
U.S. Geological Survey
Menlo Park, CA 94025

ABSTRACT

Landsat-1 and NOAA satellite images for winter 1972-73 and ice seafloor data from several sources were used to study sea ice zonation and dynamics and their relation to bottom morphology and geology on the Beaufort Sea continental shelf of arctic Alaska.

In early winter the location of the boundary between undeformed fast ice and the westward drifting pack ice of the Pacific Gyre is controlled by major coastal promontories. Pronounced linear pressure ridges, shear ridges, and hummock fields form along this boundary and are stabilized by grounding, generally between the 10 m and 20 m isobaths. Slippage along this boundary occurs intermittently at or seaward of the grounded ridges, forming new grounded ridges in a widening zone, the *stamukhi* zone, which by late winter extends out to the 40 m isobath. Between intermittent events along the stamukhi zone, pack ice drift and slippage are continuous along the shelf edge, at average rates of 3-10 km per day. Whether slippage occurs along the stamukhi zone or along the shelf edge, it is restricted to a zone several hundred meters wide and ice seaward of the slip face moves at uniform rates for tens of kilometers out into the pack ice drift without discernible drag effects.

A causal relation is seen between the spatial distribution of major ice ridge systems and offshore shoals downdrift of major coastal promontories. The shoals appear to have migrated shoreward under the influence of ice up to 400 m in the last 25 years. The seafloor seaward of these shoals within the stamukhi zone shows high ice gouge density, large incision depths, and a high degree of disruption of internal sedimentary structures. The concentration of large ice ridges and our seafloor data in the stamukhi zone indicate that much of the available marine energy

is expended here, while the inner shelf and coast, where the relatively undeformed fast ice grows, are sheltered. There is evidence that anomalies in the overall arctic shelf profile are related to sea ice zonation, ice dynamics, and bottom processes. The ice zonation proposed--(a) bottom-fast ice, (b) floating fast ice, (c) stamukhi, and (d) seasonal pack ice--emphasizes ice interaction with the shelf surface and differs from previous zonation.

Certain aspects of the results reported here are directly applicable to planned offshore developments in the Prudhoe Bay oil field. Properly placed artificial structures similar to offshore shoals should be able to withstand the forces of the ice, serve to modify the observed ice zonation, and might be used to make the environment less hostile to human activities.

INTRODUCTION

The presence of an ice cover over the continental shelves of the Arctic sea for eight or nine months of the year may imply to many marine geologists a period of quiescence, when the familiar processes controlling the sedimentological environment are dormant. Wind-driven currents are damped, sediment-laden river plumes are absent, and there is no wave activity. It is true that beaches in many areas of the Arctic are relatively stagnant for a large part of the year while they are protected by ice. But several recent reports dealing with the Beaufort Sea shelf point out that throughout the year much of it has a dynamic environment in which ice plays a dominant role [Reimnitz and Bruder, 1972; Reimnitz et al., 1972; Barnes and Reimnitz, 1974; Reimnitz et al., 1974; Reimnitz and Barnes, 1974; Walker, 1974].

The shear zone in the winter ice regime off northern Alaska occurs where ice carried along by the Pacific Gyre of the Beaufort Sea grinds against stationary fast ice on the inner continental shelf, resulting in the formation of pressure ridges, shear ridges, and hummock fields. Ice dynamics and extremely rough surface relief make the shear zone a formidable barrier to ice travel and to offshore petroleum exploration and development. Because many of the ridges survive the summer melt season and remain grounded, the shear zone also represents an obstacle to shipping. Much of the marine energy of the Beaufort Sea is expended within the offshore shear zone. We,

therefore, are tempted to make an analogy between it and the surf zone of lower latitudes, although the processes and results obviously are very different.

This report describes a study of the winter shear zone between the Arctic pack ice and the fast ice, and discusses its implications to shelf geology, morphology, and bottom processes. Most studies of the shear zone have dealt with the problem of dynamics in the interior of large fields of sea ice, with ice deformational processes, and the resulting ice features. The overall interaction of the Arctic pack with the continent has received little attention. Because the present work is based largely on remote sensing without sufficient ground observations on the shear zone, and on shipboard studies during the summer, the conclusions drawn can be considered only preliminary. But the shear zone appears to be an important morphological and geological boundary on the continental shelf.

In this report we will: (1) delineate the shear zone of Alaska's north coast from Landsat-1 and NOAA-2 satellite images and consider its relation to bathymetry and coastal configuration; (2) study interactions between the pack ice drift and the stationary shore ice during winter; (3) attempt to analyze the factors that control the early winter location of the shear zone and its subsequent shift seaward; (4) relate shear zone processes to seafloor characteristics and bottom processes; (5) speculate on possible side effects of the shear zone on the oceanographic and sedimentary environment; and (6) speculate on some aspects of offshore construction in the shear zone.

BACKGROUND INFORMATION

For a general description of the continental shelf and coast in the study areas (Fig. 1) and its marine environment, including currents, tides, wind, ice drift, breakup, and river inflow, the reader is referred to Barnes and Reimnitz [1974] and Reimnitz and Barnes [1974]. The background information given here is concerned mainly with the sea ice regime.

The sea ice on the continental shelf of the southern Beaufort Sea can be broadly divided into three zones [Kovacs and Mellor, 1974]: (1) a fast ice zone, extending from the coast to approximately the 20 m depth contour;

(2) a seasonal pack ice zone that covers the outer shelf and continental slope; and, beyond that, (3) the polar pack ice zone. Situated between the fast ice and seasonal pack ice zones, but generally considered part of the latter, is a fourth zone, the shear zone [Hibler et al., 1974; Kovacs and Mellor, 1974].

Fast Ice Zone

The term fast ice, as commonly used, refers to the ice near shore, which by virtue of being attached to the coast, to islands, and to shoals is relatively immobile for some unspecified time period during the winter. It generally consists mostly of seasonal ice grown in place, undergoes little deformation, and therefore is relatively smooth. But varying amounts of older ice may be incorporated, depending on its distribution during freezeup.

The seaward extent of the fast ice zone in the Arctic varies from one region to another, but it is similar from year to year in a given area. According to Jacobs et al. [1975], its seaward boundary in the eastern Canadian Arctic approximates the 180 m depth contour. They use as the sole criterion that the ice be fast and include any amount of newly deformed and multiyear ice. Disregarding ice types and morphology, most of the winter ice in the Canadian Archipelago, including that covering some very deep areas may qualify as fast ice, according to Dehn [Reed and Sater, 1974, p. 299]. In the White Sea the boundary lies on the 10 m depth contour, and along the Siberian Arctic coast on the 25 m line [Zubov, 1945]. In the Beaufort Sea east of the MacKenzie Delta the fast ice zone extends to the 20 m depth contour, while immediately west of the delta there may be no true fast ice, but rather "quasi-landfast ice" as described by Cooper [1974]. North of Alaska the 20 m depth contour is commonly considered to be the seaward limit of fast ice [Weeks et al., 1971; Burns and Harbo, 1972; Kovacs and Mellor, 1974; Reimnitz and Barnes, 1974]. Here the boundary is marked by a change from relatively undeformed, smooth ice inshore to highly deformed ice offshore. Stringer [1974], studying the western Beaufort Sea, subdivided the fast ice zone and added the term *attached ice*, which is a floating ice field temporarily attached to the shorefast ice. Many of the authors cited and still others,

including us, see problems with the definition of fast ice, and Cooper [1974] has suggested that the terminology should be changed.

Kovacs and Mellor [1974] give a general description of the growth, seasonal variability in extent, deformational features, and behavior of the fast ice applicable to our study area. This ice can contain pressure ridges, shear ridges, and hummock fields, which form mainly in early winter when new ice is still thin. Deformation of the fast ice decreases from midwinter to spring, as it approaches maximum thickness of about 2 m, and as its outer edge becomes stabilized by grounded pressure ridges and older ice [Stringer, 1974; Kovacs and Mellor, 1974; Reimnitz and Barnes, 1974]. Because the outer edge extends to the 10 or 20 m depth contour, much of the fast ice is floating and fluctuates with astronomical and meteorological tides. In the Alaska Beaufort Sea there are, however, extensive areas (up to 10 km wide) landward of the 2 m isobath where ice is resting on the seafloor at the end of the winter. This ice has been called *bottom fast ice* [Reimnitz and Barnes, 1974]. At and slightly seaward of the 2 m depth contour the ice is often marked by tidal cracks.

Seasonal Pack Ice Zone

This zone, which also has been called the Offshore Province [Weeks et al., 1971], extends from the fast ice boundary seaward for 100 to 200 km, which in the study area is in the vicinity of the base of the continental slope. The ice in this zone is generally unstable and mobile, and is largely composed of first-year ice that is extensively deformed [Weeks et al., 1971; Kovacs and Mellor, 1974]. The zone lies within the Pacific Gyre of the Beaufort Sea [Campbell, 1965], which rotates clockwise. Thus, the ice moves generally westward, with mean net long-term winter drift of from 2 to 2.5 km per day [Coachman and Barnes, 1961]. A drift rate of 3 km per day was recently calculated from studies of remote sensing images taken during April 1973 in this area [Campbell et al., 1975]. A short-term maximum drift rate of 50 km per day has been reported by Hnatiuk and Johnston [1973].

Studies of satellite images obtained north of Alaska have led to the conclusion that the ice within the Pacific Gyre behaves as a relatively

cohesive mass, with boundary slippage occurring in a zone 50 km wide immediately seaward of the fast ice [Crowder et al., 1973; Hibler et al., 1974]. Near the fast ice the seasonal pack ice drift velocity is thought to be reduced by drag [Kovacs and Mellor, 1974].

Shear Zone

The zone of differential ice motion, or slippage, along the fast ice boundary has been generally referred to as the shear zone. It is characterized by large shear ridges, pressure ridges, and hummock fields [Kovacs and Mellor, 1974].

Certain ice observations made by early explorers in the Beaufort Sea fit this general concept, in that the roughest ice terrain was encountered just seaward of the smooth fast ice of the coastal zone [Stefansson, 1921]. A winter shear ridge field 16 km long was reported by Stockton [1880] to be grounded in 24 m of water north of Cross Island, in the middle of our study area. A grounded pressure ridge 23 m high was measured by Stefansson [1921], and he mentions many higher ones grounded in up to 39 m of water off Banks Island. Zubov [1945] reports that stamkhi--grounded sea ice formations formed as a result of "ice heaping"--occur over a distance of about 500 km along the 20 m isobath east of the New Siberian Islands.

Recent studies by Klimovich [1972] show that in the inner 5 km of the shear zone, adjacent to the fast ice, ridges are up to 20 percent higher than in the outer part. Results from other studies showing the increased density, height, and draft (keel depth) of ridges near the coast have been summarized by Kovacs and Mellor [1974]. Stringer [1974] shows the relation of major shear events in the winter ice of this area to bathymetry. Reimnitz and Barnes [1974] report a sudden increase in ice gouge density seaward of the fast ice edge, which they relate to shear zone processes, and Barnes and Reimnitz [1974] find that internal sedimentary structures seen in box cores show the effects of physical disruption by grounded ice in the inner part of the shear zone.

METHODS OF STUDY

Our study is based heavily on interpretations of Landsat-1 and NOAA-2 satellite images of 1972-73. Coupled with these data are a variety of observations gathered during ice-based and shipboard operations. Methods used are outlined by Barnes and Reimnitz [1974] and Reimnitz and Barnes [1974]. More recent side-scan sonar and precisely controlled bathymetric surveys conducted in 1975 have also been incorporated into this study.

Utilization of Landsat-1 repetitive images over regions of high latitude has the advantage of image overlap of successive satellite passes. Cloud cover permitting, we were able to trace particular ice features for three consecutive days every 18 days.

In the Landsat images the shear zone is generally characterized by pronounced lineations in the ice cover that approximately parallel the shore. Shear ridges are common features along the northern Alaskan coast and are often tens of kilometers long [Kovacs and Mellor, 1974], whereas pressure ridges are irregular and randomly distributed [Anderson, 1970]. Therefore, we interpret many of the light-colored linear features seen in the images as shear ridges. Narrow leads and frozen leads are also often linear but are darker than the thicker ice. Comparing ground observations with the pictures we find that linear zonations less than 30 m wide can be detected under favorable conditions.

RESULTS

Remote Sensing

Landsat-1 images discussed below cover the period from freeze-up in the fall of 1972 through the breakup in the summer of 1973. No pictures were obtained during the Arctic night from November through February.

The formation of a new ice cover at the onset of winter is shown in Figure 2. This image, taken on 4 October 1972 (1073-21223) covers an area of about 180 km square. The coastal plain is blanketed by thin snow, and most of the rivers have stopped flowing. New ice is mainly seen on the shallow

inner shelf, where salinity is lower and water cools faster than it does offshore. A light southwesterly wind is moving the thin ice obliquely offshore, where in many spots it is trapped by islands. The total absence of old ice on the shelf, confirmed by Nimbus 5 microwave images for 16 December 1972 and 10 February 1973 [Campbell et al., 1974] is significant to our later discussion. Conditions therefore differed considerably from those of the previous years, in which large numbers of ice island fragments were reported grounded on the shelf (for example, Breslau et al., 1971). The last remnants of these fragments were seen in Landsat images of August 1972.

Early 1973 Landsat-1 images of the Beaufort Sea were recorded from 8 March to 21 April. At this time the fast ice along the coast between Herschel Island in Canada and Point Barrow, Alaska (Figure 1), is well stabilized and approaching its maximum thickness of about 2 m. The outer boundary of the relatively undeformed fast ice adjacent to the coast is generally marked by pronounced lineations in the Landsat-1 images. These are interpreted as shear ridges formed earlier during the winter. The first pronounced shearline near the coast, or the first marked change in ice appearance from uniform to irregular, was mapped as representing the seaward boundary of the relatively undeformed floating fast ice (seaward extent of stippled pattern in Figure 1). In some areas it was difficult to decide where to place the boundary. In these cases later images, when ice features were enhanced by melting of the sea ice surface, were used. Comparing the various images obtained along the coast from early March to ice breakup in July we found no new major ice deformational features forming within the floating fast ice zone shown in Figure 1. The cross-hatched area near the coast in Figure 1 represents regions in which water depth is less than 2 m, where the fast ice is resting on the seafloor at the end of the winter.

The most detailed analysis of ice processes was done in the area between Cape Halkett and Canning River, where our previous seafloor studies were concentrated. In this area, images made on 14-16 March (nos. 1234-21175, 1235-21241, 1236-21297) show that the most recent events were the formation of a pronounced lead trending irregularly across the shelf (B in Figure 3) and one trending parallel to the coast (A in Figure 3). Both are frozen, but the ice is still thin, as interpreted from its relatively dark color. Matching

the sides of the shore-parallel lead (A) indicates that the pack ice was displaced eastward relative to the fast ice landward of the lead by 2 km. Wind records for the North Slope suggest that this may have occurred on 7 March [Stringer, 1974] during relatively strong westerly winds. Because shearing along the shore-parallel lead was associated with the ice movement, this feature may be called a shearline. It is located seaward of the undeformed fast-ice edge (Figure 1), indicating accretion of the fast ice zone.

The shore-parallel shearline and the lead trending obliquely across the continental shelf were well preserved between 14-16 March and 1-3 April when new images were obtained in the area (nos. 1252-21175, 1253-21233, 1254-21292). No changes could be detected by matching these images and the earlier ones to coastal features and comparing the location and configuration of ice features. This match is accurate to within about 300 m. Thus, all ice across the width of the shelf moved less than 300 m, if at all, during a 20-day period.

Early April images show a large lead (D) and an active shearline (C) barely seaward of and parallel to the edge of the continental shelf (stippled area, Figure 3). The shearline may have been active for several weeks, but no image is available to confirm such activity. Matching particular ice features seen in the images of 1 and 2 April, a 4 km/day westward displacement of the pack ice relative to the stationary ice sheet over the shelf is indicated. The rate of ice movement was uniform through a 24-km-wide zone seaward of the shearline, as indicated by the length of the ice-displacement vectors on Figure 3. No drag effects along the shearline were noted.

Visible-band NOAA-2 satellite images taken during the same time period permit a large-scale view of ice conditions in the entire Beaufort Sea. Figure 4 is an example of a small portion of such an image, taken on 5 April 1973. The active shearline seen in the Landsat images of 1-3 April along the shelf edge (Figure 3,C) can be seen in the NOAA image. It also shows a pronounced linear lead (traced in Figure 5) extending hundreds of kilometers into the Arctic Ocean. Using this lead as a marker, large-scale pack ice movement and its relation to the associated shearline along the Beaufort Sea shelf were monitored.

Figure 5 shows the location of the major lead on NOAA-2 pictures of 26 March, 31 March, and 1 April. The images are somewhat distorted but can be matched with a fair degree of confidence to northern Alaska. The wide place in the shearline along the edge of the continental shelf is the large open lead (40 × 15 km) seen in Landsat images at this time (Figure 3,D). The large dots are identifiable points seen along the lead in all three images. This compilation shows that the pack ice in a 350-km-wide zone north of the shearline is moving westward rather uniformly at about 10 km per day. The lead seems to be little affected by drag along the shearline, which corresponds roughly to the edge of the shelf. This confirms the more detailed Landsat studies shown in Figure 3.

There is no usable Landsat-1 image in the study area between 3 April and 26-27 May. Ice conditions on 27 May are shown in Figure 6 (no. 1308-21290). The pronounced coast-parallel shearline and coast-normal lead seen in images from 14 March to 3 April have disappeared. These features may have been destroyed by deformation or displacement of the entire ice canopy seaward of the early winter shearline (Figure 1), leaving only the true fast ice landward of this line intact. Such deformation is suggested by the formation of short, irregular, frozen, northeast-striking leads about 10 km west of Cross Island (Figure 6), which have been previously noted by Stringer [1974]. The lead and shearline under discussion may also have been masked by new or drifting snow. A new pronounced coast-parallel lineation not present on 3 April is seen in the image of Figure 6. This lineation can be traced westward across Harrison Bay, where it bulges northward roughly following the 20 m depth contour, far seaward of the early winter shearline. This bulge was pointed out by Stringer [1974] using the same images and by Burns and Harbo [1972]. It will be discussed again below.

The onset of summer, marked by river flooding of the fast ice in the eastern part of the image area (Sagavanirktok River), is evident in Figure 6. A strongly linear active shearline can be seen on this and the previous day's image. Overlaying these images, we find that the ice landward of the shearline is immobile. Seaward of the line it is moving westward. Comparing the location of identifiable ice features during this 24-hour period, indicated by dots on Figure 6, indicates ice displacement westward at a rate of 6 km

per day. Close to the shearline the ice drift vectors are parallel. Farther seaward a small onshore component is indicated, implying that some portion of the ice canopy is used up in the formation of shear and pressure ridges. The entire ice canopy out to 90 km from the shearline is highly fractured but apparently moving as a rather coherent mass. The westward displacement rates do not seem to be affected by drag along the shearline, but are instead somewhat higher there than farther offshore.

Visible-band NOAA-2 satellite images can be used during this time period to study large-scale ice movement in the Arctic Ocean north of Alaska. The images of 5 April and 27 May (Figure 7) show the long lead discussed earlier and presented in Figures 4 and 5. The projection of these images is not the same as that of the others, resulting in a different distortion of the Earth's surface. But their match to the continent is more reliable and the ice displacement of the lead during the 52 days preceding 27 May ranges from 160 km (3 km/day) near the continent to 80 km (1.5 km/day) at a point 450 km seaward off the coast.

The next Landsat images in the study area cover the period from 13 June to 15 June. At that time no coast-parallel shear could be seen on the continental shelf, and east of Oliktok Point all ice on the shelf was stationary during the two-day period. West of Oliktok Point, ice was moving obliquely onshore toward Cape Halkett along a conspicuous lead. This movement is clearly seen seaward of the 50 m isobath but apparently did not affect the shearline first seen along the central shelf on 26 May.

From the above discussion of Landsat and NOAA-2 images, it is apparent that shear events along the inner and central shelf are intermittent, whereas westward ice drift along the shelf edge is continuous. This implies that shearing occurs seaward of the shelf edge between the times of shear events on the shelf, as was seen in early April.

Figure 8 shows the beginning of sea ice breakup, as seen in the following data cycle (30 June, no. 1342-21170; 2 and 3 July, nos. 1344-21283, 1345-2142). At this time of the year, meltwater drains from relief features, leaving the ice and snow white, and collects on smooth ice, enhancing image definition of morphological features. East of Oliktok Point, the ice is

still intact and no active shearline is seen on the shelf. Preserved shear features are clearly visible. West of Oliktok Point, the ice is beginning to break up and move westward close to the Colville Delta and along the outer shelf. However, in a 15-km-wide zone bulging seaward across Harrison Bay along the 20 m isobath, and coinciding with major shear events of late winter, the ice remains intact.

Figure 9 shows a strip of U-2 photographs, taken from an altitude of 20,000 m on 21 June 1974. This strip extending north from Prudhoe Bay shows the various ice zones and features discussed above in great detail. The sea ice morphology is similar to that of the previous year, with the relatively undeformed fast ice extending a short distance beyond Reindeer Island. It is followed by a zone of highly deformed and probably grounded ice in the stamukhi zone, and the mobile ice beyond.

The most pronounced linear ice features, taken mainly from the early July 1973 Landsat images, which record major shear events along the inner part of the shear zone, are shown in Figure 10. The resultant ice drift vectors, implying the general direction in which the pack ice is moved along the shear-lines, and the dominant wind direction, are also shown, along with the locations and approximate extent of charted shoals (hachured areas).

The striking correlation between the distribution of shoals and ice lineation (that is, shear ridges, pressure ridges, and linear hummock fields which are all known to have considerable draft) suggests that the ice is interacting with the seafloor.

Summer Ice Observations

During summer, grounded ice is commonly found on offshore shoals [Reimnitz et al., 1972, 1974]. This ice generally appears to be of pressure-ridge origin, with sail heights of 5 to 8 m, keel depth of at least 10 m, and is elongated parallel to isobaths. Drifting smaller floes frequently accumulate along the seaward side of these grounded floes, which act as fences. Sometimes the grounded ridges occur in long lines paralleling isobaths, marking a distinct boundary between scattered ice on the inner shelf and tightly packed ice on the central shelf. Figure 11 is an example of such a boundary, photographed

from the air northeast of Barrow on 31 August 1975. Such boundaries roughly correspond with the seaward boundary of the fast ice. It closely approaches major promontories and offshore islands, as at Herschel Island, Barter Island, and Cross Island. North and east of Cross Island, large stationary floes in average years block small-boat passage offshore.

A continuous belt of apparently grounded floes was observed along nearly the entire Alaskan Beaufort Sea coast by W. Stanley Hugget (Ocean and Aquatic Affairs, Dept. of Environment, Canada) in late August, 1966 [personal communication, 1974]. This belt straddled the 18 m isobath, separating relatively ice-free waters on either side, and was impenetrable to small vessels. Its location again roughly corresponds with the zone of major ice ridges formed along the seaward boundary of the undeformed fast ice (Figure 1).

Interaction of Ice and Continental Margin

The relation between pronounced ice lineation preserved by the end of the winter (Figures 8 and 10) and shelf bathymetry, the stabilizing effect of ice ridges on the fast ice, and the location of grounded ice in summer indicate that the zone broadly straddling the 20 m isobath is the locus of the strongest interaction between the ice pack and the seafloor.

Ice ridging is best defined, most concentrated, and closest to land off Narwhal and Cross Islands. Downdrift (westward) from Cross Island ridges spread in a widening zone, following the pattern of shoals at increasing distance from shore. On the seaward-facing beaches of Narwhal and Cross Islands, where ridges are formed close to shore, one can observe year after year the effects of pronounced ice push and remnant ice piles from the previous winter. Figure 12 is a photograph of ice deformation on Narwhal Island taken in June 1970. Argo and Reindeer Islands, downdrift of and somewhat protected by Cross Island, are relatively little affected by ice push. Still farther downdrift and several kilometers from the major ice ridge systems, beaches are little affected by winter ice push.

Figure 13 is a typical example of such a barrier island beach, as photographed in May 1972 on Long Island. The fast ice rests smoothly against the beach face and seafloor out to the vicinity of the 2 m isobath, which is marked by several tidal cracks. Beyond the cracks the fast ice is floating and undeformed out to the first major shoals, discussed later. Still farther westward, across Harrison Bay, the undeformed fast ice stretches for many kilometers from shore, protecting the coast. Nearshore bottom profiles off Cross Island, where the shear zone impinges on the coast, and Spy Island, where it lies some distance offshore, are very different (Figure 14). Spy Island (Figure 15), typical of regions protected from the drifting ice pack, has a gentle and smooth seaward slope, while the bottom at Cross Island is steep and irregular.

The inner shelf bathymetry of the central part of our study area is shown in Figure 15, as surveyed from 1949 to 1951. During the summer of 1975, the U.S. Geological Survey's R/V *Karluk* was used to run bathymetric surveys across some of the shoals. With a Del Norte Trisponder system and shore control stations at the established bench marks indicated by triangles in Figure 15, the navigational control for the surveys was accurate to within 5 meters. From the 1949-51 and 1975 surveys a comparison of certain ridge cross sections and their locations was made. These are presented in Figure 16, with individual profiles keyed to Figure 15 by letters A through H. The 1949-51 bottom configuration is represented by the dashed line, the new configuration by a solid line, which also shows microrelief due to ice gouging.

The shoals are very subtle features, considering that the vertical exaggeration is about 1:30. Shoals A and B, located north of Spy Island, are about 3 m high. The seaward one (A) has shifted landward by about 200 m, retaining its shape, while the landward one (B) shifted only 120 m, but increased in size. Among the shoals north of Cottle Island, C is closest to shore. Considering that the dashed line represents an average drawn through a number of data points on the contour chart, while the solid line was traced directly from the fathogram with all detail, the two profiles are remarkably similar. Ridge cross sections D through H, located farther offshore, show pronounced changes in profile and location. All have migrated landward 100-400 m (an average of 200), and all but D have undergone considerable changes

in shape. In general, the offshore ridges lying within the shear zone have changed more than those farther inshore. The 1975 bathymetric data are unsuitable for evaluating any shore-parallel migration of shoals. Side-scan sonar records obtained in 1973 across the fast ice/pack ice boundary of the previous winter show a change in ice gouge density in the vicinity of the boundary [Reimnitz and Barnes, 1974]. The present detailed analysis of shear events on the shelf has enabled us to look more closely at how these relate to gouge density on the shelf.

Shear events on the shelf that were actually observed in Landsat images, or to which some broad time limits could be assigned, are shown in Figure 17. In the eastern part of the figure, where six sonar survey lines were run the following summer, ice gouge density patterns are shown by cross hatching. Figure 17 distinguished between areas with from 50 to 100 gouges and areas with more than 100 gouges per kilometer of ship's track. The highest gouge densities occur in a zone 8-14 km wide seaward of the relatively undisturbed fast ice shown in Figures 1 and 17. The average gouge depths also are greater in this zone than on either side [Reimnitz and Barnes, 1974].

In several of our crossings of the undeformed fast-ice edge (early winter shearline) the change in gouge density was very abrupt and corresponded with this line to within the limits of resolution of Landsat images. The lower part of Figure 18 is a line drawing of ice gouges seen in sonographs along both sides of the ship's track (represented by the two parallel lines in the middle of the record) across the early winter shearline near Cross Island. In the fast-ice zone there are only a few minor gouges, but seaward the bottom is densely gouged.

The upper part of Figure 18 is a line drawing based on a high-resolution seismic reflection record obtained along exactly the same track as the sonograph below. It shows the highly irregular nature of internal reflectors within the area of abundant gouges, and rather evenly bedded materials in the area of smooth bottom.

Both the seismic record and the sonograph show a slight break in slope at the boundary between the two bottom morphologies. Landward of the break the seafloor is about 1 m shallower. The same phenomenon can be seen in

several other crossings of the ice boundary, and we therefore do not consider this a mere coincidence. If indeed a causal relation exists between ice zonation and bottom morphology, the smooth high ground overlain by a thin unit of evenly bedded materials landward of the gouged area may be the result of (1) accretion from sediment-laden waters retained inshore of the first major grounded ice barrier, (2) faster sediment accretion due to lower rates of ice gouging and related resuspension and winnowing, or (3) current scour and redeposition along a grounded ridge system serving as a circulation boundary. Other possible explanations unrelated to the present ice zonation include the outcropping of more resistant older sediments or the presence of permafrost at the seafloor. While we feel that the phenomenon observed is significant, and probably related to ice zonation, there are insufficient data to make an interpretation.

DISCUSSION

Ice Zonation and Terminology

The results of this investigation indicate the presence of a distinct ice zonation on the Alaskan Beaufort Sea shelf, a pattern that usually recurs (annually) and is process-controlled. The data also suggest that previously used terms "fast ice zone" and "seasonal pack ice zone" are too broad and ill defined, and require subdivision.

Fast ice zone. Using as the sole criterion that the ice be fast to shore or the seafloor for an unspecified period of time, and ignoring ice types and intermittent events, all ice on the shelf may qualify as fast ice, including the large early winter ridges of the shear zone, which are firmly grounded on the seafloor (Figure 19). The zone in which these occur is very important in terms of ice morphology, dynamics, interaction with the shelf surface, and future commercial offshore development. This zone should be distinguished from the zone landward.

In this report we include within the fast ice zone those areas in which the sea ice (a) has essentially grown in place, (b) has undergone relatively little deformation, (c) is truly fast after formation of the

first major shore-parallel grounded shear or pressure ridge system (in water depth generally ranging from 10 to 20 m), and (d) lies between land and the first major ridge system (Figures 1 and 19). The fast ice zone does not include the system of grounded ridges along its seaward boundary, and in this respect we differ from the definition used by Stringer [1974] and Kovacs and Mellor [1974]. While it is the most meaningful one for the northern coast of Alaska, our definition may not be useful everywhere along the margin of the Arctic Ocean.

The fast ice zone as defined here is on the average 15 km wide between Point Barrow and Herschel Island (Figure 1), with a minimum of less than 5 km at Herschel Island and a maximum of about 30 km west of the Colville Delta. In the eastern part of the area of Figure 1 the outer edge approximates the 20 m depth contour; in the western part it lies between the 10 and 15 m depth contours. Figures 8 and 10 show that seaward of the early winter shearline in Harrison Bay lies another broad zone of relatively undeformed ice extending seaward to the 20 m depth contour, up to 80 km from shore. Our observations of the ice breakup in 1973 and of ice gouge densities indicate that the major grounded ridges lie along the 20 m depth contour in this area. However, an increase in the gouge density along the early winter shearline inshore (10 m depth contour) indicates that some of the inshore ridges were also grounded. On the basis of its morphology and stability during late winter, this Harrison Bay ice between the 10 m and the 20 m depth isobath might have to be included under fast ice, or it may require still another term.

Ten to seventy-five percent of the fast ice zone along the coast of northern Alaska lies between the shore and the 2 m depth contour. Because by late winter the fast ice reaches a thickness of 2 m, it rests on the bottom in most of these areas. In Harrison Bay this zone is up to 15 km wide (Figure 1). The seaward boundary of the bottom-fast ice zone commonly is marked by tidal cracks (Figures 13 and 19). Where the 2 m contour is far from shore, the bottom from this point seaward drops off sharply [Reimnitz and Bruder, 1972], and the bottom sediments change abruptly from well-sorted sand inshore to poorly sorted mud offshore.

These facts and various other observations [Barnes and Reimnitz, 1974; Reimnitz and Barnes, 1974] lead us to conclude that in terms of ice, bottom,

hydraulic, and thermal processes the 2 m depth contour represents an important boundary. For these reasons we propose that the fast ice zone be further subdivided into floating fast ice and bottom-fast ice (Figures 1 and 19), with the boundary at 2 m water depth. Kovacs and Mellor [1974, Figure 3] use the term ice-foot for this part of the fast ice. This term, however, has generally been used for narrow belts of ice along beaches, rocky shores, or ice in contact with open water, formed by various processes of adfreezing on top or at the margin during onset of winter [for example, Zumberge and Wilson, 1953; Nichols, 1961; Owens and McCann, 1970; Gary et al., 1972; McCann and Carlisle, 1972; and Marsh et al., 1973]. An ice-foot, therefore, should be distinguished from fast ice by its means of formation.

Stamukhi zone. Large grounded ridges form along the inner part of the shear zone seaward of the fast ice. The fast ice boundary is marked by the first major ice-deformational lineament (heading out from shore) seen in Landsat images. In the area of our detailed studies this shearline runs tangential to Cross Island. Westward the line swings landward and again closely approaches the next island chain some 60 km downdrift. From here it roughly follows the 10 m isobath in a broad landward curve across Harrison Bay and then seaward past Cape Halkett [Figures 1 and 10].

Once formation of a grounded ridge stabilizes the fast ice, successive shear events generally occur farther seaward. These events commonly are localized by offshore shoals (Figures 10 and 19), where ridges interact with the sea floor. Grounded ice ridges forming on well-developed shoals in the area between Cross Island and Harrison Bay eventually stabilize the ice canopy to such a distance from shore that the westward drift of pack ice within the Pacific Gyre is deflected offshore across Harrison Bay. This protects the bay and allows the formation of another extensive sheet of undeformed and immobile ice seaward of the early winter shearline inshore. The edge of the drifting pack ice off Harrison Bay is then localized along the 20 m isobath, where ridges form in contact with shoals (Figure 10).

There appear to be great similarities between the Alaskan Beaufort Sea and the Siberian Sea in the location of the fast ice edge near the 20 m isobath, and in its protection by grounded ice seaward. As pointed out

earlier, stamukhi--grounded sea-ice features--occur for hundreds of kilometers along the 20 m isobath in the Siberian Arctic. Zubov [1945] states that stamukhi (1) often occur on shoals, (2) are made up initially of heaped blocks of various dimensions and forms, (3) usually last a few years, and (4) act like islands in the shallow regions of the Arctic Seas insofar as they protect the shore from the pressure of ice, thereby causing the ice between the shore and the row of stamukhi to be flat and even, not heaped and jumbled.

The term *stamukha* (singular for *stamukhi*) as defined in English-language glossaries does not convey the meaning implied by Zubov [1945]. According to the *Glossary of Geology* [Gary et al., 1972], a stamukha is "a fragment of sea ice stranded on a shoal or a shallows." Burke [1940] and Zubov [1945] include the grounding of floes as a mechanism that triggers the formation of stamukhi, but indicate that they also form by hummocking of thin ice over shoals.

The zone of grounded ridges that forms seaward of the relatively undeformed fast ice off northern Alaska is a very important factor in the overall marine environment and for future offshore development. It therefore seems appropriate to introduce a new term for this zone. Following the Russian use of the term stamukhi, we propose *stamukhi zone* for the recurring belt of grounded ridges and hummocks (Figure 19).

In the area of our detailed studies the stamukhi zone is encompassed by the area of heavy black arrows in Figure 10. Off Cross Island the stamukhi zone is about 20 km wide and is well defined. Off Harrison Bay it is more than 50 km wide, but actually consists of two zones separated by a broad expanse of relatively undeformed ice. Previous studies of this area have assigned the ice of this zone to the fast ice zone [Stringer, 1974; Kovacs and Mellor, 1974]. Considering ice dynamics, the stamukhi zone in early winter is a part of the shear zone [Kovacs and Mellor, 1974], where the pack ice of the Pacific Gyre rubs along the continent (Figure 10).

Pack Ice Drift

Studying repetitive Landsat and NOAA-2 satellite images from the middle of March to the end of May 1973, we found that the pack ice in the Pacific Gyre moves westward along the continental shelf at 3-10 km per day. But much higher short-term drift velocities have been reported by others [Hibler et al., 1974; Hnatiuk and Johnston, 1973]. During the period covered by our images, slippage between the Pacific Gyre and stationary ice along the coast generally occurred at the shelf edge. Ice on the continental shelf remained stationary within the spatial resolution of Landsat imagery (300 m) for up to 20 days and probably longer. Slippage occurred intermittently within or along the seaward edge of the stamukhi zone on the continental shelf, where much of the available energy is expended on the sea floor.

Regardless of where the slippage occurs, we found individual events to be restricted to a zone several hundred meters wide and not distributed over a 50-km-wide zone as stated by Crowder et al. [1973] and Hibler et al. [1974]. Thus the calculated ice movement vectors did not indicate drag effects near the edge of the stationary ice as postulated by Kovacs and Mellor [1974]. In fact, the rate of movement in several instances was higher at the shearline than it was ten or more kilometers seaward.

Factors Controlling Location of Fast Ice Edge

Because the edge of the fast ice and the stamukhi zone forms year after year at roughly the same locations in the Arctic, it is of interest to examine the causes that localize the formation of major grounded ridges and hummocks in our study area.

Croasdale [Reed and Sater, 1974, p. 298] has pointed out that the fast ice boundary, being similar from year to year regardless of the presence of multiyear floes, implies that grounded ridges along the fast ice edge must be first-year ridges. He also mentions the further implication that newly formed ridges may therefore seldom have keels deeper than 18 m, the presumed water depth at the fast ice edge. Indeed, according to Hibler, submarine sonar data indicate that only 1 percent of all ridge keels are deeper than

18 m [Reed and Sater, 1974, p. 299], a depth that may be related to the mechanisms and structure of pressure ridges [Parmerter and Coon, 1972]. Hibler [Reed and Sater, 1974, p. 300] believes that more important than the distribution of keel depths may be the increased current drag on ridge keels, where the boundary layer under a moving ice cover impinges on the bottom in shallow water. The fast ice generally grows from the shore outward in response to the faster cooling rate of shallow water and the lower salinity inshore.

Is there some factor of fast ice thickness or strength at a particular time of the season that determines at what distance from shore the forces of the pack ice are arrested? In some areas of the Arctic the extent of fast ice is determined by the configuration of land masses, providing shelter against the forces of the drifting pack. All of the above factors were considered in our attempt to answer what controls the location of the fast ice edge in our study area.

Conditions in the winter of 1972-73 were ideal for determining what ice types are involved in the stamukhi zone protecting the fast ice edge. There was no multiyear ice on the shelf from freeze up until midwinter and therefore the ridges of the stamukhi zone were formed from first-year ice. Our study of ice morphology and behavior indicates that the stamukhi zone straddles the 10-30 depth range. Ice gouge density patterns off Harrison Bay, surveyed in 1972, imply that the stamukhi zone extends to at least 40 m depth. Thus, the 18 m ridge-keel depth limit reported for 99 percent of free-floating ridges seems to have no special significance for shallow water depth. If, on the other hand, increased current drag on ice keels in shallow water were effective in stabilizing the edge of pack ice drift on the shelf, this should also result in the formation of hydraulic bedforms. Side-scan sonar techniques used in our studies are well suited for the detection of hydraulic bedforms, we have not noticed anomalous increases of current-produced bottom features in the stamukhi zone. Therefore, current drag probably is not an important factor in controlling the location of the fast ice edge and the stamukhi zone.

Evaluating how the strength of the fast ice influences the location of the stamukhi zone is difficult without adequate seasonal data. The fast ice growth rate and strength should be influenced by variations in surface water salinity and temperatures on the shelf. These parameters were plotted for August and September 1972 in the study area [Hufford et al., 1974]. The configuration of the fast ice edge during the following winter does not show irregularities that can be attributed to changes in water characteristics along the coast. Also, the greater width of fast ice in Harrison Bay, where post-summer water cooling rates in extensive shallow areas should be higher than elsewhere, apparently is best explained in terms of ice dynamics, as outlined earlier. For these reasons we feel that the fast ice itself is not a primary factor in determining where shearing events and ridge formation occur on the shelf.

The last factor to consider is the relation of coastal configuration to pack ice drift and how this may influence the location of the fast ice edge and stamukhi zone. The regional setting is that of an irregular coastline tangential to the arctic pack-ice drift within the Pacific Gyre. Hibler et al. [1974] thought of this gyre as "a large cohesive wheel slipping at the edge." In this model, the location of the wheel's (gyre's) rim is determined by the bumps in the road surface--the coastal promontories.

Major promontories in the area are Herschel Island, Barter Island, Cross Island, Cape Halkett, and Point Barrow (Figure 1). At the first three promontories our observations are consistent with the assumed model. The fast ice zone is narrow, and ridge systems seaward are closely spaced and parallel, describing the trajectories along which the wheel slips (Figures 8 and 10). Downdrift from the promontories the early winter slip surfaces tend to swing landward, following the broad indentations in the coastline. Later in the season the slip surfaces generally lie farther seaward, along rather straight lines extending from one promontory to the next. In keeping with the assumed model, the widely spaced slip surfaces in the regions between promontories can be related to changes in rotation rate of the slipping wheel. When it slows down, the pressure of the pack is applied between the promontories on the fast ice in early winter, or on the strongly resistant stamukhi zone later in winter.

The configuration of the fast ice zone in the vicinity of Cape Halkett needs further explanation in terms of our assumed model. The early winter shearline and ice ridges describe a broad landward curve across the 90-km-wide Harrison Bay (Figures 8 and 10), roughly following the 10 m depth contour. Ice slipping westward along this line piles up toward Cape Halkett and is deflected seaward for some distance north of the cape. Later in the season, shear events projecting straight across the bay interact with the early ridge systems at an angle. The interaction of early winter ridges with late winter ice drift north of Cape Halkett results in the formation of major but highly irregular ridge and hummock patterns (Figure 10). Parts of these apparently are grounded and provide shelter for the growth of another extensive sheet of undeformed ice seaward of the early winter shearline in Harrison Bay.

The data analyzed suggest that the configuration and location of the recurring stamukhi zone and extent of the fast ice in the study area may be best explained in terms of a model in which the westward pack ice drift interacts with an irregular coastline and offshore shoals.

Effects of Ice Zonation on Marine Geology and Bottom Processes

For the greater part of the year the relatively undeformed fast ice rests quietly against the shoreface, unaffected by the forces of the marine environment. Pronounced deformation of beach deposits by sea ice during winter time is largely restricted to the major promontories such as Cross Island. Even during the short summers, the grounded ridges of the stamukhi zone commonly shelter the inner shelf and shore from drifting ice and limit the fetch for wave generation.

The stamukhi zone, straddling the midshelf region, is where much of the available marine energy is expended on the shelf surface on a year-round basis. Ridging initially occurs between the 10 m and 20 m isobaths, stabilizing the fast-ice edge. Ridge accretion against the initial ridge system and stabilization by bottom contact gradually shifts the dynamically active zone seaward (Figure 19). The end result is a wide stamukhi zone. The high amount

of energy expended on the seafloor during this process and the eventual dislodging of grounded ice in the succeeding summers are manifested in the high ice gouge intensities in this zone and the chaotic nature of internal sedimentary structures. Also, a sediment textural boundary [Barnes and Reimnitz, 1974] roughly corresponds with the fast ice edge as delineated in Figure 1, suggesting a possible relation between ice zonation and sediment transport.

There is a striking relation between ice ridge lineation in the stamukhi zone and bathymetric shoals (Figure 10). This suggests that ice deformational events may be affected by ice interaction with these shoals. A similar relation has been inferred for regions along the Siberian coast, where recurrent stamukhi form on offshore shoals [Zubov, 1945]. Offshore shoals between Harrison Bay and Cross Island have been studied with seismic profiling techniques. The Holocene marine sediments in this region generally are only several meters thick on a flat-lying sub-bottom reflector. The shoals correspond to a thickening marine section, indicating that they are constructional features postdating the last marine transgression.

The shoals and the modern barrier island have rather similar cross sections. However, the shoals are composed of well-sorted sand with some individual pebbles [Reimnitz and Barnes, 1974], while the barrier islands consist of sandy gravel to gravelly sand. Because of this difference in composition the shoals do not appear to represent drowned barrier islands. Nearshore bars 2-3 m high are present along Pingok and adjacent islands. These are migrating under the influence of summer waves and currents [Short, 1975]. The much larger shoals under discussion clearly do not form or migrate under the influence of similar nearshore processes.

All available evidence leads to the conclusion that the shoals are not hydraulic bedforms related to open-water conditions, but were formed and presently are migrating under the influence of ice-related processes. Future studies will have to show whether such shoals form by (a) the bulldozing action of ice during one or several major events, (b) the cumulative effects of several thousand years of ice push by grounded ridges along the edge of the Pacific Gyre rubbing against the continent, or (c) winter currents being channeled along major grounded ridge systems to concentrate available sediments

into sand ridges, or whether several of these processes act together to form the shoals.

Shoals in the stamukhi zone are not restricted to the region of our studies but extend westward to Point Barrow, according to National Ocean Survey chart No. N.O. 16004 (1973 edition). East of Cross Island similar shoals are shown, but they are not so numerous there as in the western sector. This may be due to a lack of sounding data.

Where the stamukhi zone lies close to coastal promontories, as off Cross Island, the seafloor slopes steeply away from the beach. Where it lies several kilometers offshore, bottom slopes are gentle.

In summary then, we see a causal relation between the overall shelf profile and winter ice dynamics and ice zonation. On low-latitude shelves the high-energy surf zone shapes the shelf profile in the coastal environment. Along the Beaufort Sea coast, ice dynamics in the stamukhi zone of the central shelf leave an imprint in the form of pronounced shelf profile anomalies. But the effects of the stamukhi zone are probably not restricted to marine geology, geomorphology, and seafloor dynamics.

If major ice ridge systems conform to the bottom for considerable distances, the stamukhi zone may be an oceanographic barrier separating the inner shelf from the open ocean. The reported sediment boundary along the fast ice edge may be related to this in some still unknown way.

Winter temperature profiles of floating ridges with values as low as -24°C in the upper part, increasing to seawater temperature at the keel, have been reported. Elimination of water circulation by bottom contact would result in lower keel temperatures of a grounded ridge, and such lowered temperatures would ultimately reach the sea floor. Thus, the thermal effects of grounded ridges in the stamukhi zone may affect the nature and distribution of offshore permafrost.

Implications For Offshore Development

Several aspects of results reported here are of relevance to planned offshore development of the Prudhoe Bay oil field. In the near future offshore

development probably will be restricted to the shelf landward of the stamukhi zone, the least hostile environment. Such developments may include construction of artificial islands, as in the Mackenzie Delta region, and special drilling platforms to withstand the forces of drifting ice floes and ice island fragments.

The extent of the fast ice zone off Prudhoe Bay is controlled by Cross Island, which appears to be a typical barrier island. This island has changed little since it was mapped accurately some 25 years ago. A small house on this island has been unaffected by ice push for some 30 to 40 years. The shoals between Cross Island and Harrison Bay, whatever their origin, today take the brunt of the ice forces year round. Moreover, they seem to influence winter ice dynamics and extent of the fast ice. The shoals have migrated several hundred meters during a 25-year period, yet they have retained their overall identity.

From these observations it appears that artificial drilling islands, placed within the fast ice zone shoreward of the stamukhi zone, have a good chance of withstanding the forces of the ice in this area. Furthermore, similar structures properly placed in the stamukhi zone might be used to extend the area of fast ice seaward.

SUMMARY OF CONCLUSIONS

(1) The ice pack rotating clockwise within the Pacific Gyre rubs along the continental margin north of Alaska, resulting in the formation of major linear ridge systems every winter. Initially, their location is principally controlled by major promontories. These ridges are stabilized by grounding, which is focused by shoals downdrift of major promontories.

(2) Slippage occurs intermittently along or seaward of the grounded ridges, forming new grounded ridges in a widening zone, the "stamukhi zone," at depths of 10 to 40 m.

(3) During long periods between these intermittent events along the stamukhi zone, pack ice drift and slippage are continuous along the shelf edge at average rates of 3-10 km per day.

(4) Slippage is observed to occur in a zone several hundred meters wide, the ice for tens of kilometers seaward of the slip boundary moving at uniform rates, generally with no observed drag effects.

(5) The seasonal fast ice grows in the protected belt between the stamukhi zone and the land, remaining relatively undeformed.

(6) This fast ice zone is further subdivided into floating and bottom-fast ice. The latter may extend up to 15 km from land, and can constitute as much as 75 percent of the total fast ice zone.

(7) This zonation is different from previously used zonations, in that the stamukhi zone is not part of the fast ice zone. The proposed nomenclature emphasizes ice interaction with the shelf surface.

(8) Much of the available marine energy is expended on the seafloor within the stamukhi zone, while the inner shelf and coast are relatively protected year round.

(9) Energy expended on the seafloor is manifested in the high ice gouge density, deep ice gouges, and intensely disrupted internal sedimentary structures within the stamukhi zone. There also is strong evidence that the stamukhi zone influences distribution of sediment textures on the shelf.

(10) Shoals that presently localize major linear shear ridge elements within the stamukhi zone may originally have formed in response to ice-bottom interaction within the shear zone and today appear to be migrating under the influence of ice-bottom interaction.

(11) Anomalies in the arctic shelf profile are related to sea ice zonation and sea ice dynamics.

(12) Artificial islands similar in nature and location to the shoals studied should be able to withstand the forces of the ice for 10-20 years.

(13) It seems possible that artificial islands, properly placed, may be used to modify the location of the shear zone and open larger areas of the shelf to development.

ACKNOWLEDGMENT

We are grateful to Arctic Marine Freighters for their continuing assistance to our small boat operations staged out of Prudhoe Bay. The study of Landsat-1 images was funded by NASA (contract no. S-7024-AG). Harry Hill of the U.S. Geological Survey has operated and maintained the electronics equipment aboard our vessels, and deserves special thanks.

REFERENCES

Anderson, V. H. 1970. Sea ice pressure ridge study: an airphoto analysis. *Photogrammetria, 26*(5/6), 201-226.

Barnes, P. W., and Erk Reimnitz. 1974. Sedimentary processes on Arctic shelves off the northern coast of Alaska. In *The Coast and Shelf of the Beaufort Sea* (ed. J. C. Reed and J. E. Sater), Arctic Institute of North America, Arlington, Va., pp 439-476.

Breslau, L. R., E. J. James, and M. D. Trammel. 1971. The underwater shape of a grounded ice island off Prudhoe Bay, Alaska. In *Proceedings of the First International Conference on Port and Ocean Engineering under Arctic Conditions*, vol. 1, University of Norway, Trondheim, Norway, 119-139.

Burke, A. 1940. *Morski L'dy* (Sea Ice), Izdatel'stvo Blavsevmorputi, Leningrad. (Translation of Polar Work Library, Dartmouth College, Hanover, N.H.)

Burns, J. J., and S. J. Harbo. 1972. An aerial census of ringed seals, northern coast of Alaska. *Arctic, 25,* 279-290.

Campbell, W. J. 1965. The wind-driven circulation of ice and water in a polar ocean. *Journal of Geophysical Research, 70*(14), 3279-3301.

Campbell, W. J., P. Gloersen, W. Nordberg, and T. T. Wilheit. 1974. Dynamics and morphology of Beaufort Sea ice determined from satellites, aircraft, and drifting stations. *AIDJEX Bulletin, 25,* 1-27.

Campbell, W. J., W. F. Weeks, R. O. Ramseier, and P. Gloersen. 1975. Geophysical studies of floating ice by remote sensing. *Journal of Glaciology, 15*(73), 305-328.

Coachman, L. K., and C. A. Barnes. 1961. The contribution of Bering Sea water to the Arctic Ocean. *Arctic, 14*(3), 146-161.

Cooper, P. F., Jr. 1974. Landfast ice in the southeastern part of the Beaufort Sea. In *The Coast and Shelf of the Beaufort Sea* (ed. J. C. Reed and J. F. Sater), Arctic Institute of North America, Arlington, Va., pp. 235-242.

Crowder, W. K., H. L. McKim, S. F. Ackley, W. D. Hibler, III, and D. M. Anderson. 1973. Mesoscale deformation of sea ice from satellite imagery. In *Advanced Concepts and Techniques in the Study of Snow and Ice Resources* (comp. H. S. Santerford and J. L. Smith), National Academy of Sciences, Washington, D.C., pp. 563-573.

Gary, M, R. McAfee, and C. L. Wolfe, eds. 1972. *Glossary of Geology.* American Geological Institute, Washington D.C., 858 pp.

Hibler, W. D., S. F. Ackley, III, W. K. Crowder, H. L. McKim, and D. M Anderson. 1974. Analysis of shear zone ice deformation in the Beaufort Sea using satellite imagery. In *The Coast and Shelf of the Beaufort Sea* (ed. J. C. Reed and J. E. Sater), Arctic Institute of North America, Arlington, Va., pp. 285-296.

Hnatiuk, J., and G. H. Johnston. 1973. Environmental conditions influencing arctic decisions and design criteria. *Proc., Fifth International Congress, Arctic Oil and Gas: Problems and Possibilities,* French Foundation of Northern Studies, Le Havre.

Hufford, G. L., S. H. Fortier, D. E. Wolfe, J. F. Doster, and D. L. Noble. 1974. Physical oceanography of the Western Beaufort Sea. In *WEBSEC 71-72, an Ecological Survey in the Beaufort Sea,* Oceanographic Report No. CG 373-64, pp. 1-16.

Jacobs, J. D, R. G. Barry, R. L. Weaver. 1975. Fast ice characteristics, with special reference to the Eastern Canadian Arctic. *Polar Record, 17*(110), 521-536.

Klimovich, V. M. 1972. Characteristics of hummocks in shore ice. In *Meteorology and Hydrology,* no. 5, USSR (Department of Commerce Joint Pubs. Res. Service Translation 56595).

Kovacs, A., and M. Mellor. 1974. Sea ice morphology and ice as a geological agent in the southern Beaufort Sea. In *The Coast and Shelf of the Beaufort Sea* (ed. J. C. Reed and J. E. Sater), Arctic Institute of North America, Arlington, Va., pp. 113-161.

Marsh, W. M., B. D. Marsh, and J. Dozier. 1973. Formation, structure, and geomorphic influence of Lake Superior icefoots. *American Journal of Science, 273*(1), 48-64.

McCann, S. B., and R. J. Carlisle. 1972. The nature of ice foot on the beaches of Radstock Bay, Southwest Devon Island, N.W.T., Canada, in the spring and summer of 1970. *Institute of British Geographers, Special Publications, 4,* 175-186.

Nichols, Robert L. 1961. Characteristics of beaches formed in polar climates. *American Journal of Science, 259,* 694-708.

Owens, E. H., and S. B. McCann. 1970. The role of ice in the Arctic beach environment with special reference to Cape Ricketts, Southwest Devon Island, Northwest Territories, Canada. *American Journal of Science, 268,* 397-414.

Parmerter, R. R., and M. D. Coon. 1972. Model of pressure ridge formation in sea ice. *Journal of Geophysical Research, 77*(33), 6565-6575.

Reed, J. C., and J. E. Sater, eds. 1974. *The Coast and Shelf of the Beaufort Sea* (Proceedings of a Symposium on Beaufort Sea Coast and Shelf Research), Arctic Institute of North America, Arlington, Va., 750 pp.

Reimnitz, Erk, and K. F. Bruder. 1972. River discharge into an ice covered ocean and related sediment dispersal, Beaufort Sea, coast of Alaska. *Geological Society of America Bulletin, 83*(3), 861-866.

Reimnitz, Erk, S. C. Wolf, and C. A. Rodeick. 1972. Preliminary interpretation of seismic profiles in the Prudhoe Bay area, Beaufort Sea, Alaska. U.S. Geological Survey open-file report.

Reimnitz, Erk, C. A. Rodeick, and S. C. Wolf. 1974. Strudel scours: a unique artic marine geologic phenomenon. *Journal of Sedimentary Petrology, 44*(2), 409-420.

Reimnitz, Erk, and P. W. Barnes. 1974. Sea ice as a geologic agent on the Beaufort Sea shelf of Alaska. In *The Coast and Shelf of the Beaufort Sea* (ed. J. C. Reed and J. E. Sater), Arctic Institute of North America, Arlington, Va., pp. 301-353.

Short, A. D. 1975. Offshore bars along the Alaskan arctic coast. *Journal of Geology, 83,* 209-221.

Stefansson, V. 1921. *The Friendly Arctic.* Macmillan, New York, 784 pp.

Stockton, C. H. 1890. Arctic cruise of the USS *Thelis*. *National Geographic Magazine*, *2*, 174-198.

Stringer, W. J. 1974. Sea morphology of the Beaufort shorefast ice. In *The Coast and Shelf of the Beaufort Sea* (ed. J. C. Reed and J. E. Sater), Arctic Institute of North America, Arlington, Va., pp. 165-172.

Walker, H. J. 1974. The Colville River and the Beaufort Sea: some interactions. In *The Coast and Shelf of the Beaufort Sea* (ed. J. C. Reed and J. E. Sater), Arctic Institute of North America, Arlington, Va., pp. 513-540.

Weeks, W. F., A. Kovacs, and W. D. Hibler, III. 1971. Pressure ridge characteristics in the arctic coastal environment. In *Proceedings of the First International Conference on Port and Ocean Engineering under Arctic Conditions*, vol. 1, Technological University of Norway, Trondheim, Norway, pp. 152-182.

Zubov, N. N. 1945. *Arctic Sea Ice*. Translated by Naval Oceanographic Office and American Meterological Society under contract to Air Force Cambridge Research Center, 1963, U.S. Naval Electronics Laboratory (San Diego), 491 pp.

Zumberge, J. H., and J. T. Wilson. 1953. Effect of ice on shore development. In *Proceedings, Fourth Conference on Coastal Engineering, Berkeley, Ca.*, pp. 201-206.

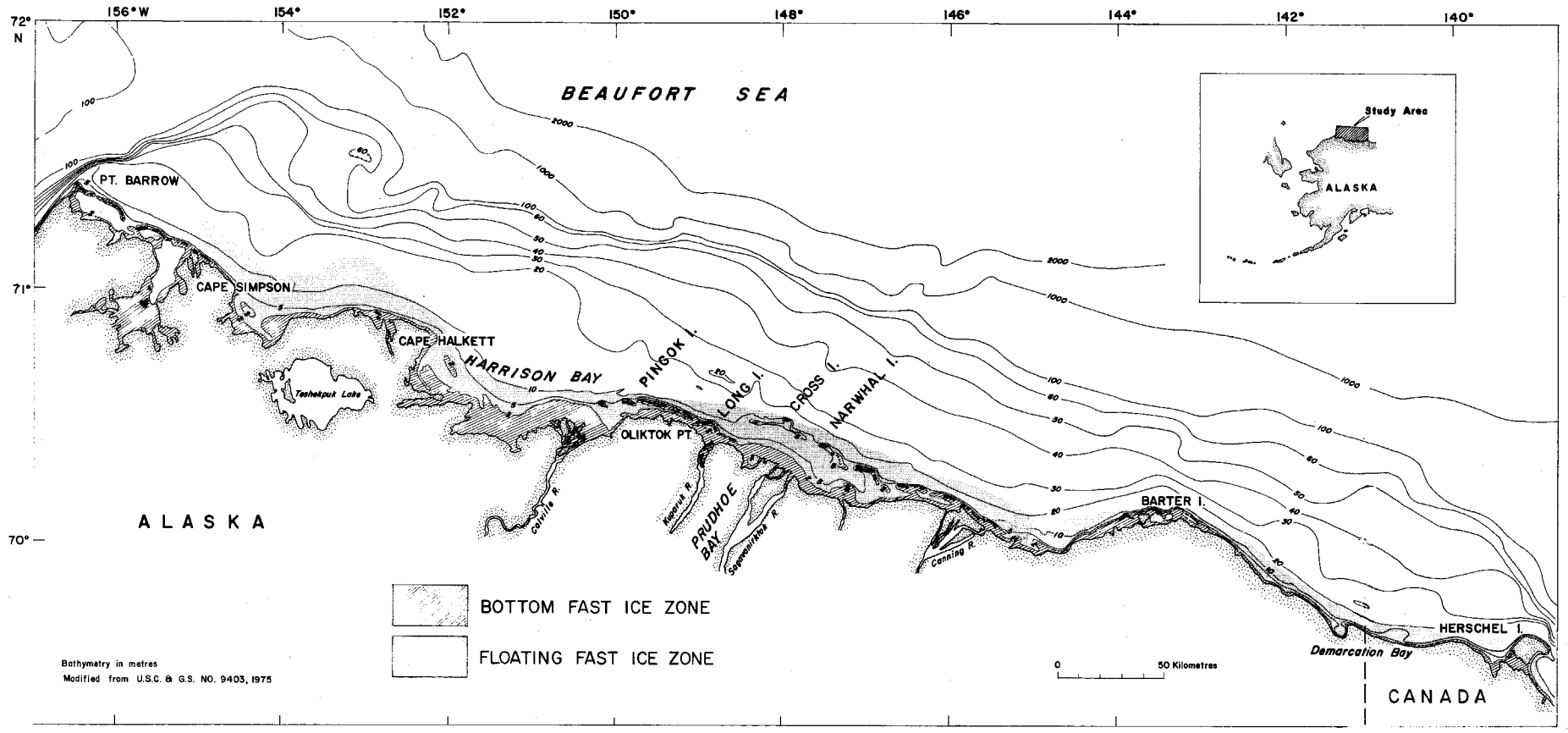

Fig. 1. Study area showing bathymetry and place names. The extent of relatively undeformed fast ice was determined largely from Landsat-1 images between 8 March and 21 April 1973. Extent of bottomfast ice 2 m thick has been traced from bathymetric contours.

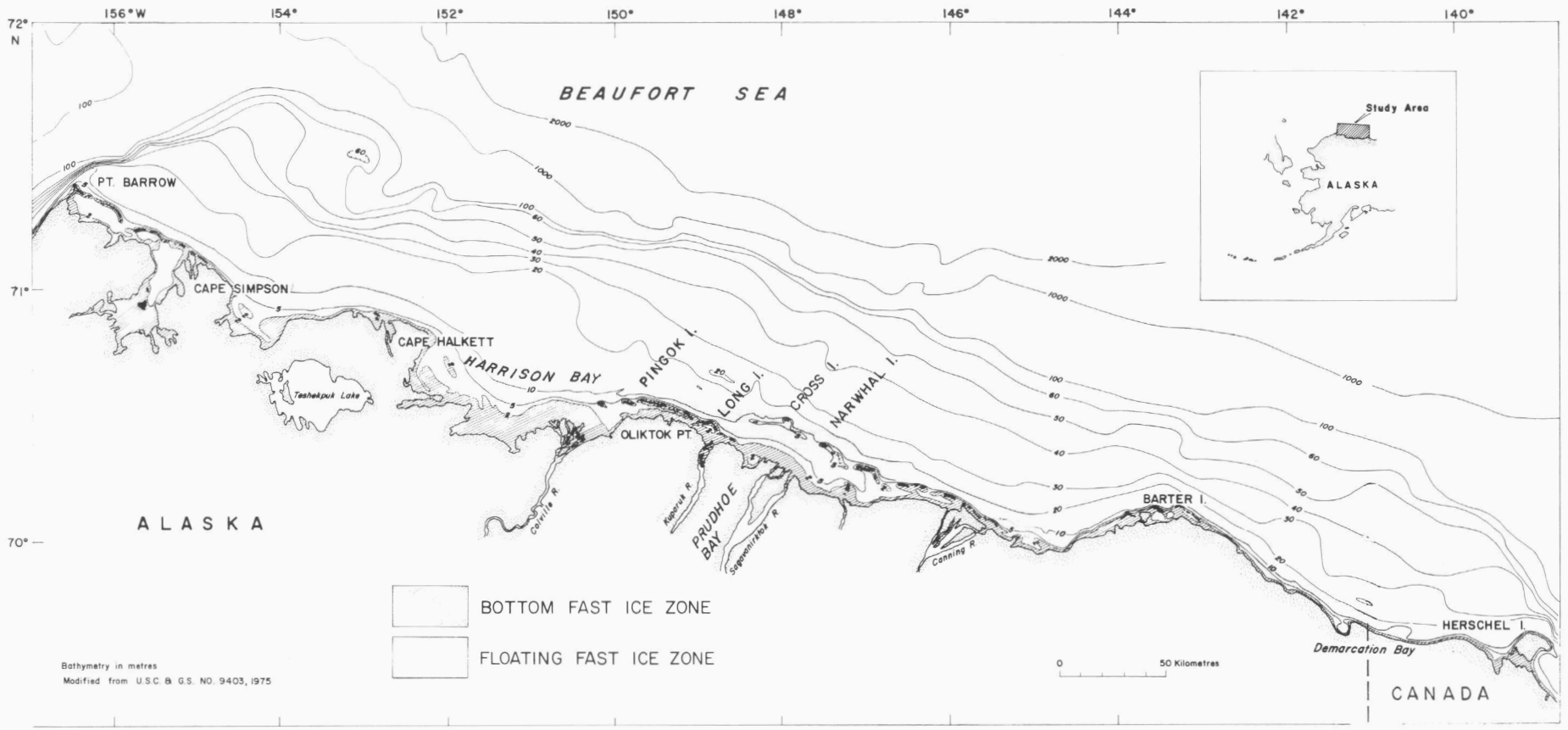

Fig. 1. Study area showing bathymetry and place names. The extent of relatively undeformed fast ice was determined largely from Landsat-1 images between 8 March and 21 April 1973. Extent of bottomfast ice 2 m thick has been traced from bathymetric contours.

Fig. 2

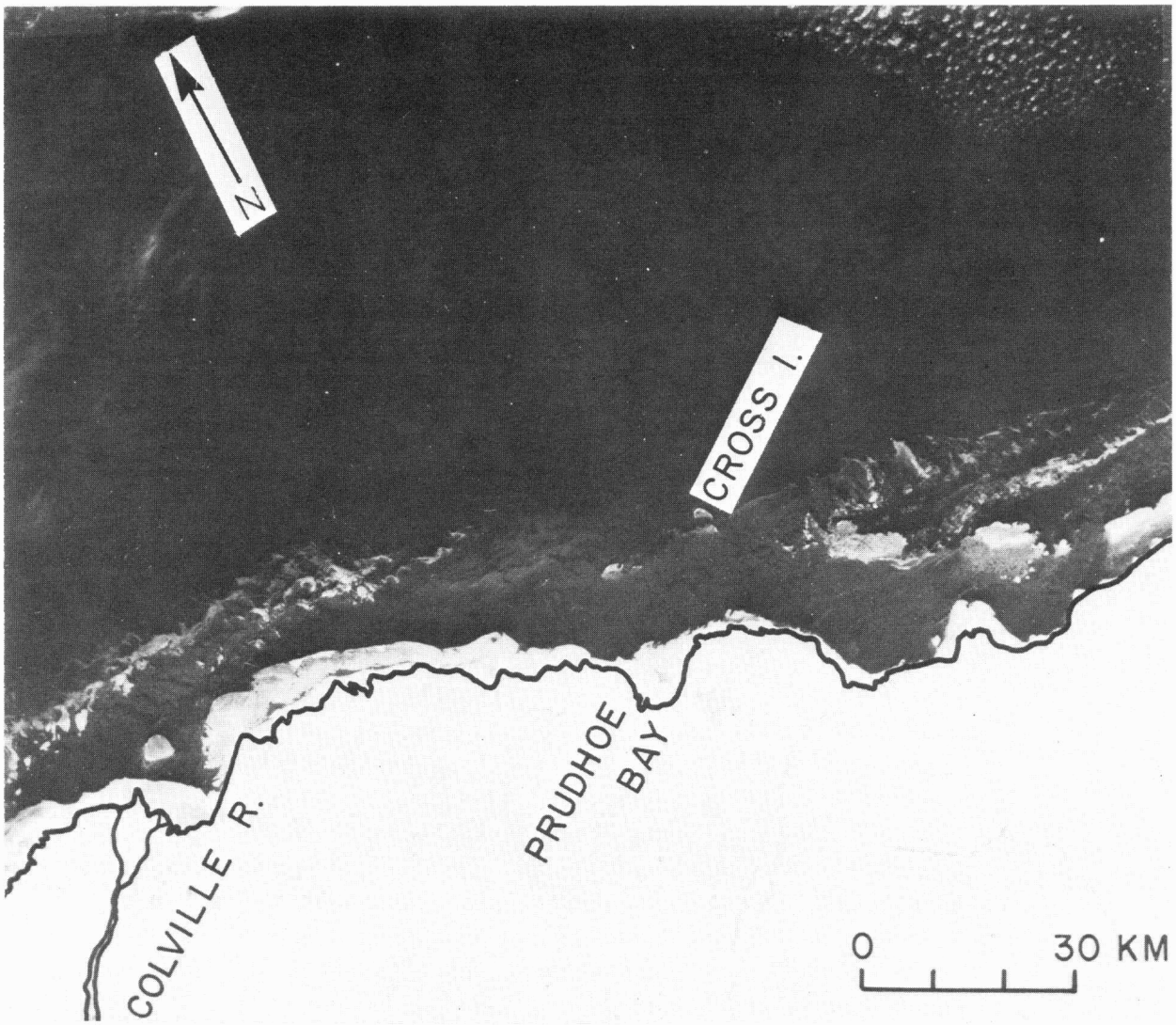
N
CROSS I.
PRUDHOE BAY
COLVILLE R.
0
30 KM

Fig. 4

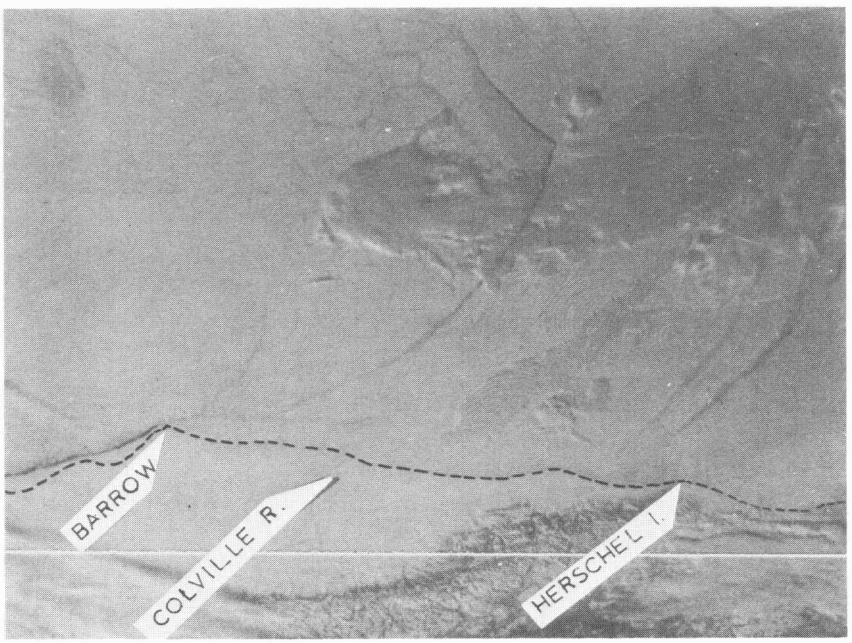
BARROW
COLVILLE R.
HERSCHEL I.

Fig. 2 (facing page). 4 Oct. 1972 Landsat-1 image showing formation of new ice on the shallow inner shelf and drift accumulation against south side of barrier islands. No old ice is visible within the area of the image (1073-21223).

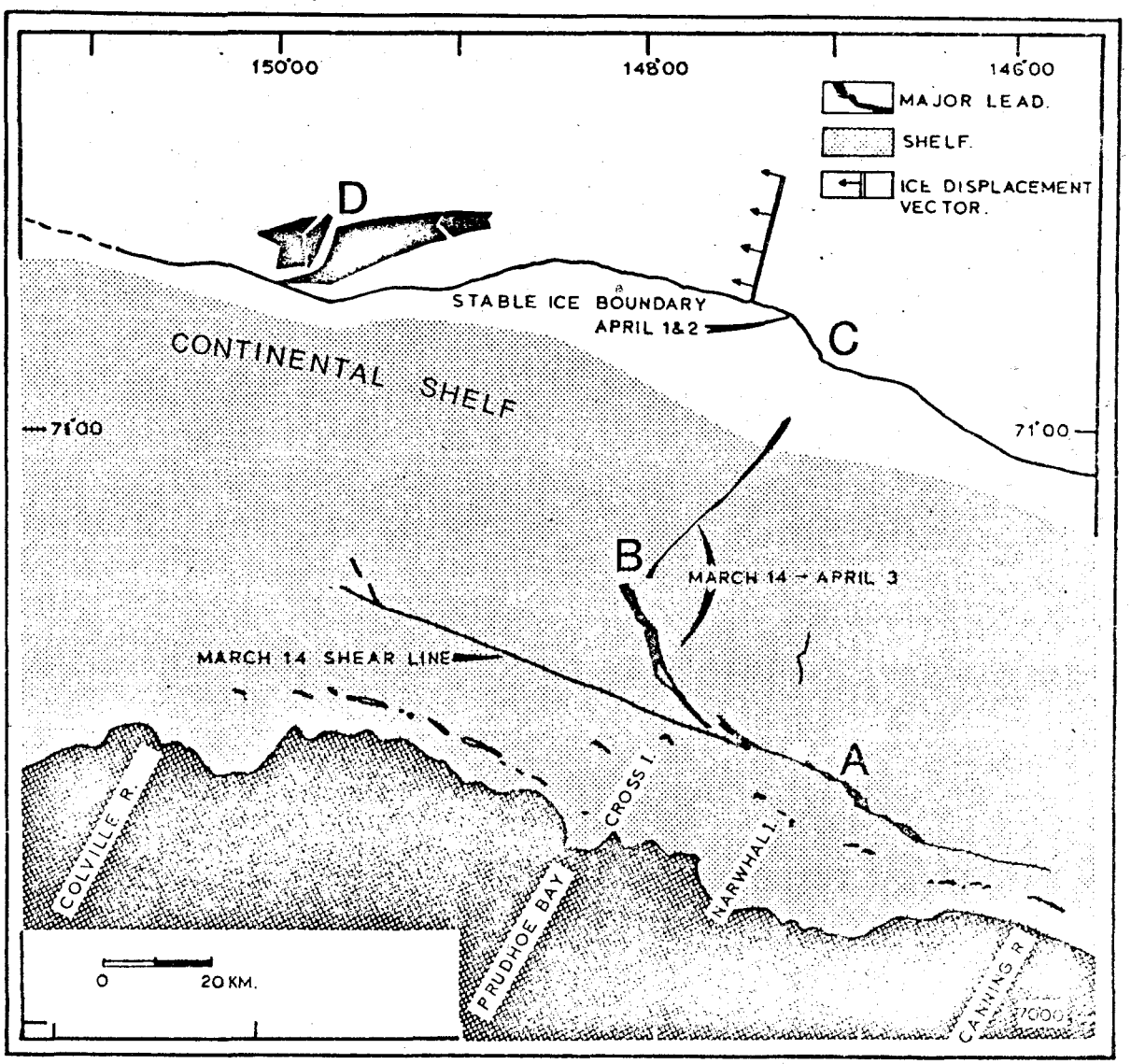

Fig. 3 (above). Landsat images for 14-16 March 1973 (1234-21175, 1235-21241, 1236-21297) show recent shore-parallel lead (A) and roughly shore-normal lead (B). Configuration of A indicates that seaward ice has been displaced eastward 2 km relative to the stationary ice. In early April (1252-21175, 1253-21233, 1254-21292), an active shearline (C) paralleling the shelf edge was associated with westward pack ice displacements of 4 km per day. The displacement, shown by length of arrows, was uniform through a zone 24 km wide seaward of the slip face.

Fig. 4 (facing page). Visible-band NOAA-2 satellite image taken 5 April 1973. The large (40x15 km) polynya shown in Fig. 3 (D) can be identified on this image. A curvilinear lead extends from the shelf-parallel shearline for hundreds of kilometers into the Arctic Ocean.

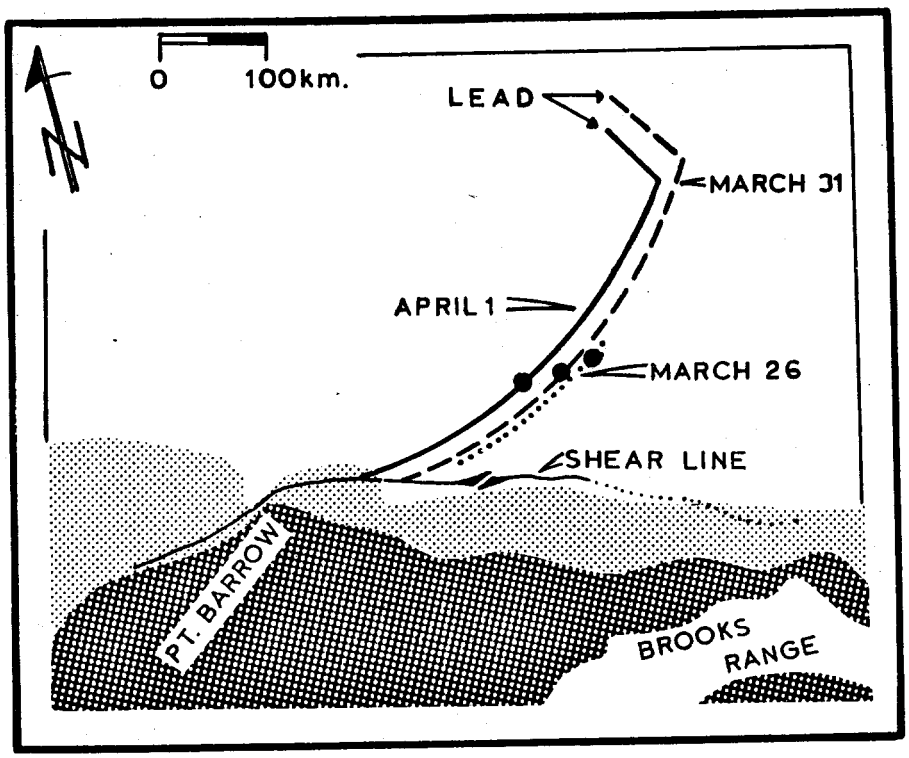

Fig. 5. Comparison of the location of major lead seen on NOAA-2 images for 26 March, 31 March, and 1 April 1973. The large dots mark points along the lead identifiable in all three images. The pack ice in a zone 350 km wide north of the coast-parallel shear-line moved uniformly at about 10 km per day.

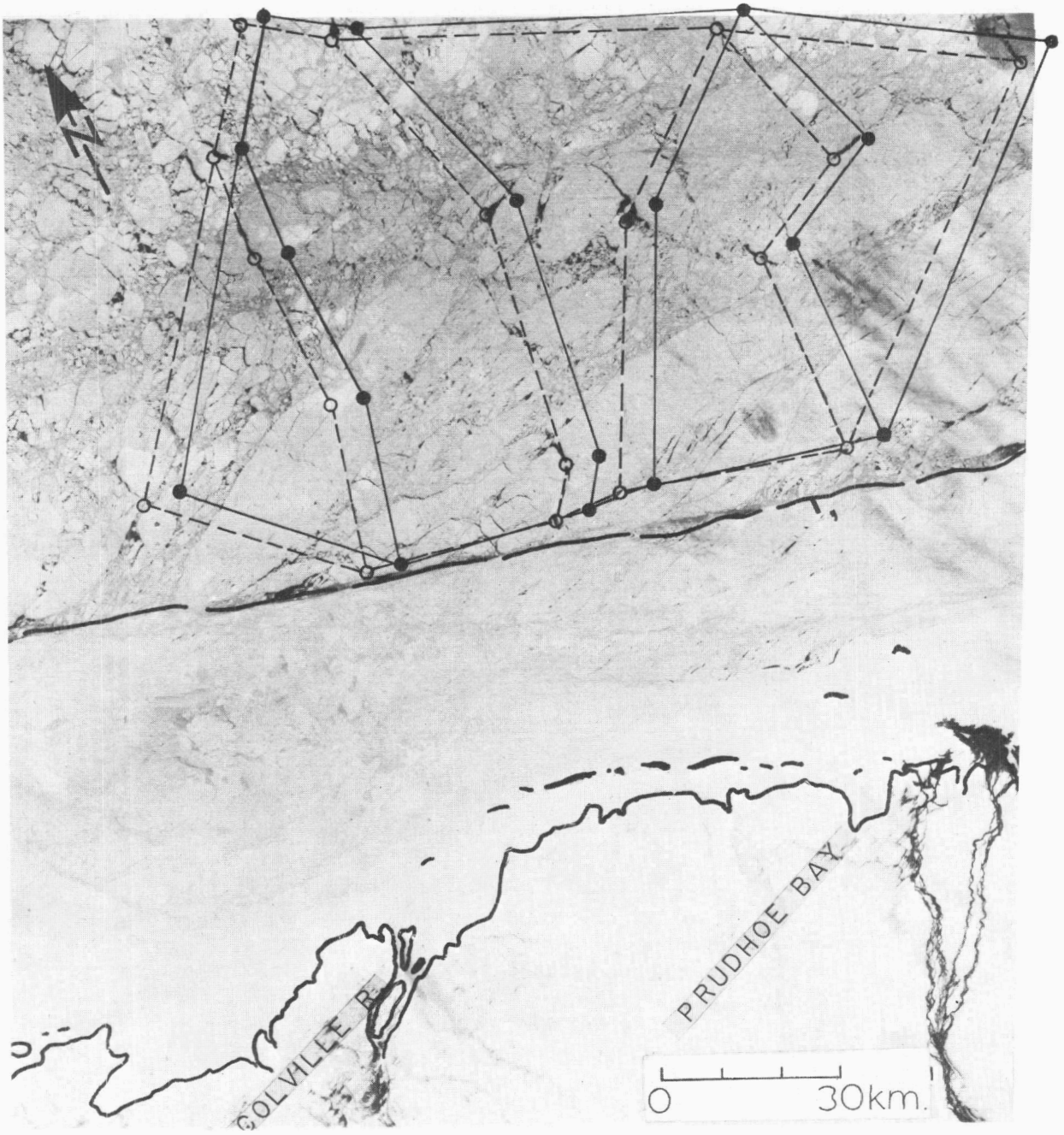

Fig. 6. Landsat image (no. 1308-21290) of 27 May 1973 showing recent irregular refrozen cracks about 10 km west of Cross Island produced by ice deformation along early winter shearline. A pronounced coast-parallel, active shearline follows the 20 m isobath across Harrison Bay. Comparison with ice features identifiable on previous day's image (solid lines) reveals uniform westward displacement of 6 km per day over the shown strain network extending some 90 km seaward of the shear-line. No drag effects are visible near the stationary ice/drifting pack ice boundary.

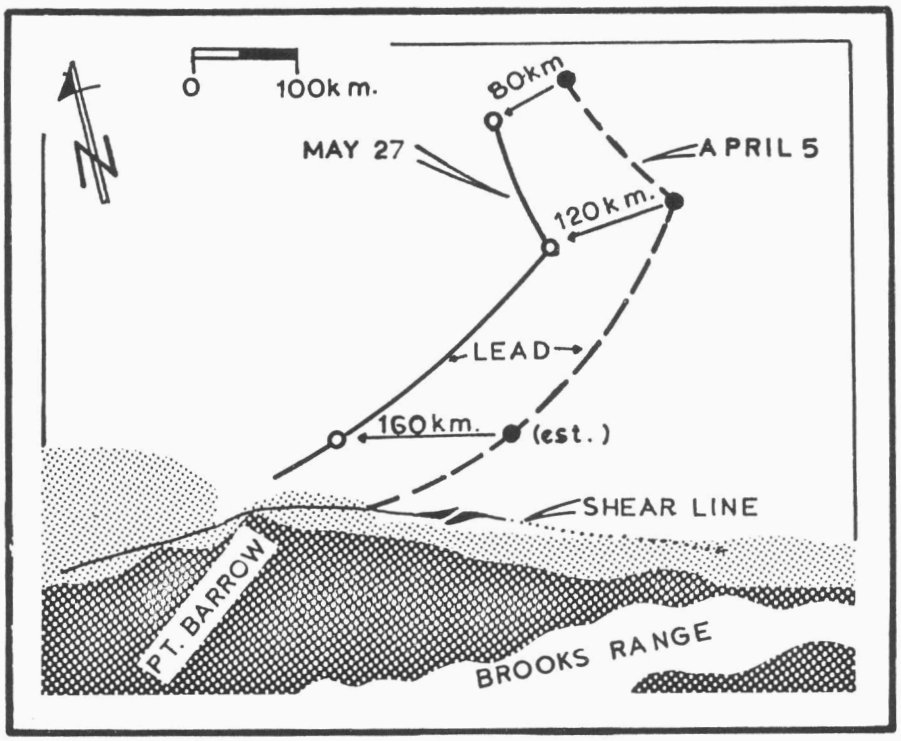

Fig. 7. Tracing from NOAA-2 visible-band images of 5 April and 27 May 1973, showing westward displacement of long lead seen in Figures 4 and 5. During the 52-day period, displacements ranged from 160 km (3 km per day) near the continent to 80 km (1.5 km per day) at a point 450 km seaward of the coast. Differences in displacements are considered to be representative of points at various distances from the center of the clockwise rotation within the Pacific Gyre.

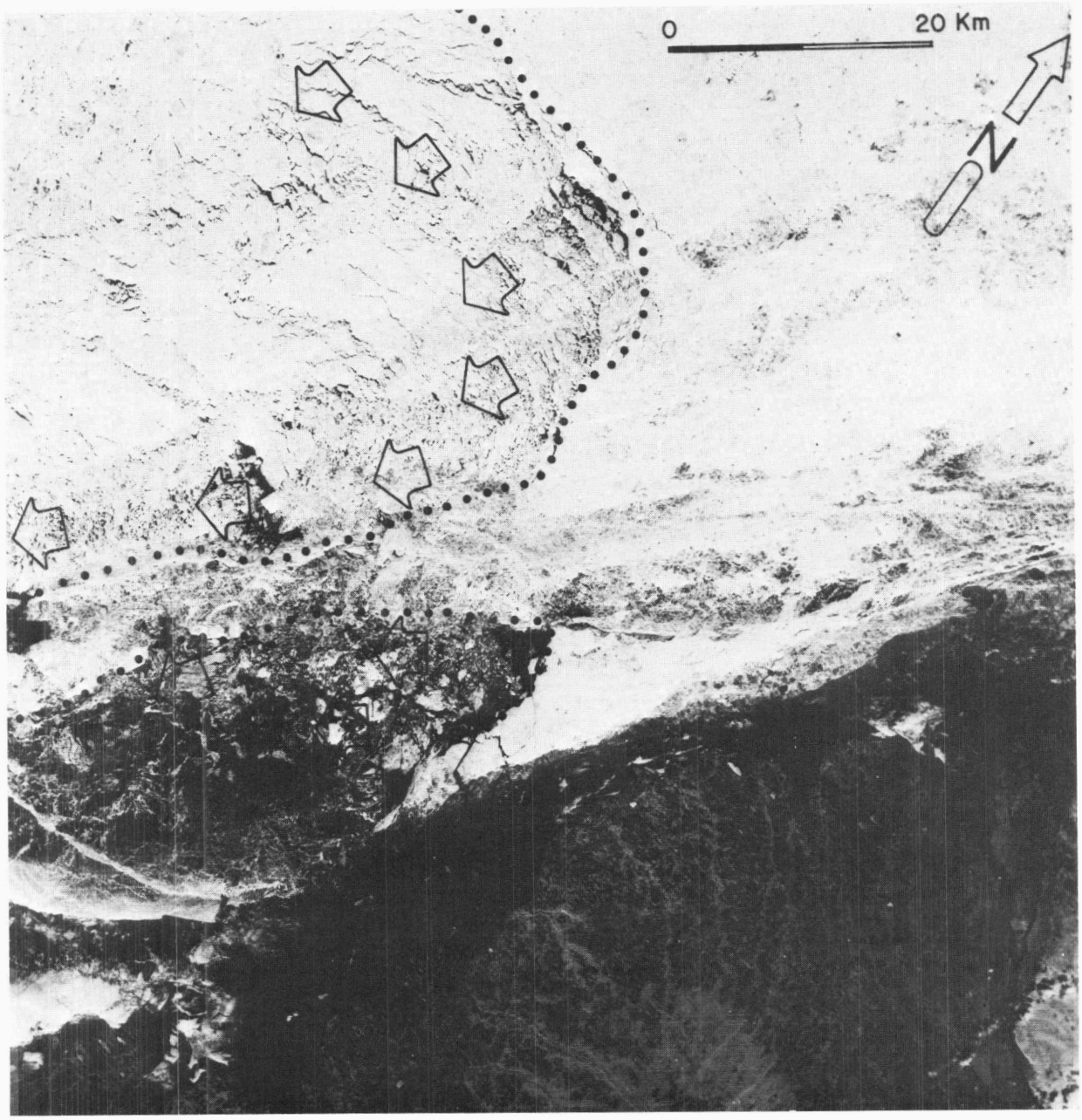

Fig. 8. Landsat-1 image (1344-21283) made 2 July 1973, showing initiation of sea ice breakup. Ice on inner and outer shelf west of Oliktok Point is breaking up and moving westward. A zone 15 km wide coinciding with zone of major shear events during winter remains intact. This breakup pattern suggests the presence of stamukhi along the 20 m isobath.

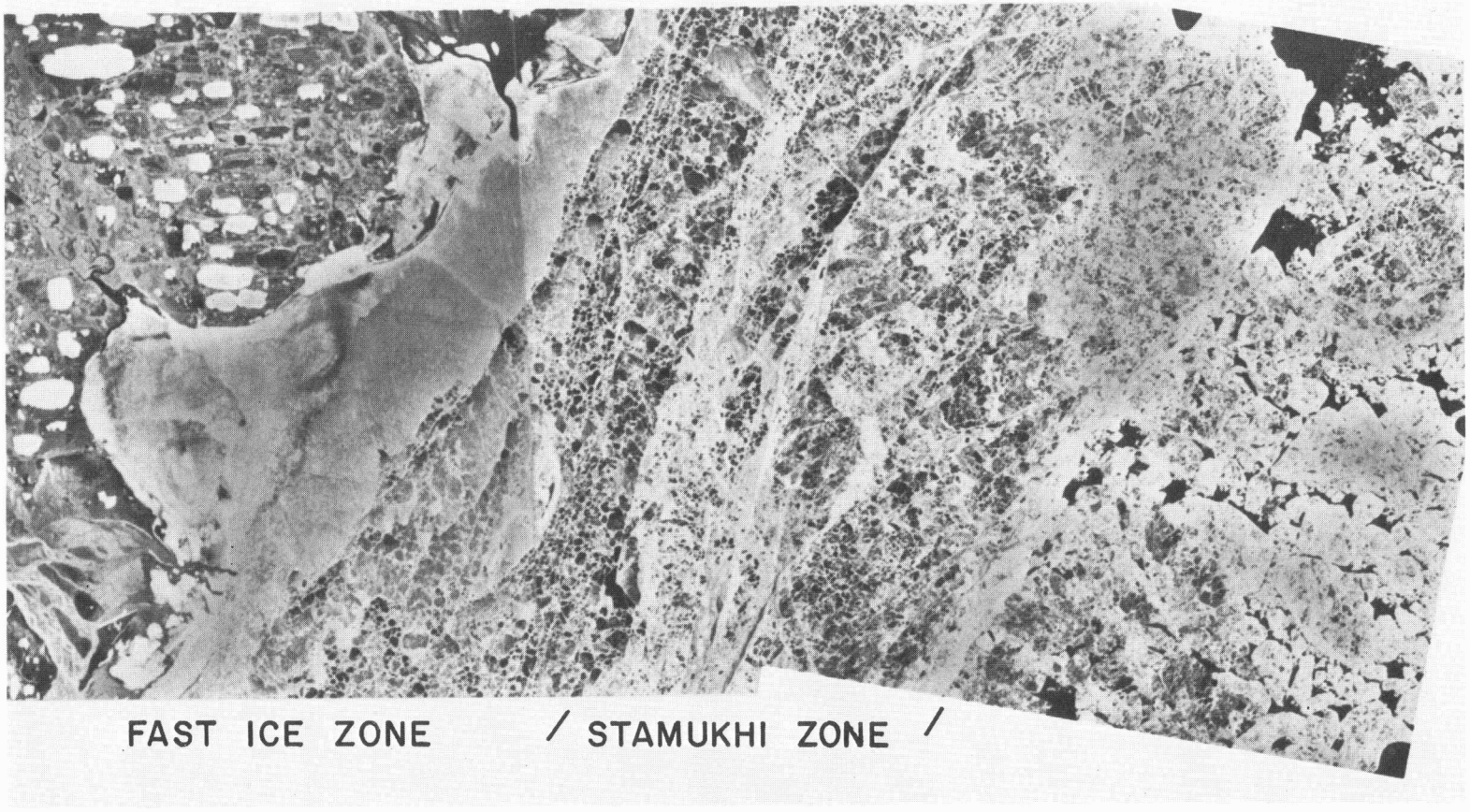

Fig. 9. Mosaic of U-2 color infrared photos taken from an altitude of 20,000 m on 21 July 1974. Flightline extends north from Prudhoe Bay. Sea ice morphology is similar to that of 1973. Smooth fast ice, lightly deformed shortly after freezeup, extends to just beyond Reindeer Island, followed by strongly lineated and rough ice in the stamukhi zone and a zone of mobile ice on the outer shelf.

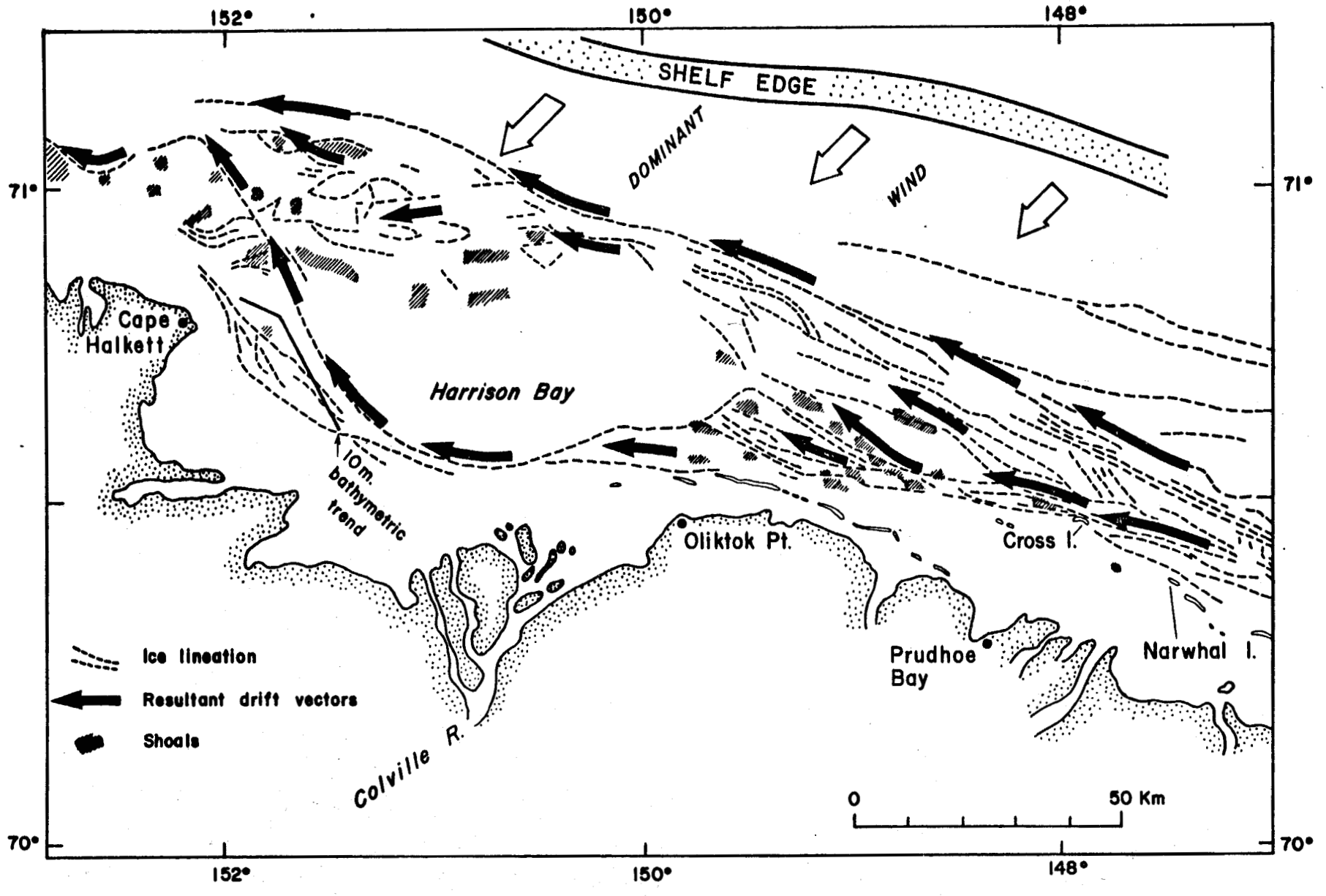

Fig. 10. Generalized model of ice drift within area of detailed study, showing predominant movement of pack ice along well-defined shearlines, dominant wind direction, and location of charted shoals. Note striking correlation between distribution of shoals and major ice lineations, traced from Landsat images, which represent shear ridges, pressure ridges, and linear hummock fields.

Fig. 11 (facing page). Oblique aerial photograph taken northeast of Pt. Barrow on 13 August 1975. Grounded ridges (stamukhi) occur along lines paralleling isobaths (upper quarter of photo), marking a distinct boundary between scattered ice on inner shelf (central part of photo) and tightly packed ice beyond. Water at bottom of photo is a lagoon.

Fig. 12 (facing page). June 1970 photograph of ice push features on Narwhal Island. Such features and associated beach deformation recur annually on major coastal promontories such as Narwhal Island and Cross Island that are exposed to shear zone dynamics.

Fig. 13 (facing page). Example of barrier island beaches that lie downdrift of major promontories and landward of shoals. Photographed in May 1972 on Long Island. The 2 m isobath seaward of beach is marked by characteristic tidal crack in relatively smooth fast ice.

Fig. 11

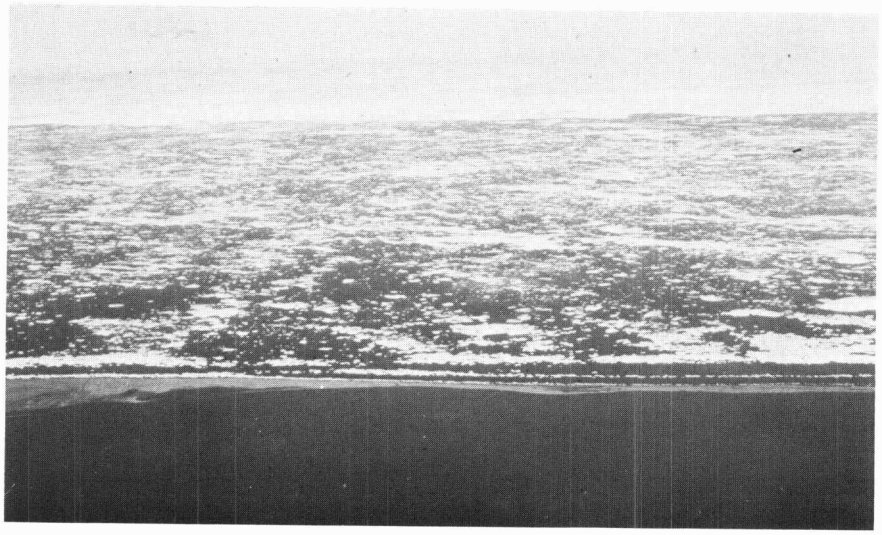

Fig. 12

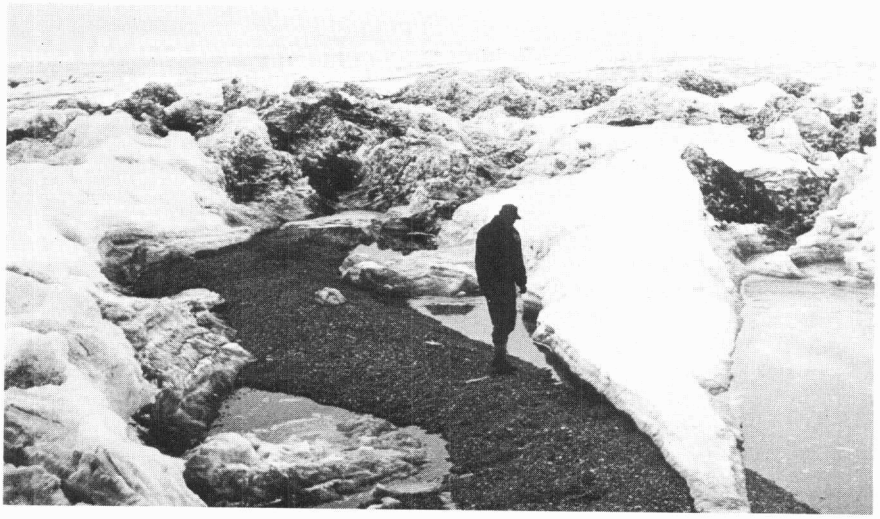

Fig. 13

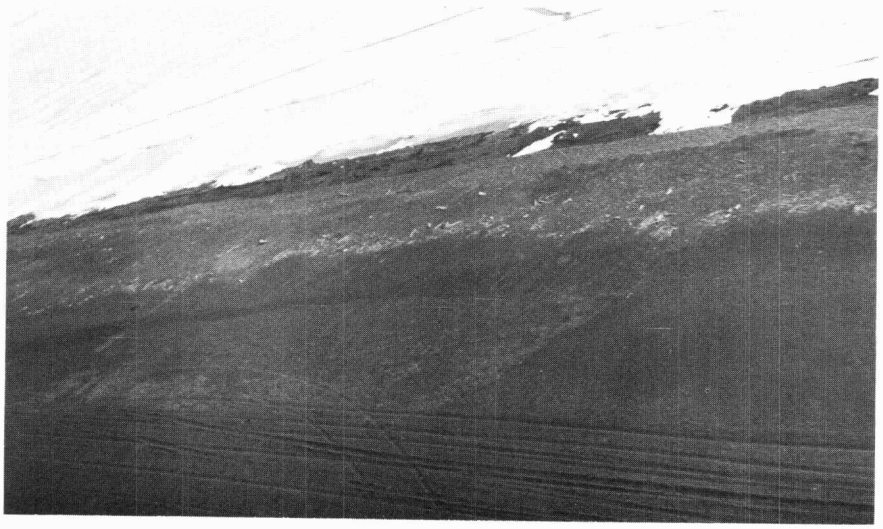

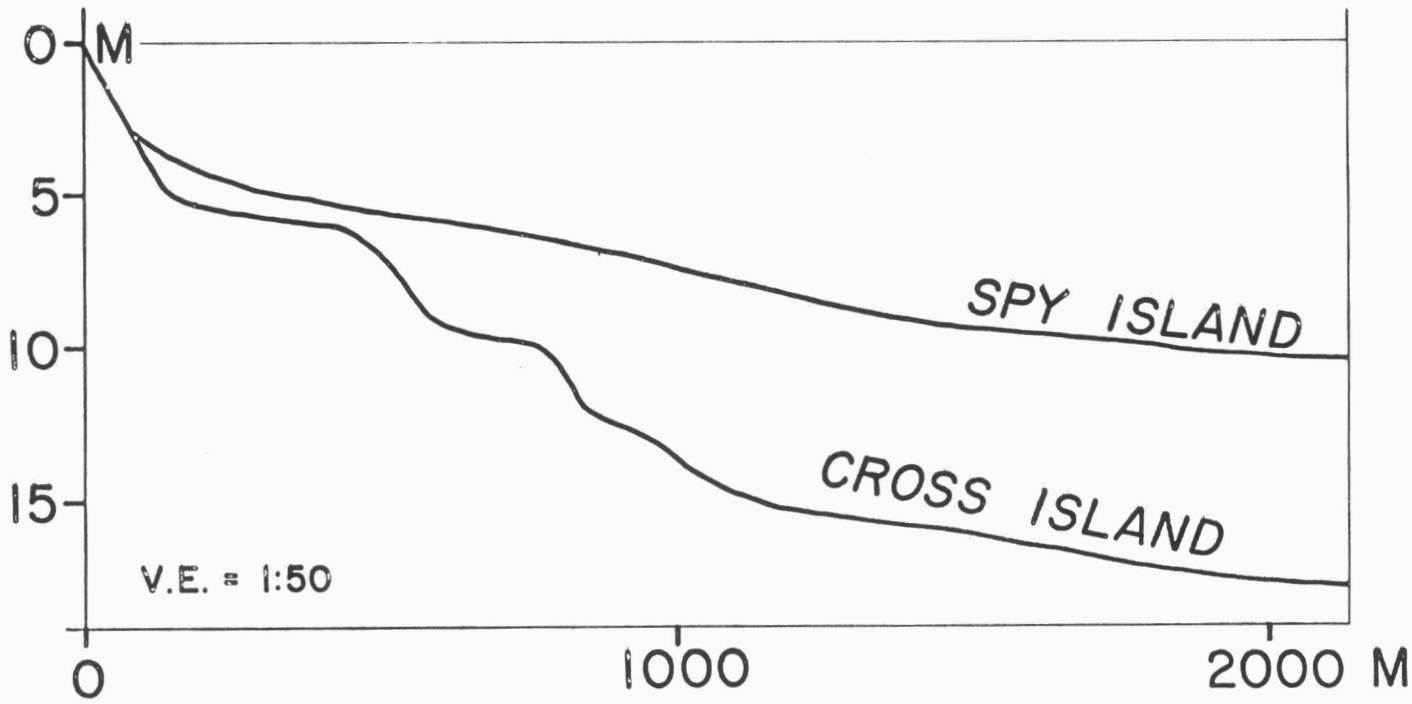

Fig. 14. Comparison of bottom profiles off Cross Island, where the shear zone impinges on the coast, and Spy Island (Fig. 15), protected by stamukhi on offshore shoals.

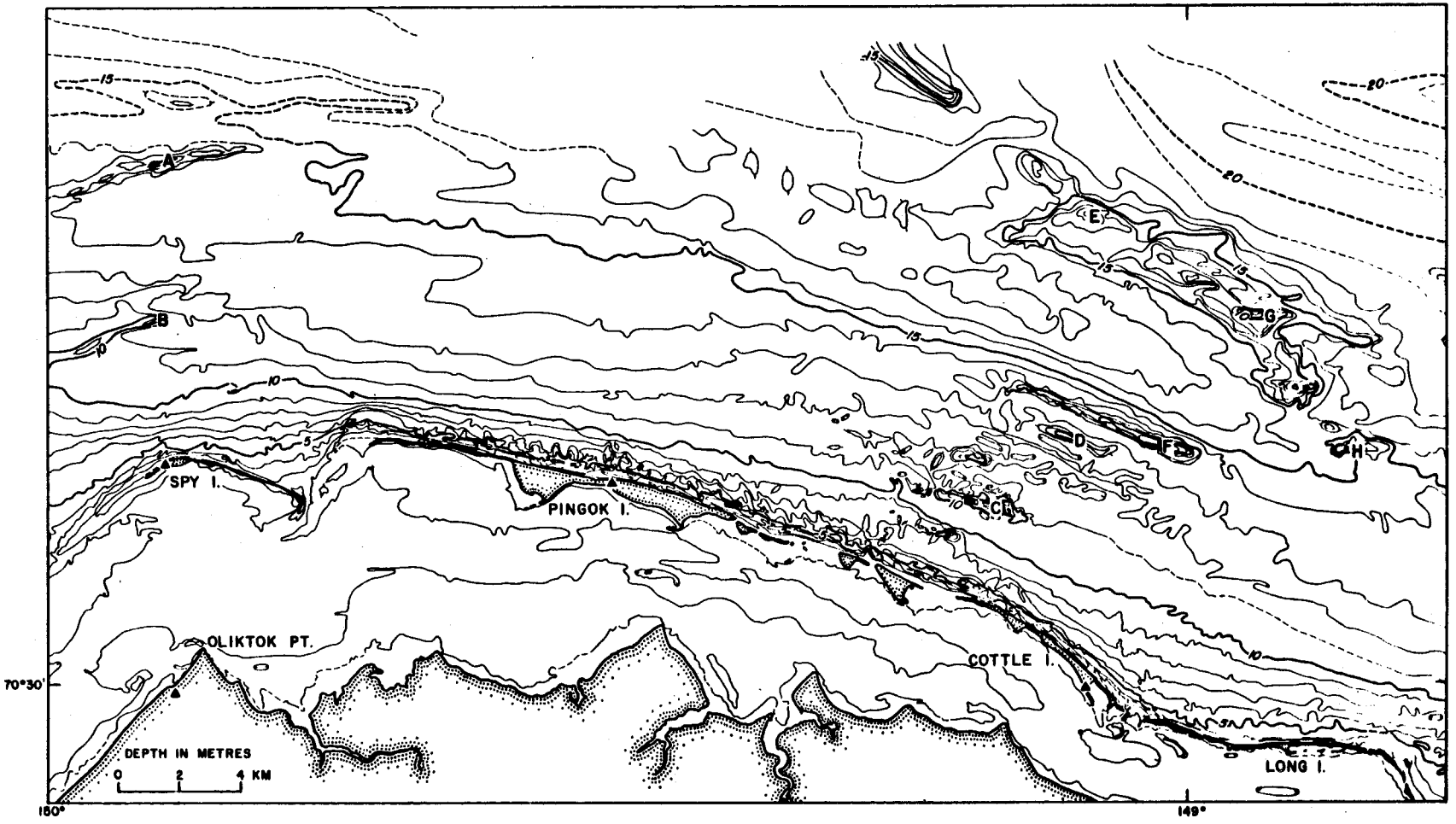

Fig. 15. Bathymetry of inner shelf within central part of study area. The contours are based on U.S, Coast and Geodetic Survey smooth sheets, surveyed from 1949 through 1951 along a dense pattern of accurately controlled sounding lines. The locations of individual shoal profiles shown in Fig. 16 are keyed by letter.

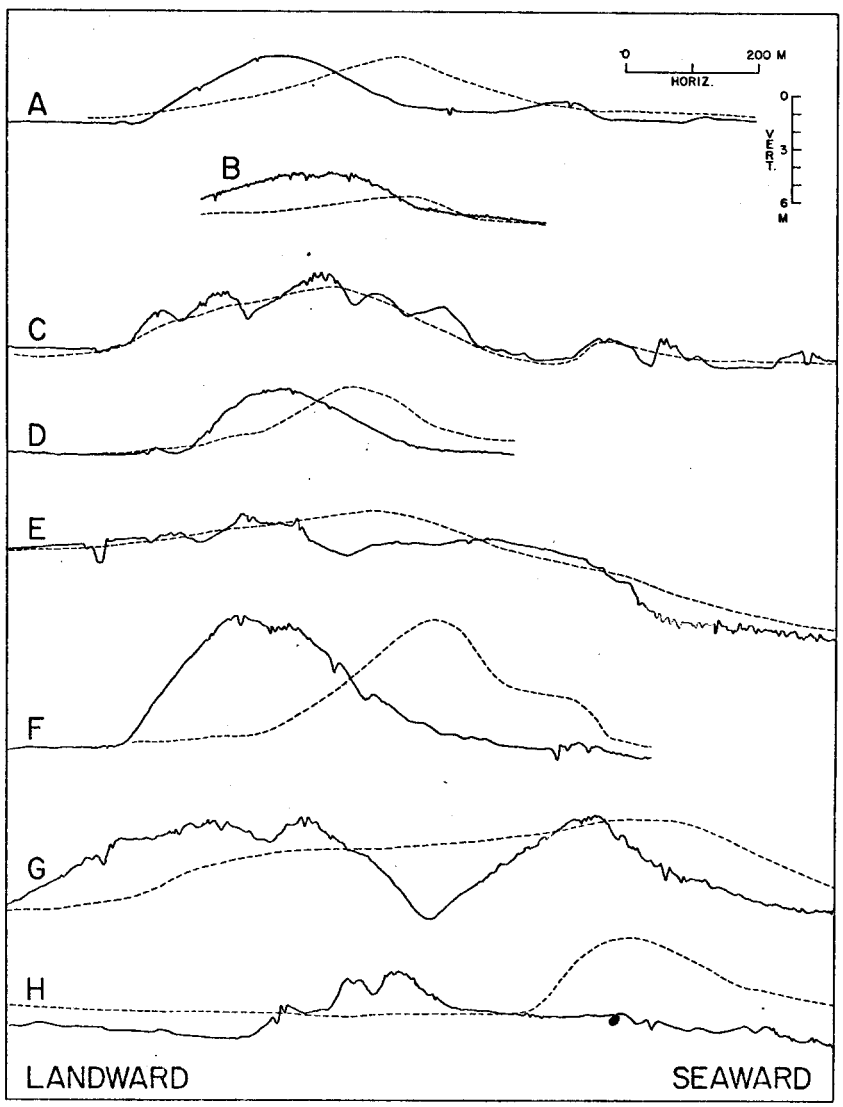

Fig. 16. Cross-sectional profiles of shoals as surveyed 1949-1951 (dashed line) and 1975 (solid line). All but one of the shoals have migrated landward through distances of 100-400 m over 25 years.

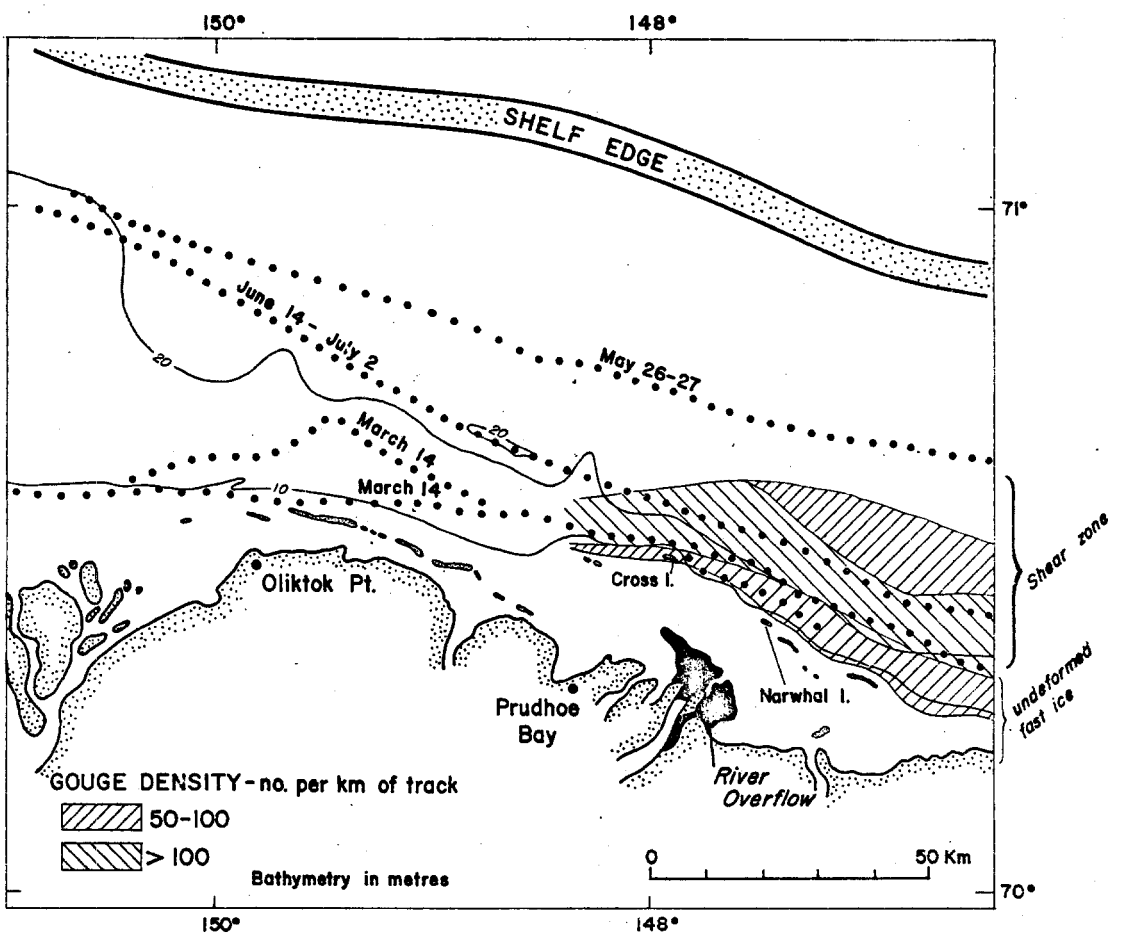

Fig. 17. Locations of several major 1973 shear events (dotted lines) that were actually observed in Landsat images or could be dated within narrow time limits. Related to these events are ice gouge density values (hachures) from 1973 sonographic surveys after Reimnitz and Barnes [1974]. The dark area off the Sagavanirktok River defines the extent of freshwater overflow during the shear event of 26-27 May.

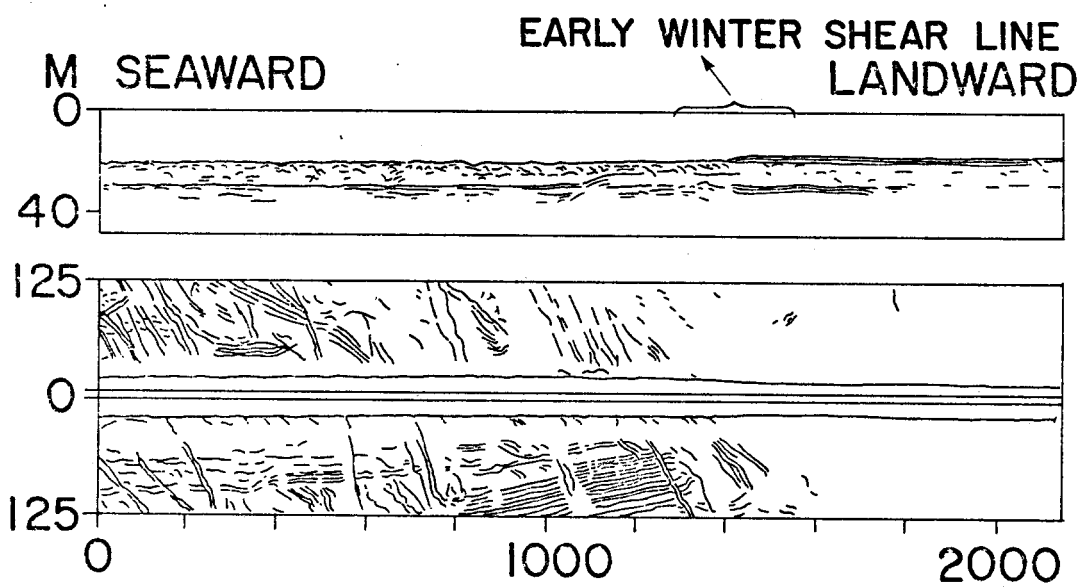

Fig. 18, Line drawing of 1973 high-resolution seismic reflection (top) and ice gouges on side-scan sonar (bottom) records, obtained concurrently across early winter (1972) shearline boundary off Cross Island. Abrupt break in ice gouge density and nature of sub-bottom reflectors coincide with slight break in bottom slope. Landward of the shearline only minor gouges are apparent, while seaward the bottom is densely gouged.

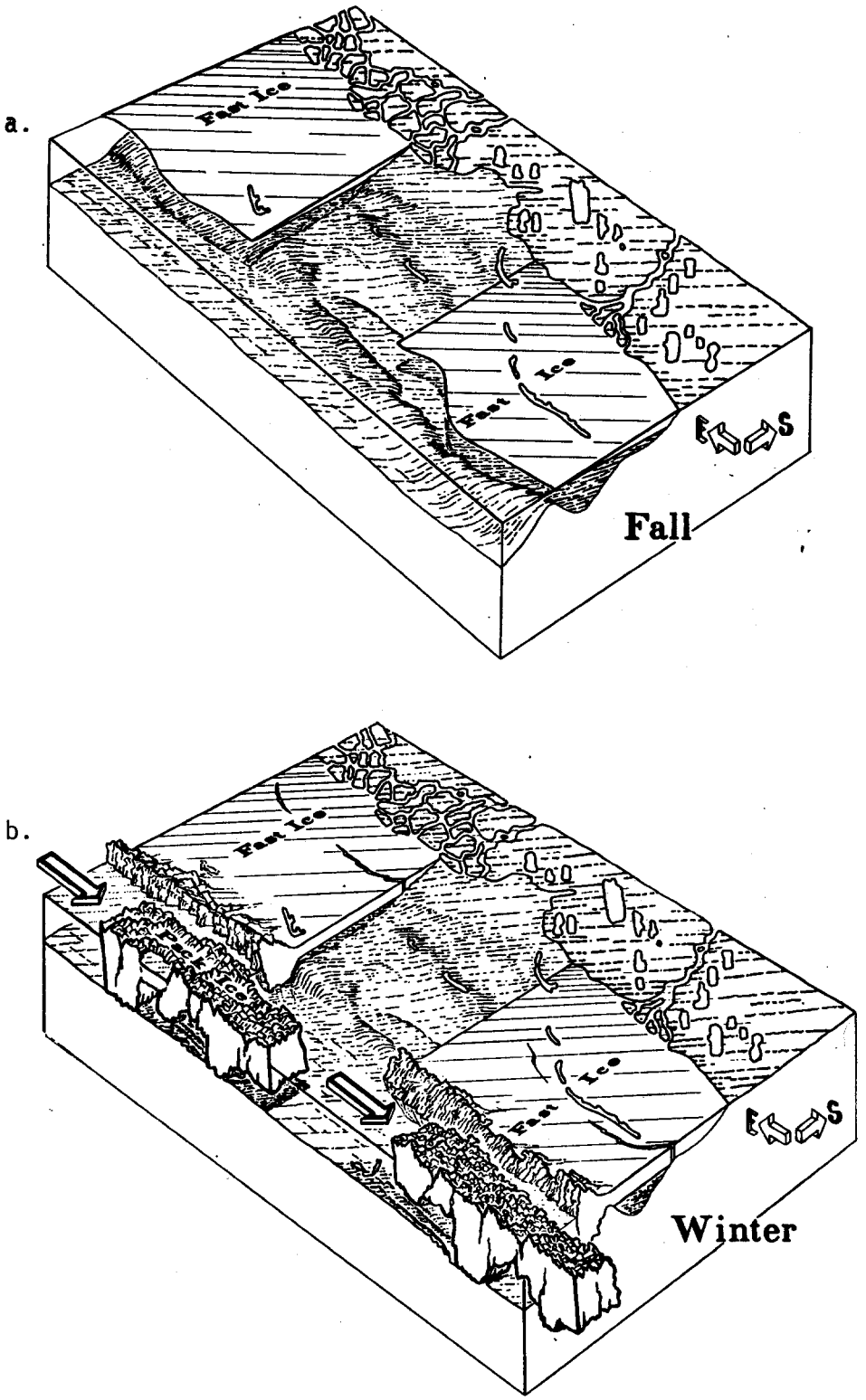

Fig. 19. Seasonal development of ice zonation in relation to bottom morphology: (a) fall, (b) winter. Drawings by Tau Rho Alpha.

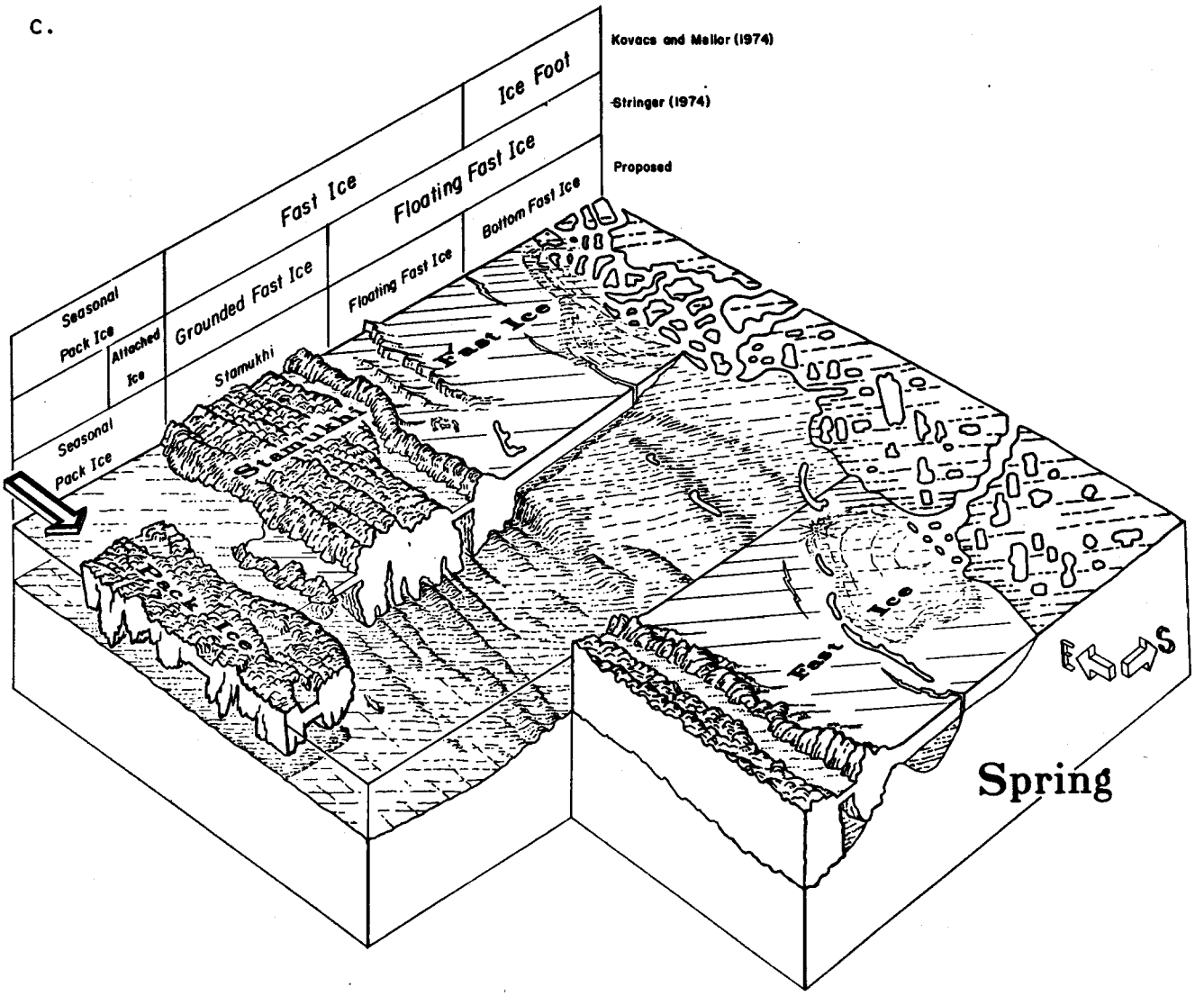

Fig. 19 (continued). Seasonal development of ice zonation in relation to bottom morphology: (c) spring. Drawing by Tau Rho Alpha.

A SIMULATION OF INERTIAL OSCILLATIONS OBSERVED IN THE DRIFT OF MANNED ICE STATIONS

by

M. G. McPhee
AIDJEX

ABSTRACT

A simple model for simulating the motion of pack ice during periods of energetic inertial oscillation is developed by writing an integrated momentum equation for the ice-upper ocean system driven by surface wind stress. Dissipation in the system is modeled by a damping term proportional to the component of mass transport parallel to the wind stress. Ice velocity is related to total transport by considering an idealization of mean boundary layer currents measured at AIDJEX camp Jumpsuit in 1972. The model is used to simulate three periods of drift measured at AIDJEX ice stations in summer and early fall of 1975. It is shown that the model much better reproduces observed inertial velocities than does a similar "free drift" model in which the ocean exerts a passive quadratic drag. At certain times the model predicts too much amplitude for the inertial waves, and this is interpreted as indicating that the internal stress gradient in the ice is then strong enough to inhibit oscillation.

1. INTRODUCTION

Trajectories of measured position for manned camps in the 1975-1976 AIDJEX (Arctic Ice Dynamics Joint Experiment) field experiment are sometimes characterized by what appears to be approximately circular motion superimposed on straight drift to the right of the surface wind. The looping motion often persists for several cycles, each cycle taking close to 12 hours. Hunkins [1967] inferred a similar cycloidal track from the speed of deep ocean currents

measured relative to ice station T-3. He ruled out tidal motions and went on to suggest qualitatively a mechanism by which inertial waves excited by abrupt changes in the observed wind could explain the drift.

Pollard and Millard [1970] presented observations of inertial oscillations in upper ocean currents records from which they formulated a model for wind-driven mass transport with linear damping. Using a rather simple mixed-layer model to relate current velocity to transport, they simulated current response to measured wind and demonstrated well the tendency of the upper ocean to "ring" in response to sudden wind shifts. Their model did not estimate a surface current, which would be required, for instance, to track a floating object.

Besides being intrinsically interesting, study of inertial motions may aid our understanding of ice dynamics by indicating, for example, how the inertia of the oceanic boundary layer compares with that of the ice cover, under what conditions rapid changes in the wind stress field are passed through the ice to the ocean, and what effect the waves have on ice production. In this paper a simple point model for the integrated momentum (mass transport) of the ice-ocean system is proposed; the equations are solved using wind stress observed at drifting ice stations in the 1975-1976 AIDJEX array; the ice velocity is related to the total transport by means of a simple boundary layer model; and the results are compared with ice drift data. The intent here is not a rigorous investigation of the time-dependent boundary layer, but rather to see if a simple model consistent with our present knowledge can simulate the observed inertial response in the ice-ocean system.

2. THE MOMENTUM EQUATION

We can write an equation of motion for any element in the ice-ocean system as the following

$$\rho\left(\frac{\partial \vec{V}}{\partial t} + f\,\hat{k} \times \vec{V}\right) = \nabla \cdot \underset{\sim}{\tau}' \qquad (1)$$

where the over-arrow indicates a vector, $\hat{k}$ is the vertical unit vector, $\underset{\sim}{\tau}'$ is an infinitesimal stress tensor, and f is the Coriolis parameter. In most

treatments of ice dynamics [e.g., Rothrock, 1975], conditions are considered uniform through the ice thickness, $\overline{h} = m/\rho_{ice}$, where m is the mass of the ice column per unit area, and the equation is written

$$m\left[\frac{\partial \vec{V}_i}{\partial t} + f\,\hat{k} \times \vec{V}_i\right] = \vec{\tau}_a + \vec{\tau}_w + \nabla_h \cdot \underset{\sim}{\sigma}_1 \qquad (2)$$

where $\vec{V}_i$ is the ice velocity; $\underset{\sim}{\sigma}_1$ is a stress tensor integrated through the ice thickness and including in some form effects like sea-surface tilt, the atmospheric pressure gradient, and contact stress between floes; and $\vec{\tau}_a$ and $\vec{\tau}_w$ are surface tractions exerted by the air and the ocean. For rapid variations, $\vec{\tau}_w$ is difficult to assess because the water column as well as the ice responds at the inertial frequency.

An alternative approach, the one taken here, is to consider the momentum of the whole ice-upper ocean column as shown schematically in Figure 1. We can define the total mass transport (i.e., the integrated momentum) as

$$\frac{\partial \vec{M}}{\partial t} + f\,\hat{k} \times \vec{M} = \vec{\tau}_a + \vec{F}_\sigma$$

where $\vec{U}$ is the velocity vector at each level in the water and H is the maximum depth of frictional influence. As written, $\vec{M}_T$ includes transport associated with the geostrophic surface current in the ocean.

As long as the underlying geostrophic flow $\vec{U}_g$ (equal to $\vec{U}(z = -H)$ is relatively constant, we can write the momentum equation in terms of the wind-driven transport relative to $\vec{U}_g$, without loss of generality, as

$$\vec{M} = \vec{M}_T - \vec{M}_g = m(\vec{V}_i - \vec{U}_g) + \int_{-H}^{0} \rho_w(\vec{U} - \vec{U}_g)\,dz \qquad (3)$$

and equation (1) can be written

$$\vec{M}_T = m\,\vec{V}_i + \int_{-H}^{0} \rho_w\,\vec{U}\,dz \qquad (4)$$

where the effect of sea-surface tilt on both ice and water is implicit in the Coriolis term on the lefthand side. $\vec{F}_\sigma$ represents the sum of all horizontal differential forces acting in the ice-water column and would include, for example, an internal stress gradient integrated through the ice, time-dependent or baroclinic pressure gradients in the boundary layer, or other such phenomena. To investigate the inertial response of the system, we wish to find a time when the effect of $\vec{F}_\sigma$, which is in general quite complex, is minimized. Intuitively, it seems $\vec{F}_\sigma$ should be small in the summer and early fall when the pack is weakened by open leads and melting. During other seasons, we might look for periods of divergence in the pack, but caution is required here since divergence in the pack implies divergence and upwelling in the water column, which might add appreciably to $\vec{F}_\sigma$.

On the other hand, there will always be some dissipative process in the system and thus $\vec{F}_\sigma$ cannot be identically zero. Pollard and Millard [1974] acknowledged this by including linear damping in their model (i.e., $\vec{F}_\sigma = -c\vec{M}$). In the present model their philosophy is taken, but the approach is modified somewhat to account for an additional factor: under most circumstances the ice will be much more effective than the upper ocean at damping differential motions. However, there may exist times when even a highly dampening ice cover may come to equilibrium under a uniform stress. This happened in 1972 when the ice tracked straight for several inertial periods with stress balanced approximately by transport 90 degrees to the right.

Therefore we wanted an expression for $\vec{F}_\sigma$ which would allow a steady-state

$$f\,\hat{k} \times \vec{M} = \vec{\tau}_a$$

and would model the tendency of the ice to jam and dissipate kinetic energy during periods of rapid change. A simple expression satisfying these constraints for any finite wind stress is given by

$$\vec{F}_\sigma = \frac{-d_0 f}{2\pi} \frac{(\vec{M} \cdot \vec{\tau}_a)}{|\vec{\tau}_a|^2} \vec{\tau}_a$$

Thus $\vec{F}_\sigma$ depends on the component of $\vec{M}$ parallel to $\vec{\tau}_a$ and acts to oppose changes in $\vec{\tau}_a$.

Given the forcing air stress, equation (4) can be written

$$\frac{\partial \vec{M}}{\partial t} + f\,\hat{k} \times \vec{M} = \vec{\tau}_a - \frac{d_0 f}{2\pi} \frac{(\vec{M} \cdot \vec{\tau}_a)}{|\vec{\tau}_a|^2} \vec{\tau}_a$$

and solved iteratively. The task still remains to provide a quantitative relationship between ice velocity and the total transport. In the Pollard and Millard [1970] model, the subsurface current is related to the transport by assuming the momentum to be uniformly distributed throughout the mixed-layer depth, i.e.,

$$\vec{M} = \rho H \vec{U}$$

This ignores the fact that there is a complicated structure to the boundary layer, and that the surface velocity (which would be the ice velocity in our case) is not perpendicular to the stress. In the next section a more realistic model is developed.

3. THE ICE-OCEAN BOUNDARY LAYER

In order to relate the transport in the water column to that of the ice, we considered detailed measurements of the flow structure made during the 1972 AIDJEX pilot study [McPhee and Smith, 1976]. Figure 2a shows a hodograph of currents measured relative to the current at 32 m over 5 hours of uncommonly steady flow. The relative velocity at 32 m was within about 2 cm sec^{-1} of the relative velocity of the bottom and thus 32 m was taken as a reference level for wind-driven transport. At the time shown the mixed layer was about 38 m thick. It is worth noting that during this storm, which lasted several days in April, there was very little indication of the inertial waves described later in this paper and, for the time period shown, flow in the boundary layer approached a steady state for several inertial periods. The x-axis is parallel to the relative current at 2 m, which is taken to be

the direction of stress between water and ice. The angle between ice velocity and interfacial stress is β. Figure 2b shows vertical profiles of U_x and U_y components relative to 32 m.

For a steady state the stress at the interface is proportional to the transport of water mass in the y-direction, which is given by the area under the U_y profile. Although U_x is large at the surface, the net area under its profile is small. From considerations of inhomogeneity discussed in detail elsewhere [McPhee, 1974], the U_y profile, representing the average net transport, is taken to be approximately linear from its value at the surface to zero at the base of the boundary layer, h_{bl}. Since the surface value is known when the turning angle, β, and the relative ice velocity, $\vec{V} = \vec{V}_i - \vec{U}_g$, are known, the area can then be estimated from h_{bl}. Evidence from McPhee and Smith [1976] indicates that h_{bl} is proportional to u_*/f and we can idealize the U_y profile as shown in Figure 3, where the proportionality constant $2c_w/\sin\beta$ is chosen so that the transport magnitude is given by

$$|\vec{M}_w| = \frac{\rho_w c_w V^2}{f}$$

Referring to Figure 2a, it is clear that the transport is directed at an angle (90° - β) clockwise form $\vec{V}$; this is represented vectorially by

$$\vec{M}_w = -\frac{\rho_w c_w}{f} V \hat{k} \times (\vec{V} \cdot \underset{\sim}{B})$$

where $\underset{\sim}{B}$ is a rotation operator

$$\underset{\sim}{B} = \begin{pmatrix} \cos\beta & \sin\beta \\ -\sin\beta & \cos\beta \end{pmatrix}$$

For steady state conditions

$$f \hat{k} \times \vec{M}_w = -\vec{\tau}_w$$

and

$$\vec{\tau}_w = -\rho_w c_w V(\vec{V} \cdot \underset{\sim}{B})$$

which is the expression for the water stress term now used in the AIDJEX ice model [McPhee, 1975].

The total relative transport is given by

$$\vec{M} = m\vec{V} + \frac{\rho_w c_w}{f} V \hat{k} \times (\vec{V} \cdot \underset{\sim}{B})$$

when the drift is steady. In the present model, we assume that this relationship is satisfied at all times, in effect ignoring that the water column at any level will not adjust instantaneously to changes in ice velocity. This assumption is crucial if simplicity is to be maintained, and is not overly restrictive as long as the somewhat artificial damping term in the momentum equation is stipulated. Thorndike, in a related work (unpublished manuscript), has analyzed the time-dependent behavior of a simple two-layer system coupled by stress proportional to the velocity difference between layers. He showed that the transient adjustment in the system to the sudden onset of a constant wind stress is both short-lived and small in amplitude when compared with the undamped inertial oscillations in each layer. With a real time-varying wind stress the effect would be more pronounced, but it seems reasonable to parameterize it as a damping term in the momentum balance as we have done here. There is also experimental evidence [McPhee, in preparation] that shows the *relative* inertial (high frequency) motion between ice and the current measured at 2 m to be quite small, even though in the mean there is substantial shear between the two levels. This implies that the magnitude of inertial motions at 2 m is almost as large as that of the ice, emphasizing the importance of the inertia of the water column.

Once $\vec{M}$ is determined, the implicit equations for components of $\vec{V}$ can be readily solved.

4. OBSERVATIONS

Positions of manned camps in the 1975-1976 AIDJEX field experiment were determined by use of Navy Navigation Satellite. Each fix, of which there are typically 30 per day possible at ice camp latitudes, is accurate to within 50-80 m, but the accuracy can be improved by spatial and temporal error smoothing by a process called Kalman filtering [Thorndike, 1974]. The output of the filter is time series of position, velocity, and acceleration at three-hour intervals. Although the filter attenuates real short-period motion along with the errors, with enough fixes it is estimated to pass about 40%-50% of the spectral power at 12.4 hours [A. Thorndike, personal communication], which corresponds to the inertial period at 75°N. In order to infer the relative ice velocity, $\vec{V}$, from the absolute position, some knowledge of the geostrophic flow in the region is necessary. It is thought to be small from previous work [Newton, 1974] and this has been borne out by observation, although its exact magnitude and orientation are not known.

A different approach to measuring ice velocity, particularly with respect to geostrophic flow in the ocean, is to suspend current meters at some level below the wind-driven boundary layer. This was done as part of the routine environmental data collection at the manned AIDJEX camps with current samples every 30 seconds at 30 m below the ice [Hunkins, 1975]. As long as the boundary layer does not exceed this depth and baroclinic currents are small, the negative of the measured velocity should be the quantity, $\vec{V} = \vec{V}_i - \vec{U}_g$. The current meter measurements are subject to directional errors of at least ±5 degrees; each meter has a dead band of 10°-15° about its zero crossing, and as currents become small, threshold problems are encountered. Care should also be taken in interpreting measurements made below the mixed layer, since baroclinic currents in the upper pycnocline are not uncommon. During periods of appreciable ice drift, STD profiles indicate that the water column is usually well mixed to below the 30 m level, although during calm periods in summer stratification can extend to the surface.

Figure 4 shows the filtered NavSat trajectory of Big Bear for the period 7 August 1975 to 17 August 1975 (00 GMT, calendar day 219 to 00 GMT day 229). The period chosen exhibits the characteristic scallops associated with inertial

waves. Figure 5 shows ice velocity components from the two sources discussed above: the absolute filtered NavSat velocities (top trace) and the negative of the current measured at 30 m (bottom trace). In the coordinate system used, U is the east-west velocity (zonal) and V is north-south (meridional).

For the most part the curves coincide fairly well. Gaps in the current record indicate large variance in the hourly means, probably caused by the dead-band problem mentioned above. The fact that excursions are greater in the current meter record is taken as confirmation that the inertial wave is better defined by the more rapid sampling. The comparatively smooth peaks in the NavSat components from day 225 to 227 reflect a reduced number of available fixes, and serve to emphasize that the sampling is not uniform in time. The curves demonstrate the general conclusion that ice velocity with respect to the 30 m level provides a believable estimate of $\vec{V}$, including the inertial content. In what follows, velocity simulations are compared with the negative of the relative current at 30 m.

5. SIMULATION

The motion of Big Bear for the 10-day period was simulated by calculating air stress from the wind measured at 10 m according to

$$\vec{\tau}_a = \rho_a \, c_{10} \, |\vec{U}_{10}| \, \vec{U}_{10}$$

with $c_{10} = 0.0027$ [E. Leavitt, personal communication]. The stress components in the x (east) and y (north) directions are shown in Figure 6.

For comparison purposes, in all the simulations the velocity was first predicted using a "free drift" version of equation (2), with "passive drag," i.e.,

$$m\left(\frac{\partial \vec{V}}{\partial t} + f\,\hat{k} \times \vec{V}\right) = \vec{\tau}_a + \vec{\tau}_w$$

with

$$\vec{\tau}_w = -\rho_w c_w \, V(\vec{V} \cdot \underset{\sim}{B})$$

so that the simulation includes only the inertia of the ice. The middle traces of Figure 7 show the results of the calculations with m = 300 gm cm^{-2}, c_w = 0.0055, and β = 23°. The inertia of the ice appears to be quickly damped by the passive water drag and the response follows the wind stress closely. Comparison between measured (top trace) and predicted (middle trace) components shows that the mean trend is fairly well represented, but that the inertial response is badly under estimated.

The total mass transport equation, (5), was then integrated for the same wind stress with d_0, the damping factor, equal ot 0.25. The time step was 4 minutes, with $\vec{M}$ solved for $\vec{V}$ at hourly intervals and the results plotted as the bottom traces of Figure 7. For the first part of the 10-day record, the inertial simulation seems to quite successfully reproduce the observed oscillations perhaps showing a little too much response to the initial wind pulse and drifting slowly out of phase as the ringing dies down. After day 226 the waves are small, which could be due to a general tightening of the ice that would, in effect, increase d_0.

The model was also tested using winds and currents measured at station Caribou for a 20-day run from 29 August 1975 (day 241) to 18 September 1975 (day 261). Results are shown in Figure 8 using the same parameters as for Big Bear, except d_0 = 1.0, which appeared to give the best fit overall. Although there are some periods (e.g., days 241-244) when the damping appears somewhat strong and others where there is phase drift, the model does a remarkable job considering the crudeness of the boundary layer treatment. Note that inertial ringing is present throughout the whole period, in contrast to the Big Bear study in which oscillations were very small on days 226-229.

6. INERTIAL OSCILLATIONS AND INTERNAL ICE STRESS

The previous examples suggest that the model might be useful for isolating periods of free drift, the theory being that if the observed wind drove inertial waves in the model when none were actually observed, one might then infer qualitatively that the ice was supporting an internal stress

gradient. An interesting example is shown in Figure 9, where the motion of Caribou has again been simulated using the same parameters as for the run on day 241-261. For brevity, only the U component is shown. Waves are clearly evident at the start and near the middle of the period, but there are also times when the motion is severely damped.

It is germane to point out that on day 275 (2 October 1975), the main AIDJEX camp Big Bear, which was about 70 km northeast of Caribou, suffered enough deformation and cracking to cause most of its scientific program to be discontinued. There was hope that the camp might be re-established, but about eleven days later (day 286) it again broke up and was subsequently abandoned. The motion record for Caribou, especially when compared with the simulation, suggests that during those times there may have been a general tightening of the ice with enough stress gradient to cause failure at weak points.

A notable sidelight on this is that Fridjof Nansen, during the drift of the *Fram*, noted periodic increases in ice pressure on the ship's hull. In his diary dated 13 October 1893, he wrote:

> "It occurs with greatest regularity. The ice slackens twice and packs twice in twenty-four hours. The pressure has happened about four, five, and six o'clock in the morning, and almost exactly the same hour in the afternoon, and in between we have always lain for some part of the time in open water." [Nansen, 1968]

He naturally enough attributed the fluctuations to tidal motion (the inertial period at 78°N, about where the *Fram* was located, is 12.27 hours), and in fact correlated them with the new moon. Later he expanded on his observations:

> "But these tidal pressures did not occur during the whole time of our drifting. We noticed them especially the first autumn, while we were in the neighborhood of the open sea north of Siberia, and the last year, when the *Fram* was drawing near the open Atlantic Ocean; they were less noticeable while we were in the polar basin." [Nansen, 1968]

From a cursory reading of his diary excerpts, it appears as if the periodic pressures were also correlated with the changes in the wind, and it seems plausible that the variations were caused by inertial accelerations rather than by tidal motion. During the summer, the waves are largely

unconstrained, and perceptible only with highly accurate navigation or current meters. However, in the fall the pack must go through a transition to its compact winter state and at these times, when part of the pack is freely oscillating and part is constrained, there must be zones with much periodic deformation. It may have been just such a zone that Nansen was describing.

7. CONCLUSIONS

Results shown here indicate that for short-term response (periods less than a day) the inertia of the water column is an important part of the total momentum balance. They also show that by a fairly simple extension of our present conceptual model of the ice-ocean boundary layer, we can simulate the inertial response with some success. It is not clear, however, what implication the study may have for large-scale modeling of pack ice, for even if short-term response were a desired goal, it is questionable whether realistic models can predict the local wind field well enough for this type of calculation. Over longer time periods, the difference made by including the inertia of the ocean in dynamical simulations might not appear above the uncertainty in drag coefficients, although this is by no means established.

The spatial variation and coherence of the waves are subjects of considerable interest (although not addressed here) because of the potential role they play in producing new ice. If the waves cause divergence and compression over large areas in newly forming ice, they would tend to mechanically thicken young ice and open new water to rapid freezing, thus greatly increasing the overall production of ice.

Aside from these considerations, the exercise emphasizes an important aspect of the ice-ocean system that may sometimes be overlooked: namely, that because ice accounts for only a fraction of the total mass transport rightward from the wind (*cum sole*), tendencies toward convergence or divergence of mass are at least as pronounced in the oceanic boundary layer as they are in the ice itself, and may have an important effect on the long-term momentum balance. How these boundary layer phenomena are included in a realistic pack ice model is still an open question.

Finally, it seems appropriate to stress the possibility, by detailed study of the summertime boundary layer under pack ice, of enhancing greatly our general knowledge of time-dependent Ekman layer dynamics. An accurate survey of mean and fluctuating currents at several levels in the upper ocean, along with rapid sampling of the density field as the ice drifts through episodes like those described in this paper, could be an invaluable data set.

ACKNOWLEDGMENTS

I am indebted to many of my colleagues at AIDJEX for help in understanding these features and amassing the data for presentation. In particular I thank F. Carsey, E. Leavitt, D. Rothrock, and A. Thorndike. R. Colony brought Nansen's observations to my attention, for which I am very grateful.

The work was supported by the National Science Foundation under grant OPP71-04031 and by AIDJEX.

REFERENCES

Hunkins, K. L. 1967. Inertial oscillations of Fletcher's ice island (T3). *Journal of Geophysical Research, 72,* 1165-1174.

Hunkins, K. L. 1975. The oceanographic program for the AIDJEX main experiment. *AIDJEX Bulletin, 28,* 61-68.

McPhee, M. G. 1975. Ice-ocean momentum transfer for the AIDJEX ice model. *AIDJEX Bulletin, 29,* 93-112.

McPhee, M. G., and J. D. Smith. 1976. Measurements of the turbulent boundary layer under pack ice. *Journal of Physical Oceanography, 6*(5), 696-711.

Nansen, Fridtjof. 1968. Adrift on the polar seas. In *Polar Secrets: A Treasury of the Arctic and Antarctic* (ed. Seon Manley and Gogo Lewis), Doubleday & Co., Garden City, New York, pp. 186-222.

Newton, J. L. 1974. The Canada Basin; mean circulation and intermediate scale flow features. Ph.D. dissertation, University of Washington, Seattle, Washington.

Pollard, R. T., and R. C. Millard, Jr. 1970. Comparison between observed and simulated wind-generated inertial oscillations. *Deep-Sea Research, 17,* 813-821.

Rothrock, D. A. 1975. The steady drift of an incompressible arctic ice cover. *Journal of Geophysical Research, 80,* 387-397.

Thorndike, A. S. 1974. Strain calculations using AIDJEX 1972 position data. *AIDJEX Bulletin, 24,* 107-129.

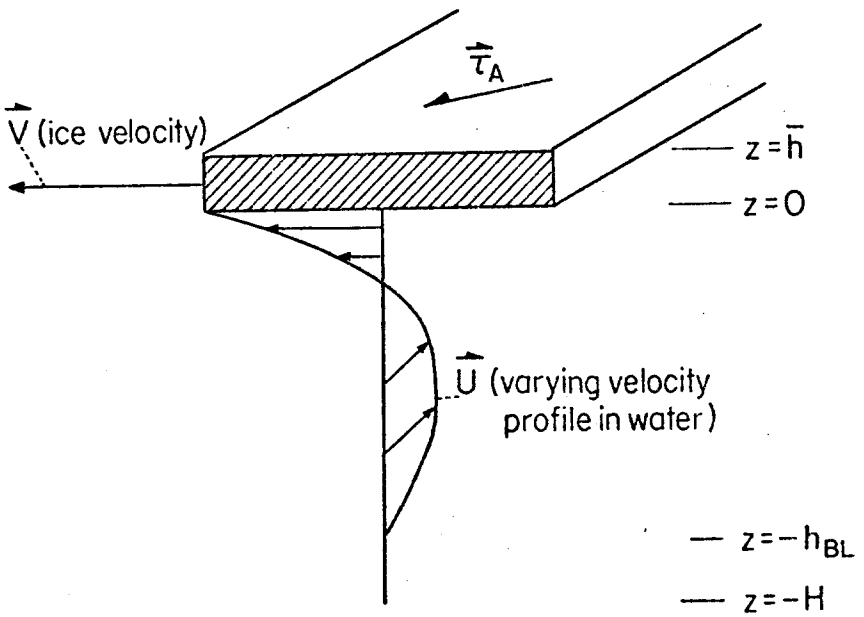

Fig. 1. Schematic of the ice-upper ocean system in motion.

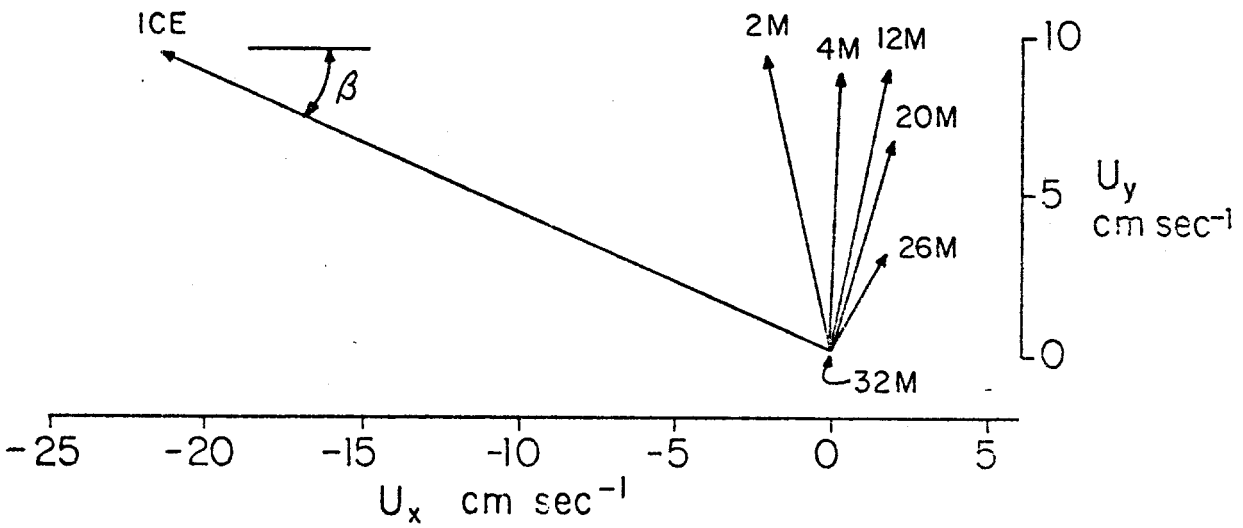

Fig. 2a. Hodograph of measured mean velocities with respect to the 32 m level at AIDJEX station Jumpsuit, afternoon of 12 April 1972. Depths are from the ice underside.

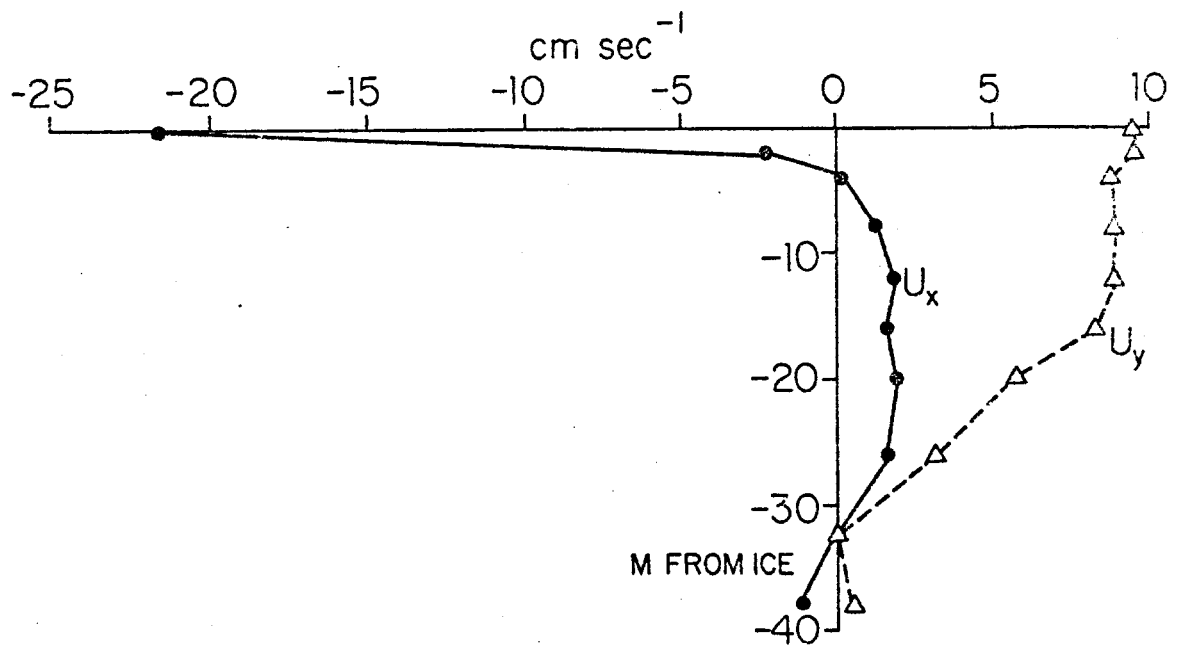

Fig. 2b. Vertical profiles of mean velocity. U_x is in direction of surface stress.

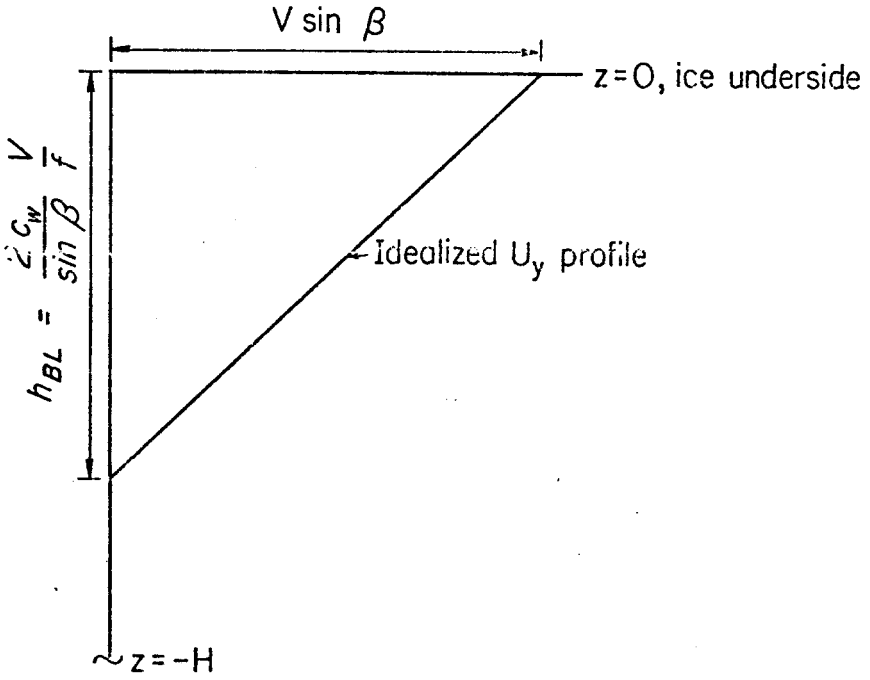

Fig. 3. Idealized profile of mean velocity perpendicular to surface stress in the upper ocean.

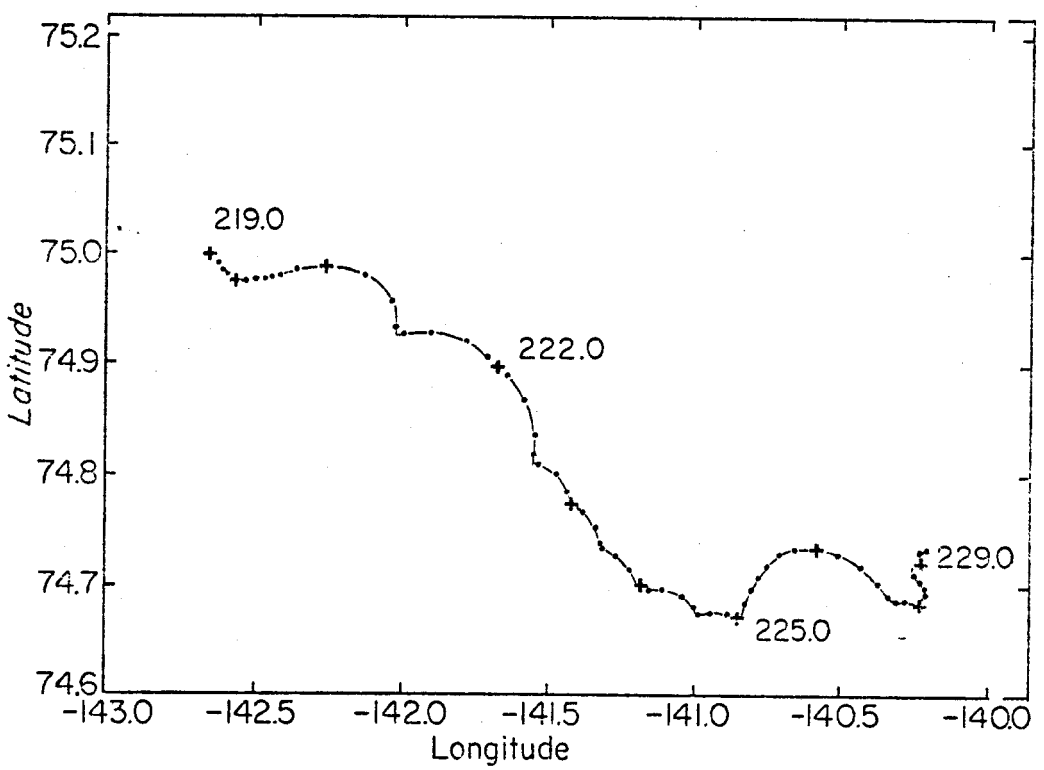

Fig. 4. Trajectory of ice station Big Bear, 7 August 1975 to 17 August 1975 (calendar days 219 to 229). Dots are three-hour samples from smoothed NavSat positions.

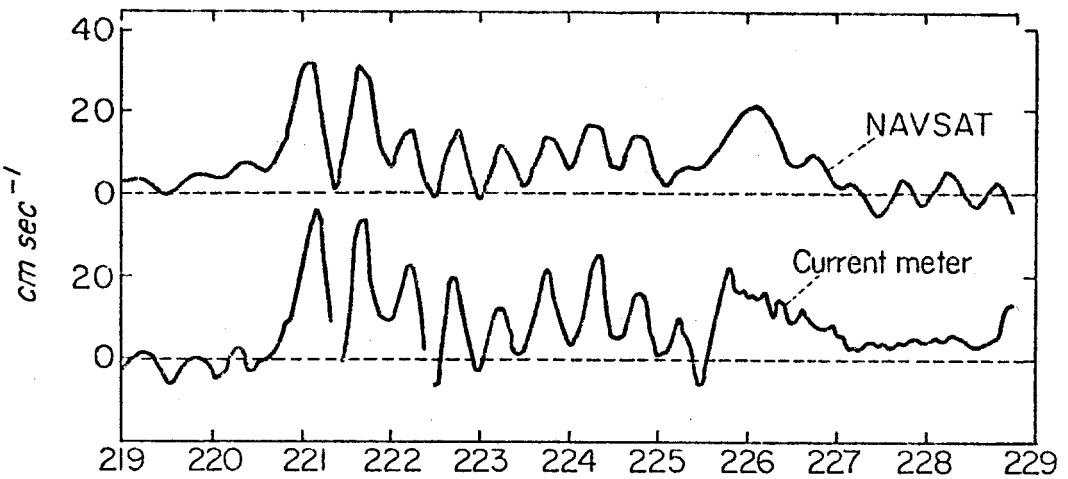

Fig. 5a. Comparison of zonal velocity (U component) obtained from NavSat positions (top trace) with velocity obtained from current meter suspended 30 m below ice (bottom trace) at Big Bear.

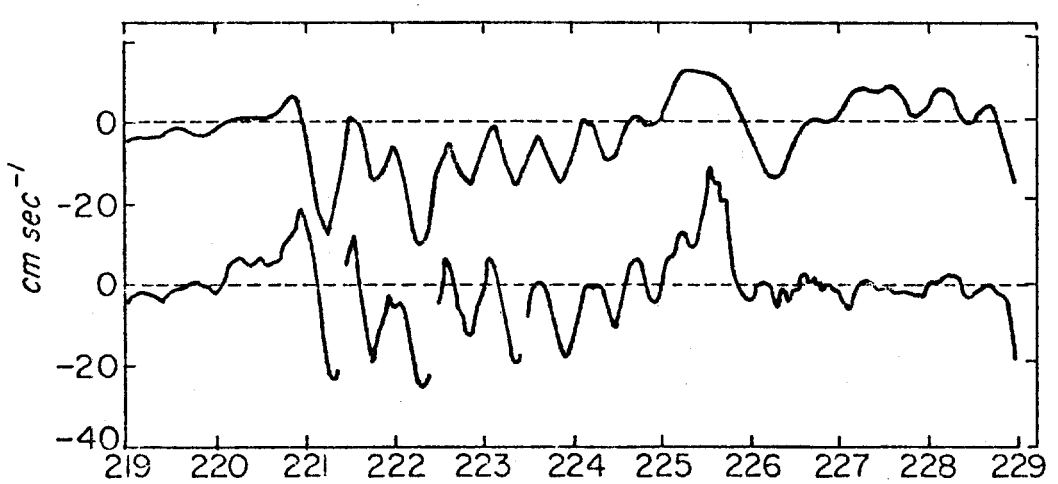

Fig. 5b. Meridional (V) component.

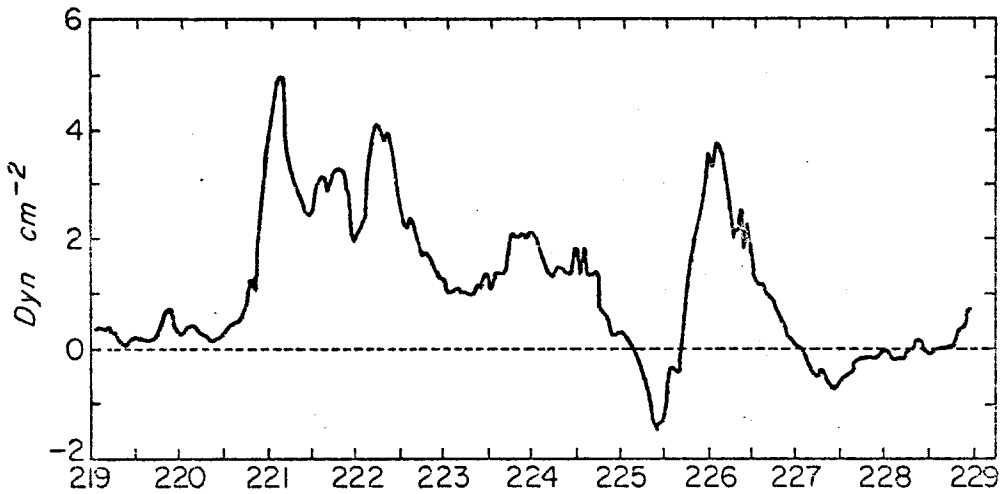

Fig. 6a. Zonal component of wind stress at Big Bear from 10 m wind with c_{10} = 0.0027.

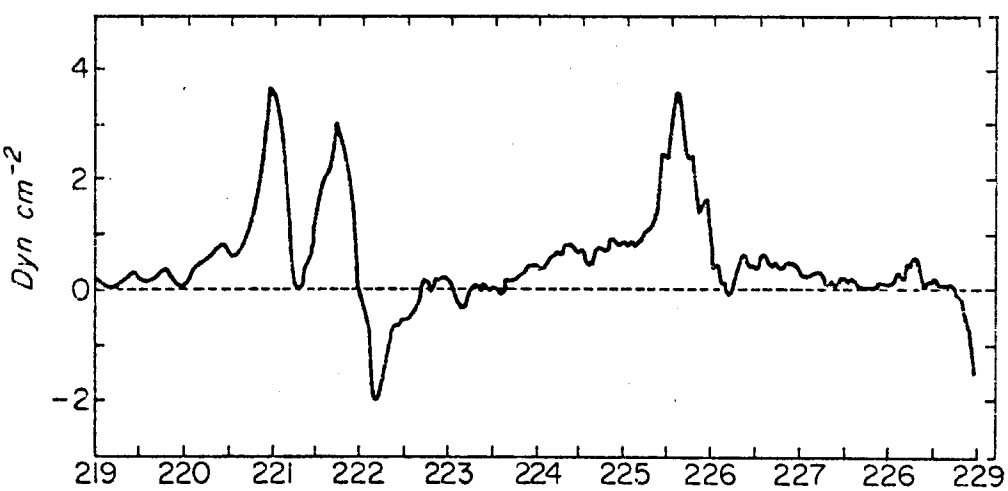

Fig. 6b. Meridional component of wind stress.

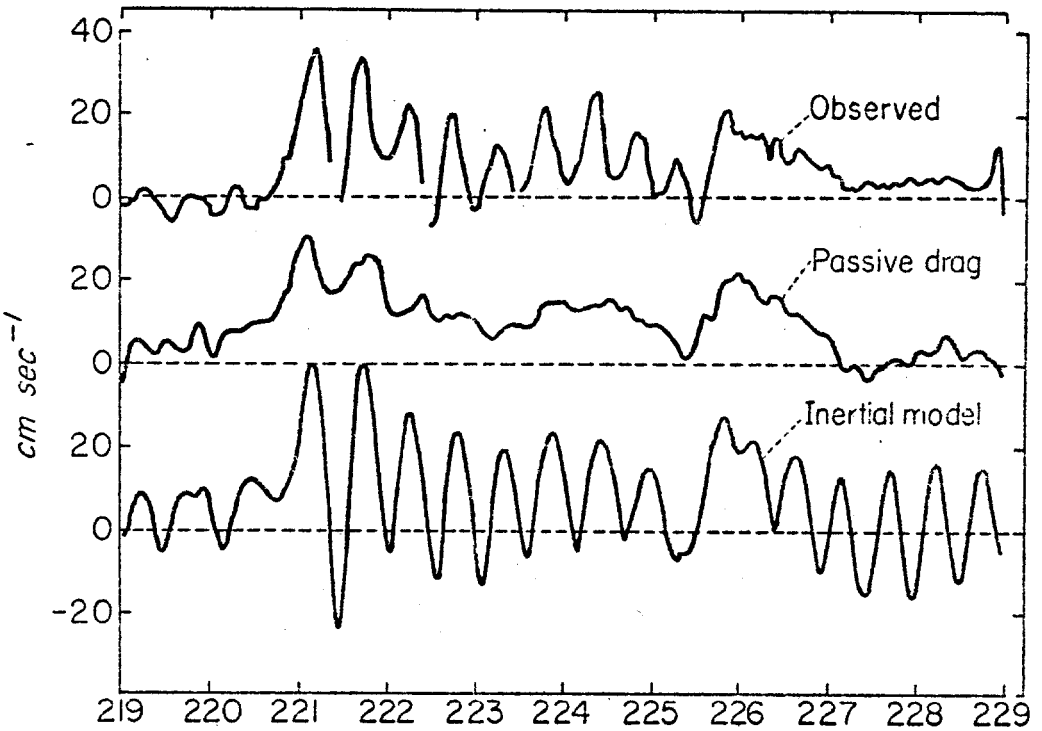

Fig. 7a. Observed and simulated zonal velocity at Big Bear. Top trace: observed; middle: simulated using passive water drag; bottom: simulated with inertial model, d_0 = 0.25.

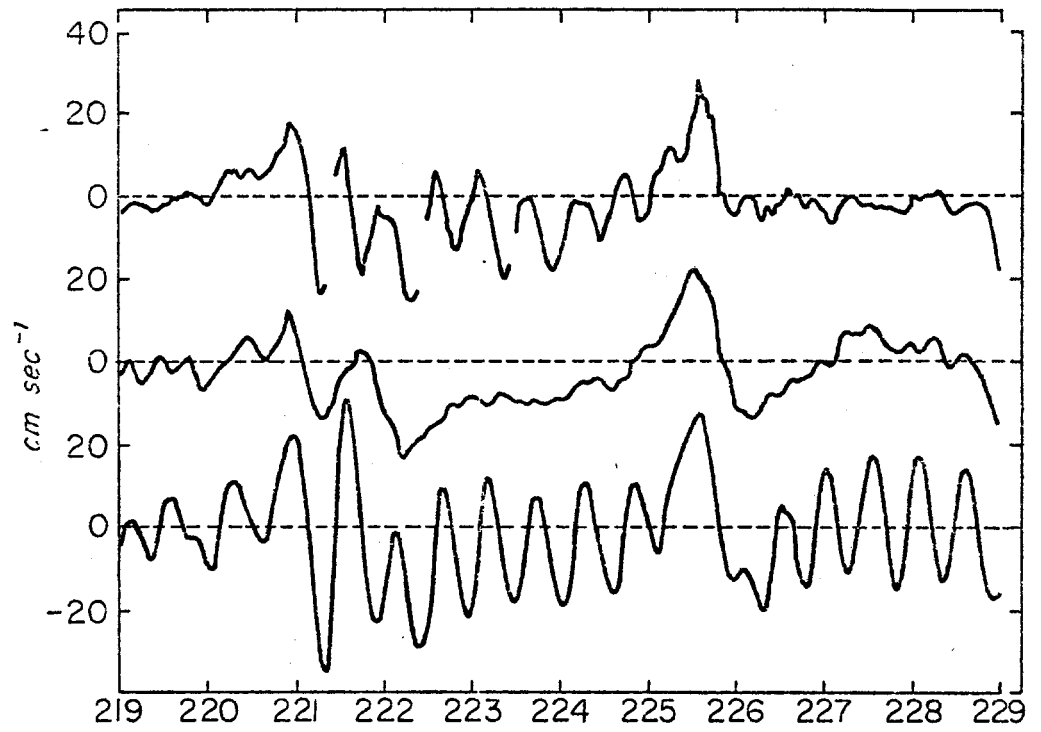

Fig. 7b. Same except meridional component.

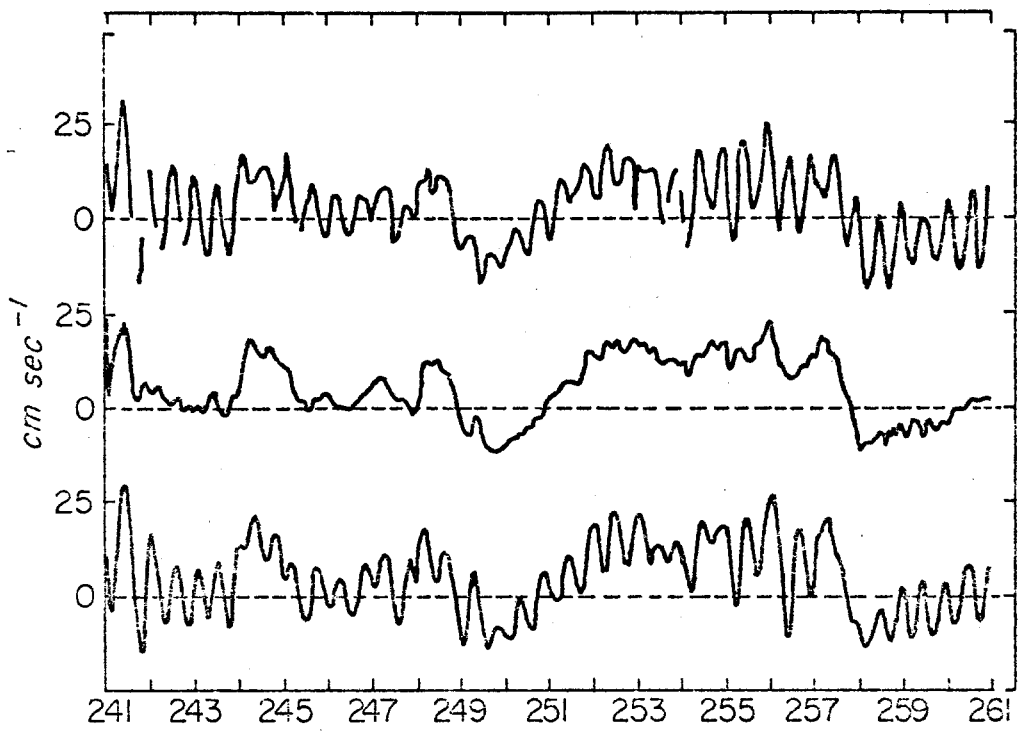

Fig. 8a. Observed and simulated zonal velocity at Caribou, 29 August 1975 to 18 September 1975. Top trace: observed; middle: simulated, passive water drag; bottom: simulated with inertial model d_0 = 0.100.

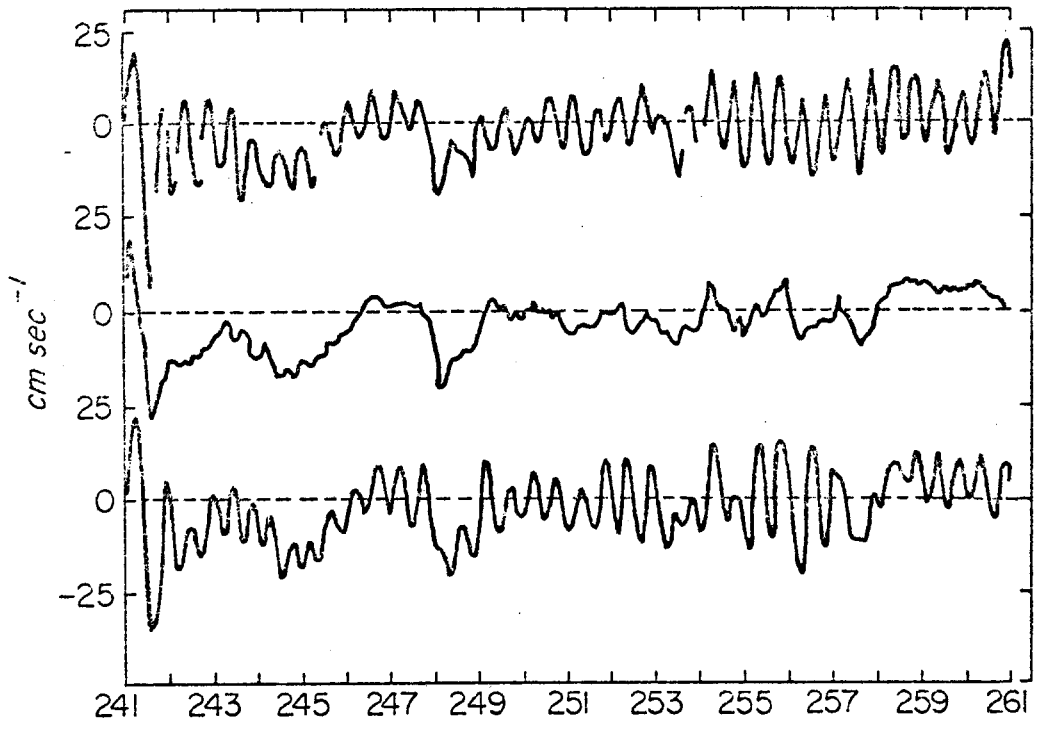

Fig. 8b. Meridional component

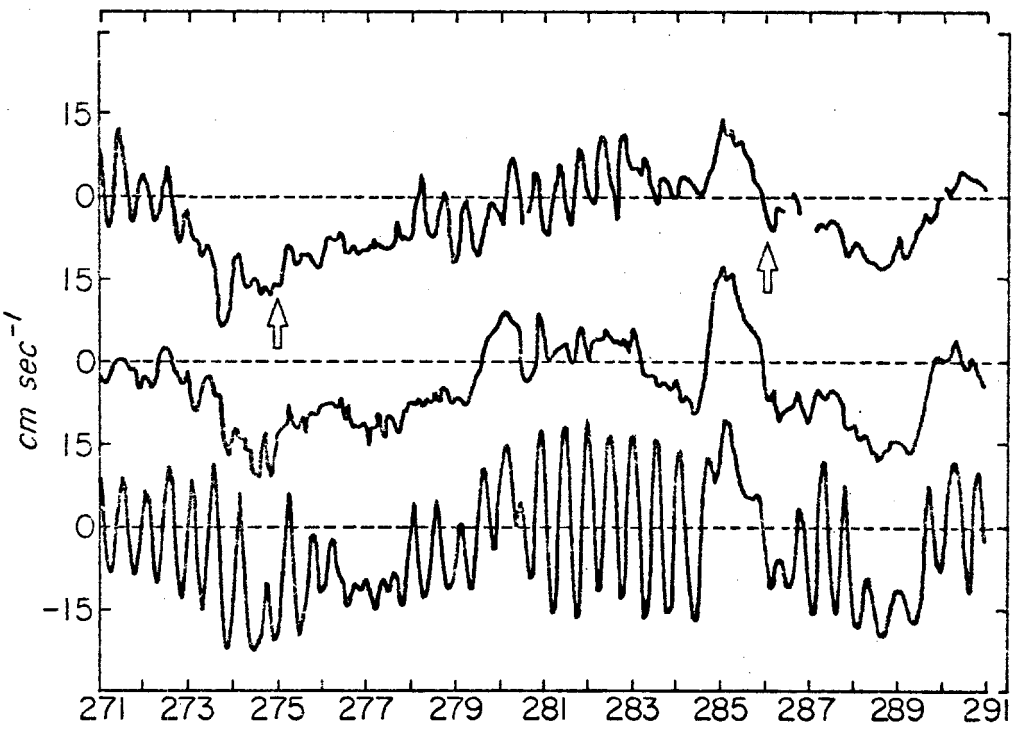

Fig. 9. Observed and simulated zonal velocity at Caribou, 28 September 1975 to 18 October 1975. Top: observed; middle: simulated, passive drag; bottom: simulated inertial, d_0 = 1.00. Note transition to conditions more typical of winter after day 274 and again after day 283.

PIBAL/ACOUSTIC RADAR DATA IN MEASUREMENT AND COMPUTATION OF AIR STRESS OVER PACK ICE

by

Frank Carsey and Eric Leavitt
AIDJEX

ABSTRACT

The use of planetary boundary layer thickness derived by acoustic radar in the estimation of air stress over pack ice is discussed. Pilot balloon winds are normalized and evaluated through this thickness prior to momentum integration of the Ekman force balance equation and prior to the construction of seasonal mean profiles. Examination of individual and constructed mean profiles leads to a stress relation $\tau = (0.5 \pm 0.1)\ \rho f\ Z_i\ G \sin \alpha$, where stress τ is obtained from Coriolis parameter f, inversion height (boundary layer thickness) Z_i, geostrophic wind speed G, and total wind turning α. The direction of mean stress from the integrated profiles over the entire year is significantly skewed some 16° to the left of the surface wind. When this skewing is interpreted as error due to baroclinic wind, a boundary layer thermal gradient parallel to the pressure gradient is indicated.

INTRODUCTION

Because air stress is the dominant force that drives the pack ice, part of the AIDJEX program to model pack ice behavior is to develop air stress models suitable to pack ice, evaluate the model parameters, and test the models with results from the year-long main field experiment. There is no simple way to measure total stress in the field; theoretical devices must be employed. In the search for proxy measurables to yield an "observed" air stress, the modeling methods that are inevitably incorporated produce a semi-empirical stress model. Each handling of the data influences the theory, and vice versa.

The purpose and limits of AIDJEX call for a model driven by measured surface atmospheric pressure. From these data the geostrophic wind can be derived and a synoptic surface chart drawn by computer-fitting a polynomial to the measured pressures [Brown et al., 1974]. Noise in the pressure measurement results in some 10% uncertainty in the value of G, which leads to considerable difficulty in evaluating the curl and divergence of the G field. For these reasons the AIDJEX air stress model should be one strongly dependent on the geostrophic wind field, weakly dependent on the field derivatives, and completely independent of measured winds and fluxes.

AIR STRESS MODELING

The first success in measuring and modeling air stress was that of Ekman [1905], who was in fact studying air stress on arctic pack ice. Ekman considered a single layer planetary boundary layer (PBL); Taylor [1915] implicitly subdivided the PBL into two layers; Rossby [1932] examined a two-layer system. Their results are:

$$\text{Ekman [1905]:} \quad u_*/G = (K_E f)^{\frac{1}{4}}/G^{\frac{1}{2}}$$

$$\text{Taylor [1915]:} \quad u_*/G = (2K_E f)^{\frac{1}{2}} \sin\alpha/G$$

$$\text{Rossby [1932]:} \quad u_*/G = \tfrac{3}{2} K_R \sin\alpha, \quad K_R = 0.065$$

where $u_* = \sqrt{\tau/\rho}$ is called the friction velocity for stress τ and air density ρ, G is the geostrophic wind speed, K_E and K_R are eddy viscosity parameters, $f = 2\Omega \sin\theta$ is the Coriolis parameter for earth's rotation Ω and latitude θ, and α is the total turning of the wind from above the PBL to the surface.

More recent modeling of the ratio u_*/G has generally resulted in parameterization schemes involving extensive input fields. Malgarejo and Deardorff [1974] and Blackadar and Tennekes [1968], for example, construct models of u_*/G which involve knowledge of heat flux and eddy viscosity fields. Brown [1974a] has devised a two-layer model including secondary flow which yields the result

$$u_*/G = [\sin\alpha + C_1(\cos\alpha - \sin\alpha)]/C_2 \qquad (2)$$

where C_1 and C_2 are defined as

$$\begin{aligned} C_1 &= \delta/h \\ C_2 &= \delta/z_s \end{aligned} \qquad (3)$$

δ is the outer layer characteristic scale height, h is the height of the interface, and z_s is the scale height of the surface layer. In general, C_1 and C_2 must be taken as nearly free parameters with C_2 reflecting surface roughness. The total turning α is the major stratification parameter, although apparently C_1 may vary with stability also.

MOMENTUM INTEGRAL MODELING

The modeling method to be discussed in this report is a stronger empirical approach which relies heavily on the early stress calculations of Ekman and Taylor as initially applied by Brown [1974b]. The Ekman force balance component equations can be written for $\vec{G} = (G,0,0)$ and horizontial homogeneity:

$$\begin{aligned} \rho f\, v &= \frac{\partial}{\partial z}(\tau^x) \\ -\rho f(u - G) &= \frac{\partial}{\partial z}(\tau^y) \end{aligned} \qquad (4)$$

in the coordinate system where $v(z)$ is the wind component normal to the geostrophic direction and $u(z)$ is the wind component along the geostrophic direction. Here τ^x is the stress in the x, or geostrophic, direction. The above equations yield independent x and y components of stress (and hence a stress direction as well as magnitude) upon being supplied with wind profiles in the vertical. To use the equations, both sides are integrated from the surface to the PBL top at $z = Z_i$, where the stress is taken to be zero. Clearly, wind wind profiles can be generated *a priori* and integrated to produce "reasonable"

results. These operations each yield a variation of a general equation for stress at $z = 0$:

$$\tau_0 = A\ f\ Z_i\ G\ S(\alpha) \tag{5}$$

where A and $S(\alpha)$ depend on the details of the shapes of $u(z)$ and $v(z)$ chosen. Examination of the PBL models for u_*/G listed above suggests that $S(\alpha) = \sin \alpha$ is a suitable trial function. For the constant A, Brown [1974b] obtains $A = 1$, Taylor [1915] suggests $A = 1/\pi$, and S. P. S. Arya (private communication) suggests $A = 0.4$ for the neutral PBL to $A = 1.0$ for the unstable PBL. The average of these numbers is 0.57. Merging all of the above, a trial stress equation would be

$$\tau_0 = 0.57\rho\ f\ Z_i\ G \sin(\alpha) \tag{6}$$

While this is not an acceptable model, since Z_i and α must be supplied in addition to G, this equation is a vehicle for a transition from measured to modeled stress.

In general, the Ekman force balance equation can be applied only with great care. The equations, as written, are true at every point in the flow which is in steady state and free of horizontal inhomogeneity. Clearly, the surface layer is not free of these contaminants and the equations cannot be applied here. Above the surface layer one must be confident that the local pressure gradient as measured at the surface, over large horizontal scales, is appropriate throughout the PBL. In a later section of this paper the effect of temperature gradients on the stress computation will be discussed. In the actual integration of wind data, a steady state wind rather than a high degree of turbulence should be represented. This problem is dealt with by the averaging of large numbers of profiles.

THE DATA SET

The total AIDJEX meteorological data set is extensive, including surface pressure maps, winds and temperatures from masts at four camps, a profile

tower, satellite cloud photographs, and NCAR Electra instrumented aircraft data. In this report the focus will be on PBL data, which consists of a continuous acoustic radar record and regular pilot balloon (pibal) derived winds. Some references will be made to surface (10 m) wind speed and computed geostrophic wind speed. Electra results will be compared with acoustic radar results in a future discussion and some aspects of this data set will be further analyzed to obtain improved seasonal and synoptic variation of important variables.

Acoustic radar data were taken in the usual way [Carsey, 1976] in which echo strength is recorded on dry paper facsimile format. The radar went into operation 13 April 1975 and was removed from the ice 18 April 1976. The month of October 1975 was lost to data taking due to the breakup on 1 October of the floe on which the main camp (Big Bear) was located. The radar was reestablished at a satellite camp (Caribou) on 5 November 1975. Otherwise, the unit performed well and continuously except for maintenance and repair.

Results of Shir [1972] and Taylor [1970] suggest that the Lagrangian behavior of the whole stable PBL changes slowly with a change in either surface heat flux or surface roughness. In their models the PBL wind profile establishes a new form some 100-300 PBL heights downstream of the change. This leads to the conclusion that in the Arctic where surface property changes are small, the Eulerian PBL should change on a basically synoptic time scale. In the Arctic a system can entirely overhaul a given point in about 24 hours. This calls for resolution which is fine with respect to one day. One hour was chosen. While it can be argued that small time scale phenomena such as gravity waves influence PBL dynamics and hence should not be ignored, these processes are very rare in the Arctic. Also, synoptic scale subsidence alters the acoustic radar record on shorter time scales. While the subsidence doubtlessly affects the PBL flow and transport and the echo structures aloft do signal the subsidence, the structures themselves have no bearing on PBL measurements since they are almost certainly above the true dynamic boundary layer.

The radar record itself shows much less variety than a typical record from a continental site. Most important, the inversion interpreted as the PBL top was essentially always present as a slowly moving echo top some

100-500 m above the surface. If that layer was not ground based, such an echo usually existed to about one third the total PBL thickness. In higher wind the upper echo often bifurcates with the produced echo-free region persisting at a small size or growing to a substantial fraction of the PBL thickness. During high winds (largest recorded gust: 18.5 m sec^{-1}) the lone inversion echo was quite steady at 300-600 m for hours at a time.

Beneath the persistent arctic summer stratus the radar occasionally recorded weak plumelike echoes. At the same time, the record consistently showed a strong echo--taken to be the (lowest) cloud top--more than 100 m above the stratus base (determined by balloon observation). On a few occasions large plumes--some 500 m high and 10 minutes in duration--were observed. In the summer the record indicated that the stratus top has the effect of changing the thermodynamic layer into a dynamic boundary layer.

Wind profiles were taken by dual theodolite tracking of slow-ascent pilot balloons (pibals), with typical observation spacing of 30m in the vertical. A goal of two ascents per day for the entire year was not quite realized, but 240 pibals were released when winds were sufficiently high (greater than 5 m sec^{-1} aloft) for useful data. During NCAR Electra overflights, release density was increased to 5-7 per day.

Individual pibal profiles often look like the plot of a random variable. For this reason the pibal measurements from a given season were normalized with the PBL thickness derived by acoustic radar and then averaged to produce a mean profile. Each pibal profile was integrated as in equation (4) to generate a total stress value. In this process the upper limit of integration was taken to be the radar-derived height. The geostrophic wind was taken to be the pibal-derived wind in the observational interval above the inversion height Z_i.

Figure 1 shows wind profiles from pibal tracking with simultaneous acoustic radar echo structure at release time for 19 July 1975. The five profiles and PBL thicknesses are similar, but they vary considerably point for point. Still, these profiles are very well behaved compared with many. Figure 2 shows five pibals from 7 February 1976. Here the acoustic radar signal is not shown, but it is employed to construct the ordinate variable

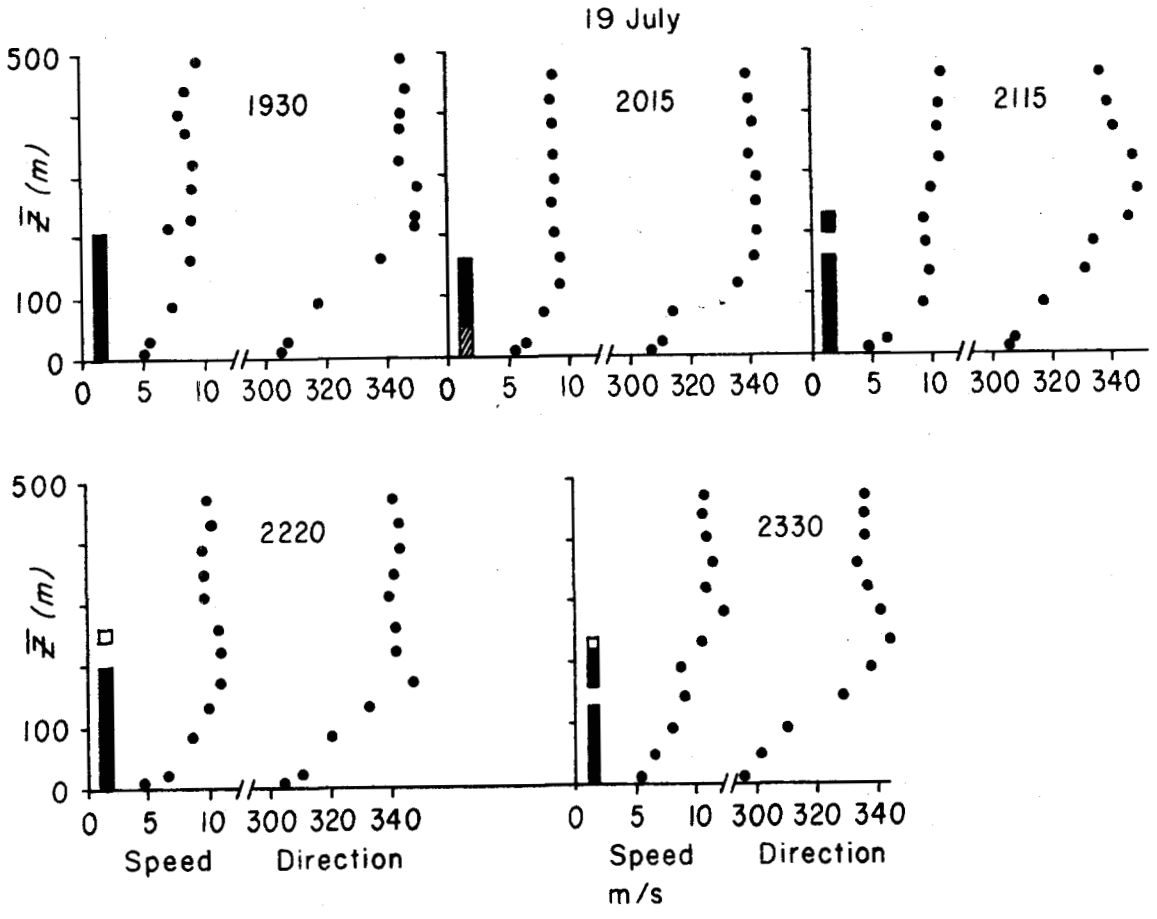

Fig. 1. Pibal-derived wind speed and direction profiles for 19 July 1975 at Big Bear. Vertical lines to the left of each profile are duplicates of acoustic radar data taken simultaneously with balloon releases; white spaces in the line signal weaker echoes.

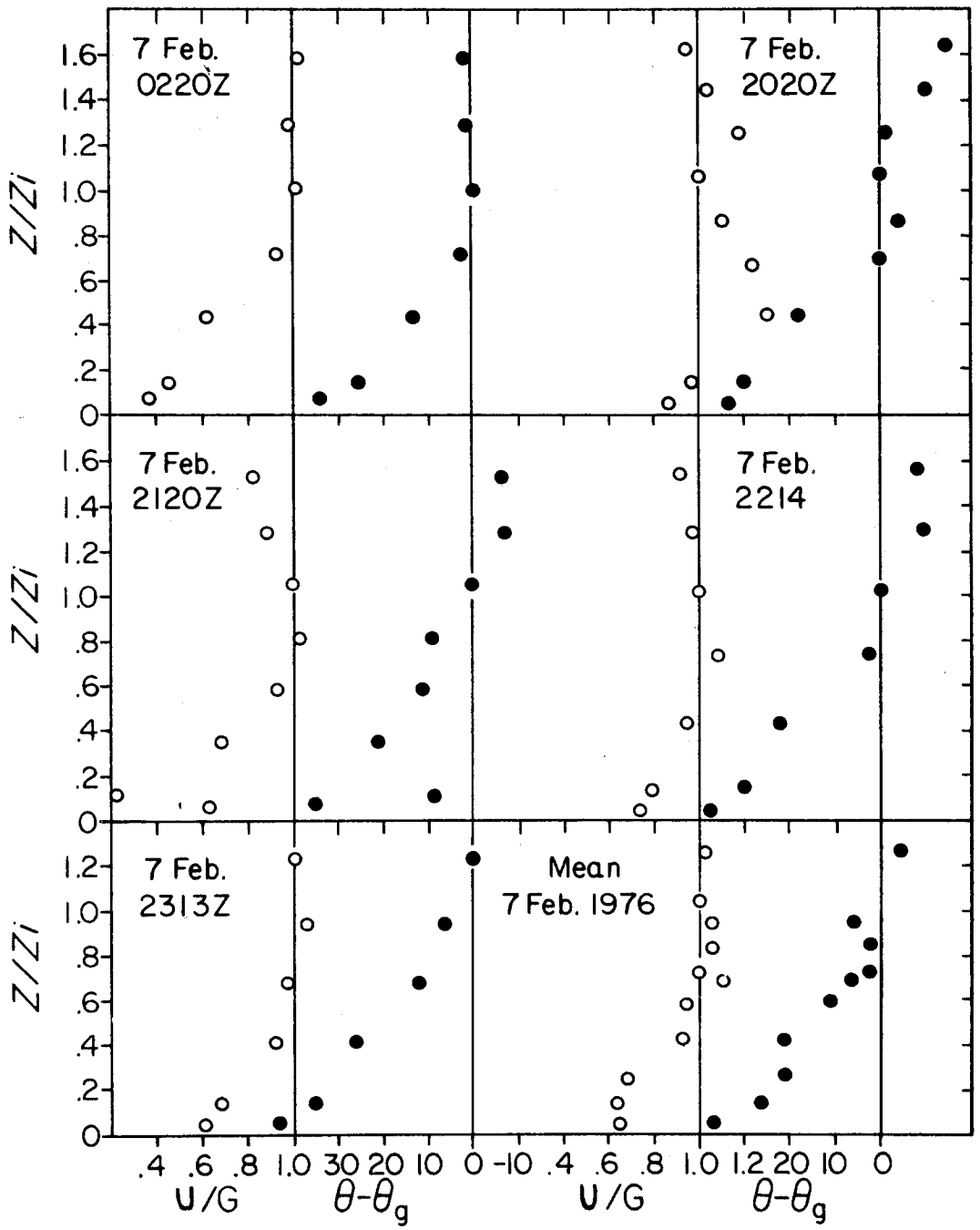

Fig. 2. Wind speed and direction profiles taken by pibal tracking 7 Feb. 1976. Height Z_i is determined by acoustic radar; speed G is taken to be wind speed in the interval above $Z = Z_i$. The axis is $\theta = 0$; in each case it is directed along the measured geostrophic wind. Baroclinicity is especially apparent at 2120Z.

Z/Z_i and the geostrophic wind speed G. Individual behavior of these pibals varies. The 0220Z release produces a small U/G ratio at the surface and, in general, is smoothly behaved. The 2020Z release, by contrast, produces a high surface U/G, turbulent flow, and a regime of backing. The mean for the 7 February profiles is shown at lower right in Figure 2. Constructing a mean from only five profiles does not produce a smooth mean (and one may not exist).

Figure 3 shows mean profiles constructed for the field year broken into six seasons. This unusual number was chosen because the spring was halved into the periods at the first and last of the experiment, and the warm months were divided into more sunny (April-June) and less sunny (July, August, and September) periods. The less sunny periods are examined separately because pibal releases into the rare and isolated clear periods produced data that are strongly biased synoptically.

In general, the mean profiles have the same shape. There is variation in surface values $\theta - \theta_g$ and U/G from season to season. This variation is expected since the total turning and total shear should respond to seasonally varying stability and surface heat flux. There is also variation in the profile behavior just below $Z/Z_i = 1$. In the warmer seasons there is a slight tendency for U/G to go to 1 at a somewhat lower height and steeper slope than for the cooler seasons. In general, in the warmer seasons $\theta - \theta_g$ tends to zero somewhat higher than U/G tends toward 1. This behavior would be in agreement with strengthened secondary flow during the less stable warmer periods.

Figure 4 contains the same data as Figure 3, but they are plotted differently. Here for each season the winds are divided into two components for each height interval and nondimensionalized by the geostrophic wind. One component, u/G, is directed in the direction of the geostrophic wind and the other component, v/G, is normal to the geostrophic flow direction (the ageostrophic, or lateral, flow). Once again the profiles from the various seasons look basically alike. The variation in surface U/G seen in Figure 3 is repeated in Figure 4 and is shown to be more attributable to changes in u/G than in v/G. Also, the seasonal differences in the relative behavior of

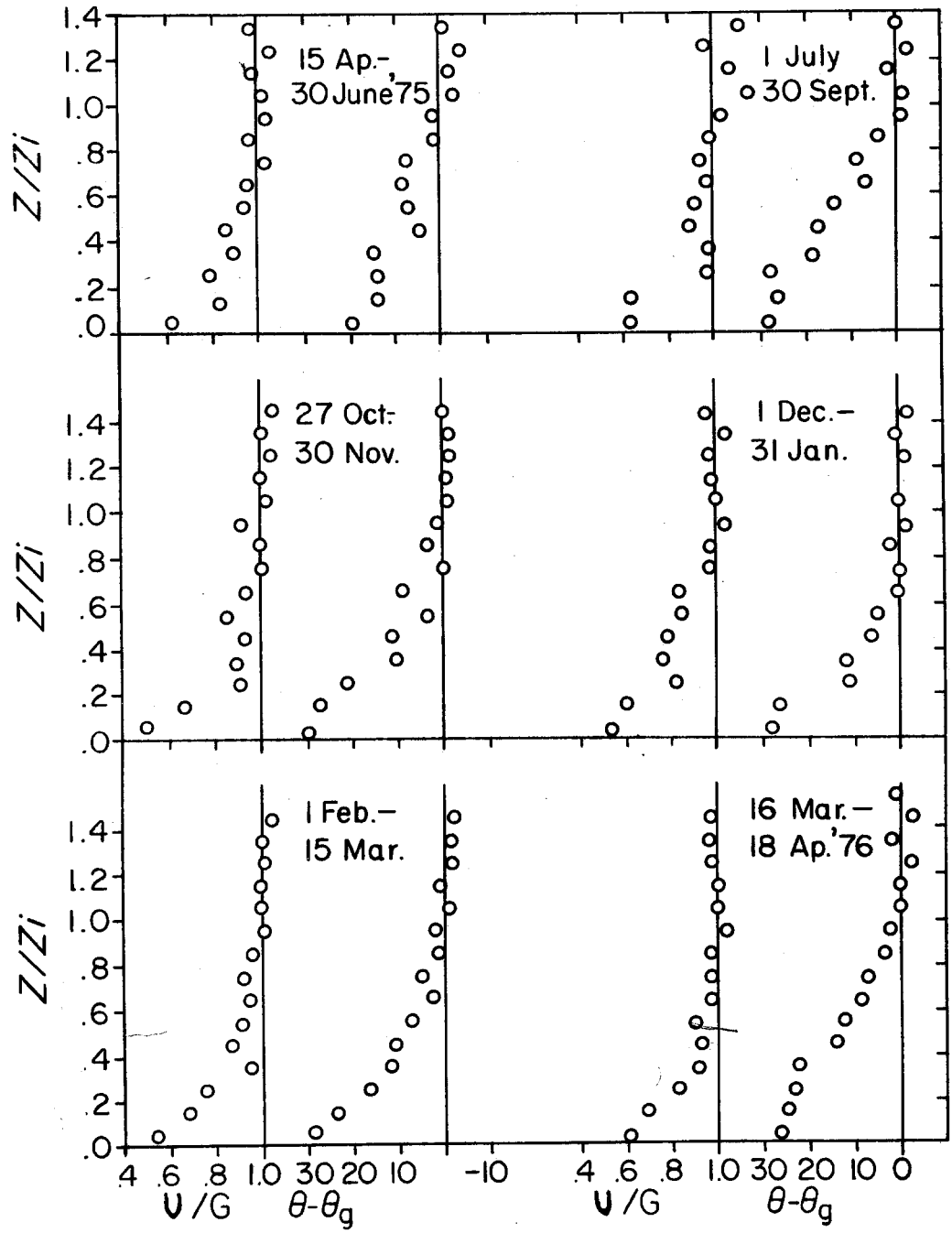

Fig. 3. Pibal profiles of seasonal mean wind speed and direction over Beaufort Sea pack ice. The PBL thickness Z_i is the inversion height measured by acoustic radar; the measured geostrophic wind is taken from the pibal interval just above that containing Z_i, and $\theta = 0$ is oriented along $\vec{G}$.

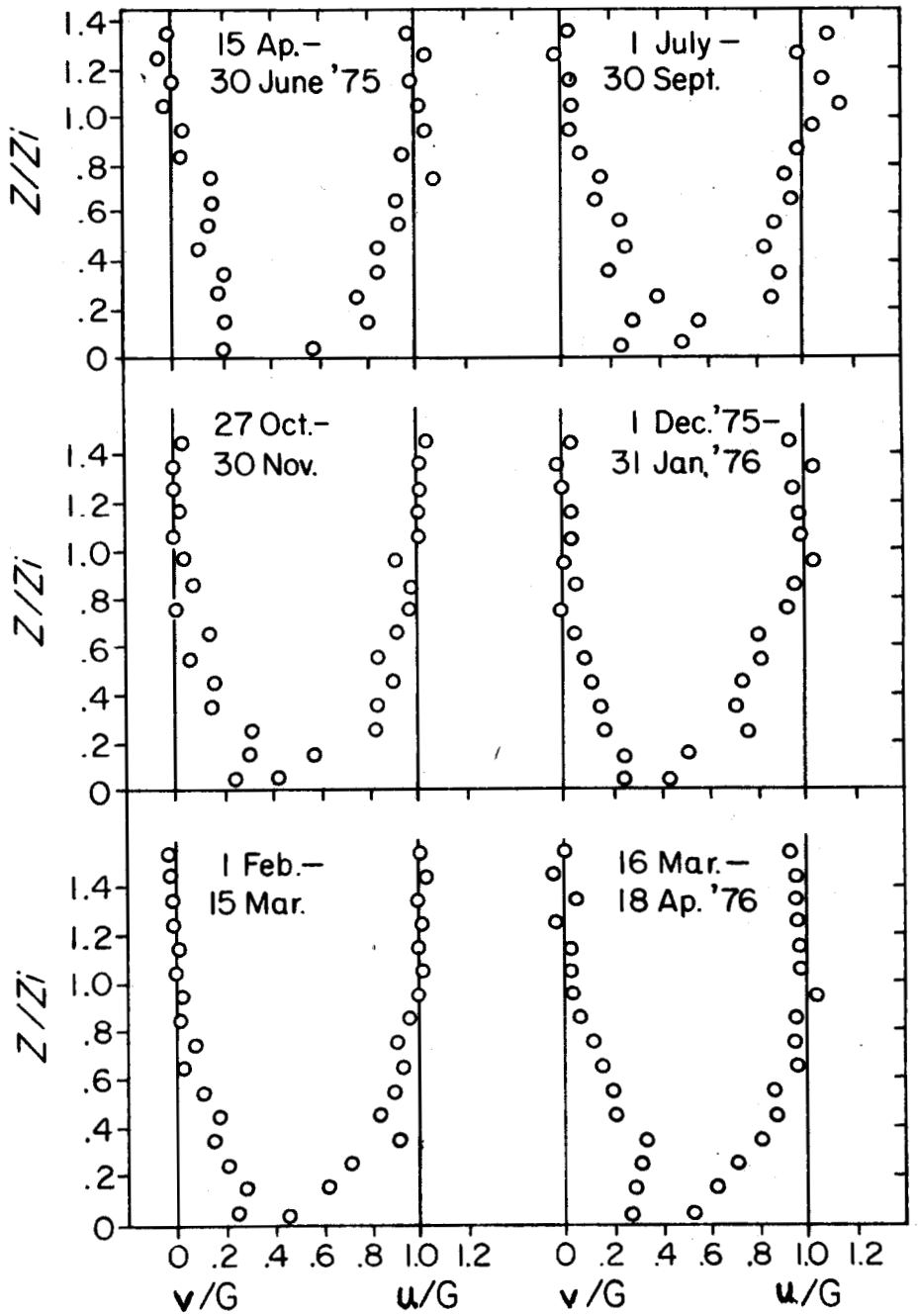

Fig. 4. Pibal-derived seasonal mean profiles of ageostrophic and along-geostrophic winds over pack ice in the Beaufort Sea. Z_i and G are obtained using acoustic radar data.

$\theta_g - \theta$ and U/G as $Z/Z_i \to 1$ are seen in this figure to be due to the behavior of v/G as $Z/Z_i \to 1$. The v/G plot for 1 February through 15 March 1976 seems to be lumpier than the u/G plot. Inflection points in the lateral flow have been predicted by Brown [1974c, p. 98]. Vertical variations in the lateral flow required to produce such inflection would necessarily result in a lumpy profile which would by smoothed only by averaging profiles with Z_i errors (which could be had by using a daily or seasonal average Z_i).

Figure 5 shows a sample of acoustic radar data for 5-7 February 1976 (AIDJEX days 401-403, where 1 January 1975 is day 1 and 1 January 1976 is day 366). The overall behavior of the top of the highest echo is as expected; substantial features changing very rapidly compared with 24 hours are not found and a ground-based echo is common. The measured geostrophic wind speed is 6 m sec^{-1} at 0000Z on 5 February and increases to 20 m sec^{-1} at 0000Z on 7 February. For so great a wind speed, appreciable subsidence is unlikely, so that the only source of an inversion is PBL dynamics and surface cooling.

With this in mind, it is surprising to find as many as four echo levels at one time. The mechanism creating and maintaining these inversions in the presence of large stress is unclear. During the times that identifiable layers are splitting and therefore increasing in number, winds are generally increasing in intensity. This leads to the conclusion that PBL growth brought on by increasing wind brings about instabilities in the flow. The flow breaks into several vertical regimes, each characterized by a flow of large scale compared with the inertial subrange. The regularity of spacing from layer to layer suggests a roll regime of similar dimension. It is interesting that although the lowest or second echo sometimes climbs above about 225 m, an echo is usually reestablished near that height. Wind measurements with high resolution taken during periods of multiple echoes would be instructive in describing the dynamics of the high-energy planetary boundary layer.

The influence of baroclinicity on PBL dynamics is not understood. In terms of momentum integration measurements of a stress via the Ekman equation, the presence of baroclinicity introduces an error which can be considered due to an error in G. Figure 6 shows the data for 7 February 1975 plotted so that wind profiles above the PBL can be examined. Clearly, there is a strong,

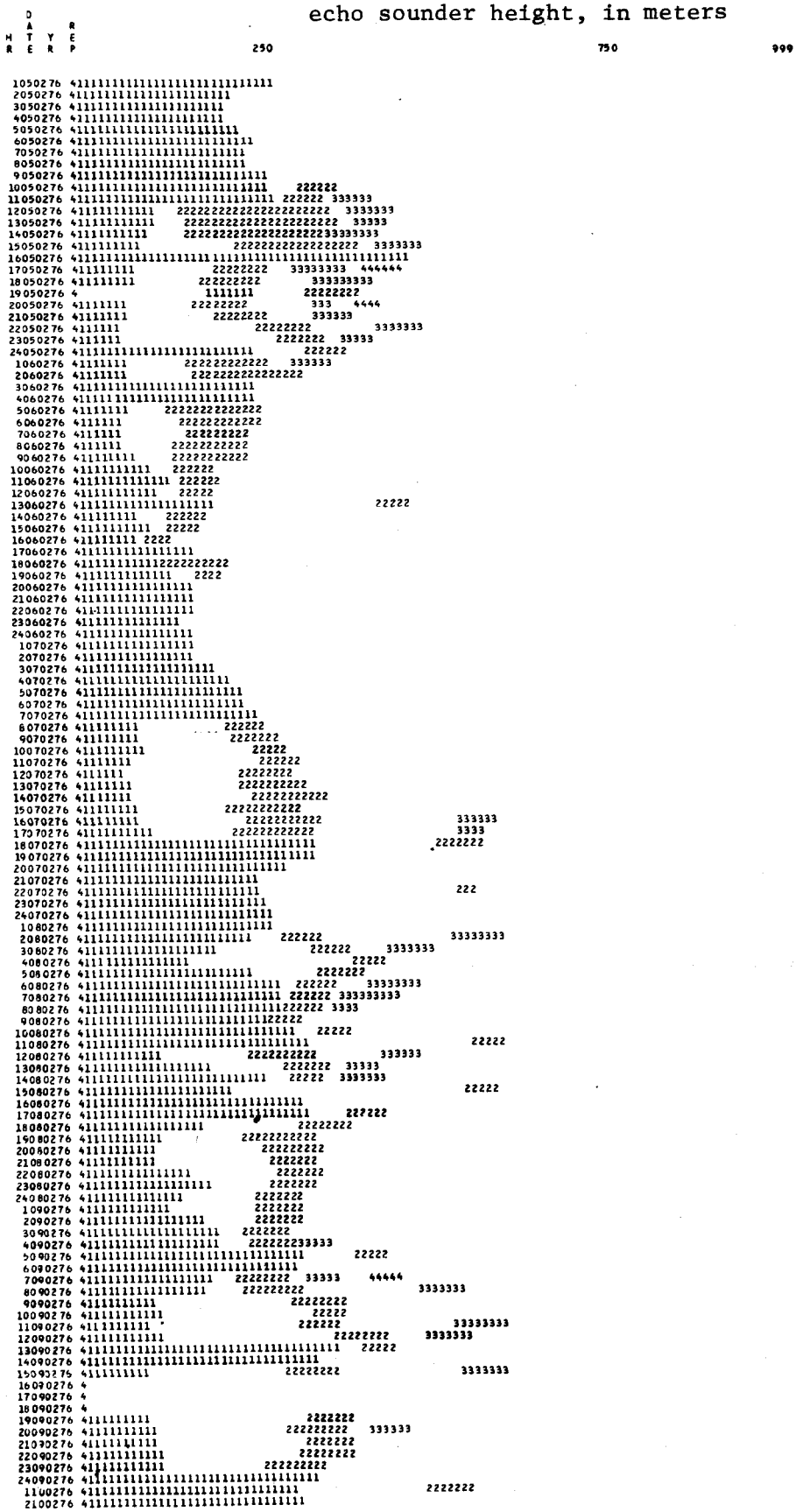

Fig. 5. Replica of acoustic radar record. The trace bottom shows hour, day, month, year, and pulse repetition rate in seconds. The echo replica is constructed with one line for each hour and one numeral for each 10 m of echo. The echo image is composed of the echo number, where echo number 1 is the lowest.

essentially linear variation with height (approximately 16 m sec^{-1} km^{-1}) which is considered due to constant baroclinicity, a linear horizontal temperature gradient throughout the troposphere. There has been no indication in the AIDJEX data that surface temperature gradients taken from point measurements on a 100 km scale reproduce the gradients required for measured winds. In general, the surface temperature gradients are far too large. If $G > 5$ m sec^{-1} and there is no average contribution to the seasonal means, an individual profile would rarely look like the averaged profile in Figure 6.

Boundary layer baroclinicity independent of upper air gradients have an impact on the stress calculations discussed below. However, thermal effects have little influence on the actual PBL flow; this is because the effect is zero at the surface and increases linearly through a thin PBL. An error in G of 1 m sec^{-1} in a PBL of 250 m height--an error comparable to experimental error--would require a thermal wind shear above the PBL top in excess of 4 m sec^{-1} km^{-1}, which is large compared with noise in the seasonal mean profiles. The impact of thermally induced turning on PBL stability [Brown, 1976] is not addressed in this report.

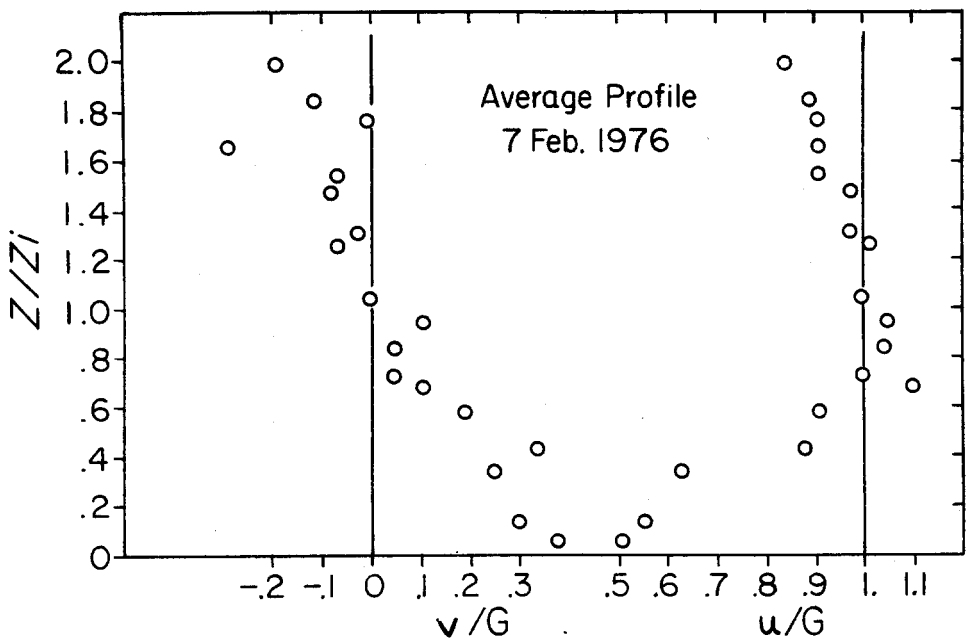

Fig. 6. Profile averaged from 5 pibal releases on 7 February 1976 over the Beaufort Sea pack ice. Height is divided into 0.1 Z_i intervals for averaging; a few points have only one value to average. Extremely strong baroclinicity, about 16 m sec^{-1} km^{-1}, is visible above $z/Z_i = 1$.

RESULTS OF COMPUTATION

The stress calculation implied in Equation (4) is performed on each pibal profile as sums in which the east-west and north-south stress components are evaluated respectively as

$$\tau^x = \rho f \int (V(z) - V_g)\, dz = \rho f \sum_{i=1}^{N} (V_i - V_g) \cdot (Z_i - Z_{i-1})$$

and (7)

$$\tau^y = -\rho f \int (U(z) - U_g)\, dz = -\rho f \sum_{i=1}^{N} (U_i - U_g) \cdot (Z_i - Z_{i-1})$$

where V_i is the north-south wind in the i-th observation (height) interval, U_i is the east-west wind in that interval, V and U are components of wind in the observational interval above the interval containing the inversion height, and Z_i and Z_{i-1} are the heights defining the height interval. The Z_i are the actual heights for which pibal coordinates are recorded in the field. Appendix A shows the results for each pibal profile.

There are two resulting quantities for each pibal profile. These can be taken to be geographical stress components as above, or they can be taken as a measured stress magnitude

$$\tau_m = [(\tau^x)^2 + (\tau^y)^2]^{\frac{1}{2}}$$

and direction. For this discussion the reference direction chosen is the direction of the surface wind; positive angles γ will be taken counterclockwise to the surface wind. Figure 7 shows the stress magnitude in the form u_*/G where

$$\frac{u_*}{G} = \sqrt{\frac{\tau_m}{\rho}}$$

plotted against the appropriate dimensionless measured variable aggregate from Equation (6): $(f Z_i \sin \alpha/G)^{\frac{1}{2}}$. The result for all pibals of late winter 1976 shows some tendency to cluster around the line of slope 0.71.

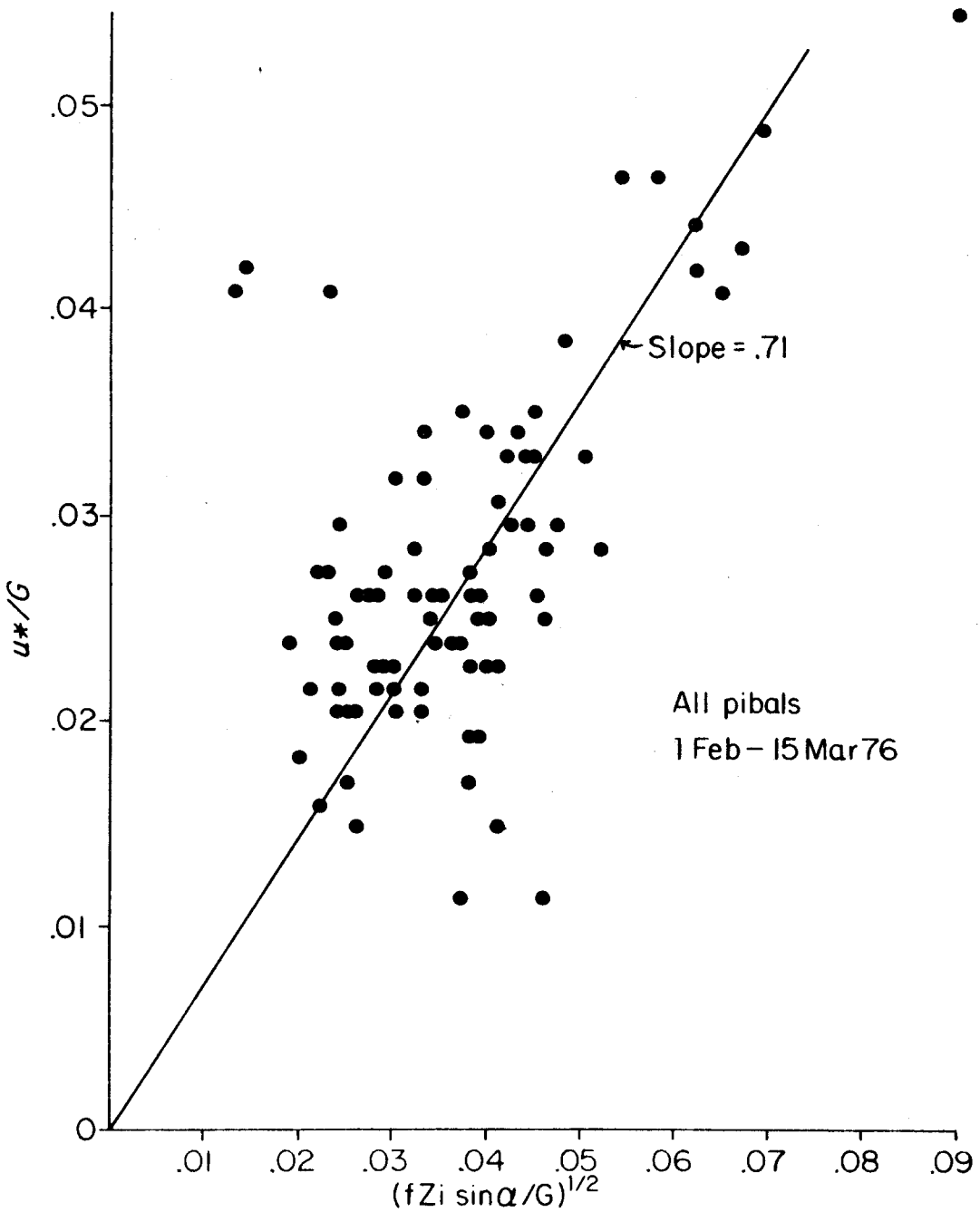

Fig. 7. Measured drag coefficient plotted against model for all data taken in early spring 1976. The solid line does not represent a best fit, but is shown for reference.

Statistics of the stress directions for each season are shown in Figure 8. Here the actual number of pibals with angle γ within limits shown is plotted against γ. High wind data with $G > 5$ m sec^{-1} are shown shaded, and all data for which $0 < \alpha < 75$ are shown unshaded. In every interval except that for 15 March - 18 April 1976 the most probable γ is between 10° and 30°. In every period the distribution is skewed toward $\gamma > 0$. The statistics for the entire year are shown in the lower left corner of the figure. The distribution has a mean $\gamma = 19° \pm 2°$ and is not significantly skewed except for large negative values of γ. The standard deviation is 20°.

The combined acoustic radar/pibal study of boundary layer winds is unique in this result. Previous workers have not had the advantage of a known PBL thickness, and have lost the independent measure of along-geostrophic and ageostrophic wind stress components. Earlier work in this area includes that of Lettau [1950], Sheppard et al. [1952], Johnson [1965], and, of course Rossby and Montgomery [1935]. Brown [1974b] in an analysis of AIDJEX 1972 data uses the momentum equation method, but constrains the stress direction to provide closure.

An examination of stress profiles is in order. Figure 9 shows profiles of u_*/G with height. All are remarkably linear except for an upward departure near the PBL top. This behavior is essentially that modeled by Wyngaard [1975], but it is not particularly informative; there is no indication of a problem in the vertical. Figure 10, showing each component of stress in profile for each season, is somewhat more illustrative. In each season the basic form of $\tau^x(z/Z_i)$ and $\tau^y(z/Z_i)$ is the same. Both are tangent to $\tau = 0$ at $z/Z_i = 1$, and both flatten out to surface values at $z/Z_i \to 0$. In each case the y component has a smaller slope as $z/Z_i \to 0$. In all seasons except early spring 1976 and summer 1975, $\tau^y(0) > \tau^x(0)$ in violation of the alignment of surface wind and surface stress for α values less than 45°, which is the case in these results. However, where $\tau^x(0) > \tau^y(0)$--as it should be--the form of the profile is the same as that for cases $\tau^y(0) > \tau^x(0)$. The violation of alignment is not due to error in integration due to "bad" points in the averages. It is unlikely that the lack of alignment is due to general failure of the method of scaling and averaging since the curves are quite similar. The error is clearly a smoothly varying contribution to the profiles which goes to zero at $z/Z_i = 1$.

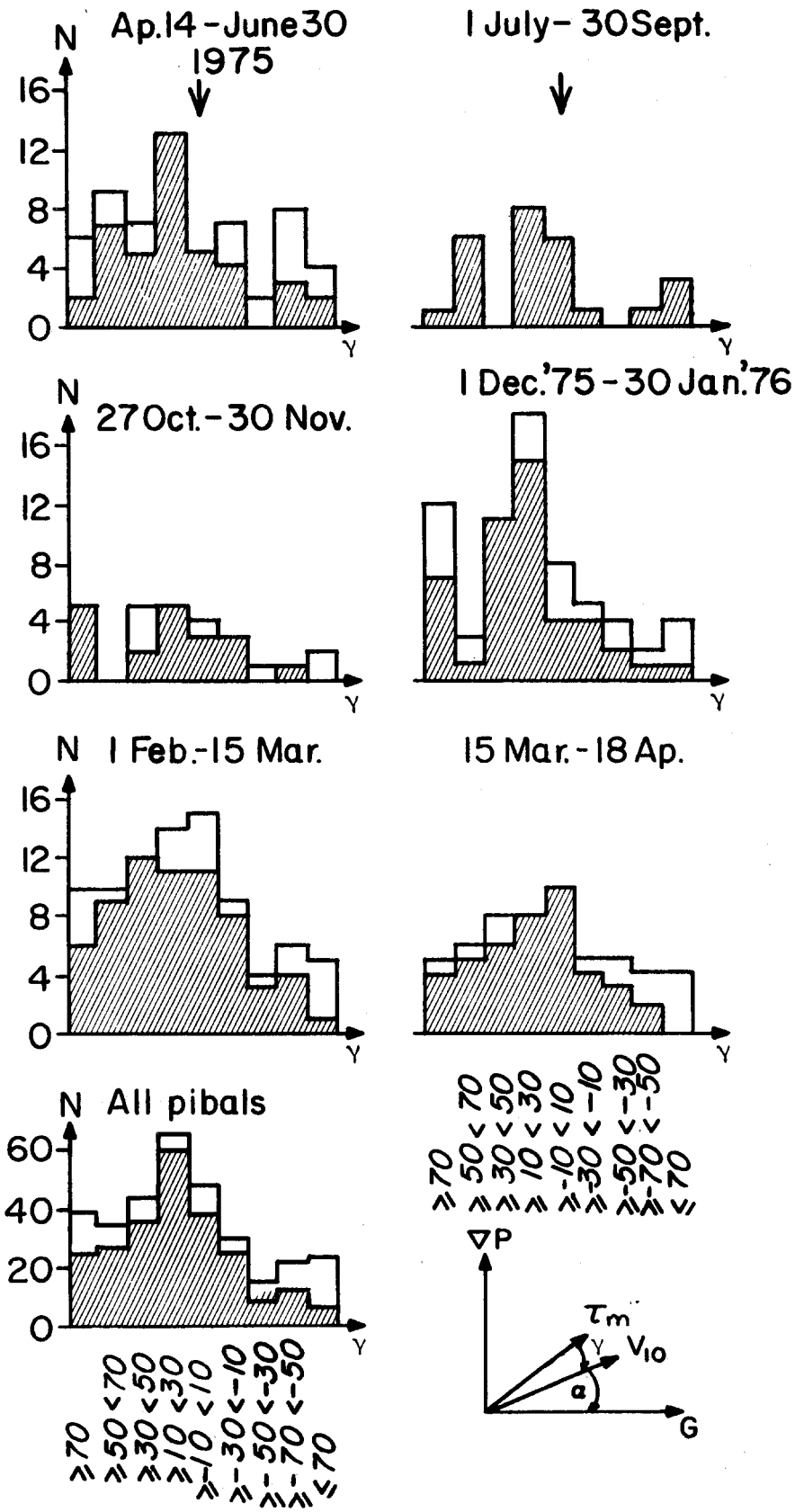

Fig. 8. Histograms of seasonal values of γ, the directional error between measured stress and surface wind.

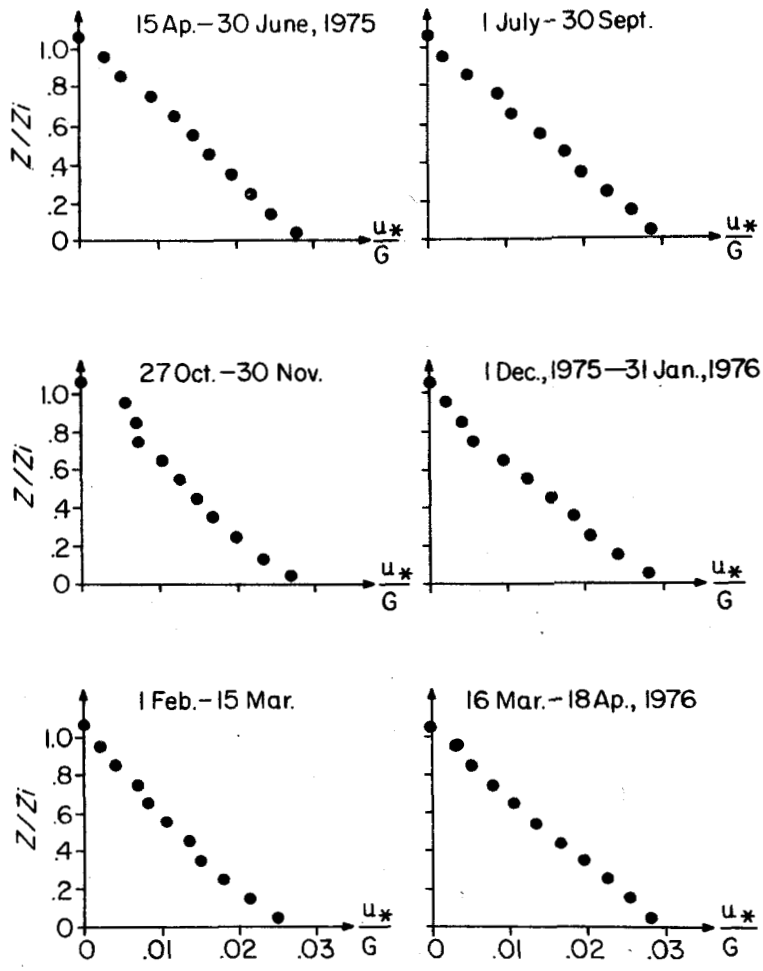

Fig. 9. Seasonal profiles of stress velocity. For this plot we are using

$$u_* = \sqrt{\tau(z)/\rho}.$$

The failure of $\tau^x(0) > \tau^y(0)$ is greatest in winter and fall and least in summer. This points to a thermal explanation, although several candidate effects are available to explain why the surface stress vector $\vec{\tau}_0$ is oriented some 20° to the left of the surface wind $\vec{u}_{10}$:

1) There is turning continuing below 10 m; the actual surface wind and stress are more nearly aligned.

2) Baroclinic behavior persists, yielding wrong stress values and geostrophic winds when the integration is performed.

3) A constant stress is impressed upon the entire PBL and hence does not appear in the force balance, but does appear at the surface as momentum flux.

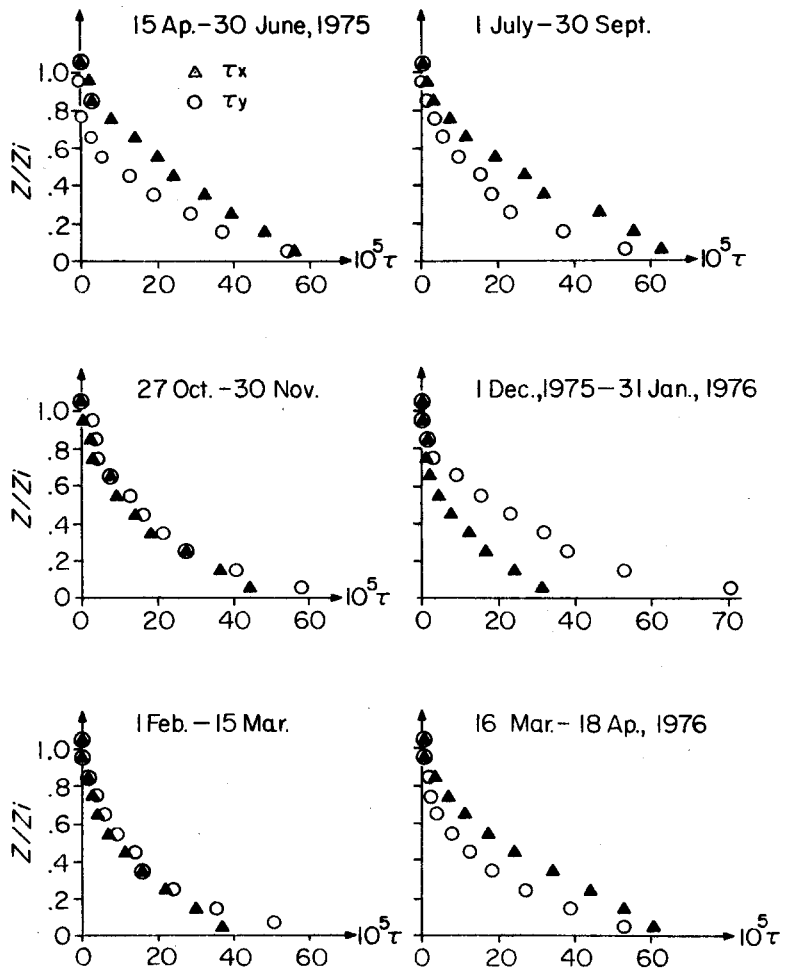

Fig. 10. Seasonal stress profiles from seasonal average wind profiles. The x coordinate is aligned with the geostrophic wind.

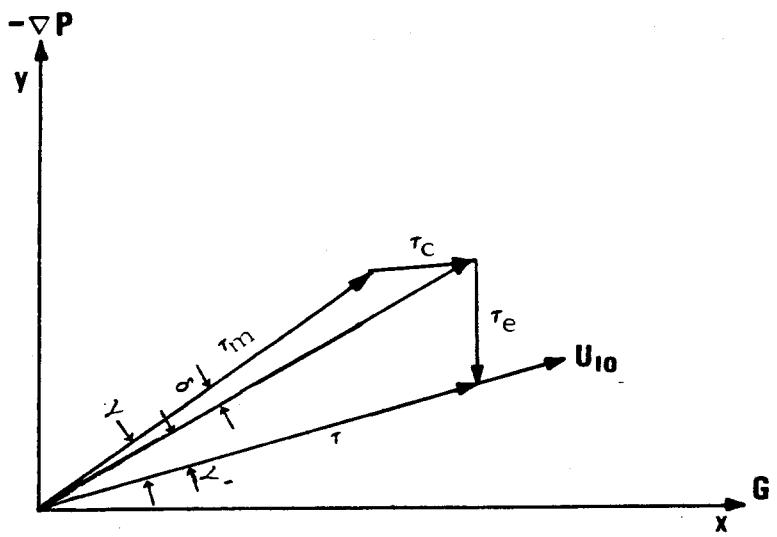

Fig. 11. Vectors of interest in the correction of the measured stress.

None of the above can be discounted. The turning profiles do not vitiate the possibility of turning at all levels. Near the surface

$$\frac{d\theta}{d(z/Z_i)} = 32 \pm 13°$$

so that we can expect the turning to 10 m to be at most $\theta_{10} = 1.5 \pm 1°$. We choose $\theta_{10} \simeq 1$ to account for reduced turning in the surface layer.

The prospect of a stress constant throughout the PBL was included by Sheppard et al. [1952] during a discussion of baroclinic wind profiles. AIDJEX data (unpublished) taken from NCAR Electra flights permit the estimate

$$u_*(z \simeq 2Z_i) \leq (0.25 \pm 0.1)\ u_*(z \simeq 0.16Z_i)$$

and the constant stress τ_c should be aligned with the geostrophic flow. Figure 11 shows the vectors of interest in this discussion. The effect of τ_c on τ is

$$\tau_c \simeq 0.06\ \tau_0$$

and

$$\sin \delta = \frac{\tau_c}{\tau_0} \sin (\gamma + \alpha)$$

or

$$\delta \simeq 2°$$

The net remaining angle γ' between surface wind and stress is

$$\gamma' = \gamma - \delta - \theta_{10} \simeq 16°$$

For this turning to be due to baroclinicity it is necessary to modify the basic equations. The coordinate system used is essentially a synoptic one where $+x$ always points along the geostrophic wind direction.

With horizontal homogeneity and steady state, equation (5) is

$$\tau^y = -\rho f \int_0^\infty [U(z) - U_g(z)]\, dz \qquad (8)$$

where ρ is the air density, f the Coriolis parameter, $U(z)$ the component of wind along x, and $U_g = \frac{-1}{\rho f}\nabla P$ is the height dependent geostrophic wind speed

along x. Requiring τ^y to become zero at Z_i and postulating $U_g(z)$ = constant, this was rewritten

$$\tau^y = -\rho f \int_0^{Z_i} [U(z) - U_g]\, dz \tag{9}$$

Equation (8) could be written for $U_g(z)$ linear in z as

$$\tau^y = -\rho f \int_0^{Z_i} \left[U(z) - U_g(Z_i) - \frac{dU(z)}{dz}\, z\right] dz \tag{10}$$

where $\frac{dU(z)}{dz}$ is taken here to be a constant. For this relationship, we get

$$\tau^y = \tau_m^y - \frac{\rho f}{2} \frac{dU(z)}{dz}\, Z_i^2 \tag{11}$$

From Figure 11 the y component stress error τ_e to correct τ is

$$\tau_e^y = \tau \sin \gamma / \cos\,(\gamma + \alpha) \tag{12}$$

It is useful to estimate for τ from above:

$$\tau \simeq \frac{1}{2} \rho f\, Z_i\, G \sin \alpha \tag{13}$$

and combine to get

$$\frac{dU(z)}{dz} = \frac{G}{Z_i} \sin \alpha \sin \gamma / \cos\,(\gamma + \alpha)$$

$$\simeq 0.16 \frac{G}{Z_i} \quad \text{for } \alpha = 28°,\ \gamma = 16° \tag{14}$$

and

$$\frac{dV}{dz} = 0$$

Plugging in mean values for 1 February - 15 March 1976, G = 11.2 m sec^{-1}, Z_i = 230 m, the gradient is

$$\frac{dU(z)}{dz} \simeq 0.008 \text{ sec}^{-1}$$

and the error component at the PBL top is

$$\Delta u \simeq 1.8 \text{ m sec}^{-1}$$

This is a large error. In reduced wind with $u' = U(z)/G$ and reduced height $z/Z_i = S$, we get

$$\frac{du'}{dS} = 0.18$$

This slope would be readily discernible in the mean wind profile above $z/Z_i = 1$ in Figure 4 if it were there. It is not. The alternative to tropospheric baroclinicity is a boundary layer baroclinicity. This horizontal temperature could be due to several effects: the entrainment of warmer air in higher pressure regions; the suppression of the inversion and subsequent onset of sloping isotherms at higher pressure regions; and the synoptic variation in surface heat flux. The first two terms produce a temperature gradient parallel to and symmetric with the pressure gradient. The last term reflects the difference in heat flux due to the sign of the ice convergence, which is positive in high pressure areas. Hence this term is antiparallel to the other two and the pressure gradient. Also, thermal gradients produced by solar insolation variations would be generally parallel to the pressure gradient.

If the entire baroclinicity were due to the inversion height suppression, the magnitude could be modeled by assuming

$$\frac{dT}{dx} = \frac{dT}{dz}\frac{dz}{dx} \tag{15}$$

and

$$\frac{dz}{dx} = \frac{dZ_i}{dx}$$

The resulting gradient would then be given by

$$\frac{dT}{dx} \simeq 2\text{K per 100 km}$$

for dT/dz of +10K per 200 m [Belmont, 1958] and dZ_i/dx of 200 m per 500 km. The wind shear required,

$$\frac{dU(z)}{dz} \simeq 0.008\ \text{sec}^{-1},$$

implies a temperature gradient of

$$\frac{dT}{dx} \simeq 3\text{K per 100 km},$$

which leaves a small temperature gradient due to subsidence plus entrainment.

Some of the estimates above can be checked with data. Figure 12 shows plots of pibal drag coefficient results for $-10° \leqslant \gamma \leqslant 10°$. These are the profiles which show no net baroclinicity in the stress direction. A least squares slope of 0.71 ± 0.08 is obtained when the results from camps Caribou and Big Bear are combined with proper weighting. Data from Big Bear, 15 April-30 September 1975, have only 13 pibals with $0 < \alpha < 75$ and $-10 < \gamma < 10$. For these profiles a slope of 0.76 ± 0.24 is obtained. At Caribou, 27 October 1975-18 April 1976, the 30 pibals that were suitable for calculation provide a slope of 0.68 ± 0.08. The larger summer value is in agreement with the trend to less stable air indicated by S. P. S. Arya (personal communication). In all the above, a least squares fitting of u_*/G versus $(fZ_i \sin \alpha/G)$ was performed in which the line was forced to contain the origin. In the lower part of Figure 12 the drag coefficient is plotted against the turning angle to compare with the behavior predicted by Brown [1974a]. The large scatter in the pibal profile integration renders this comparison unpromising, if inconclusive. A difficulty of this analysis is that contributions to stress due to random variation in the balloon path tend to enlarge the stress for the points with larger α and therefore to bias the mean.

If the distribution of computed stress directions is due to a boundary layer baroclinicity with symmetry similar to the pressure gradient, this should show up in the computed drag coefficient. This postulate supposes that the measured wind G_m is larger than true (surface) G by

$$G = 0.84\ G_m$$

for those pibals with $\gamma = 16°$ and

$$G = 0.37\ G_m$$

for those pibals with $\bar{\gamma} = 36°$. When the ordinate and abscissa values for each point are corrected for these changes, the resulting "best fit" calculation should produce larger slopes for larger $\bar{\gamma}$ values. In this case the geometry suggests

$$B_{16} = 1.10\ B_0$$

$$B_{36} \quad 1.42\ B_0$$

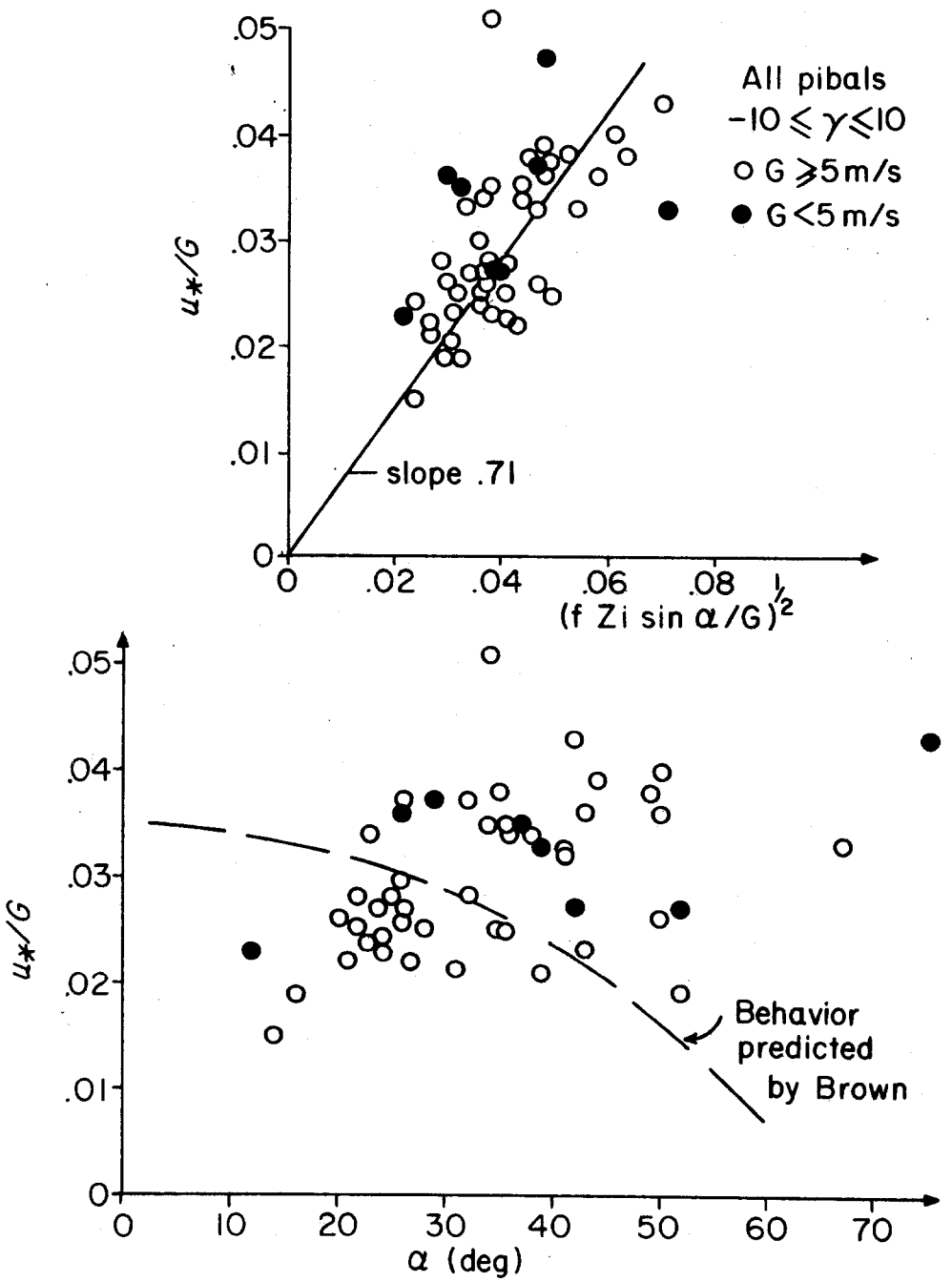

Fig. 12. Variation of the drag coefficient for pibal profiles that have direction within 10° of the 10 m wind direction. The solid line in the upper plot is a best fit.

and the best fit analysis yields

$$B_{16} = (1.08 \pm 0.09)\ B_0$$

$$B_{36} = (1.30 \pm 0.18)\ B_0$$

Clearly, the small numbers of usable profiles in each category--at Caribou 30 for $\overline{\gamma} = 0$, 37 for $\overline{\gamma} = 16$, and 34 for $\overline{\gamma} = 36$--reduce the strength of the conclusion. One can only say that the data do not contradict the statement that the correct slope is 0.71 and that the baroclinicity is directed parallel to the pressure gradient. The main conclusion of this section and of this report is that, according to pibal acoustic radar analysis,

$$\frac{u_*}{G} = (0.71 \pm 0.08)\ (fZ_i \sin \alpha/G)^{\frac{1}{2}} \qquad (16)$$

RESULTS, SEASONAL STRESS VARIATION

The seasonal averages for the parameters discussed above are shown in Table 1, with averages constructed from 10 m tower measurements of wind speed, acoustic radar heights, and pibal observations. Excluded from the pibal profiles used are those with wind speeds less than 5 m sec^{-1} at the radar-located PBL top and those with a turning angle α which fails the test $0 < \alpha < 75$. The profiles made during periods of low wind appear erratic, suggesting that subsidence and wave activity dominate the synoptic driving; profiles that display turning indicative of transient behavior tend to give stress values greatly divergent from the mean, and the AIDJEX data set is not large enough to average out these values. Fewer than 10% of all pibals are rejected for α out of range.

The first column in Table 1 is the mean of u_*/G values obtained from the along-geostrophic stress component by integrating the average profile. From the preceding discussion, an error of 10% in that column seems reasonable. The second column has the drag coefficient from (16) using seasonal mean values of variables. The standard deviation of α is 50%, the standard error of the mean of α is 10%. This small error of the mean indicates that the seasonal α variation is significant. The essentially constant values of the entries in the second column are at odds with the variations in the first, implying that the factor 0.71 in

$$u_*/G = (0.71 \pm 0.08)\ (fZ_i \sin \alpha/G)^{\frac{1}{2}}$$

TABLE 1

SEASONAL PARAMETER VALUES, PIBAL OBSERVATIONS

Date	u_*/G Average	u_*/G Best Fit	α Average	U_{10}/G Average	G Average	Z_i Average	Pibals: Usable vs. Total
15 Apr-30 Jun 1975	0.024	0.026	19.2	0.62	9.1	264	42/95
1 Jul-30 Sep 1975	0.027	0.027	28.6	0.62	9.2	204	26/49
27 Oct-30 Nov 1957	0.023	0.028	31.4	0.50	10.6	228	18/28
1 Dec 1975-31 Jan 1976	0.019	0.027	28.3	0.52	10.0	222	47/77
1 Feb-15 Mar 1976	0.020	0.026	28.5	0.54	11.2	229	66/99
16 Mar-18 Apr	0.026	0.026	26.5	0.61	9.2	204	41/66

has seasonal variation hidden in its standard deviation or that the processes are not linear so that (16) cannot be evaluated using average values.

Examining the seasonal variation of the parameters holds few surprises. The summer months must be treated with care. The clear days from July (and probably late June) through September are few but not particularly characterized by the low winds associated with subsidence. The data set is small and probably synoptically biased. In summer the surface shows bare ice, shallow melt ponds light in color, and darker, deeper ponds and leads. When the sky is clear, the surface cools because the ice and shallow water reflect solar radiation and radiate long-wave radiation. The darker water bodies fail to warm the surface because the water that absorbs the solar radiation warms toward the density maximum and sinks, exposing cooler water to the air, and the evaporation of water from the surface has a cooling effect. Hence, a clear sky period creates surface cooling and produces an extremely stable lower PBL and surface layer. This is reflected in the high value of α and low value of U_{10}/G. On the other hand, the humid PBL itself absorbs some solar energy and, possibly, warms slightly compared with the rest of the lower troposphere, tending to increase u_*/G. Mean Z_i may reflect the subsidence responsible for the clear sky, but the high wind values leave this uncertain.

The least stability and therefore the largest u_*/G, Z_i, and U_{10}/G and smallest α values occur in late spring and early summer. The stablest air is found in fall, winter, and early spring and is marked by smaller values of U_{10}/G and Z_i and larger α. The fall is a period of local contraction for the ice sheet. The contraction exposes comparatively more open water and hence larger fluxes of heat and water vapor, possibly resulting in an increase in Z_i. Seasonal variation in Z_i and G are difficult to assess because synoptic variation of each is far larger. Therefore, the quality of the mean is dependent on a large data set which does not exist.

According to Brown [1974c, p. 66], the variation in u_*/G with α is comparable to typical errors in u_*/G for α variation of some 20°, but u_*/G generally decreases as α increases. This trend is just visible in these data, although it is smaller than typical errors. To examine the relationship between u_*/G and α (the general influence of stability on u_*/G), much larger spatial or temporal data density is required. An examination of the next best thing, the variation of the above parameters with time, will be discussed in a later report.

CONCLUSIONS, MEASURING AND MODELING STRESS

In the preceding sections data have been shown which demonstrate that pibal wind profiles can be integrated to produce a reasonable measure of air stress. This stress has exhibited a variation which suggests the importance of synoptic modeling of stress. The modeling of the wind profiles is not yet possible, and so the effort is turned to modeling the fourth root of the sum of the squares of the integrals in the form

$$u_*/G = (0.71 \pm 0.08)\ [fZ_i \sin(\alpha)/G]^{\frac{1}{2}} \qquad (17)$$

where the stress velocity is $u_* = \sqrt{\tau/\rho}$ for surface stress τ and density ρ; f is the Coriolis parameter; Z_i is the inversion height measured by acoustic radar; α is the total turning of the wind; and G is the measured geostrophic wind. In order to derive utility from this relationship, all the variables must be expressed in terms of synoptic data. For frozen seas the input data are restricted to pressure maps and surface temperature maps. Therefore, even if the relation for u_*/G is valid, the job is not really done.

A seasonal variation in drag coefficient and angle of turning is indicated in the pibal analysis. Early summer has a significantly smaller turning angle than other seasons, while winter has a somewhat smaller drag coefficient.

We have also seen (although it is not related to modeling stress from surface geostrophic wind) the indication of a strong boundary layer baroclinicity. On the average, this baroclinicity is probably parallel with the pressure gradient and has a value of about 3K per 100 km. It is substantially caused by suppression of the inversion surface in regions of high pressure. Geographical features such as ice roughness and land masses may play a role in maintaining the temperature gradient.

ACKNOWLEDGMENT

The authors thank the NOAA Wave Propagation Laboratory for lending them the acoustic radar used in this study. The AIDJEX analysis of the pibal data was supported by a grant from the NSF Office of Polar Programs to the AIDJEX modeling group. We also thank the meteorological observers who maintained the acoustic sounder and took part in the pibal observations under arduous conditions.

REFERENCES

Belmont, A. D. 1958. Lower tropospheric inversions at Ice Island T-3. *Polar Atmospheric Symposium, I, Meteorology*. Pergamon, London.

Blackadar, A. K., and H. Tennekes. 1968. Asymptotic similarity in neutral barotropic PBL. *Journal of Atmospheric Sciences, 25,* 1015-1022.

Brown, R. A. 1974a. Similarity constants in the stratified planetary boundary layer. *AIDJEX Bulletin, 26,* 173-203.

Brown, R. A. 1974b. A simple momentum integral. *Journal of Geophysical Research, 79,* 4076-4079.

Brown, R. A. 1974c. *Planetary Boundary Layer Modelling*. John Wiley and Sons, London.

Brown, R. A. 1976. On the velocity shear instability. *AIDJEX Bulletin, 31,* 75-85.

Brown, R. A., P. Maier, and T. Fox. 1974. Surface atmospheric pressure fields and derived geostrophic winds, AIDJEX 1972. *AIDJEX Bulletin, 26,* 173-203.

Carsey, F. D. 1976. The AIDJEX acoustic radar and some preliminary results. *AIDJEX Bulletin, 31,* 1-19.

Ekman, V. W. 1905. On the influence of the Earth's rotation on ocean currents. *Arkiv för Matematik, Astronomi och Fysik, 2,* 1-53.

Johnson, W. B. 1965. Atmospheric boundary-layer dynamics over the forests of northeastern Wisconsin. Ph.D. dissertation, University of Wisconsin.

Lettau, H. 1950. A reexamination of the Leipzig wind profile considering some relations between wind and turbulence in the frictional layer. *Tellus, 2,* 125-129.

Melgarejo, J. W., and J. W. Deardorff. 1974. Stability functions for the boundary-layer resistance laws based upon observed boundary layer heights. *Journal of Atmospheric Sciences, 31,* 1324-1333.

Rossby, C. G. 1932. Generalization of the theory of mixing length with application to ocean and atmospheric turbulence. *MIT Meteorology Paper 1,* Massachusetts Institute of Technology, Boston.

Rossby, C. G., and R. Montgomery. 1935. The layer of frictional influence in wind and ocean currents. *MIT Meteorology Paper 3,* Massachusetts Institute of Technology, Boston, 101 pp.

Sheppard, P. A., H. Charnock, and R. R. D. Francis. 1952. Observations of westerlies over the sea. *Quarterly Journal of the Royal Meteorological Society, 78,* 563-582.

Shir, C. C. 1972. A numerical computation of air flow over a sudden change of surface roughness. *Journal of Atmospheric Sciences, 29,* 304-310.

Taylor, G. 1915. The eddy motion in the atmosphere. *Philosophical Transactions of the Royal Society, A,* 215.

Taylor, P. A. 1970. A model of airflow changes in surface heat flux, temperature and roughness for neutral and unstable conditions. *Boundary Layer Meteorology, 1,* 18-39.

Wyngaard, J. C. 1975. Modelling the planetary boundary layer; extension of the stable case. *Boundary Layer Meteorology, 9,* 441-460.

APPENDIX A
PIBAL PROFILES

The following pages contain results from pibal profiles measured during the 1975-76 AIDJEX main experiment. Only data for ascents for which the turning angle is $0 < \alpha < 75$ are included.

For the main experiment AIDJEX adopted a convention of numbering days consecutively, beginning with day 1 = 1 January 1975 and ending with day 500 = 14 May 1976. A conversion table from AIDJEX days to calendar days can be found in Thorndike and Cheung, *AIDJEX Bulletin 35* (January 1977), p. 19. AIDJEX days 105.85-273.86 in the appendix are data from camp Big Bear; days 300.99-474.85 are from camp Caribou.

AIDJEX DAY	U_*/G MEAS.	U_*/G MOD.	α (°)	G (m sec^{-1})	G (°)	z_i (m)	C_{10}	U_{10} (m sec^{-1})	U_{10} (m)	$\frac{U_{10}}{G}$	γ (°)	$\frac{fz_i}{G}$
105.85	.018	.006	2	10.7	262	200	.00094	6.3	260	.59	104	.0026
106.19	.033	.037	29	14.7	235	600	.00993	4.8	206	.33	45	.0057
106.69	.030	.038	19	13.7	221	860	.00287	7.7	202	.56	63	.0088
107.08	.033	.018	7	13.7	235	550	.00364	7.4	228	.54	60	.0056
108.04	.046	.045	26	10.4	282	680	.02381	3.1	256	.30	43	.0091
108.77	.033	.033	41	9.4	239	225	.00708	3.7	198	.39	-2	.0033
109.80	.030	.023	20	11.4	245	250	.00354	5.8	225	.51	18	.0031
111.74	.069	.035	14	2.1	20	150	.00373	2.4	6	1.14	118	.0099
112.94	.026	.026	28	7.8	293	150	.00248	4.0	265	.51	24	.0027
113.73	.033	.017	16	6.7	282	100	.00364	3.6	266	.54	42	.0021
114.73	.041	.025	33	3.0	158	50	.00226	2.6	125	.86	-62	.0023
115.82	.052	.045	69	1.6	223	50	.00697	1.0	154	.62	-54	.0044
116.02	.031	.015	21	3.3	196	30	.00218	2.2	175	.67	53	.0013
116.84	.061	.040	26	2.5	326	130	.02376	1.0	300	.39	48	.0072
118.73	.028	.028	34	5.0	218	100	.00394	2.2	184	.44	19	.0028
119.10	.037	.028	15	4.7	231	210	.00436	2.6	216	.56	61	.0063
119.80	.027	.027	24	8.4	233	210	.00235	4.7	209	.56	27	.0035
120.04	.030	.026	26	14.2	231	300	.00319	7.6	205	.53	8	.0029
120.84	.022	.022	19	11.8	239	250	.00088	8.6	220	.73	-10	.0030
122.93	.037	.032	32	6.5	89	180	.00293	4.5	57	.69	4	.0039
123.06	.045	.031	42	6.6	97	130	.00397	4.7	55	.71	-21	.0028
123.79	.020	.018	28	8.5	85	80	.00139	4.5	58	.53	18	.0013
124.09	.019	.021	30	9.2	80	110	.00151	4.6	51	.50	27	.0017
124.82	.029	.028	23	8.3	95	250	.00180	5.6	73	.68	60	.0042
128.86	.054	.029	14	5.0	77	250	.01021	2.7	64	.54	100	.0070
129.10	.063	.068	34	3.0	148	350	.00738	2.2	114	.74	-13	.0164
129.24	.282	.092	25	1.3	204	360	.04110	1.8	179	1.39	-72	.0389
129.75	.058	.067	61	3.3	221	240	.01593	1.5	160	.46	-11	.0103
132.02	.007	.010	6	6.1	0	90	.00008	4.9	355	.80	-17	.0021

AIDJEX DAY	U_*/G MEAS.	U_*/G MOD.	α (°)	G (m sec^{-1})	G (°)	z_i (m)	C_{10}	U_{10} (m sec^{-1})	U_{10} (m)	$\frac{U_{10}}{G}$	γ (°)	$\frac{fz_i}{G}$
132.82	.029	.004	0	8.9	345	300	.00176	6.1	345	.68	67	.0047
134.02	.047	.026	15	8.6	328	325	.00705	4.8	312	.56	22	.0053
134.09	.023	.015	7	10.8	284	300	.00122	7.0	277	.65	54	.0039
134.22	.033	.023	19	8.3	322	200	.00306	4.9	303	.59	29	.0034
137.11	.024	.014	8	9.3	124	200	.00217	4.7	117	.51	64	.0030
139.22	.026	.020	12	10.6	40	300	.00246	5.6	28	.53	58	.0040
139.33	.084	.070	38	5.5	45	630	.01427	3.9	7	.70	-88	.0159
142.08	.033	.023	8	5.3	194	270	.00195	3.9	186	.74	29	.0071
143.17	.062	.055	42	2.8	249	180	.01777	1.3	207	.46	23	.0090
143.93	.056	.049	17	2.9	235	320	.00269	3.1	218	1.08	-24	.0157
144.07	.031	.031	18	5.2	282	240	.00217	3.5	265	.67	-61	.0064
145.09	.047	.050	26	2.5	213	210	.00298	2.2	187	.86	-43	.0115
145.93	.017	.013	8	5.7	103	110	.00043	4.6	95	.80	23	.0027
150.18	.029	.031	58	12.8	128	200	.00216	8.0	70	.63	-34	.0022
150.93	.034	.022	20	10.8	117	225	.00527	5.0	97	.46	47	.0029
151.05	.028	.024	30	9.5	113	150	.00280	5.0	83	.53	17	.0024
151.86	.025	.030	21	6.2	85	220	.00097	5.0	64	.81	-62	.0050
152.07	.037	.026	22	9.8	88	240	.00418	5.6	66	.57	35	.0034
155.85	.030	.025	26	10.0	68	200	.00258	6.0	42	.60	12	.0028
158.86	.024	.037	19	3.8	12	220	.00130	2.5	353	.66	78	.0082
162.80	.022	.023	11	3.0	35	120	.00044	3.1	24	1.03	-56	.0056
165.84	.020	.018	10	4.3	135	110	.00053	3.7	125	.86	-67	.0036
166.07	.061	.018	3	3.7	136	330	.00804	2.5	133	.68	97	.0126
168.04	.036	.027	20	8.3	92	260	.00292	5.6	72	.67	-82	.0044
169.82	.030	.006	2	17.2	350	300	.00472	7.5	348	.44	84	.0024
170.78	.026	.022	14	7.1	91	200	.00121	5.3	77	.75	28	.0039
171.03	.023	.023	24	5.8	75	100	.00344	2.2	51	.38	9	.0024
172.05	.200	.106	80	1.2	139	190	.02390	1.5	59	1.29	-61	.0225
178.79	.028	.035	30	7.7	241	280	.00196	4.8	211	.62	-21	.0051
179.02	.027	.026	24	6.7	183	150	.00213	4.0	159	.59	4	.0031

(Carsey and Leavitt)

AIDJEX DAY	U_*/G MEAS.	U_*/G MOD.	α (°)	G (m sec^{-1})	G (°)	z_i (m)	C_{10}	U_{10} (m sec^{-1})	U_{10} (m)	$\frac{U_{10}}{G}$	γ (°)	$\frac{fz_i}{G}$
179.78	.019	.027	21	7.9	285	230	.00078	5.5	264	.70	-56	.0041
181.10	.236	.040	7	1.4	161	240	.00374	5.4	154	3.86	-87	.0240
185.80	.084	.034	33	8.5	258	260	.00962	7.3	225	.85	*6.	.0043
186.97	.042	.038	35	11.5	297	400	.00223	10.1	262	.88	-74	.0049
193.78	.038	.038	35	5.1	123	130	.00312	3.5	88	.68	-3	.0049
194.06	.040	.043	50	5.2	131	130	.00508	2.9	82	.56	-4	.0049
197.26	.031	.026	30	10.2	324	200	.00292	5.8	294	.57	15	.0028
198.80	.027	.028	31	6.9	314	150	.00203	4.2	283	.61	-2	.0030
199.05	.029	.030	28	6.3	311	170	.00243	3.7	282	.59	18	.0038
200.81	.039	.034	44	8.9	349	210	.00469	5.0	305	.56	-4	.0033
200.84	.051	.027	34	8.6	341	150	.00767	5.0	307	.58	-5	.0026
200.89	.036	.034	43	10.0	350	240	.00523	4.9	306	.49	-10	.0034
200.93	.026	.032	37	10.7	341	260	.00354	4.8	305	.44	16	.0034
200.98	.032	.031	46	12.6	341	230	.00573	5.4	295	.43	20	.0025
213.93	.026	.022	19	9.6	321	200	.00229	5.2	302	.55	51	.0029
215.97	.033	.028	30	8.9	280	190	.00299	5.4	250	.61	14	.0030
216.78	.025	.017	21	16.1	224	180	.00631	5.0	203	.31	50	.0016
219.99	.031	.026	27	5.8	272	120	.00478	2.6	245	.45	52	.0029
228.09	.025	.029	35	5.7	188	120	.00277	2.8	153	.48	-7	.0029
229.78	.048	.035	38	4.9	43	145	.01007	2.3	5	.47	38	.0041
237.09	.038	.032	37	11.5	265	280	.00387	7.0	228	.61	-59	.0034
244.02	.032	.026	28	13.3	288	250	.00316	7.6	261	.57	25	.0027
248.80	.045	.033	22	6.0	19	250	.00459	4.0	357	.67	19	.0059
251.78	.016	.018	9	9.3	240	230	.00040	7.4	231	.80	88	.0042
258.81	.023	.018	22	9.5	99	110	.00274	4.2	77	.45	*0.	.0016
259.84	.026	.025	22	5.8	99	130	.00195	3.4	76	.58	68	.0031
268.75	.025	.016	12	11.2	332	220	.00162	7.0	320	.63	51	.0028
273.05	.023	.021	20	8.7	64	160	.00257	3.9	43	.45	28	.0026
273.86	.025	.016	16	12.8	80	160	.01256	2.9	64	.23	62	.0017

AIDJEX DAY	U_*/G MEAS.	U_*/G MOD.	α (°)	G (m sec^{-1})	G (°)	z_i (m)	C_{10}	U_{10} (m sec^{-1})	U_{10} (m)	$\frac{U_{10}}{G}$	γ (°)	$\frac{fz_i}{G}$
300.99	.024	.029	19	10.8	315	400	.00144	6.9	296	.64	83	.0052
303.87	.038	.018	13	19.4	4	400	.00540	10.0	351	.52	48	.0029
304.85	.046	.043	55	9.8	11	320	.00929	4.7	316	.48	-14	.0046
304.98	.031	.038	47	9.3	338	250	.00340	5.0	290	.54	-29	.0038
305.98	.038	.045	49	7.2	341	275	.00946	2.8	292	.39	-3	.0053
311.10	.021	.022	43	14.0	232	140	.00273	5.5	189	.39	11	.0014
313.86	.023	.016	12	3.7	235	60	.00085	3.0	223	.80	3	.0022
316.85	.036	.032	37	12.1	86	300	.00462	6.5	49	.54	15	.0035
319.91	.019	.016	14	11.2	339	180	.00102	6.7	325	.60	80	.0022
320.94	.024	.026	28	4.3	355	92	.00256	2.0	327	.47	33	.0030
321.15	.031	.024	40	4.7	25	60	.00722	1.7	345	.36	32	.0018
321.90	.034	.026	38	8.7	93	136	.00545	4.0	55	.46	-1	.0022
322.90	.029	.032	31	6.6	56	133	.00407	3.0	25	.46	75	.0039
323.16	.014	.023	34	6.0	50	80	.00075	3.0	16	.50	70	.0019
323.89	.019	.017	23	9.0	108	97	.00136	4.7	85	.52	28	.0015
327.04	.017	.028	32	8.1	152	130	.00092	4.5	120	.56	-27	.0031
328.91	.489	.142	68	.2	283	60	.00904	1.0	215	5.15	*4.	.0432
329.15	.022	.028	52	5.0	117	70	.00108	3.3	65	.66	-50	.0020
330.15	.020	.026	34	19.3	124	330	.00416	6.0	90	.31	25	.0024
330.92	.025	.036	33	12.5	143	420	.00400	5.0	110	.40	-59	.0047
331.16	.031	.023	26	14.5	166	250	.00564	6.0	140	.41	48	.0024
333.16	.028	.021	22	8.0	127	130	.00323	4.0	105	.50	0	.0023
333.93	.061	.049	36	3.5	116	200	.00349	3.6	80	1.04	*5.	.0081
334.16	.057	.036	31	3.7	129	133	.00500	3.0	98	.80	42	.0050
334.95	.029	.022	23	10.5	293	190	.00248	6.2	270	.59	18	.0025
335.15	.021	.009	10	11.8	290	80	.00107	7.4	280	.63	60	.0010
335.92	.028	.026	27	10.3	6	220	.00296	5.4	339	.52	29	.0030
336.15	.026	.033	50	8.9	50	180	.00217	5.0	0	.56	-6	.0028
338.16	.034	.038	22	2.4	252	130	.00076	3.0	230	1.24	102	.0075

(Carsey and Leavitt)

AIDJEX DAY	$U_*/\bar{G}$ MEAS.	U_*/G MOD.	α (°)	G (m sec^{-1})	G (°)	z_i (m)	C_{10}	U_{10} (m sec^{-1})	U_{10} (m)	$\frac{U_{10}}{G}$	γ (°)	$\frac{fz_i}{G}$
338.93	.033	.050	39	4.5	291	260	.00504	2.1	252	.46	4	.0080
339.17	.024	.038	38	3.1	281	105	.00065	2.9	243	.93	162	.0047
339.90	.037	.033	29	3.0	279	95	.00310	2.0	250	.67	8	.0044
340.17	.037	.038	32	2.6	292	95	.00143	2.5	260	.98	-49	.0052
341.16	.014	.021	29	5.4	270	71	.00037	3.8	241	.71	28	.0019
343.06	.024	.024	33	7.3	140	112	.00217	3.7	108	.51	33	.0021
343.89	.019	.021	35	5.3	245	56	.00122	2.9	210	.55	-33	.0015
344.15	.019	.021	49	9.9	259	83	.00113	5.7	210	.58	-12	.0012
344.91	.015	.025	25	9.7	292	200	.00054	6.2	267	.64	*8.	.0029
345.15	.023	.024	25	9.4	314	180	.00141	5.8	289	.61	40	.0027
345.94	.041	.035	39	7.7	354	210	.00407	5.0	315	.65	21	.0038
346.15	.035	.023	37	4.1	1	50	.00427	2.2	324	.54	9	.0017
347.16	.041	.012	4	6.8	24	225	.01055	2.7	20	.40	86	.0046
352.05	.039	.035	12	6.5	357	520	.00279	4.8	345	.74	-39	.0112
353.16	.031	.026	36	7.9	298	130	.00206	5.4	262	.68	-58	.0023
355.08	.023	.018	33	6.8	303	60	.00396	2.5	270	.36	50	.0012
356.15	.017	.028	33	8.8	134	180	.00114	4.5	101	.51	36	.0028
361.02	.019	.018	28	12.3	95	115	.00190	5.3	67	.43	34	.0013
365.16	.054	.038	61	3.0	239	70	.00346	2.8	178	.93	-80	.0032
367.15	.150	.064	38	1.3	141	127	.00553	2.7	103	2.02	*0.	.0133
370.94	.033	.038	41	10.2	189	325	.00444	5.0	148	.49	6	.0045
371.15	.040	.025	14	5.3	173	230	.00275	4.8	159	.76	*4.	.0051
371.91	.019	.021	52	10.2	198	80	.00305	3.5	146	.34	3	.0011
372.15	.019	.018	26	14.0	175	160	.00588	3.4	149	.24	49	.0016
372.92	.027	.030	48	13.4	176	220	.00388	5.8	128	.43	15	.0023
373.15	.035	.038	67	11.6	164	265	.01189	3.7	97	.32	13	.0032
373.91	.080	.011	1	6.5	32	490	.03897	2.6	31	.40	95	.0106
374.15	.043	.028	16	9.0	7	350	.01526	3.1	351	.35	119	.0055
374.91	.033	.043	25	6.0	320	350	.00189	4.5	294	.75	12	.0081
377.15	.025	.020	20	12.8	304	210	.00202	7.0	284	.55	35	.0023

AIDJEX DAY	U_*/G MEAS.	U_*/G MOD.	α (°)	G (m sec^{-1})	G (°)	Z_i (m)	C_{10}	U_{10} (m sec^{-1})	U_{10} (m)	$\frac{U_{10}}{G}$	γ (°)	$\frac{fZ_i}{G}$
377.90	.025	.023	35	8.0	300	110	.00271	3.9	265	.49	38	.0019
378.15	.021	.019	33	7.5	302	74	.00131	4.3	269	.57	7	.0014
378.90	.022	.023	21	6.2	311	130	.00083	4.7	290	.76	44	.0030
379.14	.030	.022	37	6.4	315	71	.00285	3.6	278	.56	23	.0015
379.96	.024	.021	31	5.1	171	60	.00132	3.3	140	.65	11	.0016
380.16	.024	.030	67	4.3	155	60	.00413	1.6	88	.37	-36	.0020
381.15	.040	.028	25	3.9	301	100	.00101	5.0	276	1.27	94	.0036
381.90	.036	.026	44	4.8	308	65	.00913	1.8	264	.38	22	.0019
382.15	.178	.086	80	.8	300	80	.00449	2.0	219	2.66	-62	.0149
383.15	.040	.020	6	4.1	16	200	.00344	2.8	9	.69	105	.0069
383.89	.027	.044	28	3.3	32	190	.00214	1.9	4	.57	12	.0080
384.19	.021	.030	43	4.8	5	90	.00172	2.5	322	.52	14	.0026
384.90	.022	.024	53	9.9	312	100	.00207	4.8	259	.49	-15	.0014
385.14	.021	.020	38	13.6	295	120	.00263	5.6	256	.41	29	.0012
386.15	.035	.013	4	2.2	234	76	.00118	2.2	230	1.01	135	.0049
386.91	.028	.016	14	12.1	75	153	.00657	4.1	61	.34	59	.0019
388.15	.029	.042	45	10.7	32	380	.00617	3.9	347	.36	21	.0050
389.10	.060	.047	54	10.9	357	425	.03283	3.6	303	.33	17	.0055
389.90	.025	.043	46	9.6	337	340	.00194	5.4	290	.56	16	.0050
390.15	.047	.056	50	7.8	7	448	.00811	4.1	317	.52	-24	.0080
390.94	.031	.039	30	11.6	5	500	.00412	5.6	335	.48	25	.0061
391.11	.027	.025	30	12.9	9	221	.00422	5.3	339	.41	32	.0024
391.90	.074	.063	72	1.9	12	110	.00263	2.7	300	1.45	-59	.0083
392.10	.028	.023	18	3.0	42	75	.00154	2.2	24	.72	93	.0035
392.90	.015	.016	14	5.3	4	75	.00055	3.4	350	.64	106	.0020
393.10	.027	.029	52	4.8	38	74	.00307	2.3	346	.48	7	.0022
393.84	.045	.048	45	4.9	104	230	.00312	3.9	59	.80	-29	.0066
394.09	.026	.050	44	6.4	111	330	.00187	3.8	67	.59	32	.0072
394.85	.038	.021	16	16.1	109	345	.00998	6.1	93	.38	76	.0030
395.10	.026	.019	24	18.6	115	240	.00395	7.6	91	.41	40	.0018

(Carsey and Leavitt)

AIDJEX DAY	U_*/G MEAS.	U_*/G MOD.	α (°)	G (m sec^{-1})	G (°)	z_i (m)	C_{10}	U_{10} (m sec^{-1})	U_{10} (m)	$\frac{U_{10}}{G}$	γ (°)	$\frac{fz_i}{G}$
395.85	.030	.023	37	23.8	120	300	.00548	9.6	83	.40	25	.0018
396.09	.028	.025	32	17.7	119	300	.00318	8.7	87	.49	-14	.0024
396.85	.028	.026	22	15.9	134	410	.00510	6.2	112	.39	60	.0036
397.10	.038	.035	31	11.1	146	380	.00864	4.6	115	.41	56	.0048
398.85	.025	.027	20	11.7	220	350	.00432	4.5	200	.38	46	.0042
399.85	.096	.074	59	4.4	175	405	.02520	2.7	116	.61	-60	.0127
399.90	.055	.067	66	4.6	146	330	.01037	2.5	80	.54	-71	.0100
399.96	.067	.067	63	6.0	136	428	.00665	4.9	73	.82	-56	.0101
400.89	.039	.036	24	5.6	95	260	.00298	4.0	71	.71	-19	.0065
402.86	.023	.018	32	16.6	302	150	.00404	5.9	270	.36	26	.0013
403.10	.020	.018	34	20.4	290	180	.00293	7.6	256	.37	35	.0012
403.85	.028	.029	33	11.1	297	240	.00104	9.6	264	.87	-50	.0030
403.89	.027	.026	35	14.4	298	240	.00180	9.1	263	.63	25	.0023
403.93	.026	.028	38	13.1	300	250	.00131	9.5	262	.73	-14	.0027
403.97	.030	.030	43	14.8	309	270	.00238	9.0	266	.61	-16	.0026
404.01	.027	.027	32	13.7	306	270	.00147	9.6	274	.70	-0	.0028
404.05	.024	.026	28	11.9	308	240	.00109	8.8	280	.74	-39	.0028
404.85	.015	.011	5	16.6	293	330	.00049	11.4	288	.69	49	.0028
405.10	.027	.020	22	19.9	301	290	.00335	9.2	279	.46	52	.0020
405.85	.030	.031	28	13.3	290	380	.00145	10.6	262	.80	17	.0040
406.02	.025	.026	22	12.2	286	300	.00128	8.4	264	.69	2	.0035
406.14	.027	.025	29	15.1	287	270	.00326	7.0	258	.46	31	.0025
406.86	.030	.033	37	8.8	300	230	.00172	6.3	263	.71	-29	.0036
407.85	.021	.020	31	14.1	265	150	.00154	7.7	234	.55	3	.0015
408.89	.029	.018	8	12.0	280	400	.00243	7.1	272	.59	72	.0047
408.97	.022	.030	27	10.3	280	290	.00129	6.4	253	.62	6	.0040
409.10	.026	.028	27	9.2	284	230	.00176	5.8	257	.63	-13	.0035
409.55	.041	.047	56	6.6	276	250	.00525	3.8	220	.57	-55	.0053
409.85	.049	.048	56	5.7	281	230	.00501	4.0	225	.70	-52	.0056
410.10	.011	.023	30	6.0	266	90	.00029	3.9	236	.65	166	.0021

AIDJEX DAY	U_*/G MEAS.	U_*/G MOD.	α (°)	G (m sec^{-1})	G (°)	z_j (m)	C_{10}	U_{10} (m sec^{-1})	U_{10} (m)	$\frac{U_{10}}{G}$	γ (°)	$\frac{fz_j}{G}$
410.84	.018	.028	30	4.6	277	100	.00064	3.2	247	.70	68	.0031
410.89	.016	.015	10	4.7	272	90	.00086	2.6	262	.55	116	.0027
410.92	.024	.013	10	6.0	289	95	.00267	2.8	279	.47	69	.0022
410.97	.027	.028	42	4.8	296	85	.00229	2.7	254	.56	-1	.0025
411.01	.014	.030	35	4.5	297	100	.00046	3.0	262	.67	-13	.0031
411.06	.033	.024	67	7.1	334	65	.00741	2.7	267	.38	-7	.0013
411.10	.033	.032	42	3.1	308	68	.00121	2.9	266	.94	-50	.0031
412.10	.036	.033	59	6.7	34	120	.00997	2.4	335	.36	21	.0025
412.84	.025	.018	16	4.1	54	70	.00190	2.3	38	.56	90	.0024
413.09	.032	.006	1	2.1	13	80	.00167	1.6	12	.77	*5.	.0054
413.84	.025	.024	27	11.4	306	215	.00355	4.7	279	.41	99	.0026
413.89	.041	.009	2	9.1	305	280	.00725	4.4	303	.48	*8.	.0043
413.93	.034	.032	32	6.1	352	160	.00214	4.4	320	.72	-37	.0037
413.97	.047	.042	35	8.8	345	380	.00840	4.5	310	.51	32	.0061
414.01	.043	.050	42	8.0	358	420	.00701	4.1	316	.51	-10	.0073
414.05	.025	.028	37	8.5	359	150	.00224	4.4	322	.52	-11	.0025
414.09	.023	.028	43	9.1	7	150	.00245	4.3	324	.47	3	.0023
414.89	.020	.018	23	7.3	56	80	.00207	3.3	33	.45	55	.0015
416.10	.047	.034	75	3.5	63	60	.01175	1.5	348	.43	-5	.0024
416.84	.032	.020	29	2.9	46	35	.00384	1.5	17	.51	13	.0017
417.10	.044	.046	24	3.3	71	240	.00314	2.6	47	.79	30	.0102
418.10	.011	.031	36	8.4	51	200	.00075	3.5	15	.42	149	.0033
418.84	.028	.024	29	15.3	55	250	.00376	7.0	26	.46	34	.0023
419.10	.027	.021	17	17.1	64	380	.00384	7.4	47	.43	63	.0031
419.83	.020	.024	18	12.4	74	325	.00121	7.3	56	.59	72	.0037
420.09	.034	.025	20	20.3	81	520	.00852	7.5	61	.37	65	.0036
420.85	.024	.016	23	15.7	86	160	.00377	6.1	63	.39	41	.0014
421.09	.020	.018	27	14.7	85	142	.00320	5.2	58	.35	42	.0014
421.84	.028	.039	35	7.4	62	280	.00914	2.2	27	.30	51	.0053
422.09	.045	.047	38	5.9	83	300	.01602	2.1	45	.36	27	.0071

AIDJEX DAY	$U_*/\bar{G}$ MEAS.	U_*/G MOD.	α (°)	G (m sec^{-1})	G (°)	z_j (m)	C_{10}	U_{10} (m sec^{-1})	U_{10} (m)	$\frac{U_{10}}{G}$	γ (°)	$\frac{fz_j}{G}$
423.84	.022	.018	18	14.6	283	215	.00143	8.6	265	.59	36	.0021
424.11	.026	.021	24	9.6	323	140	.00224	5.3	299	.55	31	.0020
425.10	.025	.035	35	8.5	167	250	.00276	4.0	132	.47	-1	.0041
425.80	.024	.019	29	18.6	175	200	.00398	7.2	146	.39	47	.0015
426.06	.026	.019	28	19.3	175	210	.00472	7.3	147	.38	30	.0015
427.85	.028	.016	4	5.0	322	270	.00113	4.1	318	.83	*3.	.0076
428.10	.022	.024	43	4.1	293	50	.00099	2.8	250	.69	-10	.0017
428.84	.042	.009	4	5.1	94	90	.00401	3.4	90	.66	*4.	.0025
429.09	.027	.023	31	14.3	97	200	.00251	7.7	66	.54	21	.0020
429.84	.034	.028	35	13.7	97	280	.00264	9.2	62	.67	-13	.0029
430.15	.028	.020	25	15.3	76	205	.00227	8.9	51	.58	19	.0019
430.85	.015	.016	14	5.9	29	90	.00041	4.3	15	.73	6	.0021
431.15	.029	.029	42	4.7	32	86	.00128	3.8	350	.80	-28	.0025
431.84	.019	.026	23	6.1	84	153	.00277	2.2	61	.36	72	.0035
432.14	.021	.022	23	9.0	96	153	.00225	4.0	73	.44	46	.0024
432.89	.021	.021	39	13.4	102	135	.00176	6.8	63	.51	3	.0014
433.11	.024	.016	22	13.8	90	142	.00357	5.5	68	.40	58	.0014
433.84	.023	.020	36	10.8	107	106	.00211	5.5	71	.51	11	.0014
434.14	.020	.027	24	8.1	99	206	.00157	4.0	75	.50	15	.0036
434.85	.032	.017	15	4.5	61	74	.00754	1.7	46	.37	74	.0023
435.15	.015	.016	10	5.5	71	115	.00042	4.0	61	.73	-32	.0029
435.85	.030	.026	23	3.6	95	90	.00224	2.3	72	.64	30	.0035
436.14	.035	.027	11	2.3	59	124	.00113	2.4	48	1.05	-65	.0076
438.16	.048	.014	4	2.0	338	80	.00180	2.2	334	1.12	-56	.0057
438.84	.029	.028	15	4.1	304	180	.00149	3.1	289	.76	135	.0062
439.14	.023	.029	34	9.5	304	205	.00203	4.9	270	.51	-5	.0030
439.85	.034	.037	38	9.6	322	300	.00418	5.0	284	.52	26	.0044
440.14	.024	.026	24	11.1	319	250	.00130	7.3	295	.66	-5	.0032
440.84	.020	.013	10	10.1	332	130	.00124	5.8	322	.58	50	.0018

(Carsey and Leavitt)

AIDJEX DAY	$U_*/\hat{G}$ MEAS.	U_*/G MOD.	α (°)	G (m sec^{-1})	G (°)	z_i (m)	C_{10}	U_{10} (m sec^{-1})	U_{10} (m)	$\frac{U_{10}}{G}$	γ (°)	$\frac{fz_i}{G}$
441.14	.028	.027	25	8.0	344	200	.00226	4.8	319	.60	1	.0035
441.85	.024	.029	23	9.1	340	286	.00144	5.7	317	.62	-1	.0044
442.14	.020	.011	9	10.1	326	120	.00081	7.1	317	.70	77	.0017
442.86	.035	.031	36	10.6	331	250	.00400	5.9	295	.56	-3	.0033
443.14	.025	.022	20	7.6	313	150	.00186	4.4	293	.58	18	.0028
443.84	.056	.034	21	1.0	80	45	.00082	1.9	59	1.95	-86	.0065
444.85	.046	.038	30	2.0	5	80	.00233	1.9	335	.96	*6.	.0057
445.14	.025	.033	27	6.3	38	220	.00244	3.2	11	.50	-20	.0049
445.85	.019	.023	16	7.2	13	192	.00100	4.3	357	.60	-5	.0037
446.14	.034	.034	39	6.7	356	180	.00349	3.9	317	.58	-25	.0038
446.85	.034	.026	29	7.5	336	150	.00450	3.8	307	.51	25	.0028
447.14	.008	.023	16	6.9	338	204	.00020	3.9	322	.57	171	.0042
447.85	.036	.041	50	8.1	52	250	.00542	4.0	2	.49	2	.0043
448.15	.027	.025	42	9.2	62	124	.00324	4.4	20	.48	-16	.0019
448.85	.032	.031	31	3.6	17	90	.00106	3.5	346	.97	-38	.0035
449.14	.031	.041	61	4.2	339	115	.00221	2.8	278	.66	-41	.0038
449.84	.018	.014	23	13.3	268	100	.00165	6.0	245	.45	50	.0011
450.14	.025	.023	28	12.2	284	190	.00196	7.0	256	.58	2	.0022
450.85	.024	.021	20	10.5	263	183	.00232	5.2	243	.49	48	.0024
451.14	.028	.025	24	7.4	253	160	.00151	5.3	229	.72	-31	.0030
451.85	.029	.045	45	4.0	217	162	.00148	3.0	172	.75	-72	.0056
452.15	.045	.040	48	2.9	151	90	.00213	2.8	103	.97	-57	.0044
452.85	.035	.030	30	9.4	78	233	.00420	5.1	48	.54	22	.0035
453.15	.034	.027	19	8.4	54	265	.00334	5.0	35	.60	33	.0044
453.87	.015	.021	9	7.3	312	265	.00039	5.4	303	.74	103	.0051
454.18	.024	.023	24	5.7	305	100	.00075	5.0	281	.88	-40	.0025
454.84	.026	.026	20	5.2	274	150	.00274	2.6	254	.50	10	.0040
455.14	.041	.012	6	2.6	249	50	.00144	2.8	243	1.09	-86	.0027
456.86	.036	.021	26	3.1	72	45	.00177	2.6	46	.85	7	.0020
457.15	.020	.016	25	4.9	43	40	.00104	3.1	18	.63	42	.0011

AIDJEX DAY	U_*/G MEAS.	U_*/G MOD.	α (°)	G (m sec^{-1})	G (°)	z_i (m)	C_{10}	U_{10} (m sec^{-1})	U_{10} (m)	$\frac{U_{10}}{G}$	γ (°)	$\frac{fz_i}{G}$
457.86	.028	.017	14	7.3	32	120	.00338	3.5	18	.48	71	.0023
458.14	.028	.027	27	7.0	67	160	.00371	3.2	40	.46	24	.0032
458.85	.020	.017	17	8.2	76	121	.00149	4.3	59	.52	44	.0021
459.15	.030	.026	36	7.6	82	124	.00218	4.8	46	.63	-18	.0023
459.86	.027	.021	27	8.1	80	115	.00192	4.9	53	.61	12	.0020
460.14	.024	.021	31	12.5	78	153	.00226	6.4	47	.51	36	.0017
461.89	.178	.090	46	2.9	143	470	.00781	5.9	97	2.01	-58	.0224
462.14	.060	.048	23	3.9	128	340	.00406	3.7	105	.94	-34	.0121
463.86	.049	.018	6	1.6	31	74	.00524	1.1	25	.68	67	.0064
464.14	.044	.044	27	6.1	85	390	.00488	3.9	58	.64	31	.0087
464.84	.032	.025	17	13.7	144	395	.00359	7.4	127	.54	29	.0040
465.14	.022	.016	16	19.0	123	240	.00219	8.9	107	.47	48	.0018
466.14	.036	.036	26	8.3	60	350	.00244	6.1	34	.73	-37	.0059
467.14	.022	.011	8	12.2	72	162	.00270	5.3	64	.43	61	.0019
467.86	.035	.027	34	13.3	116	245	.00267	8.9	82	.67	6	.0026
468.15	.037	.033	26	9.4	132	340	.00215	7.6	106	.81	-1	.0051
470.14	.080	.055	89	6.2	112	270	.01782	3.7	23	.60	-56	.0061
470.85	.025	.015	11	12.0	260	190	.00119	8.7	249	.73	55	.0022
471.14	.020	.014	7	10.9	248	260	.00105	6.6	241	.60	69	.0033
471.85	.034	.028	25	11.6	249	300	.00351	6.6	224	.57	25	.0036
472.15	.034	.031	36	11.1	240	257	.00432	5.7	204	.52	-6	.0033
472.85	.068	.055	62	2.5	208	121	.02338	1.1	146	.45	31	.0069
473.14	.038	.019	13	2.3	350	50	.00170	2.1	337	.93	148	.0031
474.85	.026	.021	26	6.4	78	95	.00132	4.6	52	.72	-4	.0021

FIELD CALIBRATION REPORT, AIDJEX METEOROLOGY PROGRAM APRIL 1975 - APRIL 1976

by

Mel Clarke, Dave Bell, Eric Leavitt
AIDJEX

ABSTRACT

This report summarizes meteorological data collected during routine systems calibrations and three special calibration visits to the AIDJEX ice camps in spring 1975, summer-fall 1975, and spring 1976. The report lists the factory calibration values for the sensors and describes offsets introduced by the data reading and recording. A set of equations is given for transforming the measurements into physical units.

INTRODUCTION

The main objective of the AIDJEX meteorological program was to obtain air stress and surface heat flux estimates for use in testing ice models. As described by Paulson and Bell [1975], observations at each camp included wind speed and direction at 10 m and temperature at 2 m and 9 m; dew point temperature was measured only at the main camp. These data were collected as continuously as possible throughout the AIDJEX main experiment. They not only provide time series of mean winds and temperature, but, when coupled by NISSI circuits with simultaneous measurements of the variance of wind speed in the frequency band 0.02-1.0 Hz, also serve as an independent means of measuring the variation of the surface drag at each camp [see Leavitt, 1975, for details].

Because it was important that the calibration of the sensors and recording system be accurate, a program of testing was carried out periodically during the experiment. This report describes the results of the testing program and suggests how and when to apply corrections to the various data sensors.

DATA ACQUISITION SYSTEM

The block diagram in Figure 1 outlines the data system. Wind speed, wind direction, and air temperature were sensed, respectively, by cup anemometers, vanes, and aspirated platinum resistance elements, all manufactured by Climate, Inc.; dew point was measured with a Cambridge Research Laboratories cooled mirror sensor manufactured by EG&G. Table 1 summarizes the sensor specifications. Sensor signals were input to the various signal conditioners (translators), which produced output in the range 0-5 volts for recording. The NavSat system, the primary data collector, consisted of a Data General Nova 2-10 minicomputer with analog-to-digital capability and

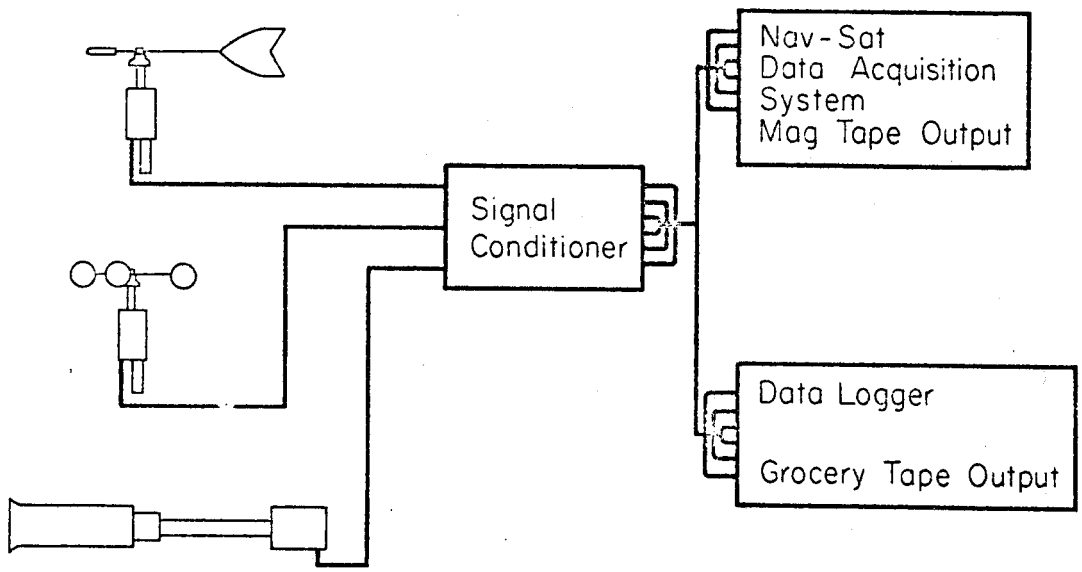

Fig. 1. System block diagram.

TABLE 1

SENSOR SPECIFICATIONS AND EQUATION CONSTANTS

Quantity	Sensor	A/D Channel	*R* full-scale	*F* offset	Instrument Accuracy
Wind speed	3-cup anemometers, optical chopper	21	50 mph 43.4 knots 24.4 m s^{-1}	0	greater of ±1% and 0.07 m s^{-1}
Wind speed (60 sec time-weighted average)	"	24	"	0	"
Wind direction	vane, potentiometer	25	360°	0	±2°
Wind direction (60 sec time-weighted avg.)	"	23	"	0	"
Temperature, 9 m	platinum resistance thermometer	20	80°C	-60°C	±0.05°C
Temperature, 2 m	"	19	"	-60°C	"
NISSI Lo	--	22	5 volts	0	--
NISSI Hi	--	28	"	0	--
EG&G temperature	bead thermistor	--	100°F	-50°F	±0.5°F
EG&G dew point	cooled mirror	26	"	-50°F	"

magnetic tape recorder. The A/D system was 10 bits (0-1023 digitizer units over the 0-5 volt range) with a resolution of 0.005 volts. During recording, data were sampled from all sensors once every 30 seconds. The Digitec Data later provided back-up recording and monitoring capability with a printed paper tape output. Its resolution was 0.001 volts.

CALIBRATIONS

Errors in the sytem may result from voltage offsets or calibration changes in the digitizers or translators and changes in the calibrations of the sensors. A general equation relating voltages recorded by the NavSat systems to a given meteorological parameter can be written as

$$X = \frac{R}{V_r} \cdot (V + b + V_{mn}) + F$$

where

$V = D \cdot 5.0/1023$ is the voltage as reported by the NavSat system, D being the recorded output in digitizer units;

b = NavSat A/D bias in volts;

V_{mn} = minimum voltage obtained during zero check of signal conditioner, $\simeq$ 0 volts;

V_r = voltage output range of signal conditioner, $V_r = V_{mx} - V_{mn} \simeq 5$ volts;

V_{mx} = maximum voltage obtained during full-scale check, $\simeq$ 5 volts;

R = range of environmental parameters between 0 and 5 volts, in physical units (obtained from equipment manufacturer);

F = value in physical units that corresponds to the zero volt output.

X = environmental data in physical units, after corrections.

Values of R and F for each sensor are given in Table 1.

The NavSat A/D and the data logger biases were measured by placing a known voltage from a precision voltage source at the input and observing the recorded output. These voltages were monitored by an HP3460A digital voltmeter and were accurate to 0.0005 volts. Measurements were made over the range of 0-5 volts. An average bias was calculated for each camp. Subsequent spot checks comparing the A/D output with the data logger confirm the results tabulated in Table 2. These bias values should be considered if the NavSat records are to be compared with the data logger records.

The signal conditioner normalizes the various sensor outputs to voltages between 0 and 5 volts. Provision was made on the signal conditioner to check the zero and full-scale voltage levels routinely. A summary of these

TABLE 2

NAVSAT A/D AND DATA LOGGER BIAS (b)

Camp	A/D	Data Logger
Big Bear	0.000	0.000
Caribou	+0.004	0.000
Blue Fox	-0.007	0.000
Snow Bird		
before 17-8-75	+0.018	0.000
after 17-8-75	-0.011	0.000

Note: b = (voltage standard) - (recorded voltage) volts.

checks is included in Appendix 1. If the assumption is made that the zero and full-scale levels are 0.000 volts and 5.000 volts respectively, then the maximum error from the signal conditioner would be 0.1 m s^{-1} for wind speed, 0.4° for wind direction, and 0.95°C for temperature. For wind speed and direction the error is within the accuracy of the wind instruments (Table 1), but for the temperature data this assumption is a potential source of error.

Wind Speed Calibration

To apply the general equation to wind speed data, some simplification can be made. Assuming that the ideal 0-5 volt output for the signal conditioner is true, the equation for wind speed, S, becomes

$$S = \frac{R}{5} (V + b)$$

The worst case error contribution of b, the A/D bias, is only 0.08 m s^{-1}, which is within the sensor accuracy, and the equation for wind speed reduces further to

$$S = \frac{R}{5} (V)$$

or

$$S = 4.48 \cdot V, \text{ in m s}^{-1} \qquad (1)$$

The wind speed system was checked periodically to ensure that it was functioning properly. Electrical tests of the signal conditioner demonstrated that any windspeed problem would have to be related to the sensor. It should be noted that the wind speed system was provided with switches to select any of three ranges (0-25 mph, 0-50 mph, 0-100 mph). Ranges set to other than the standard 0-50 mph are possible for brief periods because of operator error. The most serious difficulty with the system were errors caused by ice forming on the cups. An extract from the Caribou meteorology log (page 27) illustrates this problem: "30 Sept. 75, 1740-1745Z: Climbed tower and cleaned heavy frost from all sensors. Wind speed jumped from 5 to 8 m/s." It was not possible to make on-site calibrations of the wind speed sensors, so the manufacturer's calibration had to be relied upon.

Wind Direction Calibration

Application of the general equation for the wind direction gives the relative wind direction, which must be corrected for camp azimuth changes as described below to obtain the true wind direction. The assumption that the signal conditioner produces an ideal 0-5 volt output is also adequate for wind direction data. The equation for relative wind direction, d_r, then becomes

$$d_r = \frac{R}{5} (V + b)$$

The method used to compute the true wind direction, d_t, will absorb b (the A/D bias). Thus, the usable equation becomes

$$d_r = \frac{R}{5} \cdot V$$

or

$$d_r = 72 \cdot V, \text{ in degrees} \qquad (2)$$

The placement and orientation of towers, theodolites, sensors, and antennas vary considerably from camp to camp. However, each camp positioned the theodolite somewhere on the line that intersected the two NavSat antennas, making possible a uniform method of determining the "true" wind direction. Figure 2 should be referred to as the following definitions are developed.

$$d_t = d_r + \theta_c - \theta_0$$

Here d_t is the true wind direction; d_r is the relative wind direction; θ_c is the camp azimuth (the clockwise angle from true North to the A→B line as determined by the NavSat system); and θ_0 is the relative zero azimuth. This last term is equal to $\alpha + \beta$, where α is the clockwise angle from the theodolite met tower line (between the theodolite and the tower wind-direction

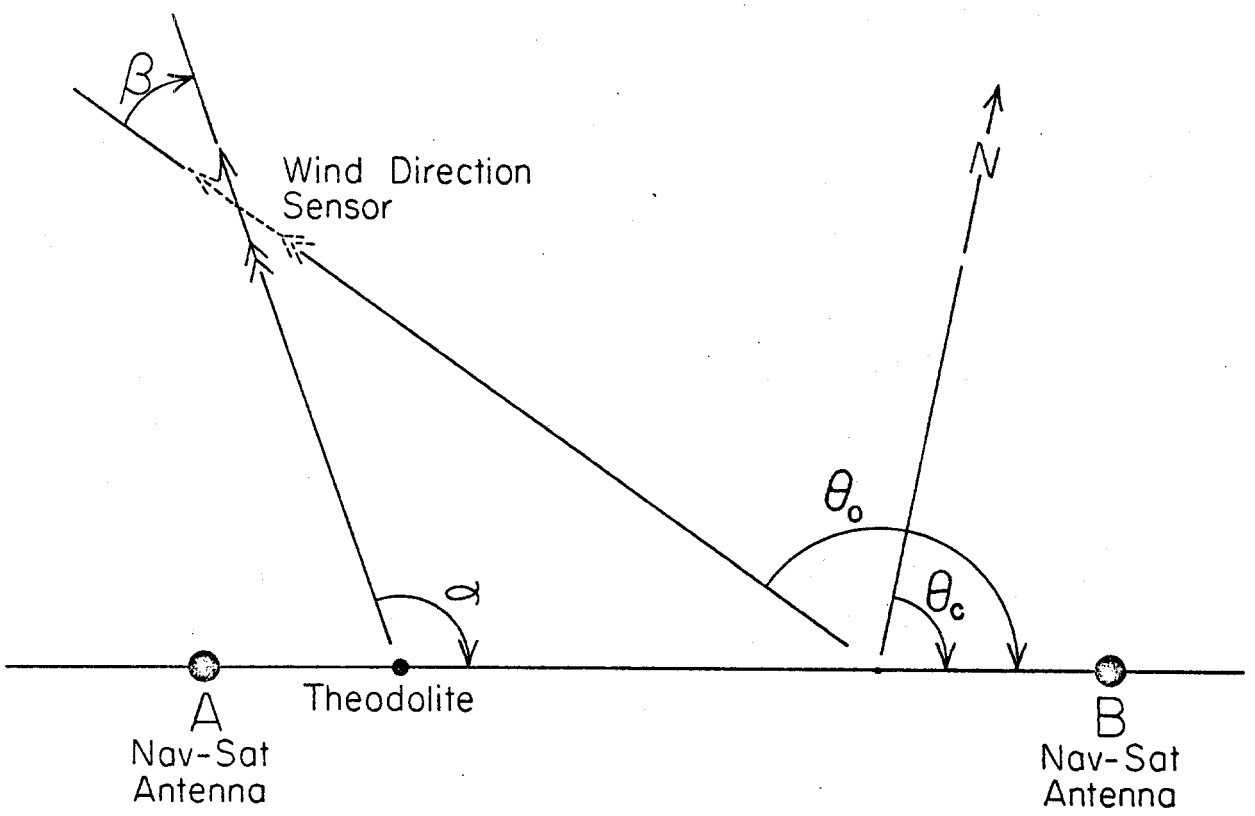

Fig. 2. True wind direction determination.

sensor housing) to the NavSat antenna A→B line, and β is the indicated direction when the tail of the wind direction vane was pointed at the theodolite.

Camp azimuths at 3 hr intervals are available from the AIDJEX data bank. Appendix 2 includes a tabulation of θ_0, α, and β as measured during routine calibration checks using the above definitions.

Periodic checks of the wind direction systems ensured proper operation, but some slippage of the vane shaft relative to the sensor element was found; the results are reflected in the periodic θ_0 checks. During these tests the vane had to be held by hand, and this introduced small variations in the θ_0 measurements.

Temperature Calibration

For the best estimation of the absolute temperature, T, the full general equation is required. This gives the temperature as

$$T = \frac{R}{V_r} (V + b + V_{mn}) + F$$

A simplification can be made if it is desired only to observe the difference in temperatures between the 9 m and 2 m levels. (The exact heights are given in Appendix 3.) Periodic routine tests were performed in which the two temperature probes were placed together at the 2 m level for a side-by-side comparison. The results of these tests are tabulated in Appendix 4 using the assumption that the zero and full-scale outputs from the signal conditioner were 0.000 and 5.000 volts, respectively. The A/D bias, b, was set at zero, as this term will drop out when the difference is taken. The resulting idealized equation for air temperature becomes

$$T = \frac{R}{5} (V) + F$$

or

$$T = (16\ V - 60), \text{ in degrees Celsius} \qquad (3)$$

A few checks of the temperature system were made by placing the sensor elements in a controlled temperature bath, usually an ice bath. Where possible, a precision Hewlett Packard 2801A quartz thermometer was used to monitor the bath temperatures. Table 3 summarizes these tests and includes the temperature computed using both the general form of the equation and the idealized form.

The most serious problem with the temperature data was the variations in the recorded differences between sensors. We believe these variations to be a result of inadequate aspiration. This argument is supported by evidence that temperatures changed when the wind direction varied or when the aspirator motors failed completely. For example, when the 9 meter aspirator motor failed at Caribou on 5 March 1976, the temperature increased about 1°C relative to the 2 m probe. When the motor was repaired, that sudden increase disappeared.

Dew Point Calibration

Dew-point temperature was monitored only at the main camp: first at Big Bear, then, from 2 November 1975 on, at Caribou. At both camps, the sensor was positioned approximately 2 m above the snow or ice surface. Since no provision had been made to calibrate the unit during its use, the manufacturer's calibrations and specifications were relied on heavily. It is necessary to assume that a temperature range of -50°F to +50°F corresponds to the specified output range of 0.000-5.000 volts. With this assumption, the general equation for dew/frost-point temperature, E, reduces to

$$E = \frac{R}{5} (V + b) + F$$

or

$$E = 20\ (V + b)\ - 50°F$$

The conversion from degrees Fahrenheit to degrees Celsius is

$$°C = (F - 32)\ \frac{5}{9}$$

TABLE 3

TEMPERATURE BATH TESTS

Date	Time	Monitor Temp. (°C)	Volts T_9	Volts T_2	General Equation (°C) T_9	General Equation (°C) T_2	Idealized Equation (°C) T_9	Idealized Equation (°C) T_2	Notes
Big Bear									
27 Apr 75	0037-0046	+ 0.02	3.956	---	+ 3.36	---	+ 3.30	----	old probe
27 Apr 75	0623-0631	0.00	3.752	---	+ 0.09	---	+ 0.03	---	new probe
28 Jul 75	0704-0725	+ 0.01	3.763	3.752	+ 0.27	+ 0.04	+ 0.21	+ 0.03	
Caribou									
13 Aug 75	0027-0058	- 0.01	3.751	3.749	- 0.10	+ 0.11	+ 0.02	- 0.02	
13 Aug 75	0123-0140	- 0.01	3.754	3.749	+ 0.01	+ 0.11	+ 0.06	- 0.02	adj. to sig. con.
16 Mar 76	2120-2310	---	3.789	3.742	- 0.03	+ 0.04	+ 0.62	- 0.13	ice bath
1 Apr 76	2225-2321	+ 0.01	3.789	3.742	- 0.03	+ 0.04	+ 0.62	- 0.13	
2 Apr 76	0007-0038	+18.54	4.949	4.902	+18.31	+18.64	+19.18	+18.43	
3 Apr 76	1651-1730	-28.79	1.987	1.934	-28.52	-28.94	-28.21	-29.06	
Blue Fox									
12 Jul 75	0704-0725	+ 0.01	3.755	3.768	- 0.08	+ 0.23	+ 0.08	+ 0.29	
23 Feb 76	2158-0001	---	3.743	3.763	- 0.14	+ 0.24	- 0.11	+ 0.21	ice bath
22 Mar 76	2128-0015	---	3.743	3.763	- 0.14	+ 0.24	- 0.11	+ 0.21	ice bath
27 Mar 76	2134-2204	+ 0.01	3.739	3.749	- 0.21	+ 0.01	- 0.18	- 0.02	
27 Mar 76	2312-2330	-20.40	2.437	2.439	-21.11	-21.00	-21.01	-20.98	
27 Mar 76	2358-0023	+ 7.73	4.223	4.236	+ 7.56	+ 7.82	+ 7.57	+ 7.78	
19 Apr 76	2003-2120	---	3.738	3.752	- 0.22	+ 0.06	- 0.19	+ 0.03	ice bath
19 Apr 76	2134-2300	+15.80	4.724	4.738	+15.60	+15.88	+15.58	+15.81	
Snow Bird									
18 Aug 75	0218-0236	+ 0.01	3.759	3.759	- 0.08	+ 0.04	+ 0.14	+ 0.14	
18 Aug 75	0327-0340	+ 0.01	3.763	3.759	+ 0.01	+ 0.04	+ 0.21	+ 0.14	adj. to sig. con.
21 Mar 76	0115-0145	+ 0.01	3.777	3.753	+ 0.32	- 0.06	+ 0.43	+ 0.05	
21 Mar 76	0301-0332	+18.60	4.946	4.923	+19.05	+18.69	+19.14	+18.77	
21 Mar 76	0442-0515	-25.57	2.170	2.147	-25.43	-25.80	-25.28	-25.65	
7 Apr 76	2128-2330	+ 0.08	3.759	3.753	+ 0.03	- 0.06	+ 0.14	+ 0.05	
19 Apr 76	2320-0020	---	3.757	3.746	0.00	- 0.18	+ 0.11	- 0.06	ice bath

Combining this information gives a usuable equation of

$$E = \frac{5}{9} [20 (V + b) - 82], \quad \text{in degrees Celsius} \qquad (4)$$

For temperatures below 0°C the temperature recorded by this system is the frost point. A table has been included in Appendix 5 to make the conversion from frost point to a true dew point. The following equation was derived from this table to aid in the calculation of dew point directly from the recorded voltage. Define A as

$$A = 20 (V + b) - 82$$

If the air temperature T, is 0°C or higher, then the dew point temperature is $5/9A$; if T is lower than 0°C, then the dew point temperature is

$$\frac{5}{9}\,(1.129A + 0.0005\,A^2) \qquad (5)$$

Once every twelve hours the cooled mirror in the dew/frost point sensing system was heated automatically to above the ambient temperature to clear away ice and moisture. It took the system about 10 minutes to return to its normal temperature-balancing mode and about 15 minutes to return to a stable temperature that indicated the dew/frost point.

SUMMARY

In general, the meteorological systems performed well during the AIDJEX activities. The accuracies given below should be considered typical for all camps. The camps were maintained by a dedicated group of observers who helped to minimize the effect of such environmental influences as icing of the anemometers and snow packing into the aspirators and temperature shields.

Combining the basic wind speed accuracy of the larger of 0.07 m sec^{-1} and 1% with the observed influence of the recording system of 0.1 m sec^{-1}, the overall accuracy is 0.17 m sec^{-1} or 1%, whichever is greater. The resolution of the wind speed data is 0.11 m sec^{-1} from the NavSat records. This assumes that the instruments were clear of ice.

The true wind direction can be given to ±5° by combining the basic sensor accuracy of ±2° over the range 0°-354° with 0.4° contribution from the recording system and ±2° from the routine relative zero measurements. The resolution of the wind direction data was 0.36°.

During controlled bath tests the absolute temperature was observed to be accurate to 0.05°C, with a standard deviation of 0.19°C after using the general form of the equation with all bias values accounted for. The idealized equation gives the same accuracy, but increases the standard deviation of all

tests to 0.27°C. For clean aspirated probes operating side by side, the standard deviation of their differences was 0.25. The resolution available was 0.08°C.

The dew point temperatures should be good to 0.5°C with a resolution of 0.3°C.

REFERENCES

Leavitt, E. 1975. Determination of air stress from surface layer data. *AIDJEX Bulletin, 28,* 11-20.

Paulson, C.A., and D. L. Bell. 1975. Meteorological observations during the AIDJEX main experiment. *AIDJEX Bulletin, 28,* 1-10.

APPENDICES

Appendix

1 ..... Zero and full-scale summaries.

2 ..... Relative zero azimuths.

3 ..... Instrument heights.

4 ..... Side-by-side comparison of temperature probes.

5 ..... Conversion from dew point to frost point.

Note: For the main experiment AIDJEX adopted a convention of numbering days consecutively, beginning with day 1 = 1 January 1975 and ending with day 500 = 14 May 1976. Some of the appendices use this system, under columns headed "AIDJEX Day."

APPENDIX 1
ZERO AND FULL-SCALE SUMMARIES

Values tabulated are averages of voltages obtained from Digitec records during routine zero and full-scale checks.

ZERO CHECK

Quantity	Big Bear	Caribou	Blue Fox	Snow Bird
Wind speed	0.000	0.000	0.000	0.000
Wind speed (t.w.a.)	+0.001	-0.001	0.000	0.000
Wind direction	0.000	0.000	0.000	0.000
Wind direction (t.w.a.)	+0.001	0.000	+0.001	0.000 -0.001[a]
Temperature, 9 m	0.000	-0.014 -0.005[b] -0.002[c] 0.000[d]	-0.007	-0.005 -0.002[a]
Temperature, 2 m	-0.006	0.000	-0.001	0.000 -0.002[c]

FULL SCALE CHECK

Quantity	Big Bear	Caribou	Blue Fox	Snow Bird
Wind speed	+4.998	+4.994 +4.991[c]	+4.987 +5.000[e] +4.992[c]	+4.996 +4.991[c]
Wind speed (t.w.a.)	+5.002	+5.001	+5.001	+5.001 +5.004[c]
Wind direction	+4.998	+5.000 +4.997[c]	+4.997	+4.994 +4.998[a]
Wind direction (t.w.a.)	+4.997	+5.004	+5.001	+5.000 +4.999[a]
Temperature, 9 m	+4.995	+4.982 +4.998[b] +4.995[c] +5.060[d]	+4.988 +4.977[c]	+4.992 +4.997[a] +4.990[c]
Temperature, 2 m	+4.985	+4.995 +4.991[c]	+4.993 +4.986[c]	+4.994 +4.990[c]

[a] after 18 August 1975.
[b] after 13 August 1975.
[c] after 1 October 1975.
[d] after 24 November 1975.
[e] after 12 July 1975.

APPENDIX 2
RELATIVE ZERO AZIMUTHS

Relative zero azimuth (θ_0) is the sum of α and β, where α is the clockwise angle from the theodolite→met tower line (between the theodolite and the tower wind direction sensor housing) to the NavSat antenna A→B line, and β is the indicated direction when the tail of the wind direction vane was pointed at the theodolite. The tabulation below gives θ_0, α, and β as measured during routine calibration checks using the above definitions.

BIG BEAR

AIDJEX DAY	Date	Time	α	+ β	= θ_0	Notes
99	9 Apr 75		140.3°	2.0°	142.3°	β assumed from later measurements.
141	21 May 75		140.3	2.0	142.3	β measured here.
160	9 Jun 75	2039		2.0		
253	10 Sep 75		28.95	114.48	143.4	One-time-only measurement from different theodolite position on A→B line.
258	15 Sep 75		140.3	2.0	142.3	
266	23 Sep 75	1713	140.4	2.0	142.4	
269	26 Sep 75		140.4	2.0	142.4	
		--camp breakup; end of data--				

CARIBOU

116	26 Apr 75	1030	131.1°	3.4°	134.5°	
125	5 May 75	2304	131.1	179.9	311.0	Wind direction sensor turned 180° in its mounting.
130	10 May 75	1820	131.1	3.4	134.5	Sensor returned to normal.
133	13 May 75	1900	131.1	3.4	134.5	
150	30 May 75	0045	131.1	5.0	136.1	
157	6 Jun 75	2145	131.1	5.1	136.2	
165	14 Jun 75	0100	131.1	4.2	135.3	

CARIBOU (continued)

AIDJEX DAY	Date	Time	α	+	β	=	θ_0	Notes
173	22 Jun 75	2310	131.1°		4.0°		135.0°	
182	1 Jul 75	0001	131.1		3.4		134.5	
187	6 Jul 75	2245	131.1		4.6		135.7	
193	12 Jul 75	2212	131.1		5.2		136.3	
201	20 Jul 75	0120	131.1		4.3		135.4	
209	28 Jul 75	0042	131.1		3.9		135.0	
214	2 Aug 75	2341	131.5		2.7		134.2	Tower straightened.
223	11 Aug 75	0020	132.0		2.2		134.2	
225	13 Aug 75	1951	131.8		2.2		134.0	
234	22 Aug 75	2204	131.4		2.2		133.6	
242	30 Aug 75	2330	131.4		1.9		133.3	
251	8 Sep 75	2224	131.4		3.2		134.6	
251	8 Sep 75	2343	82.0		50.3		132.3	New theodolite position on A→B line; windy weather.
257	14 Sep 75	2250	82.0		52.7		134.7	
263	20 Sep 75	2146	82.0		51.7		133.7	
270	27 Sep 75	0241	82.0		50.1		132.1	
278	5 Oct 75	2340	82.0		52.1		134.1	
279	6 Oct 75	1740	--		--		--	Vane replaced.
285	12 Oct 75	2150	81.9		51.3		133.2	
291	18 Oct 75	0020	81.9		52.6		134.5	
297	24 Oct 75	1852	91.5		41.0		132.5	New theodolite position on A→B line.
306	2 Nov 75	2310	91.5		38.7		130.2	
307	3 Nov 75	2020	91.5		40.4		131.9	
312	8 Nov 75	2030	91.4		40.8		132.2	
320	16 Nov 75	2310	91.4		40.1		131.50	
334	30 Nov 75	2320	91.5		40.5		131.97	Tail held toward theodolite.
372	7 Jan 76	2128	91.4		41.2		132.6	
379	14 Jan 76	2319	91.4		41.9		133.27	
393	28 Jan 76	2109	91.4		41.1		132.48	
401	5 Feb 76	0020	91.3		41.2		132.5	
416	20 Feb 76	1910	91.2		40.4		131.6	

CARIBOU (continued)

AIDJEX Day	Date	Time	α	+	β	=	θ_0	Notes
422	26 Feb 76	0056	91.3°		40.4°		131.7°	
428	3 Mar 76	2110	91.3		41.5		132.8	
443	18 Mar 76	0020	91.3		39.5		130.8	
457	1 Apr 76	0338	91.3		40.6		131.1	Assumed value.
		--end of data--						

BLUE FOX

109	19 Apr 75	0400	33.3°	182.4°	215.7°	β assumed from next measurement, when procedure was changed.
148	28 May 75	2141	33.3	182.4	215.7	
164	13 Jun 75	0220	33.3	179.9	213.2	
193	12 Jul 75	2330	33.3	181.1	214.4	
194	13 Jul 75	0036	33.3	179.8	213.1	
207	26 Jul 75	2037	33.3	177.6	210.9	Tower stump found loose in the ice.
213	1 Aug 75	2342	33.3	178.0	211.3	
228	16 Aug 75	0602	33.3	180.3	213.6	
230	18 Aug 75	0454	33.4	178.9	212.3	Theodolite moved slightly.
245	2 Sep 75	2002	33.4	177.2	210.6	
256	13 Sep 75	1933	33.3	178.0	211.3	
265	22 Sep 75	1913	33.3	176.6	209.9	
272	29 Sep 75	1911	33.3	172.7	206.0	
279	6 Oct 75	2114	33.3	169.1	202.4	High winds during measurement.
281	8 Oct 75	1944	33.3	170.0	203.3	
287	14 Oct 75	0028	33.3	167.5	200.8	Suspect changes caused by loose sensor vane coupling set screw.
287	14 Oct 75	2030	33.3	185.4	218.7	New sensor set in place.
293	20 Oct 75	2038	33.3	186.2	219.5	
293	20 Oct 75	2040	33.3	191.6	224.9	Coupling screw tightened.
294	21 Oct 75	0012	33.3	175.8	209.1	Sensor adjusted slightly. Final value obtained.
304	31 Oct 75	0045	33.3	175.6	208.9	
307	3 Nov 75	1849	33.3	176.0	209.3	
314	10 Nov 75	1857	33.3	175.0	208.3	

BLUE FOX (continued)

AIDJEX DAY	Date	Time	α	+	β	=	θ_0	Notes
321	17 Nov 75	2052	33.3°		174.3°		207.6°	
328	24 Nov 75	2003	33.3		176.0		209.3	
335	1 Dec 75	2024	33.3		177.0		210.3	Darkness hampered measurement.
342	8 Dec 75	2129	33.3		176.9		210.2	
349	15 Dec 75	2145	33.3		176.3		209.6	
360	26 Dec 75	2150	33.3		176.1		209.4	
370	5 Jan 76	2119	33.3		176.6		209.9	
378	13 Jan 76	2113	33.3		176.9		210.2	
384	19 Jan 76	2040	33.3		177.0		210.3	
388	23 Jan 76	0600	32.5		--		--	Theodolite moved during deriming.
391	26 Jan 76	2110	33.3		176.2		209.5	Theodolite back in original position.
398	2 Feb 76	2050	33.3		177.0		210.3	
398	2 Feb 76	2050+	108.7		107.2		210.9	Oceanographer's theodolite used.
407	11 Feb 76	2319	33.3		177.5		210.8	
412	16 Feb 76	1958	33.3		177.2		210.5	
412	16 Feb 76	1958+	108.7		102.0		210.7	Oceanographer's theodolite used.
421	25 Feb 76	2028	33.3		177.3		210.6	
426	1 Mar 76	2116	33.3		177.3		210.6	
433	8 Mar 76	2123	33.3		176.9		210.2	
440	15 Mar 76	2030	33.1		177.0		210.1	
447	22 Mar 76	1956	33.3		177.2		210.5	
447	22 Mar 76	1956+	108.7		101.8		210.5	Oceanographer's theodolite used.
452	27 Mar 76	1844	33.3		177.2		210.5	
452	27 Mar 76	1844+	108.7		101.5		210.2	Oceanographer's theodolite used.
463	7 Apr 76	0017	33.3		177.3		210.6	
468	12 Apr 76	2047	33.3		177.1		210.4	
476	20 Apr 76	1955	33.3		177.5		210.8	
			--end of data--					

SNOW BIRD

AIDJEX DAY	Date	Time	α	+	β	=	θ_0	Notes
135	15 May 75	2230	113.2°		2.2°		115.4°	
165	14 Jun 75	0230	113.2		351.3		104.5	Loose set screw suspected in vane coupling.
166	15 Jun 75	0406	113.2		352.0		105.2	
181	30 Jun 75	0610	113.2		351.6		104.8	
197	16 Jul 75	0705	113.2		350.3		103.5	
215	3 Aug 75	0730	113.2		350.5		103.7	
229	17 Aug 75		113.2		348.6		101.8	
235	23 Aug 75	2350	113.2		353.6		106.8	
236	24 Aug 75	0001	113.2		352.4		105.6	Set screws tightened.
257	14 Sep 75	2215	113.2		351.7		104.9	
269	26 Sep 75	2215	113.2		351.0		104.2	
277	4 Oct 75	0040	113.2		350.6		103.8	
283	10 Oct 75	2250	113.2		351.1		104.3	
292	19 Oct 75	0100	113.2		351.9		105.1	
298	25 Oct 75	0030	113.2		351.8		105.0	
299	26 Oct 75	2010						Wind direction system not operating; power supply problem.
307	3 Nov 75							Wind direction vane replaced.
311	7 Nov 75	2330	113.2		6.0		119.2	
314	10 Nov 75		113.2		4.3		117.5	
315	11 Nov 75	1955	113.2		352.22		105.42	New wind sensor #142 (original) replaces #151.
329	25 Nov 75	2330	113.2		3.82		117.02	#151 replaces #142 after #142 slips in shaft.
333	29 Nov 75	2303	113.2		3.46		116.66	Changed theodolite position so observers could see both antennas.
339	5 Dec 75	2105	101.34		13.68		115.02	
346	12 Dec 75	2105	101.34		13.82		115.16	
353	19 Dec 75	2113	101.34		13.97		115.31	
360	26 Dec 75	2131	101.35		13.82		115.17	
381	16 Jan 76	2126	101.6		12.74		114.34	Measured after A→B line was sheared.
384	19 Jan 76	0000	101.37		13.97		115.34	Before B antenna was reconnected.
384	19 Jan 76	0000	100.7		13.39		114.09	After theodolite was moved.
388	23 Jan 76	2142	100.7		13.03		113.73	
397	1 Feb 76	2325	100.7		13.03		113.73	

SNOW BIRD (continued)

AIDJEX DAY	Date	Time	α	+	β	=	θ_0	Notes
403	7 Feb 76	--	--		--		--	New lead causes shearing. Antenna A disconnected.
406	10 Feb 76	--	--		--		--	Antenna A hooked up again. Angle intersecting A→theodolite→B is now 180°31'.
409	13 Feb 76	0101	100.7°		13.32°		114.02°	Theodolite in same position relative to A. Moved B 31 ft to old A→B line.
416	20 Feb 76	2346	100.7		13.2		113.9	
425	29 Feb 76	0028	100.8		12.67		113.47	
428	3 Mar 76	--	--		--		--	Lead through camp separates antennas A and B.
431	6 Mar 76	0013	100.8		13.25		114.05	Using A antenna as if B were still in position.
437	12 Mar 76	0030	100.8		13.39		114.19	
444	19 Mar 76	0249	100.8		13.32		114.12	
451	26 Mar 76	2110	280.8		12.6		293.4	Results from reversing A→B line. B put on opposite side of A some time before 22 March.
463	7 Apr 76	0235	280.8		13.54		294.34	
468	12 Apr 76	2041	280.8		13.97		294.77	Slanted wind vane?
474	18 Apr 76	2325	280.8		15.05		295.85	A/D bias may be reason for change in β.

--end of data--

APPENDIX 3
INSTRUMENT HEIGHTS

The heights of the instruments on the tower were measured relative to the tower baseplate (Table A). The height of baseplates relative to the surface (Table B) varied with snowfall and ice ablation. At Blue Fox, a careful record of baseplate elevation was made; at the other camps, elevation histories have been constructed from the snow depth/ice ablation measurements of Arne Hanson. The height of the instrument relative to the surface is found by adding the baseplate height above the surface to the height recorded in Table A.

A. HEIGHTS ABOVE BASEPLATE (in cm)

Camp	Wind Sensors	T_9	T_2
Big Bear	965	875	154
Caribou			
until day 198	963	881	192
after day 198	963	841	152
Blue Fox	963	839	149
days 193-256 only			110
days 406-408 only		799	
Snow Bird			
until day 291 (approx.)	964	881	192
after day 291	964	841	152

B. TOWER BASEPLATE HEIGHTS ABOVE SNOW (in cm)

Day	Big Bear	Caribou	Blue Fox	Snow Bird
110	0	- 8	28	8
130	0	- 8	18	8
150	0	- 8	25	8
170	10	- 4	20	13
190	25	12	32	32*
210	40	36	32	50*
230	45	43	32	49*
250	42	50	32	49*
270	40	50	28	47*
290		48	22	47*
310		47	21	46
330		47	20	45
350		47	17	44
370		46	15	43
390		46	15	42
410		45	13	41
430		43	14	40
450		41	15	38
470		38	15	38
490		38	--	37

(*) These values good only to ±10 cm.

APPENDIX 4

SIDE-BY-SIDE COMPARISON OF TEMPERATURE PROBES

The temperature sensors were compared with each other by temporarily repositioning the sensor from the 9 m level next to the sensor at 2 m. The table below gives the time of the test, the mean temperature as measured by the 2 m sensor during the test, the average difference between the sensors ($T_9 - T_2$), and the standard deviation, σ, of this difference.

BIG BEAR

AIDJEX Day	Date	Time	T_2 (°C)	T_9-T_2 (°C)	σ (°C)	Notes
111	21 Apr 75	1845-2100	-21.6	+1.60	0.10	Suspect problem with 9 m probe.
113-114	23-24 Apr 75	2330-0420	-19.8	+3.30	0.10	Continued problem.
116	27 Apr 75	0752-0818	-26.2	-0.17	0.02	9 m probe replaced.
142-143	22-23 May 75	1920-0540	-10.4	+0.07	0.18	Wind direction change during test corresponding to change of sign of T_9-T_2 in test.
171-172	20-21 Jun 75	2000-0000	- 3.8	+0.12	0.06	
199	18 Jul 75	0213-0637	+ 0.3	+0.18	0.05	
215-216	3-4 Aug 75	1915-0630	- 0.2	+0.29	0.04	
248-249	5-6 Sep 75	2230-0030	- 3.9	-0.02	0.02	

CARIBOU

123	3 May 75	0211-0700	-16.1	-0.10	0.06	
133	13 May 75	0124.....				T_2 CH19 placed on CH26.
139	19 May 75	1918-2331	-12.6	-0.22	0.18	
149	29 May 75	1845-2126	- 5.5	-0.14	0.02	
155-156	4-5 Jun 75	2200-0230	- 2.1	-0.06	0.10	
162	11 Jun 75	1936-2334	- 1.5	+0.30	0.16	
170	19 Jun 75	0031-0430	- 2.0	+0.04	0.05	
176-177	25-26 Jun 75	2122-0215	+ 0.0	+0.02	0.10	
183-184	2-3 Jul 75	2225-0215	0.0	+0.11	0.04	
190-191	9-10 Jul 75	2240-0216	+ 0.5	+0.17	0.04	

CARIBOU (continued)

AIDJEX Day	Date	Time	T_2 (°C)	T_9-T_2 (°C)	σ (°C)	Notes
197-198	16-17 Jul 75	2147-0319	+ 0.8	+0.02	0.02	
204-205	23-24 Jul 75	2230-0234	- 1.5	+0.16	0.06	
211-212	30-31 Jul 75	2140-0240	- 0.5	-0.05	0.08	
218	6 Aug 75	1931-2343	+ 0.2	-0.13	0.07	
224	12 Aug 75	0359	.....			T_2 returned to CH19.
224	12 Aug 75	1940-2320	- 1.7	-0.15	0.15	
232	20 Aug 75	1820-2220	+ 0.4	+0.18	0.04	
239	27 Aug 75	1800-2200	+ 0.1	+0.10	0.01	High winds noted in log.
246	3 Sep 75	1940-2340	- 0.3	+0.27	0.03	
253	10 Sep 75	1940-2340	- 0.4	-0.07	0.05	
260-261	17-18 Sep 75	1820-0120	- 1.9	+0.20	0.10	High winds blowing into aspirator.
274-275	1-2 Oct 75	2008-0043	-12.1	+0.09	0.04	
282	9 Oct 75	0230-0600	.....			No Digitec record.
289	16 Oct 75	0250-0620	-12.1	+0.18	0.02	
296	23 Oct 75	0320-0510	-26.2	+0.07	0.30	
303	30 Oct 75	1630-1730	-24.8	-0.07	0.02	
310	6 Nov 75	0550-0740	-28.2	+0.41	0.02	
330	26 Nov 75	0050-0410	-27.4	+0.85	0.05	
353	19 Dec 75	0220-0500	-32.7	+0.96	0.05	
374	9 Jan 76	0020-0600	-33.6	+0.84	0.04	
380-381	15-16 Jan 76	2350-0340	-39.3	+0.88	0.01	
387-388	22-23 Jan 76	2152-0037	-29.8	+0.78	0.01	Data obtained from very short time series.
395	30 Jan 76	0040-0440	-31.8	+0.82	0.01	
403	6 Feb 76	0240-0409	-25.3	+0.78	0.01	Short time series.
409-410	12-13 Feb 76	2300-0500	-29.4	+0.83	0.08	
416-417	19-20 Feb 76	2243-0229	-33.1	+0.76	0.06	Short time series.
422-423	26-27 Feb 76	1940-0040	-32.8	+1.11	0.24	Wind shift, blowing into horn at end of run.
430	5 Mar 76	0400-0440	-25.5	+2.08	0.18	9 m aspirator not working.
430	5 Mar 76	0600-0720	-28.9	+0.99	0.07	Aspirator probe repaired.
442	17 Mar 76	0030-0250	-23.2	+0.83	0.02	
457	1 Apr 76	1920-2130	-30.3	-0.64	0.03	

-- end of data --

BLUE FOX

AIDJEX Day	Date	Time	T_2 (°C)	T_9-T_2 (°C)	σ (°C)	Notes
113-114	23-24 Apr 75	2337-1900	-21.2	-0.35	0.23	
126-127	6-7 May 75	2000-0020	- 7.9	-0.08	0.03	
136-137	16-17 May 75	2200-0320	- 8.5	-0.19	0.06	
148-149	28-29 May 75	2100-0100	- 8.8	-0.20	0.06	
156-157	5-6 Jun 75	2020-0300	- 2.1	-0.24	0.12	
163	12 Jun 75	0410-0620	- 3.7	-0.12	0.05	
169	18 Jun 75	2140-2340	- 2.1	-0.04	0.09	
176-177	25-26 Jun 75	2140-0100	+ 0.2	-0.01	0.06	
184	3 Jul 75	0300-0600	+ 0.4	-0.20	0.02	
190-191	9-10 Jul 75	2140-0140	+ 0.6	-0.05	0.04	
192-193	11-12 Jul 75	2200-0150	- 0.2	+0.01	0.07	
197-198	16-17 Jul 75	2200-0150	+ 0.5	-0.02	0.05	
204-205	23-24 Jul 75	2300-0140	- 0.3	-0.06	0.06	
212-213	31-1 Aug 75	2350-0220	+ 0.3	-0.31	0.02	
218	6 Aug 75	2130-2340	- 0.4	-0.29	0.04	
225-226	13-14 Aug 75	2200-0020	+ 0.6	-0.27	0.03	
232	20 Aug 75	1830-2040	+ 0.5	-0.19	0.02	
240-241	28-29 Aug 75	2200-0230	- 1.1	-0.32	0.09	
246	3 Sep 75	1900-2130	- 2.1	-0.24	0.04	
253-254	10-11 Sep 75	2200-0260	- 1.7	-0.17	0.07	
260-261	17-18 Sep 75	2200-0010	- 4.1	-0.37	0.02	
268	25 Sep 75	0200-0440	- 8.2	-0.34	0.05	
272	29 Sep 75	1840-2340	-12.5	-0.35	0.04	
279	6 Oct 75	1920-2320	- 4.8	-0.25	0.04	
286-287	13-14 Oct 75	1955-0045	-24.6	-0.77	0.04	
293-294	20-21 Oct 75	1940-0000	-14.8	-0.45	0.04	
307-308	3-4 Nov 75	1900-0000	-33.4	-0.45	0.05	
321	17 Nov 75	1825-2330	-28.5	-0.33	0.03	Before aspirator cleaned.
321-322	17-18 Nov 75	2330-0205	-27.1	-0.33	0.01	After aspirator cleaned.
335	1 Dec 75	1849-2345	-33.6	-0.53	0.03	
349-350	15-16 Dec 75	1920-0145	-34.2	-0.61	0.04	
352-353	18-19 Dec 75	1843-0120	-29.7	-0.42	0.03	T_2 clean, T_9 not; beacon on during test.
353	19 Dec 75	0607-0907	-32.6	-0.36	0.02	Both probes cleaned.

BLUE FOX (continued)

AIDJEX Day	Date	Time	T_2 (°C)	T_9-T_2 (°C)	σ (°C)	Notes
356-357	22-23 Dec 75	2207-0234	-28.6	-0.52	0.04	
358	24 Dec 75	0220-0520	-20.4	-0.47	0.12	Both probes have new aspirators.
363-364	29-30 Dec 75	2056-0022	-19.8	-0.32	0.03	
377	12 Jan 76	1842-2340	-38.1	-0.42	0.02	
391	26 Jan 76	1912-2255	-41.4	-0.37	0.02	
406-407	9-10 Feb 76	2117-0114	-31.4	-0.37	0.01	
419	23 Feb 76	1845-2122	-35.7	-0.10	0.14	Snow in probes, but not blocking air flow.
420	24 Feb 76	0112-0454	-39.2	-0.07	0.01	Probes dried and cleaned.
421	25 Feb 76	1818-2045	-37.8	-0.05	0.02	
423	27 Feb 76	1928-2046	-18.0	-0.23	0.01	
426	1 Mar 76	1840-1928	-24.8	-0.06	0.01	Probes cleared of snow.
428	3 Mar 76	1836-2157	-37.8	-0.03	0.02	
440	15 Mar 76	1903-2120	-24.2	-0.21	0.04	
440	15 Mar 76	2202-2320	-24.6	-0.11	0.02	After snow removed from probes.
447	22 Mar 76	1821-2110	-24.6	-0.14	0.05	
448	23 Mar 76	0100-0406	-25.5	-0.05	0.05	
452	27 Mar 76	1813-2100	-21.4	+0.21	0.08	
453	28 Mar 76	0051-0508	-21.3	+0.04	0.03	
461-462	5-6 Apr 76	1822-0054	-20.3	+0.17	0.13	
468	12 Apr 76	1838-2340	-15.9	-0.13	0.11	
475-476	19-20 Apr 76	2350-0400	-19.1	-0.31	0.08	
477	21 April 75	--end of data--				

SNOW BIRD

119	29 Apr 75	1825-1844	-24.4	-0.24	0.02	
133	13 May 75	1810-1829	-11.0	-0.31	0.01	
149	29 May 75	0018-0037	- 6.9	+0.39	0.07	
158	7 Jun 75	0900				T_9 sensor replaced; aspirator motor stopped.
158	7 Jun 75	2213-2249	+ 0.7	-0.28	0.06	

SNOW BIRD (continued)

AIDJEX Day	Date	Time	T_2 (°C)	T_9-T_2 (°C)	σ (°C)	Notes
159	8 Jun 75	0043-0104	+ 0.5	+0.04	0.03	
173	22 Jun 75	2125-2155	- 0.2	-0.19	0.01	
189	8 Jul 75	0630-0649	- 0.9	-0.10	0.01	
206	25 Jul 75	2332-2351	- 0.9	-0.03	0.01	
229	17-18 Aug 75	2140-0100	- 1.6	+0.03	0.31	
249	6 Sep 75	2012-2310	- 9.8	+0.38	0.05	
272	29 Sep 75	1932-2320	-11.8	+0.51	0.06	
279	6 Oct 75	1900-2050	- 9.6	+0.45	0.03	
286	13 Oct 75	1918-2338	-23.8	+0.75	0.08	
293	20 Oct 75	1830-2045	-13.0	+0.61	0.04	
307-308	3-4 Nov 75	1915-0040	-32.9	+0.07	0.02	
314	10 Nov 75	2020-2200	-33.8	+0.05	0.03	
317	13 Nov 75	0130-0400	-24.94	+0.04	0.01	Sensors dried in met hut.
321	17 Nov 75	1840-2200	-34.15	-0.05	0.02	
329-330	25-26 Nov 75	2350-0150	-28.97	-0.03	0.04	T_9 reading higher than T_2 by 0.02°C at end of test.
335	1 Dec 75	2030-2140	-35.58	+0.10	0.02	
336	2 Dec 75	2140-2330	-37.71	-0.003	0.04	T_9 reading higher than T_2 by 0.03°C at end of test.
342	8 Dec 75	1910-2100	-30.92	+0.04	0.02	
349	15 Dec 75	2120-2340	-35.77	+0.05	0.01	
357-358	22-23 Dec 75	2350-0150	-32.0	+0.02	0.02	Using values as computed.
363	29 Dec 75	2130-2350	-21.0	+0.03	0.03	
370	5 Jan 76	2010-2210	-26.0			
370-371	5-6 Jan 76	2330-0130	-28.0	+0.097	0.02	After defrosting.
378-379	13-14 Jan 76	2220-0200	-38.7	-0.12	0.02	
384-385	19-20 Jan 76	2040-0100	-41.2	-0.07	0.06	
391	26 Jan 76	1940-2120	-42.3	-0.04	0.02	
391-392	26-27 Jan 76	2340-0130	-41.8	-0.08	0.03	After thawing in hut.
399	3 Feb 76	1840-2240	-31.7	-0.019	(0.05)	Much scatter. T changed by 6°C during test.
405	9 Feb 76	1940-2320	-34.1	-0.034	(0.02)	
412	16 Feb 76	1900-2320	-35.3	+0.046	(0.03)	
419	23 Feb 76	1900-2220	-35.2	+0.18	(0.08)	
420	24 Feb 76	0100-0340	-36.3	+0.01	0.02	After warming in hut.

SNOW BIRD (continued)

AIDJEX Day	Date	Time	T_2 (°C)	T_9-T_2 (°C)	σ (°C)	Notes
426	1 Mar 76	1900-2300	-19.11	-0.01	0.03	
440-441	15-16 Mar 76	1820-0100	-23.77	+0.15	0.10	
445	20 Mar 76	0750-1200	-27.96	+0.42	0.05	
454	29 Mar 76	1940-2340	-28.21	-0.06	0.11	
463	7 Apr 76	1740-2100	-18.86	-0.03	0.07	Before ice bath.
464	8 Apr 76	0020-0200	-17.96	+0.12	0.06	Back outside.
469	13 Apr 76	1940-2340	-14.56	+0.003	0.09	
475	19 Apr 76	1820-2300	-19.71	-0.05	0.10	Before ice bath.
476	20 Apr 76	0045-0500	-18.77	+0.04	0.03	Back outside.
		-- end of data --				

APPENDIX 5

CONVERSION FROM DEW POINT TO FROST POINT

Below 0°C, dew point hygrometers measure the frost point temperatures rather than the dew point. The table below permits conversion from dew point to frost point; values from the EG&G equipment manual have been converted from degrees Fahrenheit to degrees Celsius. For a more accurate conversion, consult *Smithsonian Meteorological Tables*, page 371, Table 102.

(in degrees Celsius)

FP	DP	FP	DP	FP	DP
0.0	0.0	-16.7	-19.2	-33.9	-37.2
- 0.6	- 0.7	-17.8	-19.8	-34.4	-37.8
- 1.1	- 1.3	-18.3	-20.4	-35.0	-38.4
- 1.7	- 1.9	-18.9	-21.0	-35.6	-39.0
- 2.2	- 2.5	-19.4	-21.6	-36.1	-39.6
- 2.8	- 3.1	-20.0	-22.2	-36.7	-40.2
- 3.3	- 3.8	-21.6	-22.8	-37.2	-40.8
- 3.9	- 4.4	-21.1	-23.4	-37.8	-41.3
- 4.4	- 5.1	-21.7	-24.1	-38.3	-41.9
- 5.0	- 5.7	-22.2	-24.7	-38.9	-42.5
- 5.6	- 6.3	-22.8	-25.3	-39.4	-43.1
- 6.1	- 6.9	-23.3	-25.9	-40.0	-43.7
- 6.7	- 7.5	-23.9	-26.4	-40.6	-44.3
- 7.2	- 8.1	-24.4	-27.1	-41.1	-44.8
- 7.8	- 8.8	-25.0	-27.7	-41.7	-45.4
- 8.3	- 9.4	-25.6	-28.3	-42.2	-46.0
- 8.9	-10.0	-26.1	-28.9	-42.8	-46.6
- 9.4	-10.6	-26.7	-29.5	-43.3	-47.2
-10.0	-11.2	-27.2	-30.1	-43.9	-47.8
-10.6	-11.8	-27.8	-30.7	-44.4	-48.3
-11.1	-12.4	-28.3	-31.3	-45.0	-48.9
-11.7	-13.1	-28.9	-31.9	-45.6	-49.5
-12.2	-13.7	-29.4	-32.4	-46.1	-50.1
-12.8	-14.3	-30.0	-33.1	-46.7	-50.7
-13.3	-14.9	-30.6	-33.7	-47.2	-51.3
-13.9	-15.5	-31.1	-34.2		
-14.4	-16.2	-31.7	-34.8		
-15.0	-16.8	-32.2	-35.4		
-15.6	-17.4	-32.8	-36.0		
-16.1	-18.6	-33.3	-36.6		

COMPUTATION OF AIR STRESS AND SENSIBLE HEAT FLUXES FROM SURFACE LAYER PROFILE DATA, AIDJEX, 1975

by

Eric Leavitt, David Bell, Mel Clarke, Roger Andersen
AIDJEX

and

Clayton Paulson
Oregon State University
Corvallis, Oregon

ABSTRACT

During spring 1975, mean atmospheric surface layer profiles of wind and temperature were measured at the Big Bear camp of AIDJEX. Surface air stress and sensible heat flux have been computed from these profiles. The mean 10 m drag coefficient is 1.2×10^{-3}, but there is a significant variation of 40% in the coefficient which correlates with wind direction.

A primary objective of the AIDJEX experiment is development and testing of a model of ice dynamics in the Beaufort Sea [Coon et al., 1974]. An extensive program of meteorological observations [Paulson and Bell, 1975] was designed to provide estimates of the surface air stress required for driving the ice model. The air stress ($\vec{\tau}$) is generated from $\vec{\tau} = \rho_a C_D G^2 \vec{r}_\alpha$, where ρ_a is air density, C_D is a geostrophic drag coefficient, G is the geostrophic wind speed computed from the measured surface pressure field, and $\vec{r}_\alpha$ is a unit vector oriented at an angle α from the geostrophic wind direction.

Several direct measurements of air stress were made to provide data for estimating the magnitude of C_D and α. Included in this program were measurements of wind and temperature profiles in the lowest 20 m of the atmosphere at two sites--Big Bear (spring 1975) and Caribou (spring 1976). This paper describes the results of an analysis of the Big Bear profiles to obtain stress and sensible heat fluxes.

The Experiment

The profile tower, 22 m high, was erected at Big Bear in April 1975 and observations were continued until July. A plan of the camp giving the tower location is shown in Figure 1. True wind directions between 270° and 50° were not used for flux analysis because the camp was then upwind of the tower. (Wind direction is the direction from which the wind is blowing.) The camp and tower were located on a floe that was fairly smooth, but on aerial photographs it appeared rougher (more hummocky) in the 120°-270° sector than in the 50°-100° sector. The nearest hummocks greater than 0.5 m high were about 70-100 m away from the tower in the 240° direction.

Sensors were mounted initially at five levels for both wind speed (1.66, 2.97, 5.99, 12.09, and 21.48 m) and temperature (0.9, 2.9, 6.7, 12.35, and 20.0 m). After run 23 an extra wind level at 0.72 m and an extra temperature level at 0.48 m were added, and the 0.9 m temperature sensor was moved to 1.68 m. Wind direction was measured at three levels: 2.59, 11.89, and 20.85 m. The heights of the sensors varied in time as ablation or drifting occurred, with the net change from 20 April to 23 July being -0.52 m. These heights were measured from a visual average of the snow-ice cover around the immediate base of the tower. Level traverses by Banke et al. [1976] indicate that the mean level typically varied less than 0.05 m in the 50 m around the tower.

The sensors used were 3-cup anemomenters, aspirated platinum resistance thermometers, and wind vanes, all manufactured by Climate, Inc. (Identical sensors were used on the 10 m tower located at each camp [Paulson and Bell, 1975]; a detailed description of sensor performance and calibrations are given in a paper by Clarke, Leavitt, and Bell in this Bulletin.) Although the manufacturer specified an absolute temperature measurement error of ±0.05°C, the errors were at least ±0.1°C, large enough to cause an error in the sign of the sensible heat flux during nearly neutral conditions. Attempts to decrease this error by side-by-side comparisons were not successful, as differences between sensors were random. We have concluded that this was the variable effect of radiation due to variations in the sensor aspiration rate.

Cup anemometer errors are difficult to give estimates for. One side-by-side comparison of the profile tower sensors indicated agreement within

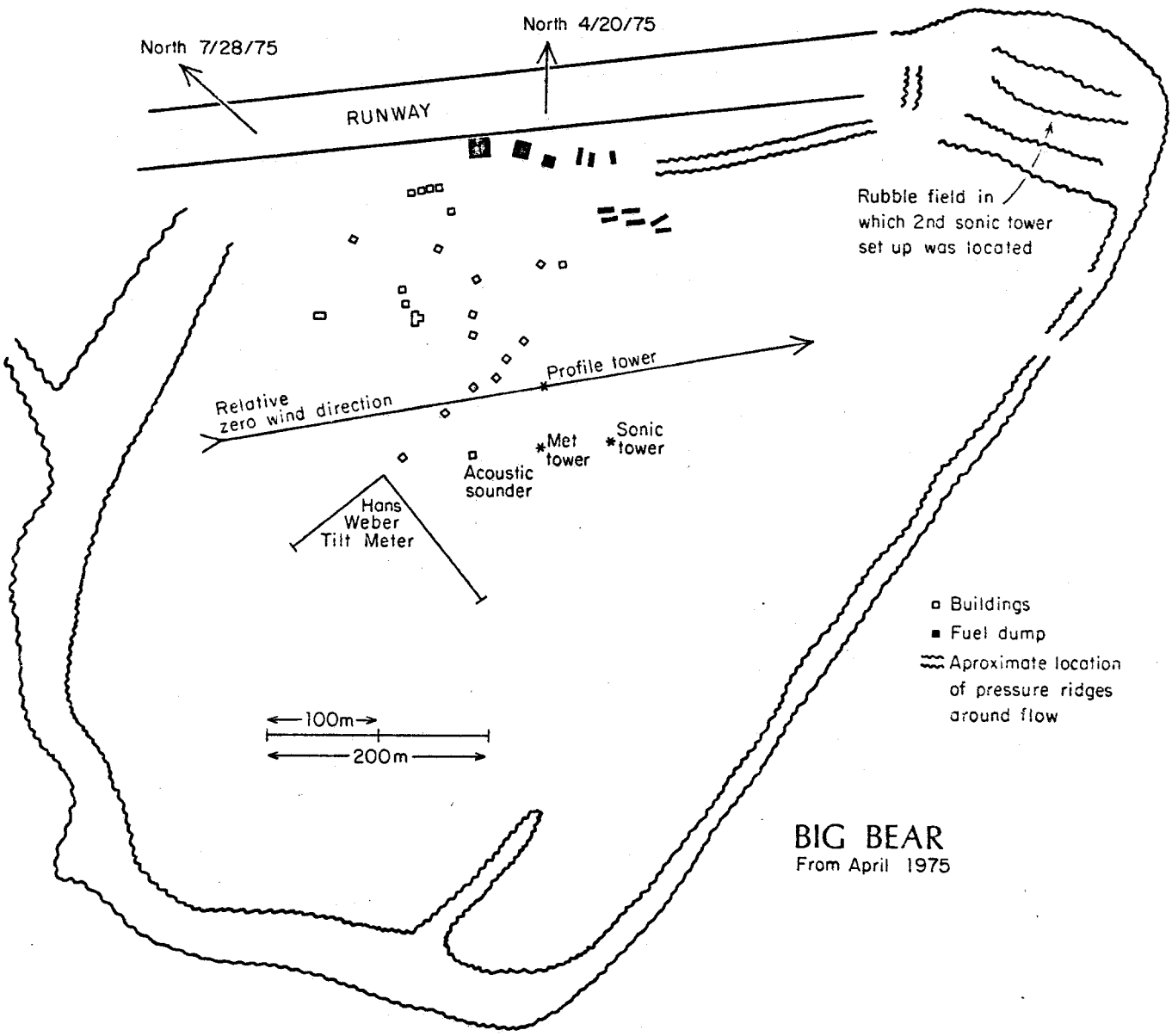

Fig. 1. Map of camp Big Bear in April 1975. The locations of the three towers are indicated, as well as the relative wind direction zero line.

specifications for the six profile-tower anemometers (the larger of 1% and 0.7 m sec^{-1}). Riming was at times a definite problem; fortunately its occurrence was usually manifest in the performance of the anemometers, and riming periods can be detected in the mean profiles.

The wind direction sensors behaved very well; riming on those sensors did not affect the measurements as long as the wind speed exceeded 3 m sec^{-1}. The zero direction reference of the 2 m sensor was fixed relative to that of the 10 m met tower, which was located about 100 m away from the profile tower. Then the three profile tower sensors were matched by assuming a mean zero wind direction change during high winds. During the profile-measuring period the wind direction, as determined by sensors on the two towers, agreed within ±2°.

Data from the sensors were recorded digitally using a mini-computer (Data General Nova 2/10) with a 12-bit digitizer. The wind sensors were sampled at 5, 10, or 20 Hz, depending on the wind speed, and the temperature sensors were sampled at about 1 Hz.

Flux Computation

The semi-empirical theory used for computation of stress and heat fluxes is essentially that described by Paulson [1970] and detailed by Leavitt [1975]. The mean vertical gradients of horizontal wind and temperature can be written as

$$\partial U/\partial z = u_* \, \Phi_M(z/L)/kz \qquad (1)$$

$$\partial \Theta/\partial z = \theta_* \, \Phi_H(z/L)/kz \qquad (2)$$

Here k is von Karman's constant, u_* [$= (-\tau/\rho)^{0.5}$] is the friction velocity, θ_* [$= -\overline{w\theta}/u_*$] is a temperature scale, $\overline{w\theta}$ [$= H_0/\rho \, C_p$] is the vertical flux of temperature; and

$$z/L = -kz \, \overline{w\theta} \, u_*^{-3} \, g/T \qquad (3)$$

is a nondimensional height, where L is the Monin-Obukhov length.

For the profile analysis we chose

$$\Phi_M = 1 + \gamma_1 \, z/L \qquad z/L > 0 \qquad (4)$$
$$\Phi_H = \alpha + \gamma_1 \, z/L$$

$$\Phi_M = (1 - \gamma_2 \, z/L)^{-0.25} \qquad z/L \leq 0 \qquad (5)$$
$$\Phi_H = \alpha(1 - \gamma_3 \, z/L)^{-0.5}$$

Equation (4) is the log-linear law. The value of γ_1 has been found equal to 5.2 by Webb [1970], 4.7 by Businger et al. [1971], and 7 by Paulson [1970]. A value $\alpha = 0.75$ was suggested by Businger et al. Equation (5) was suggested independently by Businger [1966] and Dyer (unpublished). Values of the constant γ_2 are 16 according to Paulson [1970] and 15 according to Businger et al. [1971]. Estimates of γ_3 range between 16 [Paulson, 1970] and 9 [Businger et al., 1971]. Businger et al. also determined that k is equal to 0.35 rather than the commonly accepted 0.4.

Equations (1) and (2) can be integrated:

$$U = u_*/k \; (\log z/z_0 - \psi_1) \qquad (6)$$

$$\Theta - \Theta_0 = \alpha\theta_*/k \; (\log z/z_0 - \psi_2) \qquad (7)$$

Here z_0 is the roughness length. The forms of ψ_1, ψ_2 appropriate to (4) and (5) are given by Paulson [1970]. Using the method of least squares, u_* is obtained from the slope and z_0 from the intercept of a straight line fitted to the observations of U versus $\log z - \psi_1$. A similar procedure for the temperature profile yields an estimate of Θ_*. Differences between the fitted curves and the observations provide a measure of how well the theory fits the observations for different choices of γ_1, γ_2 and γ_3; but k and α must be assumed known or be evaluated by comparison with independent flux estimates.

A drag coefficient can be defined as

$$C_{10} = u_*^2/U_{10}^2$$

where the 10 refers to 10 m height. However, this C_{10} is dependent on stability, and an alternative definition of C_{10} which is independent of stability will be used in this paper:

$$C_{10} = (k/\log z/z_0)^2$$

The computation procedure is to first determine the Richardson number, Ri, from a least-squares fit of U and Θ versus log z:

$$\mathrm{Ri} = \partial\Theta/\partial z \cdot g/T \cdot (\partial U/\partial z)^{-2} \tag{8}$$

For logarithmically varying profiles, Ri is calculated at height $z_r = (z_u z_\ell)^{\frac{1}{2}}$ where z_u is the upper height and z_ℓ the lower. Substituting from (1), (2), and (3), we can rewrite (8) as

$$z_r/L = \mathrm{Ri}\ \Phi_M^2(z_r/L)/\Phi_H(z_r/L) \tag{9}$$

As a first approximation, let z_r/L = Ri on the right-hand side of (9); then

$$L = z_r\ \Phi_H(\mathrm{Ri})/\mathrm{Ri}\ \Phi_M^2(\mathrm{Ri}) \tag{10}$$

This value of L is used to compute ψ_1 and ψ_2 values, and u_* and θ_* are calculated from a least-squares fit using (6) and (7). Corrected values of U and θ are also computed from the least-squares fit, and these corrected values are then used to compute a new value of Ri. This iteration continues (the original U and Θ data are used in the computation of u_* and Θ_*) until the change in u_* between iterations is small.

The values selected for the constants in the flux equations were $\gamma_1 = 4.5$, $\alpha = 1.0$, $\alpha_2 = \alpha_3 = 16.0$, and $k = 0.4$.

Von Karman's constant was left as 0.4 although there is dispute about its true value [see Businger et al., 1971]. The values of γ_2 and γ_3 are from Paulson [1970]. Initially, γ_1 was set equal to 7.0 [also from Paulson], but this value made the stable drag coefficients appear smaller than the near-neutral values; therefore, γ_1 was set equal to 4.5, which is close to the values suggested by Webb [1970] and Businger, et al. Substituting these constants in equation (9) gives

$$z_r/L = \mathrm{Ri},\ \mathrm{Ri} < 0$$

$$z_r/L = \mathrm{Ri}/(1 - \gamma_1 \mathrm{Ri}),\ \mathrm{Ri} > 0$$

Air density (ρ) was set at 1.35 kg m^{-3} and specific heat of air (C_p) equalled 1012 J $kg^{-1}K^{-1}$.

Profiles were rejected for analysis if the camp was upwind of the tower, if winds were less than 3.5 m sec^{-1}, or if the plotted profiles showed evidence of severe riming or other significant deviation from logarithmic behavior. During analysis, profiles for which $\mathrm{Ri} \geq 0.19$ were also rejected since for these cases eq. (9) cannot be used to predict z_r/L. In some cases the computed stress was brought closer to the observed stress by deleting the upper two wind speed levels from the profiles, a course chosen because of riming on the upper anemometers or because of the possibility that the assumed profile shapes were incorrect. As mentioned earlier, the temperature sensors showed random errors on the order of $\pm 0.1°C$. At first, fluxes were computed using a linear fit of all temperature sensors, but in the final computations the sensors that deviated the most from this fit were deleted from the profiles. This is a somewhat subjective approach, but we were trying to produce results that were consistent with the observed wind profile and with the temperature gradient measured on a nearby 10 m met tower. If it was not possible to decide which temperature sensors should be deleted, they were all used in the flux computation.

Results

The results of the flux analysis are given in Table 1. The usual averaging period was one hour, which is short enough to be considered as pseudo-stationary

TABLE 1

FLUX COMPUTATIONS FROM MEAN PROFILE, 23 APRIL - 28 JULY 1975

RUN	JULIAN DAY	DATE MN/DAY	TIME START GMT	RUN LENGTH MIN	USTAR M/S	HEAT FLUX W/M2	Z/L	U(10M) M/S	W/D TRUE DEG	W/D REL DEG	AIR TEMP C	C10 X1000	ZO CM
4A	113.39	4/23	922	45	.082	-5.6	2.00	3.9	261	363	-27.6	1.13	.007
4C	113.45	4/23	1052	44	.072	-4.4	2.37	3.8	257	359	-28.3	.92	.002
4D	113.48	4/23	1137	44	.130	-11.8	.97	4.4	254	356	-28.2	1.58	.043
4E	113.51	4/23	1221	45	.103	-7.2	1.20	4.2	255	357	-28.0	1.12	.007
4F	113.55	4/23	1306	45	.101	-6.3	1.10	4.1	257	359	-27.9	1.08	.005
4G	113.58	4/23	1351	44	.109	-6.6	.90	4.2	254	356	-27.6	1.06	.005
4H	113.61	4/23	1436	44	.125	-6.3	.52	4.2	256	358	-27.0	1.19	.009
5A	113.75	4/23	1801	27	.159	5.8	-.13	3.8	250	352	-24.5	1.63	.049
5B	113.77	4/23	1828	27	.163	2.5	-.06	4.1	248	350	-24.3	1.55	.038
5C	113.84	4/23	2007	63	.138	-.2	.007	3.7	248	349	-22.1	1.39	.022
9A	117.97	4/27	2316	31	.156	34.3	-1.11	3.5	237	338	-18.5	1.53	.036
12A	119.86	4/29	2044	62	.253	9.4	-.07	6.5	205	306	-19.8	1.48	.030
12B	119.91	4/29	2146	61	.255	5.5	-.04	6.8	204	305	-19.0	1.37	.021
12C	119.97	4/29	2310	82	.315	10.1	-.04	8.3	201	303	-18.1	1.42	.024
13A	120.03	4/30	43	82	.326	3.9	-.01	8.4	201	302	-17.4	1.49	.031
14A	120.16	4/30	354	69	.363	-13.8	.03	9.1	194	295	-16.4	1.63	.050
14B	120.21	4/30	503	68	.402	-9.8	.02	9.8	196	297	-16.1	1.70	.061
14C	120.27	4/30	624	102	.408	-8.3	.01	10.5	196	297	-15.8	1.53	.037
15A	120.35	4/30	820	82	.418	-9.4	.01	10.5	201	302	-15.9	1.59	.044
15B	120.40	4/30	942	82	.421	-9.4	.01	10.5	210	311	-16.2	1.62	.049
16A	120.84	4/30	2004	68	.303	9.6	-.04	8.2	219	319	-13.0	1.35	.019
17A	120.90	4/30	2131	59	.287	6.6	-.03	7.9	224	324	-12.0	1.28	.014
17B	120.94	4/30	2230	60	.270	5.7	-.03	7.6	229	330	-11.6	1.22	.011
19A	122.91	5/ 2	2155	59	.169	21.8	-.55	4.7	53	152	-18.6	1.13	.007
19B	122.95	5/ 2	2254	60	.165	15.0	-.41	4.6	53	152	-18.2	1.12	.007
19C	123.00	5/ 2	2354	62	.155	6.3	-.20	4.6	50	150	-17.8	1.04	.004
19D	123.04	5/ 3	56	45	.169	2.2	-.05	4.9	53	151	-17.8	1.16	.008
20A	123.95	5/ 3	2249	60	.192	4.7	-.08	5.1	45	142	-14.9	1.37	.020
20B	123.99	5/ 3	2349	60	.202	3.1	-.04	5.1	44	142	-14.9	1.52	.035
20C	124.03	5/ 4	49	59	.190	-1.0	.02	5.1	46	143	-15.0	1.40	.023
20D	124.07	5/ 4	148	45	.183	-3.1	.05	4.8	52	149	-15.0	1.52	.034
21A	124.12	5/ 4	257	60	.146	-5.2	.21	5.0	48	144	-15.4	.97	.003
21B	124.16	5/ 4	357	60	.161	-9.0	.28	4.9	45	142	-16.3	1.31	.016
21C	124.21	5/ 4	457	59	.152	-10.7	.41	5.0	50	147	-17.1	1.22	.011
21D	124.25	5/ 4	556	60	.124	-9.6	.71	4.8	44	142	-18.2	1.05	.004
21E	124.29	5/ 4	656	60	.134	-12.3	.73	4.8	40	138	-19.1	1.26	.013
21F	124.33	5/ 4	756	60	.143	-14.2	.70	5.2	44	141	-19.6	1.14	.007
21G	124.37	5/ 4	856	89	.162	-16.6	.55	5.1	51	148	-20.2	1.47	.030
22A	124.46	5/ 4	1058	60	.119	-9.6	.84	4.6	56	153	-21.2	1.08	.005
22B	124.50	5/ 4	1158	59	.102	-7.6	1.06	4.3	51	148	-21.5	1.03	.004
22C	124.54	5/ 4	1257	60	.132	-10.0	.62	4.5	50	147	-21.4	1.33	.018
22D	124.58	5/ 4	1357	60	.147	-10.3	.45	4.7	49	146	-20.9	1.30	.015
22E	124.62	5/ 4	1457	59	.174	-8.4	.20	5.3	50	147	-20.2	1.26	.013
22F	124.66	5/ 4	1556	60	.170	-6.2	.16	5.3	57	154	-19.3	1.15	.007
22G	124.71	5/ 4	1656	60	.163	-2.1	.06	5.4	60	157	-18.5	.94	.002
22H	124.75	5/ 4	1756	75	.176	4.2	-.08	5.4	64	161	-17.5	1.00	.003
23A	125.09	5/ 5	216	60	.278	15.3	-.07	7.6	50	147	-12.2	1.27	.013
23B	125.14	5/ 5	316	59	.284	3.1	-.01	8.1	53	150	-11.8	1.22	.011
23C	125.18	5/ 5	415	90	.289	3.9	-.02	8.1	56	153	-11.5	1.24	.012
24A	125.35	5/ 5	820	61	.288	4.2	-.02	7.9	53	151	-11.8	1.31	.016
24B	125.39	5/ 5	921	61	.274	3.7	-.02	7.7	56	153	-11.9	1.25	.012

TABLE 1 (continued)

RUN	JULIAN DAY	DATE MN/DAY	TIME START GMT	RUN LENGTH MIN	USTAR M/S	HEAT FLUX W/M2	Z/L	U(10M) M/S	W/D TRUE DEG	W/D REL DEG	AIR TEMP C	C10 X1000	ZO CM
24C	125.43	5/ 5	1023	61	.262	.4	-.003	7.4	55	152	-11.7	1.26	.013
24D	125.47	5/ 5	1124	61	.243	-3.6	.03	7.4	47	144	-11.1	1.11	.006
24E	125.52	5/ 5	1226	61	.260	-5.1	.03	7.8	50	148	-10.5	1.14	.007
24F	125.56	5/ 5	1327	61	.276	-2.8	.01	8.0	57	154	-10.6	1.20	.010
24G	125.60	5/ 5	1429	61	.275	-1.2	.006	8.0	56	153	-10.5	1.19	.009
24H	125.65	5/ 5	1530	61	.262	-1.0	.006	7.9	59	157	-9.9	1.09	.006
26A	126.34	5/ 6	810	60	.230	1.3	-.01	7.1	68	166	-6.9	1.06	.004
26B	126.38	5/ 6	910	60	.219	-1.0	.010	7.2	60	158	-7.6	.92	.002
26C	126.42	5/ 6	1010	60	.196	-1.6	.02	6.7	65	163	-8.0	.86	.001
26D	126.47	5/ 6	1110	59	.216	-1.9	.02	7.1	67	165	-8.1	.93	.002
26E	126.51	5/ 6	1209	60	.233	-1.5	.01	7.3	74	172	-8.5	1.01	.004
26F	126.55	5/ 6	1309	60	.235	2.0	-.02	7.6	64	162	-9.9	.95	.002
26G	126.59	5/ 6	1409	59	.220	1.5	-.02	6.9	73	171	-10.4	1.02	.004
26H	126.63	5/ 6	1508	60	.218	.7	-.007	6.5	79	177	-10.1	1.11	.006
27A	126.77	5/ 6	1823	61	.242	12.5	-.09	6.6	84	183	-9.0	1.27	.013
27B	126.82	5/ 6	1942	61	.232	4.0	-.03	6.7	85	184	-8.4	1.18	.009
27C	126.88	5/ 6	2110	48	.234	8.2	-.07	6.4	91	190	-7.6	1.29	.015
28A	127.06	5/ 7	127	64	.203	5.0	-.06	5.7	88	186	-6.0	1.23	.011
28B	127.10	5/ 7	231	55	.202	3.9	-.05	6.0	88	186	-5.8	1.12	.006
28C	127.14	5/ 7	326	64	.193	2.2	-.03	5.7	88	186	-5.7	1.14	.007
28D	127.19	5/ 7	430	64	.166	.4	-.009	4.8	87	186	-5.4	1.17	.008
29A	127.27	5/ 7	627	64	.204	-1.6	.02	6.0	84	183	-5.7	1.18	.009
29B	127.38	5/ 7	902	64	.182	-.4	.007	5.1	92	191	-7.1	1.27	.013
29C	127.42	5/ 7	1006	64	.157	.2	-.005	4.5	87	186	-7.7	1.24	.012
29D	127.47	5/ 7	1110	64	.135	-.7	.03	4.0	81	179	-9.2	1.18	.009
31A	137.92	5/17	2203	60	.241	18.5	-.14	7.3	77	171	-12.1	1.03	.004
31B	137.96	5/17	2303	59	.257	18.2	-.11	7.7	71	165	-11.9	1.06	.005
31C	138.00	5/18	2	60	.260	14.0	-.08	7.7	77	170	-12.2	1.09	.005
31D	138.04	5/18	102	60	.242	8.2	-.06	7.3	78	172	-12.0	1.06	.005
32A	138.79	5/18	1900	59	.256	25.2	-.16	7.3	54	147	-14.5	1.15	.008
32B	138.83	5/18	1959	60	.245	29.5	-.21	7.0	59	152	-14.0	1.11	.006
32C	138.87	5/18	2059	60	.274	27.9	-.14	7.8	72	166	-13.4	1.15	.008
32D	138.92	5/18	2159	60	.218	25.7	-.25	6.6	64	157	-12.6	1.01	.004
34D	141.57	5/21	1348	59	.171	4.6	-.10	3.9	164	256	-10.8	1.80	.081
34E	141.62	5/21	1447	60	.171	4.4	-.10	4.1	165	257	-11.0	1.64	.052
34F	141.66	5/21	1547	60	.175	6.3	-.13	4.1	169	260	-10.8	1.69	.060
35A	141.90	5/21	2134	59	.169	13.6	-.32	4.0	156	247	-10.2	1.59	.044
35B	141.94	5/21	2233	60	.172	10.1	-.22	4.3	164	255	-9.8	1.44	.027
35C	141.98	5/21	2333	60	.165	8.2	-.21	4.0	158	250	-9.9	1.57	.041
35D	142.02	5/22	33	60	.150	4.5	-.15	3.9	175	267	-9.4	1.41	.023
36A	145.73	5/25	1727	59	.191	10.7	-.17	4.8	118	208	-11.7	1.47	.029
36B	145.77	5/25	1826	60	.176	11.7	-.24	4.4	107	197	-11.3	1.46	.028
36C	145.81	5/25	1926	60	.205	12.3	-.16	5.2	117	206	-11.1	1.44	.027
36D	145.85	5/25	2026	60	.204	16.7	-.22	5.2	113	202	-10.9	1.42	.024
37A	145.95	5/25	2253	90	.226	25.3	-.23	5.8	89	179	-11.1	1.36	.020
40A	147.22	5/27	510	60	.212	8.5	-.09	6.4	73	161	-9.9	1.07	.005
40B	147.26	5/27	610	60	.222	6.5	-.06	6.9	78	166	-10.1	1.01	.004
40C	147.30	5/27	710	59	.219	5.0	-.05	6.6	77	165	-10.4	1.06	.005
40D	147.34	5/27	809	60	.225	5.5	-.05	6.9	75	163	-10.8	1.05	.004
41A	147.41	5/27	945	60	.210	3.4	-.04	6.4	74	162	-11.2	1.05	.004
41B	147.45	5/27	1045	59	.190	3.2	-.05	6.0	76	165	-11.1	.98	.003

TABLE 1 (continued)

RUN	JULIAN DAY	DATE MN/DAY	TIME START GMT	RUN LENGTH MIN	USTAR M/S	HEAT FLUX W/M2	Z/L	U(10M) M/S	W/D TRUE DEG	W/D REL DEG	AIR TEMP C	C1C X1000	ZC CM
41C	147.49	5/27	1144	60	.218	3.3	-.03	6.6	77	165	-11.4	1.07	.005
41D	147.53	5/27	1244	60	.215	5.4	-.06	6.6	71	160	-11.9	1.02	.004
41E	147.57	5/27	1344	60	.236	6.8	-.05	7.0	81	169	-12.2	1.10	.006
41F	147.61	5/27	1444	59	.254	7.9	-.05	7.8	77	165	-12.6	1.05	.004
41G	147.65	5/27	1543	60	.267	9.9	-.05	8.0	76	164	-12.3	1.09	.006
41H	147.70	5/27	1643	90	.243	12.7	-.09	7.4	75	164	-12.0	1.05	.004
42A	147.92	5/27	2201	60	.265	25.2	-.14	7.6	89	177	-11.1	1.13	.007
42B	147.96	5/27	2301	60	.260	24.2	-.14	7.5	89	178	-11.0	1.14	.007
42C	148.00	5/28	1	59	.265	17.6	-.10	7.9	80	169	-11.3	1.08	.005
42D	148.04	5/28	100	60	.255	17.5	-.11	7.7	88	176	-11.2	1.05	.004
43A	148.09	5/28	212	60	.287	14.9	-.07	8.2	94	183	-11.7	1.17	.008
43B	148.14	5/28	324	59	.269	4.8	-.03	7.9	94	182	-12.1	1.14	.007
43C	148.18	5/28	423	60	.236	1.0	-.008	7.3	95	183	-12.3	1.04	.004
43D	148.22	5/28	523	90	.242	-1.3	.010	7.5	91	180	-12.6	1.04	.004
45A	148.49	5/28	1141	60	.244	2.2	-.02	7.6	78	166	-13.5	1.01	.004
45B	148.53	5/28	1241	59	.246	3.2	-.02	7.4	84	173	-13.1	1.10	.006
45C	148.57	5/28	1340	60	.257	8.1	-.05	7.6	84	172	-12.5	1.12	.006
45D	148.61	5/28	1440	60	.252	7.0	-.05	7.5	85	174	-11.9	1.10	.006
45E	148.65	5/28	1540	60	.250	6.7	-.05	7.5	85	174	-11.2	1.10	.006
45F	148.69	5/28	1640	59	.280	10.5	-.05	8.1	86	175	-10.5	1.16	.008
45G	148.74	5/28	1739	60	.286	17.6	-.08	8.0	89	178	-9.9	1.23	.011
45H	148.78	5/28	1839	90	.292	11.5	-.05	8.4	91	180	-9.4	1.18	.009
46A	148.85	5/28	2026	59	.290	9.0	-.04	8.1	102	191	-8.8	1.25	.012
46B	148.89	5/28	2125	60	.276	9.7	-.05	7.9	104	194	-8.3	1.20	.010
46C	148.93	5/28	2225	60	.285	11.6	-.05	8.0	104	193	-7.9	1.23	.011
46D	148.98	5/28	2325	60	.277	11.0	-.05	7.8	104	193	-7.5	1.22	.011
47A	149.06	5/29	120	60	.265	8.7	-.05	7.5	105	194	-7.0	1.22	.011
47B	149.14	5/29	315	85	.237	4.0	-.03	7.0	105	194	-6.1	1.14	.007
47C	149.19	5/29	440	90	.241	1.2	-.009	7.2	103	193	-5.5	1.11	.006
48A	149.35	5/29	822	60	.217	-3.2	.03	6.8	106	195	-5.4	1.06	.005
48B	149.39	5/29	922	59	.188	-7.	.13	6.4	108	198	-5.7	.93	.002
48C	149.43	5/29	1021	60	.166	-4.1	.10	5.6	106	196	-6.0	.93	.002
48D	149.47	5/29	1121	60	.197	.3	-.004	6.2	98	188	-6.0	1.01	.004
48E	149.51	5/29	1221	60	.183	-2.7	.05	6.2	96	185	-6.6	.91	.002
48F	149.56	5/29	1321	59	.205	.9	-.01	6.2	97	187	-6.8	1.09	.005
48G	149.60	5/29	1420	60	.190	-2.3	.04	5.9	99	189	-7.1	1.08	.005
48H	149.64	5/29	1520	90	.219	.1	-.001	6.6	97	187	-7.0	1.11	.006
49A	149.73	5/29	1732	70	.234	6.9	-.06	6.8	96	186	-6.5	1.13	.007
49B	149.78	5/29	1842	60	.250	7.9	-.06	7.4	96	185	-6.3	1.11	.006
49C	149.82	5/29	1942	60	.234	7.5	-.06	7.1	96	186	-5.9	1.04	.004
49D	149.86	5/29	2042	60	.226	4.3	-.04	7.4	94	184	-5.6	.92	.002
50A	150.42	5/30	1003	60	.137	-7.3	.36	5.2	95	184	-10.0	.86	.001
50B	150.46	5/30	1103	60	.151	-6.8	.24	5.7	93	182	-10.2	.81	.001
50C	150.50	5/30	1203	59	.167	-6.3	.11	6.3	94	183	-10.0	.94	.002
50D	150.54	5/30	1302	60	.194	-6.1	.10	6.2	98	187	-9.8	1.03	.004
50E	150.58	5/30	1402	60	.194	-2.2	.03	6.0	99	188	-9.5	1.08	.005
50F	150.63	5/30	1502	59	.175	-.1	.001	5.3	98	186	-9.1	1.07	.005
50G	150.67	5/30	1601	60	.166	4.0	-.09	5.2	97	185	-8.8	.99	.003
50H	150.71	5/30	1701	90	.169	6.9	-.15	5.2	97	185	-8.1	.98	.003
51A	150.83	5/30	1955	90	.165	9.8	-.22	5.0	94	182	-6.3	1.01	.003
58A	167.78	6/16	1840	60	.130	11.9	-.54	4.2	90	177	-3.6	.84	.001

TABLE 1 (continued)

RUN	JULIAN DAY	DATE MN/DAY	TIME START GMT	RUN LENGTH MIN	USTAR M/S	HEAT FLUX W/M2	Z/L	U(10M) M/S	W/D TRUE DEG	W/D REL DEG	AIR TEMP C	C10 X1000	ZO CM
58B	167.82	6/16	1940	59	.140	13.4	-.49	4.5	83	170	-3.7	.85	.001
58C	167.86	6/16	2039	60	.161	12.3	-.29	5.1	91	178	-3.3	.90	.002
58D	167.90	6/16	2139	60	.155	11.1	-.30	5.0	93	179	-2.8	.87	.001
59A	167.97	6/16	2315	59	.178	4.2	-.08	5.8	86	173	-2.2	.89	.002
59B	168.01	6/17	14	60	.206	5.7	-.07	6.5	91	177	-2.0	.96	.003
59C	168.06	6/17	131	60	.227	3.6	-.03	7.2	95	181	-1.8	.99	.003
59D	168.10	6/17	231	60	.252	4.9	-.03	7.8	97	183	-1.9	1.02	.004
60A	168.27	6/17	626	60	.239	2.1	-.02	7.5	98	184	-1.0	1.00	.003
60B	168.31	6/17	726	60	.237	-2.2	.02	7.7	94	180	-1.2	.97	.003
60C	168.35	6/17	826	59	.232	.1	-.001	7.4	93	179	-1.2	.98	.003
60D	168.39	6/17	925	60	.247	.2	-.001	7.7	94	180	-1.2	1.02	.004
63A	172.69	6/21	1637	60	.201	15.7	-.21	5.4	110	194	-2.8	1.28	.014
63B	172.73	6/21	1737	60	.215	9.8	-.11	5.9	115	199	-2.2	1.26	.013
63C	172.78	6/21	1837	60	.213	4.5	-.05	6.4	116	200	-2.1	1.07	.005
63D	172.82	6/21	1937	59	.230	5.9	-.05	7.0	109	192	-1.8	1.04	.004
64A	173.02	6/22	34	60	.296	5.1	-.02	8.1	123	206	-1.1	1.31	.016
64B	173.07	6/22	134	60	.297	6.4	-.03	7.8	124	208	-1.0	1.43	.025
64C	173.11	6/22	234	59	.273	3.0	-.02	7.2	130	213	-.9	1.43	.025
64D	173.15	6/22	333	60	.261	2.3	-.01	6.8	132	216	-.8	1.48	.031
65A	174.26	6/23	621	59	.187	9.5	-.14	5.7	93	176	-1.3	1.04	.004
65B	174.31	6/23	720	60	.179	7.5	-.13	5.7	84	167	-1.4	.92	.002
65C	174.35	6/23	820	60	.169	5.7	-.12	5.7	78	161	-1.4	.85	.001
65D	174.39	6/23	920	60	.187	4.1	-.06	6.3	71	154	-1.4	.86	.001
66C	176.46	6/25	1059	60	.150	1.4	-.04	4.2	224	311	-.2	1.23	.011
66D	176.50	6/25	1159	59	.161	1.4	-.03	4.6	234	322	-.1	1.17	.008
66E	176.54	6/25	1258	60	.156	1.6	-.04	4.9	237	324	-.1	.99	.003
67A	176.89	6/25	2115	60	.220	4.9	-.05	5.9	226	315	.0	1.33	.017
67B	176.93	6/25	2215	60	.214	4.3	-.05	5.8	229	317	-.1	1.34	.018
67C	176.97	6/25	2315	60	.199	5.4	-.07	5.5	233	319	-.3	1.23	.011
67D	177.01	6/26	15	59	.170	5.7	-.13	4.6	231	319	-.1	1.28	.014
68A	178.05	6/27	119	60	.210	.4	-.005	5.7	82	169	.1	1.36	.020
68B	178.10	6/27	219	90	.233	-.4	.003	6.2	78	165	.1	1.41	.024
69A	179.29	6/28	651	60	.245	5.6	-.04	6.2	205	289	-.2	1.50	.033
69B	179.33	6/28	751	60	.257	6.6	-.04	6.1	206	291	-.5	1.71	.062
69C	179.37	6/28	851	89	.196	3.2	-.05	5.1	194	279	-.5	1.43	.026
70D	180.91	6/29	2149	59	.296	31.6	-.13	7.0	171	253	-.2	1.65	.053
71A	181.70	6/30	1655	59	.302	-4.9	.02	8.0	159	240	.5	1.45	.028
71B	181.75	6/30	1754	60	.280	-2.1	.010	7.3	163	245	.5	1.47	.030
71C	181.79	6/30	1854	90	.275	.7	-.003	6.8	165	247	.5	1.63	.050
72A	183.99	7/ 2	2344	60	.291	9.6	-.04	7.0	215	298	.2	1.67	.056
72B	184.03	7/ 3	44	59	.266	5.4	-.03	6.4	211	293	.3	1.70	.062
72C	184.07	7/ 3	143	60	.302	3.9	-.01	7.1	209	291	.3	1.77	.074
75A	187.03	7/ 6	39	60	.415	-.7	.001	10.6	263	343	.6	1.55	.038
75B	187.07	7/ 6	139	60	.452	.2	-.000	11.0	259	338	.5	1.68	.058
75C	187.11	7/ 6	239	59	.425	1.5	-.002	10.8	260	339	.3	1.54	.037
75D	187.15	7/ 6	338	60	.406	1.5	-.002	10.1	264	343	.2	1.60	.045
78D	208.96	7/27	2256	60	.201	7.2	-.10	5.1	280	334	.1	1.48	.030
78E	209.00	7/27	2356	59	.202	7.5	-.10	5.2	279	334	.0	1.42	.025
78F	209.04	7/28	55	60	.208	6.8	-.08	5.3	277	330	.1	1.50	.032
78G	209.08	7/28	155	60	.188	.1	-.002	5.2	280	333	-.0	1.29	.014
78H	209.12	7/28	255	90	.192	.8	-.01	4.9	272	325	-.1	1.56	.040

while it can still be expected to contain most of the momentum-transferring eddies. Sensible heat fluxes are generally very small (10 w m^{-2} = 1 mw cm^{-2} = 20.7 cal cm^{-2} day^{-1}); and considering possible errors in temperature measurements, an approximate error is ±3 w m^{-2}. Based on the comparison with data from Banke et al. [1976] given below and the changes in stress when different profile levels are used in the flux computation, the error in the computed stresses is estimated to be ±15%. The mean value of C_{10} is 1.2 ± 0.26 × 10^{-3}; but, as shown in Figure 2, C_{10} exhibits a significant variation with relative wind direction. Relative wind direction is used because the camp azimuth rotated about 50° during the experiment. In the following discussion, D152 refers to profiles with wind direction 152°-185°, D185 to profiles with wind direction 185°-220° and D220 to profiles with wind direction 220°+. Where L is greater than 100 m, 1000 $\overline{C}_{10}$ is 1.07 ± 0.14 for D152, 1.18 ± 0.16 for

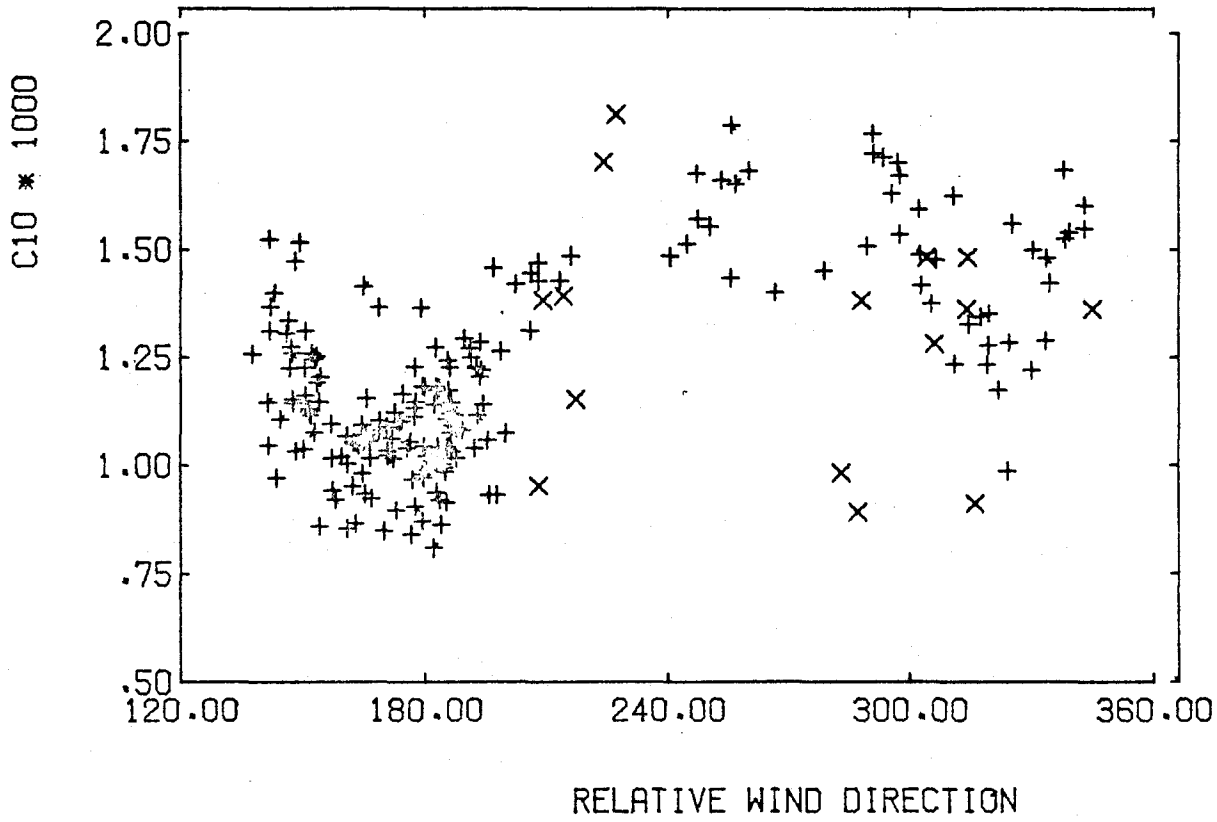

Fig. 2. Variation of C_{10} with relative wind direction: + is profile data; X is sonic data from Banke et al. [1976].

D185, and 1.46 ± 0.14 for D220. C_{10} is also shown plotted versus U_{20} and z/L in Figures 3 and 4, but no dependence on either parameter can explain the variation of C_{10} with wind direction. The increase in C_{10} for directions 140°-152° probably reflects an influence of the camp or tower on the profiles, and these values have not been included in computation of the mean values.

Banke et al. [1976] report fluxes measured with a sonic anemometer at 10 m height on a tower located about 100 m southeast of the profile tower. Unfortunately, their data-taking period at that site ended just as the profile tower became operational and there were only three simultaneous profile-sonic runs. Initial computation of fluxes gave profile stresses and corresponding

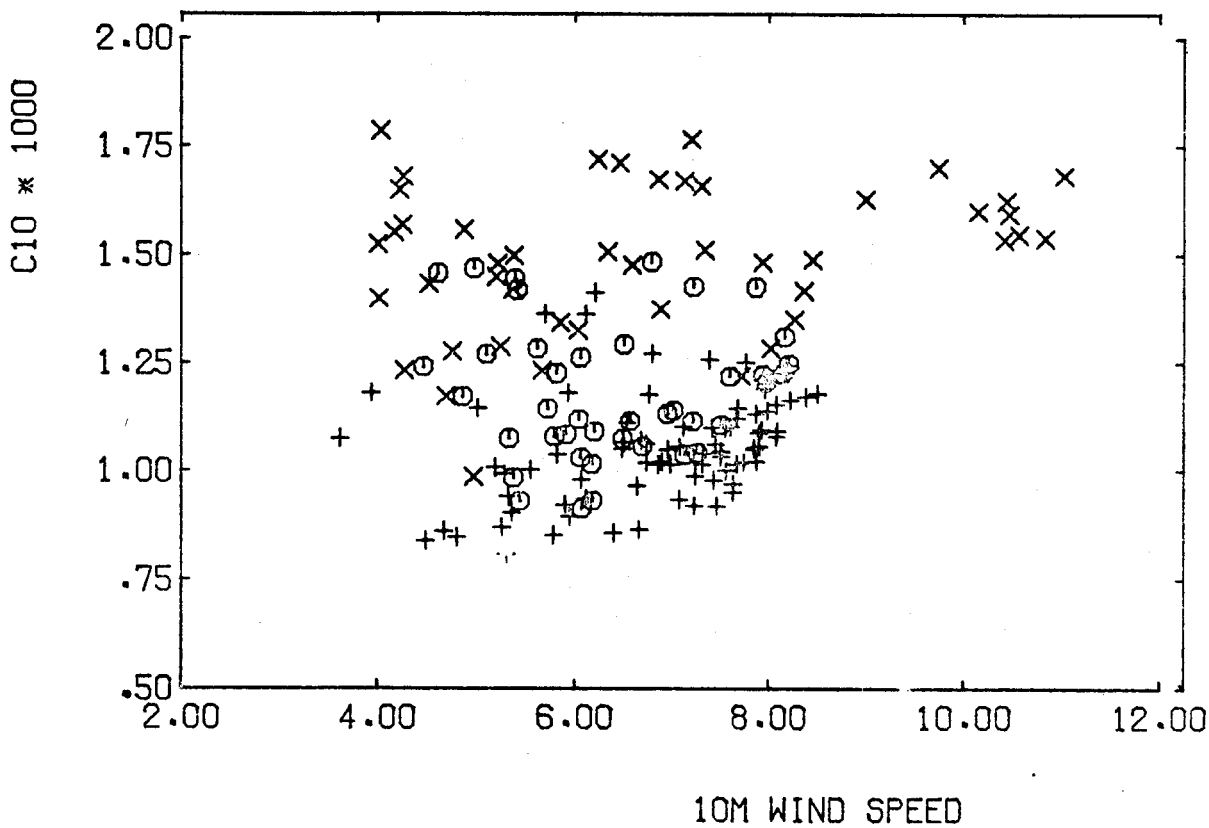

Fig. 3. Variation of the profile C_{10} with 10 m wind speed separated by relative wind directions: + is wind direction 152°-185°; 0 is wind direction 185°-220°; and X is wind direction greater than 220°.

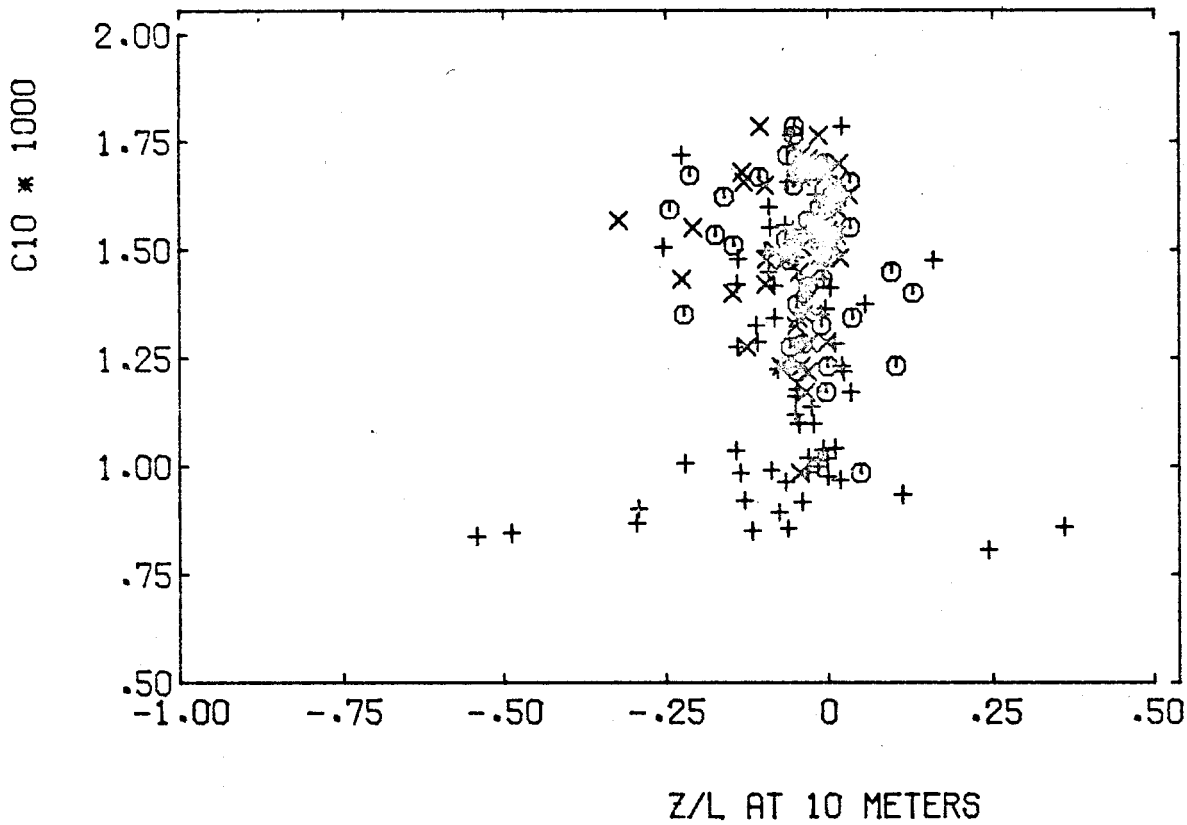

Fig. 4. Variation of profile C_{10} with z/L at 10 m separated by relative wind direction as in Fig. 3.

drag coefficients approximately three times the sonic measurements. Recomputation of the fluxes using only the lower two profile levels gave better agreement between the two sets of data (Table 2). The assumption that the sonic data are more correct permits fluxes to be computed for Runs 3 and 5 using just the lower two levels of wind speed. Banke et al.'s [1976] wind directions were limited to D185, D220; the mean value of their C_{10} estimates is 1.42×10^{-3}, which agrees very well with the profile estimates.

They also made measurements at a more hummocky site about 1 km away from the profile tower were the mean C_{10} of six runs was 1.69×10^{-3}. Several profiles were run simultaneously during this period; the results are also given in Table 2. The profile u_*'s are slightly lower than the sonic values and the heat fluxes show considerable disagreement.

TABLE 2

COMPARISON OF PROFILES AND DIRECT SONIC MEASUREMENTS BY BANKE ET AL. [1976]

Run No.		Time (GMT)		U_* (m s^{-1})		Heat Flux (w m^{-2})		C_{10} (×1000)	
Profile	Sonic	Profile	Sonic	Profile	Sonic	Profile	Sonic	Profile	Sonic
3A	27	0531-0615	0545-0614	too stable	0.11	--	- 7.2	--	0.49[a]
4E	28	1220-1303	1221-1306	0.10	0.11	- 7.2	- 2.7	1.12	0.55[a]
5A	29	1801-1828	1736-1820	0.16	0.14	5.8	0.96	1.63	1.29
12C	34[b]	2310-0032	2346-0020	0.32	0.34	10.1	0.82	1.42	1.41
14B	35[b]	0503-0611	0545-0620	0.40	0.38	- 9.8	-11.6	1.70	1.45
17A,B	38[b]	2131-2330	2213-2257	0.28	0.32	6.2	3.6	1.25	1.58

[a] Not corrected for stability. [b] These data from rougher site.

Equation (6) predicts that U plotted versus $\log z - \psi$ would be a straight line, and averaging many profiles of $U(z)$ versus $\log z - \psi$ would reveal any systematic deviations from this linear relationship. Such an ensemble averaging is shown in Figure 5. The data have been separated by wind directions and limited to L values greater than 100 m. The D152 cases appear to fit the theoretical shapes extremely well for the lower four profile levels in both stable and unstable stratification. The D220 cases are not so well behaved (here the data are subdivided by time as well). The unstable data from the early part of the experiment are well behaved, but the stable data appear to be kinked. The data for D220 from the latter part of the experiment also show a similar kink.

These kinks are probably induced by riming of the middle level anemometers during these periods. Although the problem looks significant on this scale, correcting the affected anemometers will increase the computed stresses by less than 5% and will certainly not reduce the variation of the drag coefficient with direction. Curvature in the profiles can also result from (1) variation in surface roughness upwind of the tower, (2) incorrectly estimating the heat flux, (3) incorrect profile formulation, or (4) underestimating the height of the wind speed instruments. Both (3) and (4) seem unlikely as

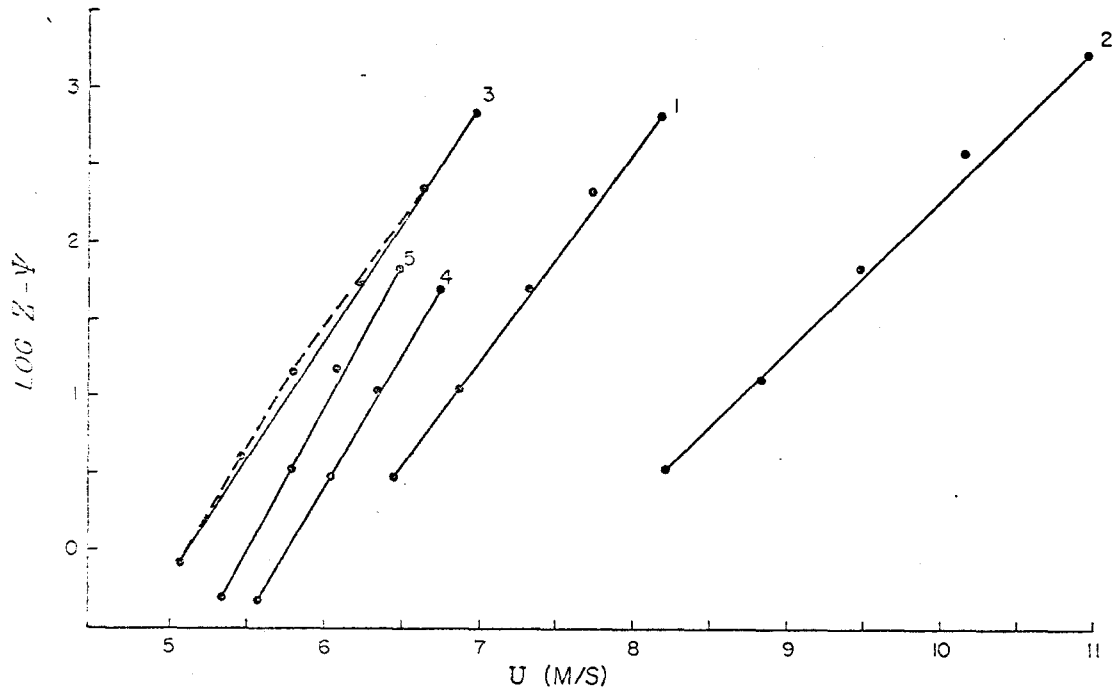

Fig. 5. Ensemble averages of log z - ψ versus wind speed. Groups are as given in Table 3.

the profiles would be affected equally over all wind directions, and the required height error is about 20 cm. Using only profiles, there is no way to distinguish between (1) and (2). Initially, we had hoped that the curvature in the profile was evidence for Arya's [1975] simple model of the effect of upwind obstacles on the measured wind profiles. This was especially interesting since, as mentioned earlier, the hummocks were nearest the tower in the D220 direction. Accepting instrument error as the cause of the curvature suggests that surface features with relatively small vertical extent, which were a function of wind direction and fetch, are responsible for the observed variation in drag coefficient. A 40% variation occurring over such terrain suggests that even greater variation exists over the full range of sea ice surfaces.

Acknowledgments

It is impossible to name all the people who contributed to the success of this program, but we especially want to mention the meteorological observers

TABLE 3

CRITERIA FOR GROUP SELECTION IN FIG. 5

Group	Wind Direction	Period	z/L	Number of Profiles
1	220°-	before day 120	-	7
2	220°-	before day 120	+	5
3	220°-	after day 120	-	19
4	152°-185°	--	-	44
5	152°-185°	--	+	10

who participated in setting up and maintaining the profile tower at Big Bear and Caribou: John Anderson, Gudrun Bodvarsson, Darrell Brown, Dave Short, and Gary Wohl. We also express our appreciation for the administrative support of the program by Richard Trowbridge and the field support organized by Andreas Heiberg and Rolf Bjornert. This work was supported by the Office of Polar Programs, National Science Foundation.

References

Arya, S. P. S. 1975. A drag-partition theory for determining the large scale roughness parameter and wind stress on arctic pack ice. *AIDJEX Bulletin, 28,* 29-47.

Banke, E. G., S. D. Smith and R. J. Anderson. 1976. Recent measurements of wind stress on arctic sea ice. *Journal of Fisheries Research Board of Canada, 33,* 2307-2317.

Businger, J. A. 1966. Transfer of heat and momentum in the atmospheric boundary layer. In *Proceedings of a Symposium on Arctic Heat Budget and Atmospheric Circulation,* The RAND Corp., Santa Monica, Calif., RM-5233-NSF, pp. 305-332.

Businger, J. A., J. C. Wyngaard, Y. Izumi, and E. F. Bradley. 1971. Flux profile relationships in the atmospheric surface layer. *Journal of Atmospheric Science, 28,* 181-189.

Clarke, M., D. Bell, and E. Leavitt. 1977. Field calibration report, AIDJEX meteorology program, April 1975 - April 1976. In this Bulletin.

Coon, M. D., G. A. Maykut, R. S. Pritchard, D. A. Rothrock, and A. S. Thorndike. 1974. Modeling the pack ice as an elastic-plastic material. *AIDJEX Bulletin, 24,* 1-105.

Leavitt, E. 1975. Determination of air stress from surface layer data. *AIDJEX Bulletin, 28,* 11-20.

Paulson, C. A. 1970. The mathematical representation of wind speed and temperature profiles in the unstable atmospheric surface layer. *Journal of Applied Meteorology, 9,* 11-20.

Paulson, C. A., and D. L. Bell. 1975. Meteorological observations during the AIDJEX main experiment. *AIDJEX Bulletin, 28,* 1-10.

Webb, E. K. 1970. Profile relationships: the log-linear range and extension to strong stability. *Quarterly Journal of the Royal Meteorological Society, 96,* 67-90.

NCAR ELECTRA PLANETARY BOUNDARY LAYER FLIGHTS DURING AIDJEX

by

R. A. Brown
AIDJEX

ABSTRACT

During the AIDJEX main experiment in 1975-76, the NCAR Electra flew two missions of four flight days each over the manned camps. Half the flights were directed toward a study of the planetary boundary layer, the other half toward a study of arctic stratus clouds. The basic data set from the PBL flights are discussed here, with some "first look" observations.

INTRODUCTION

In July 1975 and February 1976 the NCAR Electra aircraft flew missions over the AIDJEX study area to make measurements in the planetary boundary layer and to investigate the radiative and macrophysical properties of arctic stratus clouds. The July mission comprised four flights, three of them devoted primarily to the cloud study and one to the boundary layer; it is covered by a report in AIDJEX Bulletin 30 [1975]. In February the balance shifted, with three flights for the boundary layer and one for the stratus study. (This mission was a rescheduling of one originally set for October 1975 but postponed when Big Bear, the AIDJEX main camp, broke up.) This paper discusses only the boundary layer flights, which were made on 19 July 1975 and 7, 14, and 17 February 1976.

The National Science Foundation through the National Center for Atmospheric Research funded the program, and the Naval Arctic Research Laboratory at Barrow, Alaska, supplied fuel and logistic support. The research program for the PBL study was organized and carried out under the direction of R. A. Brown and F. Carsey of AIDJEX, that for the arctic stratus cloud study by G. Herman of Harvard University.

THE FLIGHTS

The flight patterns, shown in Figures 1 and 2, were designed to allow vertical profiling (assuming steady state) and calculation of crosswind spectra to delineate secondary flows, with flight legs long enough to permit averaging of these long-wave variations. Each pattern included reverse check legs to assure the best possible evaluation of bias errors. The outside loops, after they pass over the camps, also allow bias checks on each leg intersecting over the camp [see Grossman, 1976]. The last leg of each flight was extended an additional 100 km to provide horizontal variation data. The flights were oriented parallel and perpendicular to observed wind.

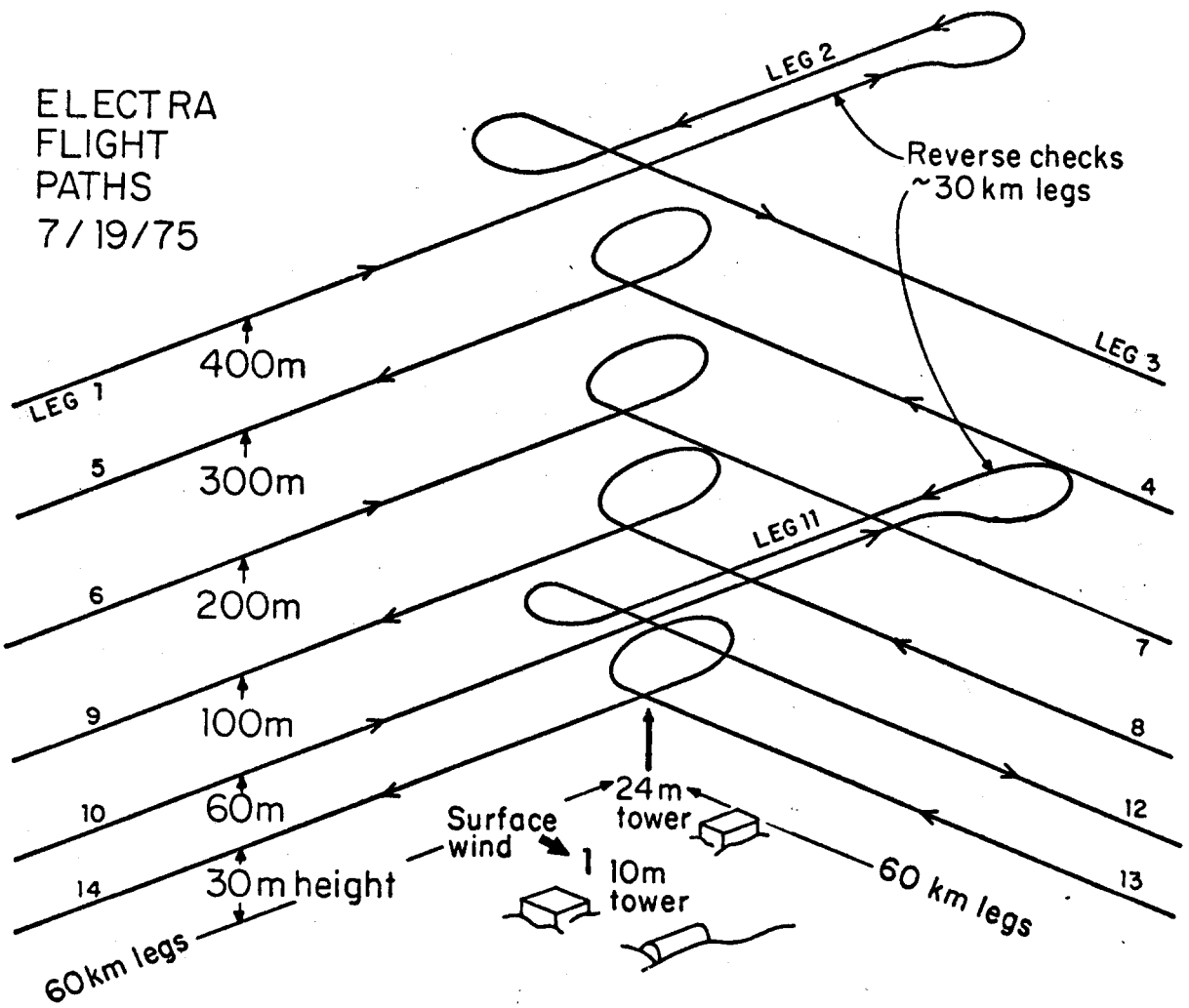

Fig. 1. NCAR Electra flight pattern for investigation of the planetary boundary layer over the AIDJEX area, 19 July 1975.

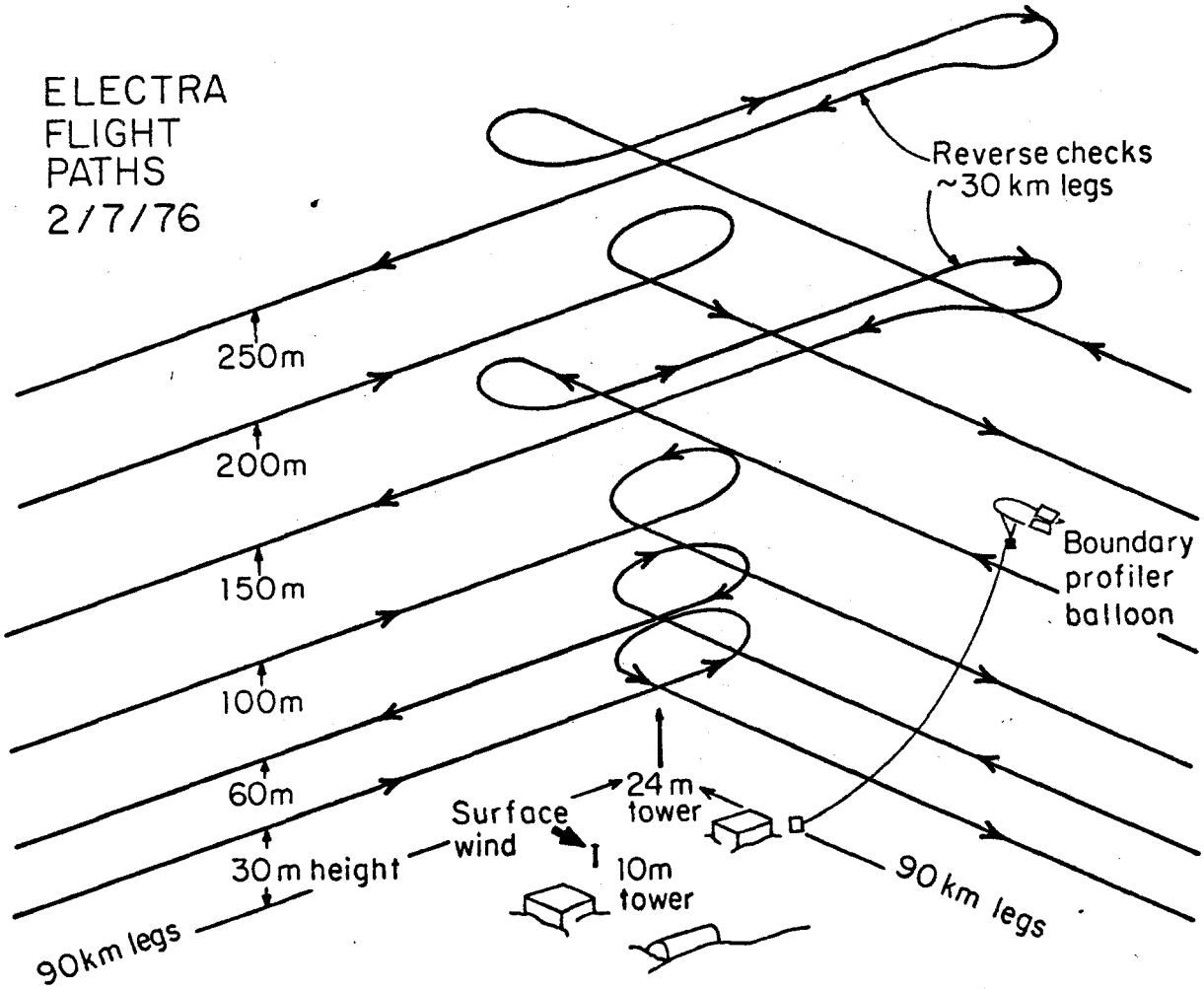

Fig. 2. NCAR Electra flight pattern for investigation of the planetary boundary layer over the AIDJEX area, 7 February 1976.

To assure some quality control of the data, a continuous readout of basic parameters was available: time, geometric (radio) and pressure altitudes, ambient (Rosemount) and surface (PRT5) temperatures, wind speed, and wind direction. The strip charts are stored in the AIDJEX Data Bank. A TV readout of flight data--those parameters and aircraft speed, direction, and altitude--and forward-looking TV and radar were on display at several stations aboard the Electra.

The flights included several levels within the PBL, beginning as low as possible and ending with levels immediately below and above the inversion height. The inflight temperature versus height readout gave a good check on

this reference height and could be used with the pibal and sounder data to locate the inversion and indicate its horizontal variation. A segment of the readout is shown in Figure 3. During ascent and descent, continuous temperature records clearly showed the capping inversion level. On 14 February the inversion height at Pt. Barrow was approximately 300-320 m; at the AIDJEX site 260 km to the north, it was about 300-350 m (Fig. 3).

During the July 1975 flight, the surface of the AIDJEX area was covered by turquoise-colored melt ponds. Many leads were open, their widths ranging from meters to kilometers. In February 1976, the entire area from the AIDJEX site to the shore was under compression, and open leads were rare and never wider than tens of meters. During the February flights, observers noted significant buoyant (lifting) effects on the low-level flights when the aircraft passed over the thinner ice in frozen leads. Excerpts from the observers' flight log appear in the Appendix; systematic errors have not been corrected.

DATA PROCESSING

Some aircraft motion and systematic bias were eliminated form the data by standard NCAR processing and resulted in approximately three tapes per flight. These are stored in the AIDJEX Data Bank.

Programs are now being developed at AIDJEX to calculate mean velocities and temperature from 1 per sec data and to perform averaging and spectral analysis on the velocity and temperature records which were taken at 20 measurements per second. Since our first interest is in establishing vertical variations in the mean values of velocity, temperature, and humidity, we must first eliminate from the measurements as many systematic errors as possible. The net random error introduced by the system capabilities yields winds to 0.1 m sec^{-1} for the short-term (less than 2 minute) averages. When long-term averages are calculated, the error increases to $\pm 1.0 + 0.5t$, where t is in hours, as described by Lenschow [1975]. The larger error is a result of bias introduced by the differences between measured and true air speed and direction. This difference is the true wind vector, and the accuracy in determining it is proportional to the accuracies and magnitudes of the two location vectors. These vectors are shown in Figure 4 for check legs 1 and 2

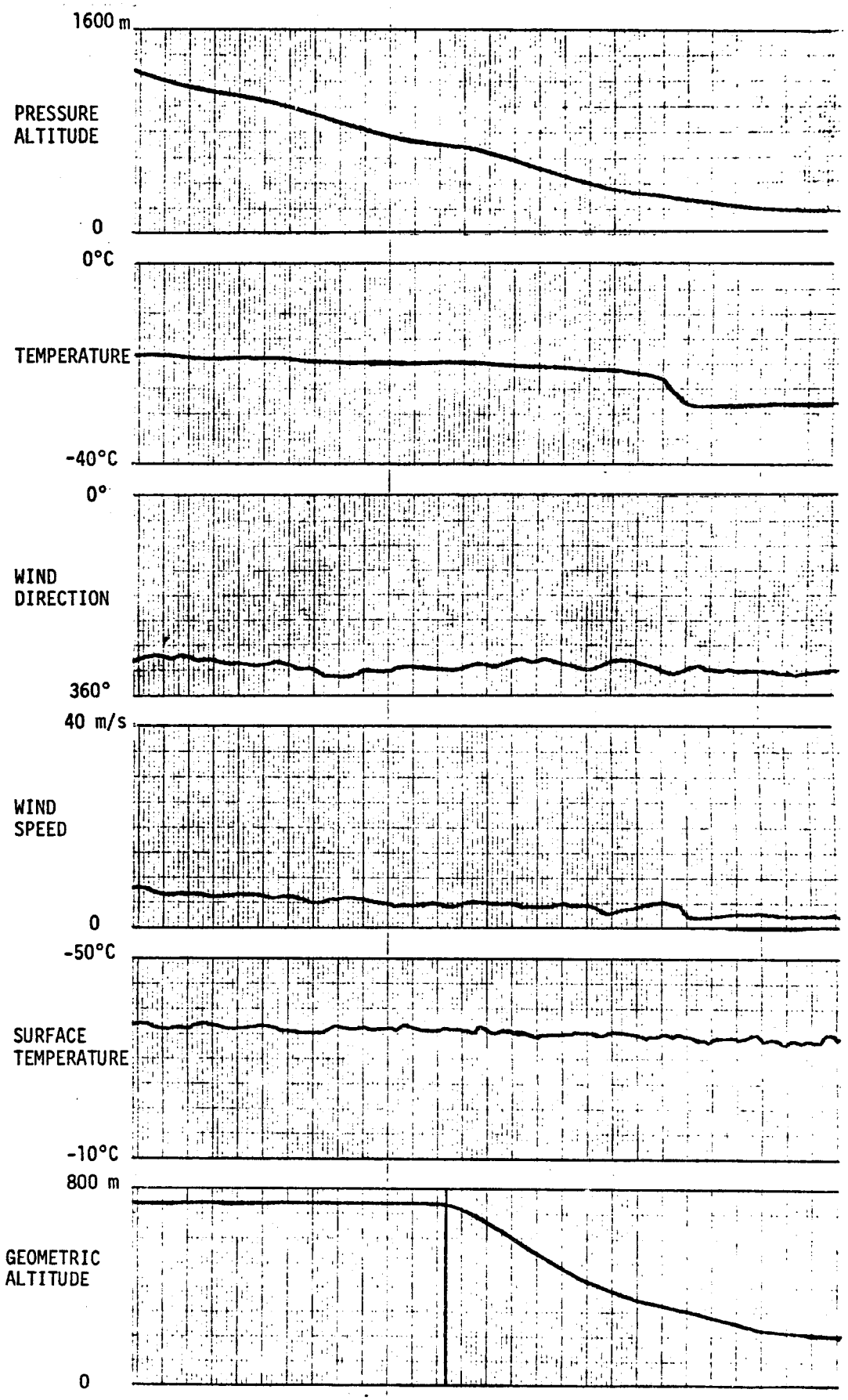

Fig. 3

Portion of in-flight data read-out during descent into planetary layer. Inversion height is denoted by a sharp drop in temperature and wind speed.

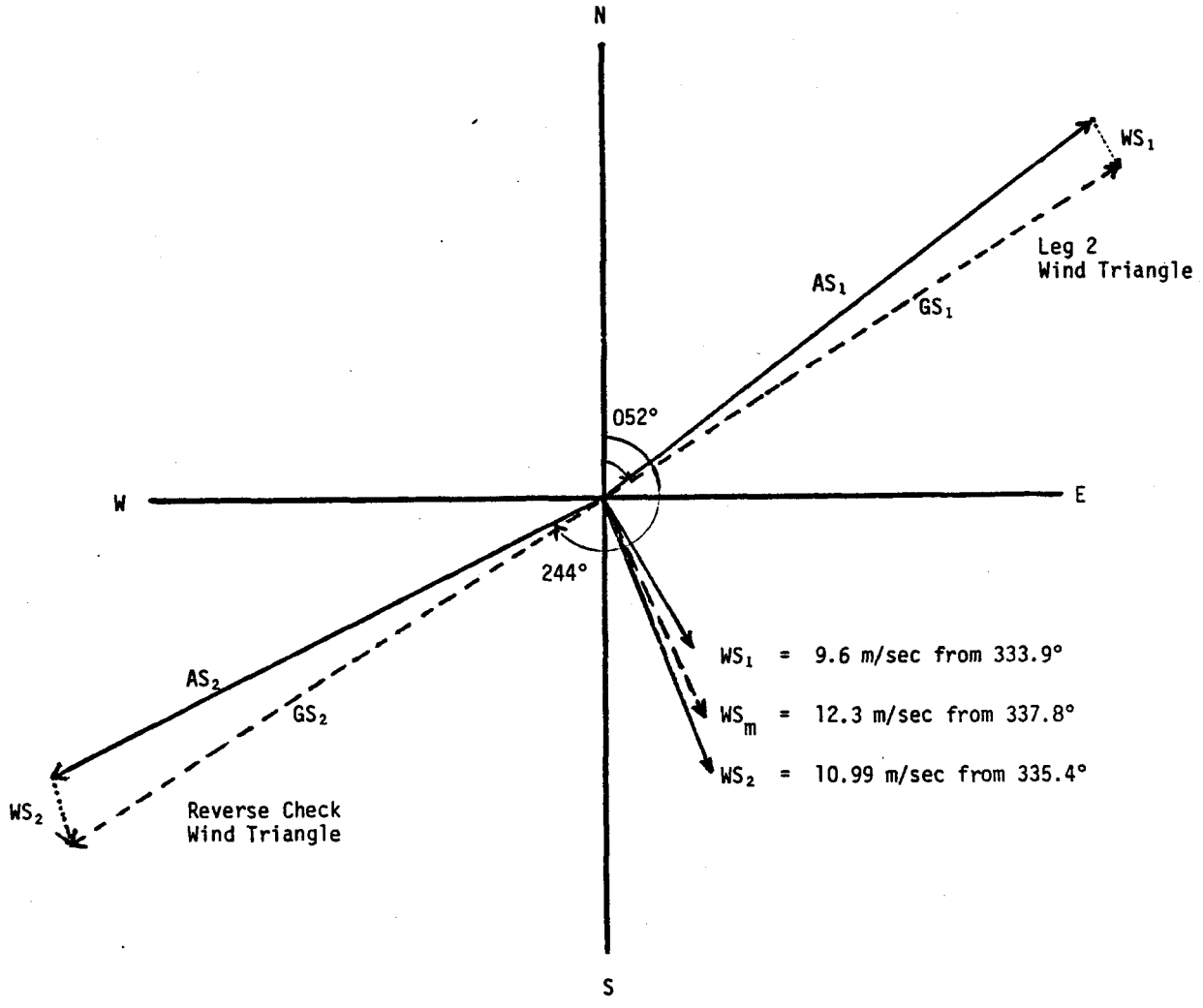

Fig. 4. Wind triangle showing vectors differenced to obtain wind speed and vector correction to mean wind velocity.

on 19 July 1975. The differences between the two values of wind vector are then used to determine the errors in the air and ground velocity vectors, giving the correction for all mean wind values. The geometric velocity resolution formulas are given by Grossman [1976].

EARLY RESULTS AND PLANNED CALCULATIONS

Initial programs for calculating the mean winds and temperature, the bias and flux components including stress have been developed by David Katz. Since the surface uniformity and the PBL stratification and stability of this data

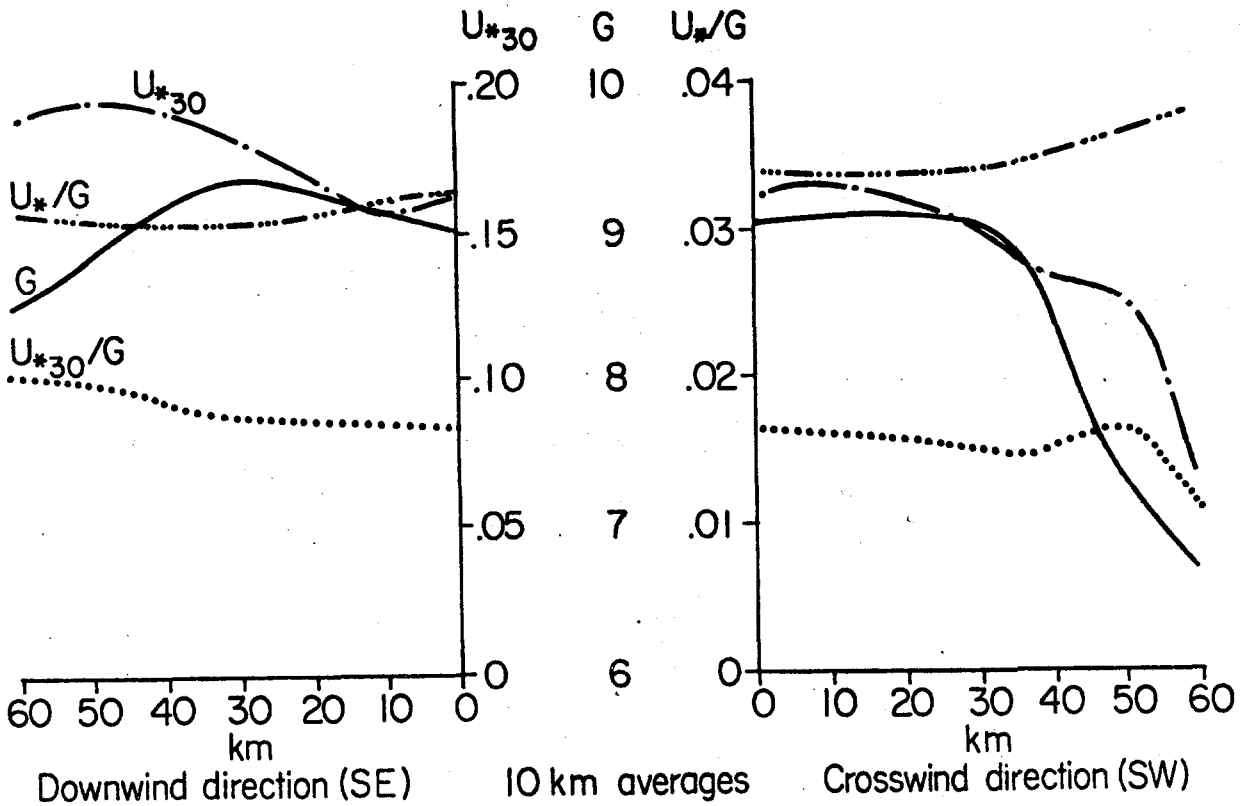

Fig. 5. Preliminary results showing horizontal variation of measured G (above inversion), u_{*30} from flux measurements at 30 m, and drag coefficient u_{*30}/G. Also shown is the momentum integral calculation

$$\frac{u_*}{G} = \frac{fz_i}{G} \sin \alpha$$

where z_i is inversion height and α is wind turning through the PBL.

set are unique, we are encountering many new problems in the data reduction. The basic procedure is to look at time averages with respect to periods of from 10 seconds to 30 minutes. The 10 km (100 sec) averages for cross wind and downwind legs have been calculated for the July 1975 flight and are shown in Figure 5. The variation in geostrophic velocity, G, corresponds to the surface geostrophic wind field as determined from the AIDJEX surface pressure analyses (Figure 6). The flux values of u_* are preliminary only. The indicated values of u_*/G at 30 m are low, approximately half those of the values determined by Frank Carsey [AIDJEX, 1976] using the geostrophic departure method on

a. 19 July 1975, 1400 local

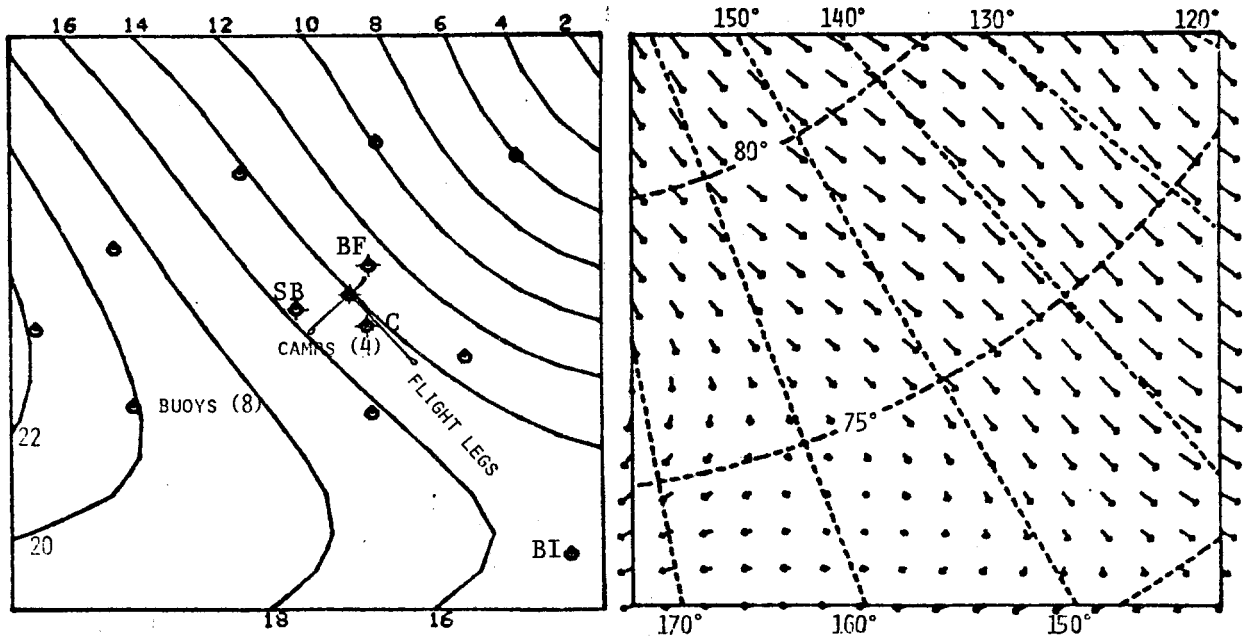

b. 4 February 1976, 1400 local

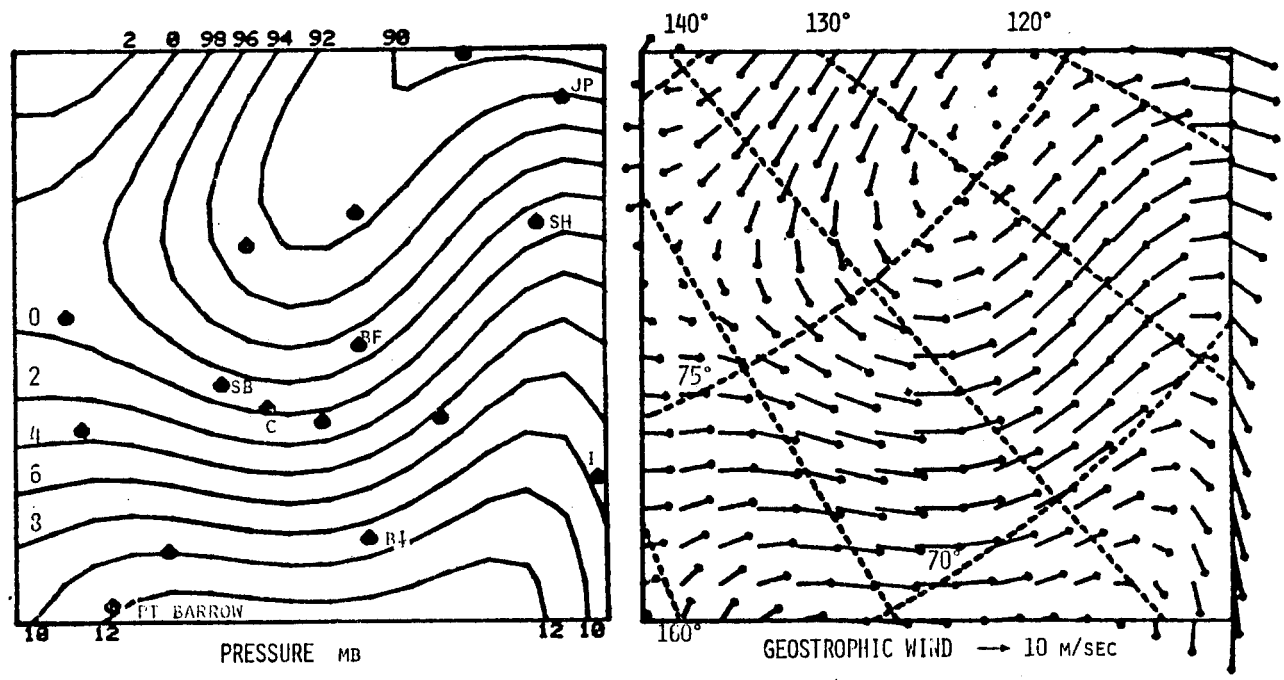

Fig. 6. At left, surface pressure fields derived from locally smoothed, manned camp, buoy, periphery, and National Weather Service data; at right, geostrophic wind fields corresponding to surface pressure fields for each flight day in the PBL. C, Caribou; SB, Snow Bird; BF, Blue

c. 14 February 1976, 1400 local

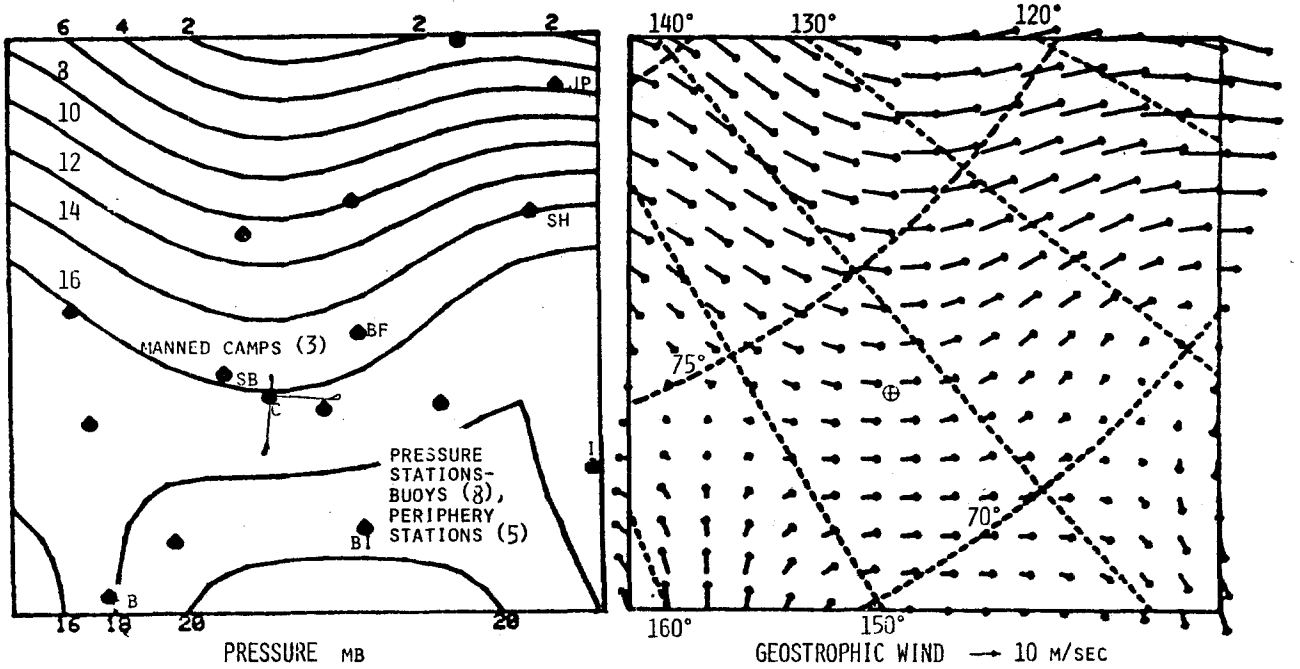

d. 17 February 1976

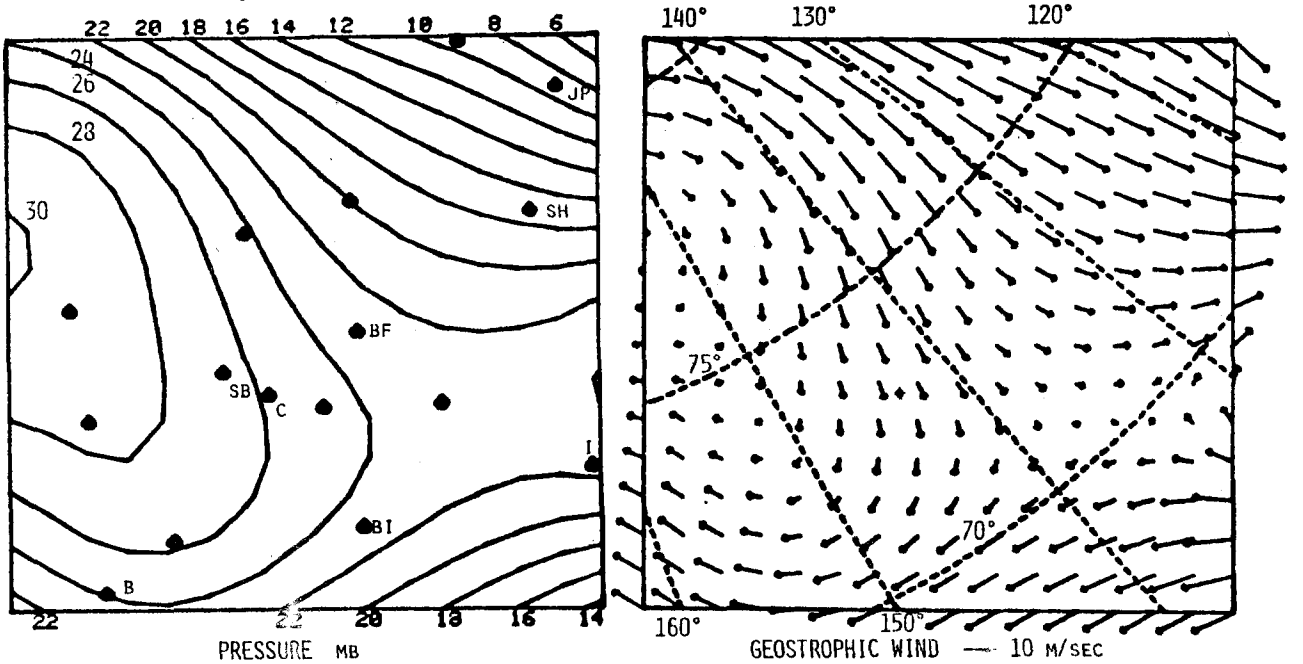

Fig. 6 (continued)

Fox; BI, Barter Island; I, Inuvik; SH, Sachs Harbour; JP, Johnson Point; B, Barrow. Circle toward center of geostrophic wind maps indicates location of main AIDJEX camp (Big Bear in July 1975, Caribou in February 1976).

pibal and acoustic sounder data. However, the value of $u_*/G = 0.02$ obtained by linearly extrapolating to the surface, agrees well with the tower profile values.

The process of determining the peculiar characteristics of turbulence in the neutral to stably stratified PBL requires systematic averaging techniques, and detrending and filtering programs. These are being developed.

Priority calculations include horizontal and vertical variations of wind, temperature, and stress; heat flux variations, wave number spectra, secondary flow resolution, and implied eddy viscosity distribution. Subsequent calculations will include humidity fluxes and higher-order moments.

REFERENCES

Arctic Ice Dynamics Joint Experiment. 1975. The NCAR Electra flights, a report. *AIDJEX Bulletin, 30,* November, 119-125.

Arctic Ice Dynamics Joint Experiment. 1976. The inversion height as determined with acoustic radar. *AIDJEX Bulletin, 32* (First Data Report), June, 45-47.

Grossman, R. F. 1976. A simple procedure for the correction of biases in winds measured from aircraft. *GATE Bulletin No. 11,* March, 29-45.

Lenschow, D. 1975. Present limitations of air motion measurements. Memo, NCAR, 16 April, 6 pp.

APPENDIX

EXCERPT FROM NCAR ELECTRA FLIGHT LOG

Lat.N, Long.W	Local Time	Altitude (meters)	Temp. (°C)	Wind m s^{-1}	Wind °N	Remarks
7 Feb 1976						
71°53' 153°05'	1040	0	-38	---		Takeoff.
72°47' 146°52'	1100	6025	-45	9.5	180	Ferry.
	1130	350	-33	16.8	330	On station at inversion height.
	1132	250	-27	16.4	285	Leg 1.
	1211	30	--	18.0	201	90% snow-covered ice; leads frozen from downwind side.
	1240	60	-31	11.4	260	
	1317	150	-32	14.8	280	Few open leads, narrow ridges smooth, snow covered.
	1406	200	-31	15.6	280	
	1436	100	-28	15.3	300	
14 Feb 1976						
71°17' 156°48'	1040	0	-29	1.3	321	Takeoff.
	1115	5750	-40	12.0	092	Start descent on site, no leads.
72°55' 143°39'	1135	200	-26	7.0	272	Inversion at 300-320, ΔT~7°, ΔV~3 m/s.
	1205	100	-31	11.1	260	Patchwork ridges, some new extensive ones SE and SW of camp.
	1233	100	-29	7.1	269	Over camp.
	1253	60	-32	3.4	290	Occasional frozen leads.
	1325	30	-33	7.1	294	
	1402	150	-27	4.5	300	
	1430	100	-31	3.5	290	Over camp.
	1513	100	-30	6.8	327	Ground speed about 102 m/s.
72°25' 149°26'	1530	--	--	--		Climb out.
71°22' 156°43'	1612	0	-31	2.1	110	Barrow airport.
17 Feb 1976						
	1045	0	-33	--		Barrow airport.
71°58' 153°50'	1110	6041	-38	11.6	090	Ferry.
72°33' 149°45'	1130	5855	-37	14.4	010	Begin descent.
72°51' 143°29'	1155	200	-29	9.9	323	Ice packed, many ridges, no leads.
	1235	60	-32	6.5	324	
	1312	30	-32	8.4	294	
	1415	250	-29	8.2	030	
	1450	150	-31	8.6	345	
	1520	100	-32	9.5	351	Some cracking observed.
	1545	100	-30	9.5	017	Extended leg, 100 km SW.
	1630	6670	-43	25.4	340	Ferry leg.
	--	50	-30	5.7	117	Leg over rough nearshore ice W of Barrow, 50 km long.

CONTENTS OF PAST AIDJEX BULLETINS

No. 1 (Sept. 1970): Status Report

Time schedule
Program elements and working groups
  Analysis and simulation
  Air and water stress
  Ice mechanics and morphology
  Radiation and heat budget
  Automatic data buoy
  Remote sensing
  Ice roughness measurement
1971 pilot studies
International participation
Budget outlook
Mailing list

No. 2 (Oct. 1970, rep. Oct. 1971): Theoretical Discussions

Campbell, W., and A. Rasmussen
  Latest experiments with ice rheology. pp. 11-12.
Evans, R. J.
  Notes on a possible constitutive law for arctic sea ice. pp. 13-17.
Glen, J. W.
  Thoughts on a viscous model for sea ice. pp. 18-27.
Hibler, W. D. III, and L. A. LeSchack
  Power spectrum analysis of ice ridges. pp. 66-70.
Rothrock, D. A.
  The kinematics and mechanical behavior of pack ice: the state of the subject. pp. 1-10.
Solomon, H.
  A study of ice dynamics relevant to AIDJEX. pp. 33-50.
Thorndike, A.
  Techniques for measuring strain rate. pp. 51-65.

No. 3 (Nov. 1970): Selected Soviet Research

Bushuyev, A. V., N. A. Volkov, Z. M. Gudkovich, and V. S. Loshchilov
  Results of expedition investigations of the drift and dynamics of the ice cover of the Arctic Basin during the spring of 1961. pp. 1-21.
Doronin, Y P.
  On a method of calculating the compactness and drift of ice floes. pp. 22-39.
Nikiforov, E. G., Z. M. Gudkovich, Yu. N. Yefimov, and M. A. Romanov
  Principles of a method for calculating the ice redistribution under the influence of wind during the navigation period in arctic seas. pp. 40-64.

No. 3 (continued)

Timokhov, L. A.
Dynamics of the ice cover and changes in its compactness. pp. 65-79.
Timokhov, L. A.
Dynamics and kinematics of ice floes. pp. 94-105.
Timokhov, L. A.
One-dimensional stochastic ice drift. pp. 80-93.
Yakovlev, G. N.
On relief forms of floating ice. pp. 106-118.

No. 4 (Jan. 1971): Water Stress Studies

Coachman, L. K., and J. D. Smith
A report on the 1970 AIDJEX pilot study. pp. 8-37.
Coachman, L. K., and J. D. Smith
University of Washington water stress studies: 1971 AIDJEX water stress pilot studies. pp. 48-55.
Hunkins, K.
Lamont measurements of water stress and ocean currents: 1971 AIDJEX water stress pilot studies. pp. 44-47.
Martin, P.
An arctic under-ice diving experiment. pp. 39-41.
Smith J. D.
AIDJEX oceanographic investigations. pp. 1-7.
Smith, J. D.
Introduction: 1971 AIDJEX water stress pilot studies. pp. 42-43.

No. 5 (Feb. 1971): Remote Sensing and Ice Morphology

Bjornert, R.
Logistic support for AIDJEX-71 pilot studies. pp. 47-50.
Campbell, W. J.
Remote sensing and ground truth investigations. pp. 11-23.
Fleming, M. H.
NOAA satellite resources available to AIDJEX. pp. 34-36.
Fletcher, J. O.
AIDJEX spokesmen. p. 46.
Johnson, J., J. McIntosh, and L. Breslau
U.S. Coast Guard research relevant to AIDJEX. pp. 30-31.
Ketchum, Robert D.
NAVOCEANO participation in AIDJEX. pp. 32-33.
Langleben, M. P. and E. R. Pounder
Remote sensing, ice mechanics and morphology: an outline of the problem. pp. 1-9.
Petersen, E.
NASA flight program. pp. 26-29.
Weeks, W., and A. Kovacs
CRREL-USGS ice mechanics and morphology program.

No. 6 (Mar. 1971): Ice Dynamics

Abstracts
Progress report, 1971 AIDJEX pilot study
Koerner, R. M.
Ice balance in the Arctic Ocean. pp. 11-62.
Timokhov, L. A.
On the relation between turbulent and averaged ice-floe motion. pp. 27-36.
Weber, J. R., and R. L. Lillestrand
Measurement of tilt of a frozen sea. pp. 1-9.
Yegorov, K. L.
Theory of the drift in ice fields in a horizontally inhomogeneous wind field. pp. 37-45.

No. 7 (April 1971): Arctic Data Buoy and Positioning Systems

Anderson, J. O. and B. Buck
A remote automatic multipurpose station (RAMS). pp. 37-44.
Campbell, W. J.
AIDJEX mesoscale measurements. pp. 59-62.
Defence Research Establishment Pacific (Canada)
Sono-Drift-Buoys. pp. 25-26.
Haugen, D. P.
Experimental Arctic data buoy. pp. 27-35.
Hunkins, K. and J. Hall
The navigation of Fletcher's ice island (T-3). pp. 47-58.
Martin, P.
A review of radio positioning for AIDJEX. pp. 63-67.
Olenicoff, S. M.
The Soviet DARMS. pp. 5-23.

No. 8 (May 1971): 1971 Pilot Study Narratives

Bjornert, R.
Logistics report of the 1971 AIDJEX pilot study. pp. 33-36.
Brown, J. H.
1971 Arctic floe studies, Arctic submarine lab. pp. 31-32.
Coachman, L. K. and J. D. Smith
University of Washington oceanographic studies. pp. 21-29.
Hunkins, K.
Lamont ocean current program. pp. 15-19
Moen, A. D.
Report of NASA Convair 990 remote-sensing missions over AIDJEX site, March 9-16, 1971. pp. 9-14.
Weeks, W. F., and W. J. Campbell
CRREL-USGS program at Camp 200. pp. 1-8.

No. 9 Aug. 1971): AIDJEX Planning Conference

Introduction
AIDJEX planning conference minutes

No 9. (continued)

AIDJEX organization
Pai, S. I., and H. Li
Mathematical model of two-phase flow for the dynamics of pack ice in the Arctic Ocean. pp. 35-40.
Untersteiner, N., and J. O. Fletcher
AIDJEX Planning Conference: preface. p. 1.

No. 10 (Sept. 1971): Trudy, AANII, Vol. 296

Bazolova, T. I.
Effect of measurement errors upon the accuracy of determinations of the vertical temperature profile from outgoing microwave radiation. pp. 219-232.
Borisenkov, E. P.
A problem in the forecasting of the geopotential and wind fields with the aid of energy models. pp. 83-96.
Borisenkov, E. P., and A. P. Nagurnyi
Analogous energy levels in the atmosphere and the ocean. pp. 111-116.
Borisenkov, E. P., and A. F. Treshnikov
Role of the polar regions in global investigations of the oceanic and atmospheric circulations. pp. 9-28.
Doronin, Yu. P.
Interaction between the atmosphere and the ocean (basic problems). pp. 29-40.
Doronin, Yu. P.
Investigation of the interaction between the atmosphere and the ocean in the Arctic by means of hydrodynamical models. pp. 41-60.
Doronin, Yu. P., and I. V. Semenova
The role of cloudiness in variations of the thermobaric field in the atmosphere. pp. 97-109.
Khrol, V. P.
Large-scale interaction between the ocean and the atmosphere. pp. 117-163.
Nagurnyi, A. P.
Integration of the full equations of hydrothermodynamics in the numerical forecasting of meteorological fields. pp. 61-82.
Nikolaev, Yu. V.
Detection of a hidden periodicity in a set of multidimensional quantities. pp. 177-188.
Ordanovich, A. S., A. P. Nagurnyi, and V. D. Andreev
Investigation of the turbulence of the lower atmospheric layer over the ocean. pp. 207-217.
Vladimirov, O. A., and Yu. V. Nikolaev
Some physical and statistical characteristics of the water- and air-temperature fields in the North Atlantic. pp. 165-176.
Vladimirov, O. A., and Yu. V. Nikolaev, and N. P. Smirnov
Solar activity and fluctuations of the baric fields in high latitudes of the Northern Hemisphere. pp. 199-206.

No. 10 (continued)

Vladimirov, O. A. and N. P. Smirnov
Semi-annual periodicity in the seasonal changes of some hydrometeorological quantities in the North Atlantic. pp. 189-198.

No. 11 (Nov. 1971)

Translations now under contract
Scientific operations of the 1972 AIDJEX pilot study
Bjornert, R. and A. Heiberg
Logistics plan for the 1972 AIDJEX pilot study. pp. 31-41.
Borisenkov, E. P. and A. F. Treshnikov
The polar experiment. pp. 1-10.
Treshnikov, A. F., E. P. Borisenkov, N. A. Volkov, and E. G. Nikiforov
The American "Arctic Ice Dynamics Joint Experiment" project. pp. 11-22.
Untersteiner, N.
Safety precautions on the ice. p. 43.

No. 12 (Feb. 1972)

Banke, E. G. and S. D. Smith
Turbulence measurements over ice at Camp 200, 1971. pp. 29-33.
Coachman, L. K. and J. L. Newton
Water and ice motion in the Beaufort Sea, Spring 1970. pp. 61-91.
Hibler, W. D. III, W. F. Weeks, and S. J. Mock
Statistical aspects of sea-ice ridge distributions. pp. 117-162.
Hunkins, K.
Water stress and ocean current measurements at Camp 200, 1971. pp. 35-60.
Kovacs, A., W. F. Weeks, S. Ackley, and W. D. Hibler, III
A study of a multiyear pressure ridge in the Beaufort Sea, 1971. pp. 17-28.
Mock, S. J., A. D. Hartwell, and W. D. Hibler, III
Spatial aspects of pressure ridge statistics. pp. 117-162.
Thompson, T. W., R. J. Bishop, and W. E. Brown
Progress report on 25 cm radar observations of the 1971 AIDJEX studies. pp. 1-15.

No. 13 (May 1972)

Hartwell, Allan D.
Airphoto analysis of ice deformation in the Beaufort Sea, March 1971. pp. 1-33.
Hibler, W. D. III, S. Ackley, W. F. Weeks, and A. Kovacs
Top and bottom roughness of a multiyear ice floe.
Hibler, W. D. III, W. F. Weeks, S. Ackley, A. Kovacs, and W. J. Campbell
Mesoscale strain measurements on the Beaufort Sea pack ice. pp. 35-77.

No. 13 (continued)

Lewis, E. L. and R. B. Sudar
The measurement of conductivity and temperature in the sea for salinity determination. pp. 93-113.
Perkin, R. G. and E. R. Walker
Salinity calculations from in situ measurements. pp. 115-125.

No. 14 (July 1972): 1972 AIDJEX Pilot Study

Camp operations
Project summaries
Preliminary data

No. 15 (Aug. 1972): AIDJEX Scientific Plan

Abstract
Introduction
Scientific objectives
Experiment design
Analysis and modeling
Practical applications of AIDJEX
Appendix
References

No. 16 (Oct. 1972): Trudy, AANII, Vol. 303 (First Half)

Arikainen, A. I.
Wave drift of an isolated floe. pp. 125-131.
Doronin, Yu. P., N. A. Zhukovskaya, and A. V. Smetannikova
Testing a numerical model of spring-summer redistribution of sea ice. pp. 35-45.
Egorov, K. L.
Ice drift in an inhomogeneous pressure field. pp. 119-124.
Gudkovich, Z. M. and S. N. Evdokimov
The effect of long-period tides on ice drift in the Arctic Basin. pp. 108-118.
Kheisin, D. E.
Excitation of compressive stresses in ice during the hydro-dynamic stage of compact ice drift. pp. 97-107.
Kirillov, A. A., and M. S. Khromtsova
Many-year variations of the ice coverage of the Greenland Sea and methods of forecasting it. pp. 46-55.
Nikolaev, Yu. V., and E. G. Kovalev
Application of discriminant analysis to long-range ice forecasting for the arctic seas. pp. 64-76.
Volkov, N. A., Z. M. Gudkovick, and V. D. Uglev
Results of the study of nonuniform ice drift in the Arctic Basin. pp. 82-96.
Volkov, N. A., B. A. Sleptsov-Shevlevich
Cyclic variation of the ice-cover coefficient of the arctic seas. pp. 1-34.

No. 16 (continued)

Vorob'ev, V. N., and Z. M. Gudkovich
The effect of long-period tides on ice conditions in the arctic seas. pp. 77-81.
Zakharov, V. F.
Manifestation of atmospheric cycles in ice-cover coefficient. pp. 56-63.

No. 17 (Dec. 1972): Trudy, AANII, Vol. 303 (Second Half)

Buzuev, A. Ya., and V. F. Dubovtsev
Statistical characteristics of some ice cover parameters in the Arctic. pp. 55-70.
Gudkovich, Z. M., and T. I. Santsevich
Seasonal features of the "polar tide" pressure wave over the Arctic. pp. 1-19.
Karelin, I. D., and L. A. Timokhov
Experimental determination of the wind drag on an ice sheet. pp. 41-53.
Legen'kov, A. P., and V. D. Uglev
Observations of ice motion with optical theodolites on the *Severnyi Poluys-17* drifting station. pp. 89-103.
Legen'kov, A. P., V. D. Uglev, and N. I. Blinov
Shear measurements of natural ice with optical theodolites. pp. 85-87.
Nazintsev, Yu. L.
Estimating the lateral melting of drift ice. pp. 71-76.
Nazintsev, Yu. L.
Snow accumulation on Kara sea ice. pp. 77-83.
Nikolaeva, A. Ya.
The relation of the resultant monthly average wind to the pressure gradient. pp. 21-40.
Novikov, Yu. R.
Application of computers for determining age characteristics of arctic ice. pp. 105-110.

No. 18 (Feb. 1973)

AIDJEX and the AGU Symposium
Some impressions of AIDJEX
Abstracts
Berkson, J. M., C. S. Clay, and T. K. Kan
Mapping the underside of Arctic sea ice by backscattering sound. pp. 51-59.
DeRycke, R. J.
Some seasonal variations of the ice cover in the Beaufort Sea: Evidence of macroscale ice dynamics phenomena. pp. 45-50.
Heiberg, A.
AIDJEX field operations, fall 1972. pp. 1-4.
Mohaghegh, M.
Determining the strength of sea ice sheets. pp. 96-109.

Mukherji, B.
Crack propagation in sea ice: A finite element approach. p. 81.
Newton, J. L. and L. K. Coachman
Observations of ice motion and interior flow field during 1971 AIDJEX pilot study. pp. 5-30.
Rooth, C.
Some impressions of AIDJEX. pp. 77-78.
Rothrock, D. A.
Circulation of an imcompressible ice cover. pp. 61-68.
Welch, M., E. Partch, H. Lee, and J. D. Smith
Diving report, 1972 AIDJEX pilot study. pp. 31-44.

No. 19 (Mar. 1973)

Abstracts
AIDJEX Data Bank digital data indices and preliminary user's guide
Arya, S. P. S.
Air friction and form drag on Arctic sea ice. pp. 43-57.
Cox, G. F. N., and W. F. Weeks
Salinity variations in sea ice. pp. 1-17.
Kozo, T. L., and O. I. Diachok
Spatial variability of topside and bottomside ice roughness and its relevance to underside acoustic reflections loss. pp. 113-121.
Newton, J. L., and L. K. Coachman
1972 AIDJEX interior flow field study: Preliminary report and comparison with previous results. pp. 19-42.
Parmerter, R. R., and M. D. Coon
Mechanical models of ridging in the Arctic sea ice cover. pp. 59-112.

No. 20 (May 1973)

Data management report on 1972 AIDJEX pilot study
Abstracts of interest
Brown, R. A.
On the atmospheric boundary layer: theory and methods. pp. 1-141.
Pai, S. I., and H. Li
Some critical remarks on turbulent diffusion theory on ice dynamics. pp. 143-152.

No. 21 (July 1973)

Index of AIDJEX Pictorial Data
A New Arctic Journal
Abstracts of Interest
Hibler, W. D., W. F. Weeks, A. Kovacs, and S. F. Ackley
Spatial and temporal variations in mesoscale strain in sea ice. pp. 79-113.
Hibler, W. D. III
Comparison of mesoscale strain measurements with linear drift theory predictions. pp. 115-137.
Kan, T. K., C. S. Clay, and J. M. Berkson
Sonar mapping of the underside of pack ice. pp. 115-169

No. 21 (continued)

Ling, C. H.
A method for calculating boundary stress in an atmospheric boundary layer. pp. 143-153.

Maykut, G. A., and A. S. Thorndike
An approach to coupling the dynamics and thermodynamics of Arctic sea ice. pp. 23-29.

Mukherji, B.
Numerical integration of quadrilateral elements in the finite element method. pp. 139-141.

Nye, J. F.
A note on the power spectra of sea-ice profiles. pp. 20-21.

Nye, J. F.
Is there any physical basis for assuming linear viscous behavior for sea ice? pp. 9-17.

Nye, J. F.
The meaning of two-dimensional strain-rate in a floating ice cover. pp. 1-8.

Nye, J. F.
The physical meaning of two-dimensional stresses in a floating ice cover. pp. 1-8.

Rothrock, D. A.
The steady drift of an incompressible Arctic ice cover. pp. 20-21.

Thorndike, A. S., and G. A. Maykut
On the thickness distribution of sea ice. pp. 31-47.

Tucker, W. B. III, and V. H. Westhall
Arctic sea-ice ridge frequency distributions derived from laser profiles. pp. 171-180.

No. 22 (Aug. 1973): Arctic Data Buoys

Brown, W. P.
Shrams and Lorams: Two unmanned data telemetry systems for ice covered seas. pp. 55-74.

Haugen, D. P, and E. G. Kerut
In Arctic data buoy, a system for envirnomental monitoring in the Arctic pp. 37-53.

Kahn, E. H.
A resonant capsule pressure transducer for data buoys. pp. 113-137.

Martin, P.
Arctic data buoys and AIDJEX. pp. 1-7.

Martin, P.
Barometric pressure measurements from buoys during AIDJEX 1972. pp. 89-111.

Olenicoff, S. M.
The Soviet DARMS program: twenty years of development, deployment, and data. pp. 8-34.

Stevenson, J.
Communicating with your head. pp. 139-141.

E. A. Westerfield
Using the Navy navigation satellite system to determine the position of a drifting buoy. pp. 75-87.

No. 23 (Jan. 1974)

Abstracts of Interest

Brown, R. A.
Similarity constants in the stratified planetary boundary layer. pp. 147-155.

Hibler, W. D. III, S. J. Mock, and W. B. Tucker III
Classification and variation of sea ice ridging in the Arctic basin. pp. 127-146.

Hunkins, K. L.
Subsurface eddies in the Arctic Ocean. pp. 9-36.

Ling, Chi-Hai, and N. Untersteiner
On the calculation of the roughness parameter of sea ice. pp. 117-125.

Nye, J. F.
Three notes on the theory of sea-ice movement. pp. 37-44.

Parmerter, R. R.
Dimensionless strength parameters for floating ice sheets. pp. 83-95.

Parmerter, R. R.
A mechanical model of rafting. pp. 94-115.

Paulson, C. A., and J. Dungan Smith
The AIDJEX lead experiment. pp. 1-8.

Rothrock, D. A.
A relation between the potential energy produced by ridging and the mechanical work required to deform pack ice. pp. 45-51.

Rothrock, D. A.
Redistribution functions and their yield surfaces in a plastic theory of pack ice deformation. pp. 53-81.

No. 24. (May 1974): Numerical Modeling Report

Coon, M. D., G. A. Maykut, R. S. Pritchard, D. A. Rothrock, and A. S. Thorndike
Modeling the pack ice as an elastic-plastic material. pp. 1-105.

Schwaegler, R. T.
Fracture of ice sheets due to isostatic imbalance. pp. 131-146.

Thorndike, A.
Strain calculations using AIDJEX 1972 position data. pp. 107-129.

No. 25 (July 1974)

Ackley, S., W. Hibler III, F. Kugzruk, A. Kovacs, and W. Weeks
Thickness and roughness variations of Arctic multi-year sea ice.

Campbell, W. J., P. Gloersen, W. Nordberg, and T. T. Wilheit
Dynamics and morphology of Beaufort Sea ice determined from satellites, aircraft, and drifting stations. pp. 1-27.

Goddard, W. B.
A climate simulation model applied to arctic pack ice. pp. 55-73.

Hibler, W. D. III, and S. F. Ackley
Height variations along sea ice pressure ridges and the probability of finding "holes" for vehicle crossings. pp. 97-106.

No. 25 (continued)

Hibler, W. D. III, and S. F. Ackley
A sea ice terrain model and its application to surface vehicle trafficability. pp. 107-126.
Mukherji, B.
Structuring large-capacity computer programs. pp. 49-54.
Stateman, M. J.
ERTS-1 imagery acquired by the AIDJEX data bank. pp. 29-48.

No. 26 (Sept. 1974)

Ackley, S., and W. Hibler III
Measurements of Arctic Ocean ice deformation and fracture patterns from satellite imagery. pp. 33-47.
Brown, R.
A simple momentum integral model. pp. 153-162.
Brown, R., P. Maier, and T. Fox
Surface atmospheric pressure fields and derived geostrophic winds, AIDJEX 1972. pp. 173-203.
Heiberg, A.
AIDJEX lead experiment, spring 1974, field operations report. pp. 23-31.
Hunkins, K.
An estimate of internal wave drag on pack ice. pp. 141-152.
Hunkins, K.
The oceanic boundary layer and ice-water stress during AIDJEX 1972. pp. 109-128.
Hunkins, K., and M Fliegel
Ocean current observations at the AIDJEX 1974 main camp. pp. 75-108.
Hutter, K.
On possible constitutive equations for sea ice. pp. 163-172.
Pritchard, R.
What? Strain? What strain? pp. 59-74.
Pritchard, R. and R. Colony
One-dimensional difference scheme for an elastic-plastic sea ice model. pp. 48-58.
Rigby, F.
Theoretical calculations of internal wave drag on sea ice. pp. 129-140.
Untersteiner, N.
Arctic ice dynamics joint experiment, progress 1970-1974. pp. 1-21.

No. 27 (Nov. 1974)

Reports from the principal investigators, AIDJEX lead experiment
Holmgren, B., G. Shaw, and G. Weller
Turbidity in the arctic atmosphere. pp. 135-148.
Holgren, B. and L. Spears
Sodar investigations of the effect of open leads on the boundary layer structure over the Arctic basin. pp. 167-179.

No. 27 (continued)

Holmgren, B., and G. Weller
Local radiation fluxes over open and freezing leads in the polar pack ice. pp. 149-166.

Kelley, J. J.
Effect of open leads on the exchange of CO_2 between the atmosphere and surface sea water. pp. 121-124.

Ling, C.
Comparison of shear stress calculations between two profile methods using some drag-plate measurements. pp. 84-89.

Martin, P. and A. Thorndike
Ice island report. pp. 108-116.

Nye, J. F. and D. R. Thomas
The use of satellite photographs to give the movement and deformation of sea ice. pp. 1-21.

Pritchard, R. S.
Elastic strain in the AIDJEX sea ice model. pp. 45-62.

Rothrock, D. A.
The energetics of plastic deformation in pack ice. pp. 63-83.

Smith, J. Dungan
Oceanographic investigations during the AIDJEX lead experiment. pp. 125-133.

Weber, J. R.
Hydrostatic leveling on floating ice. pp. 91-107.

Weeks, W. F., Max D. Coon, W. J. Campbell
The remote sensing program required for the AIDJEX model. pp. 22-44.

No. 28 (Mar. 1975)

Arya, S. P. S.
A drag-partition theory for determining the large-scale roughness parameter and wind stress on Arctic pack ice. pp. 29-47.

Banke, E. G. and S. D. Smith
Measurement of form drag on ice ridges. pp. 21-27.

Colony, R.
The boundary determination problem for the AIDJEX ocean. pp. 87-97.

Evans, R. J.
On the continuum approximation for the AIDJEX model. pp. 99-117.

Foster, T. D.
Heat exchange in the upper Arctic Ocean. pp. 151-166.

Helms, W. J. and H. R. Willard
Polar communications via geostatic satellites. pp. 173-187.

Hunkins, K.
Geostrophic drag coefficients for resistance between pack ice and ocean. pp. 61-67.

Hunkins, K.
The oceanographic program for the AIDJEX main experiment. pp. 48-59.

Leavitt, E.
Determination of air stress from AIDJEX surface layer data. pp. 11-19.

No. 28 (continued)

Nye, J. F.
A test of the ice thickness redistributing equations by measurements of ERTS pictures. pp. 141-149.
Nye, J. F.
Discontinuities in the AIDJEX model. pp. 119-126.
Nye, J. F.
Suggested procedure for observing ice displacement, strain, and thickness distribution during the AIDJEX main experiment. pp. 127-140.
Pai, S. I. and H. Li
A note on the dynamics model of pack ice in the Arctic Ocean and its surrounding seas. pp. 167-172.
Paulson, C. A. and D. L. Bell
Meteorological observations during the AIDJEX main experiment. pp. 1-9.
Weber, J. R. and M. Erdelyi
Ice and ocean tilt measurements in the Beaufort Sea. pp. 69-85.

No. 29 (July 1975)

Bjornert, R.
Field operations report for the AIDJEX main experiment. pp. 173-180.
Brown, R. A.
Planetary boundary layer models and parameters for AIDJEX 1975-76. pp. 113-130.
Coon, M. D. and R. J. Evans
On wind-induced cracking of sea-ice sheets. pp. 131-134.
McPhee, M. G.
Ice-ocean momentum transfer for the AIDJEX ice model. pp. 93-111.
McPhee, M. G. and J. D. Smith
Measurements of the turbulent boundary under pack ice. pp. 49-92.
Pease, Carol, H.
A model for the seasonal ablation and accretion of Antarctic sea ice. pp. 151-172.
Rothrock, D. A. and R. T. Hall
Testing the redistributing of sea ice thickness from ERTS photographs. pp. 1-19.
Schwaegler, R. T.
Effect of changing the yield surface and the kinematic relationship in the AIDJEX sea ice model. pp. 135-154.
Weeks, W. F. and W. J. Campbell
Remote sensing plan for the AIDJEX main experiment. pp. 21-48.

No. 30 (Nov. 1975)

The NCAR electra flights, a report
Colony, R. and R. S. Pritchard
Integration of elastic-plastic constitutive laws. pp. 55-80.
Criminale, W. O., Jr., and G. F. Spooner
Fluctuations and structure within the oceanic boundary layer below the Arctic ice cover. pp. 29-54.

No. 30 (continued)

McPhee, M. G.
The effect of ice motion on the mixed layer under Arctic ice. pp. 1-27.
Parmerter, R. R.
On the fracture of ice sheets with part-through cracks. pp. 94-114.
Pritchard, R. S.
A difference approximation to the momentum equation. pp. 81-93.

No. 31 (Mar. 1976)

Brown, R. A.
On the velocity shear instability. pp. 75-85.
Brown, R. A.
The resistance law. pp. 21-31.
Brown, R. A.
The similarity planetary boundary layer model with baroclinicity and secondary flow. pp. 32-44.
Carsey, F. D.
The AIDJEX acoustic radar and some preliminary results. pp. 1-19.
Colony, R.
The simulation of arctic sea ice dynamics. pp. 151.
Coon, M. D., R. Colony, R. S. Pritchard, and D. A. Rothrock
Calculations to test a pack ice model. pp. 170-187.
Evans, R. J. and R. Parmerter
Gravitational stresses in floating ice sheets. pp. 86-91.
Hanzlick, D. J.
Oscillations and pedestaling on T-3. pp. 93-100.
Hibler, W. D., Tucker, W. B., and Weeks, W. F.
Techniques for using Landsat imagery without land references to study sea drift and deformation. pp. 115-135.
Maykut, G.
Energy exchange over young sea ice in the central arctic. pp. 45-74.
Pritchard, R. S., and R. Colony
A difference scheme for the AIDJEX sea ice model.
Pritchard, R. S., and R. T. Schwaegler
Applications of the AIDJEX ice model. pp. 137-150.
Westhall, V. H., and H. Li
An analysis of sea ice bottomside data in the Denmark Strait. pp. 101-114.

No. 32 (June 1976): First Data Report

The AIDJEX data report series--Introduction
Ice position and velocity estimates
Azimuths of the manned camps
Deformation of the manned array
Surface layer meteorological data
Atmospheric surface pressure
Surface geostrophic winds
The inversion height as determined with acoustic radar

No. 32 (continued)

Oceanic mixed layer characteristics
Ocean current velocities at 2 m and 30 m
Ice thickness
Snow depth

No. 33 (Dec. 1976)

Ackley, S. F., W. D. Hibler III, and F. K. Kugzruk
Misgivings on isostatic imbalance as a mechanism for sea ice cracking. pp. 85-94.

Ackley, S. F., and T. E. Keliher
Antarctic sea ice dynamics and its possible climatic effects. pp. 53-76.

Becker, E. B.
The finite element method in AIDJEX. pp. 144-157.

Lindsay, R. W.
Wind and temperature profiles taken during the arctic lead experiment (Summary of Master's Thesis). pp. 102-104.

Ling, C., and W. J. Campbell
Antisymmetric stress for sea ice. pp. 77-84.

Nye, J. F.
A coordinate system for two-dimensional stress and strain-rate and its application to the deformation of sea ice. pp. 105-130.

Nye, J. F.
Disclinations and catastrophes in the vector and tensor fields of sea ice. pp. 105-130.

Timokhov, L., R. Brown, I. Kulakov, E. Leavitt, G. Trushina, and R. Colony
A description of a model of the atmospheric boundary layer. pp. 95-101.

Wadhams, P.
Sea ice topography in the Beaufort Sea and its effect on oil containment. pp. 1-52.

No 34 (Sept. 1976)

Brown, C. B.
Interaction of pack ice with structures and associated ice mechanics. pp. 207-242.

Keliher, T. E.
An investigation of the effect of large-amplitude ocean waves on antarctic pack ice. pp. 114-136.

Pritchard, R. S.
An estimate of the strength of arctic pack ice. pp. 94-113.

Pritchard, R. S., M. D. Coon, and M. G. McPhee
Simulation of sea ice dynamics during AIDJEX. pp. 73-93.

Rigby, F. A.
Evolution of a large arctic pressure ridge. pp. 43-72.

Toimil, L. J. and A. Grantz
Origin of a bergfield in the northeastern Chukchi Sea and its influence on the sedimentary environment. pp. 1-42.

No. 34 (continued)

Weeks, W. F.
Sea ice conditions in the arctic. pp. 173-206.
Weeks, W. F.
Sea ice properties and geometry. pp. 137-172.

No. 35 (Jan. 1977)

Thorndike, A. S., and J. Y. Cheung
AIDJEX measurements of sea ice motion 11 April 1975 to May 1976. pp. 1-149.

No. 36 (May 1977)

Walsh, John E.
Ice forecasting limitations imposed by the accuracy of atmospheric prediction models. pp. 1-13.
Reimnitz, E., L. Toimil, and P. Barnes
Arctic continental shelf processes and morphology related to sea ice zonation, Beaufort Sea, Alaska. pp. 15-64.
McPhee, M. G.
A simulation of inertial oscillations observed in the drift of manned ice stations. pp. 65-85.
Carsey, Frank, and Eric Leavitt
Pibal/acoustic radar data in measurement and computation of air stress over pack ice. pp. 87-128.
Clarke, M., David Bell, and Eric Leavitt
Field calibration report, AIDJEX meteorology program, April 1975-April 1976. pp. 129-155.
Leavitt, E., D. Bell, M. Clarke, R. Andersen, and C. Paulson
Computation of air stress and sensible heat fluxes from surface layer profile data, AIDJEX, 1975. pp. 157-174.
Brown, R. A.
NCAR Electra planetary boundary layer flights during AIDJEX. pp. 175-185.
Staff
Contents of past Bulletins. pp. 187-202.
Stateman, Murray J.
Data available from the Arctic Ice Dynamics Joint Experiment as of 1 May 1977. pp. 203-210.

DATA AVAILABLE FROM THE ARCTIC ICE DYNAMICS JOINT EXPERIMENT AS OF 1 MAY 1977

by

Murray J. Stateman
AIDJEX Data Bank

INTRODUCTION

The AIDJEX Data Bank is the primary repository for data acquired on the Beaufort Sea pack ice during the AIDJEX pilot study in 1972 and the AIDJEX main experiment in 1975-76. AIDJEX Bulletin No. 19 (March 1973) shows the data sets from the first period. This note outlines the data which have been validated and entered into the AIDJEX Data Bank from the main experiment. In addition to the source data, there are some post-processed data sets and several supplementary supportive data sets supplied by outside sources.

These data are being used for the analysis of air-ice-sea interactions and associated phenomena. Many articles published in the AIDJEX Bulletin relate to these analyses, and some of the articles include a brief overview of the actual data.

Data in digital form are stored on magnetic tape and are housed in the Computer Center at the University of Washington. Duplicate copies are held at the AIDJEX office for security. Nondigital data, such as satellite photographs and sample printouts, are also housed at the AIDJEX office.

Any files or subfiles listed below may be obtained by writing to AIDJEX, noting the files desired and the medium on which they should be produced. Digital data can be provided as a printout, as a set of key-punched cards, or on half-inch 7-track magnetic tape. These would be accompanied by a narrative description of the file contents and the format of the data sets. The cost of these outputs will be approximately the cost of reproduction and mailing. Supplementary data such as satellite photos or weather maps are available for

inspection at the AIDJEX office during business hours. Copies of these materials are best obtained from the original source.

All comments and inquiries concerning the AIDJEX Data Bank should be addressed to Murray J. Stateman, AIDJEX Data Manager, 4059 Roosevelt Way N.E., Seattle, Washington 98105.

DATA FILES

1. Position of the manned camps and buoys, in latitude and longitude vs. time

Approximately 10 positions were calculated each day for each operating station using the Transit Navigational Satellite or the Nimbus F satellite. Data for the manned camps were taken from 10 April 1975 to 20 April 1976. Data for buoys in the Beaufort Sea were taken from April 1975 up to November 1976. Note that the lifetime of most buoys is about six months. These data characterize the motion of the pack ice in the Beaufort Sea for all seasons of the year.

Data are organized in a time series for each station with a separation marker at the end of each 20-day period.

2. Smoothed position, velocity, and acceleration for manned camps and buoys, in Cartesian coordinates

Data from file 1 above have been post-processed using a Kalman filter technique. In one form--sorting on time--position, velocity, and acceleration from each operating buoy are arrayed together at three-hour intervals. In another form--sorting on station--position and velocity are given as a time series, separately for each station. A variance measure accompanies each element of data to characterize its error.

3. Source data for RAMS buoys tracked by Nimbus F satellite

Position data acquired from the start of Nimbus F operation in June 1975 have been provided by the NASA Goddard Space Flight Center and, after decoding and editing, have been incorporated into file 1 above. Several land-based

RAMS packages are included in order to determine the temporal and spatial accuracy of the tracking system.

4. Rotation of the manned camp floes

The orientation of the camp floes, to which the Navigational Satellite positioning system was aligned, was determined together with the camp position. Each camp azimuth, with respect to true North, has been smoothed for the period 10 April 1975 to 22 April 1976. Angular position and rate of rotation for all camps are given at three-hour intervals in a time-sorted data file together with error estimates for each datum.

5. Ice thickness and snow depth

Periodic measurements were made at various sites near the manned camps. Statistical evaluation of ice and snow conditions were made from frequent measurements around a given site. Data are not continuous. Tabulations of available data for the period 10 April 1975 to 29 June 1975 have been published in AIDJEX Bulletin 32 (June 1976). Data to April 1976 are available in a similar form.

6. Ice surface profile

One profile of the ice surface was taken using a laser altimeter in the NASA 990 as it traveled a 72 km track between two manned camps. A data point is a height above a reference plane every 0.4 m along the track. The measurements were made on 24 April 1975.

7. Landsat (ERTS) 1 and 2 images

Satellite photos of the Beaufort Sea region have been obtained from the EROS Data Center for qualitative and quantitative analysis. About 1500 photos taken when visibility and cloud cover permitted are on file. Each photo covers a square region 100 miles on the side. Time periods are the spring and fall seasons of 1972, 1973, and 1975.

8. NOAA-4 and NOAA-5 satellite images

Photos of the Arctic from Greenland to the Bering Straits have been received daily from NESS since 2 January 1975. Two images cover the belt between 70° and 80° N latitude; that is, each photo covers a square area about 600 miles on the side. Only infrared photos are available for the winter (November through January); both IR and visible photos are taken during the rest of the year. These are source data for examining large-scale ice movements in the Arctic as well as large-scale weather patterns.

9. Surface-level air pressure (derived data)

From the combination of National Weather Service surface pressure maps and pressures measured at scattered points in the Beaufort Sea, two-dimensional pressure contours have been derived for every six-hour interval. These contours are a sixth-order polynomial in X and Y, the grid coordinates overlying the Beaufort Sea region. The grid is rectangular and each element is 75 miles on the side. The coefficients of the polynomial are the data of this file. They can be used to determine the surface pressure at any point in the area at any six-hour interval by translating latitude and longitude of the point to the grid coordinates and employing the polynomial coefficients for the time desired.

To date the coefficients have been calculated for the period 11 April 1975 to 19 July 1975. This work will continue until all coefficients to 30 April 1976 are obtained.

10. Geostrophic surface winds (derived)

From the derived pressure data of file 9 above, geostrophic wind speed and direction are obtained and are available in files separated into one for the grid points and one for the AIDJEX stations, with data given at six-hour intervals.

11. Pressure charts (source data)

Surface and 850 mb pressure charts prepared by the National Meteorological Center for the Northern Hemisphere have been received for 0000 GMT and 1200 GMT each day since April 1975. These analog charts are used in the derivation of the digitized data of files 9 and 10 above.

12. Surface-level meteorological data

Weather stations were operated at the AIDJEX manned camps from April 1975 through April 1976. Hourly averages of observed wind speed and direction at 10 m and air temperatures at 2 m and 9 m above the surface have been prepared. Time series for each camp are available for the full operating period of the main experiment. There are separation markers between each 20-day interval.

13. Atmospheric inversion levels

Inversion heights in the atmosphere were monitored continuously by acoustic radar at the manned camp designated as the main camp. Analog records were digitized at hourly intervals for the periods 13 April-1 October 1975 and 5 November 1975-18 April 1976. As many as seven distinct inversion heights are given when they exist simultaneously.

14. Ocean currents (combined files for manned camps)

The manned camps served as floating platforms from which ocean currents relative to ice motion were measured continuously at depths of 2 m and 30 m. Hourly averages of ocean currents combined with hourly geostrophic winds and three-hour smoothed ice velocity (files 10 and 2) from each manned camp for the full operating period of the AIDJEX program are available in a single file. They are sorted by camp by time, with separation markers between 20-day intervals.

15. Ocean currents combined with position measured from RAMS buoys

Two RAMS spar buoys deployed offshore in the Beaufort Sea in November 1975 contained sensors which measured ocean currents at depths of 2 m and 30 m.

A magnetic compass heading for the buoy and internal bearing of the sensors are given with the data at three-hour intervals. These data have been combined with buoy positions to allow for absolute current determination. One buoy operated until 1 October 1976; the other provided meaningful data only until 28 March 1976.

16. Oceanic mixed layer characteristics

The upper ocean mixed layer is defined in depth by the point, or points, at which a rapid change in salinity occurs. This layer was measured for surface temperature, surface salinity, and depth twice daily at each manned camp. All available measurements (one per day) were published in tabular form in AIDJEX Bulletin 32 (June 1976).

17. Ocean depth

The depth of the ocean beneath the path of the main AIDJEX camp was measured during two periods. Acoustic soundings were taken every hour from 25 May to 3 August 1975 and from 18 December 1975 to 25 April 1976. Round-trip time of sound travel is given together with interpreted depth.

18. Surface pressure (validated), offshore RAMS buoys

Four RAMS buoys deployed offshore in the Beaufort Sea measured surface pressure. These measurements have been corrected for scale and sensor drift and have been smoothed and interpolated to three-hour readings. Buoys were operational for the following periods: buoy 207, 18 March-28 August 1976; buoy 1015, 23 March-30 September 1976; buoy 1245, 4 November 1975-1 October 1976; and buoy 1416, 5 November 1975-28 March 1976.

The data are sorted by buoy by time, and are merged with buoy position in latitude and longitude.

19. Surface pressure (validated), AIDJEX camps and selected buoys

NavSat systems at the four manned camps and nine Navigational Satellite buoys had pressure sensors to make detailed measurements not specifically

included in the surface pressure charts of file 11 above. After appropriate corrections and calibration, these validated measurements were incorporated into the derivation of area-wide geostrophic winds (file 10). These source data are available with their geographic position at three-hour intervals. Data are sorted by station. The manned camps were operational from April 1975 to April 1976. Some of the buoys (supplemented by nearby RAMS buoys) continued to operate as late as 6 December 1976.

20. Weather observations, manned camps

Handwritten weather notes logged daily by observers in the manned camps noted wind velocity, surface pressure, temperature, visibility, and weather. They back up the digitized data in the files noted above.

21. Logbook entries, manned camps

Members of the scientific groups recorded informal notes about events, equipment performance, changes or calibration of sensors, etc. Their logbooks back up the data collection procedures followed during the main experiment.

DATA BEING PROCESSED BUT NOT YET AVAILABLE

The following data sets are in the process of being validated and calibrated. They will be added to the AIDJEX Data Bank files and made available to the scientific community together with the files noted above.

22. Wind speed and direction measured by pilot balloon

Pibal measurements using two tracking theodolites were made each day at the main camp during the AIDJEX experiment.

23. Ocean current profile

Twice a day at each manned camp, a current meter was lowered to a depth of 194 m and raised at a steady rate to determine the stratification of the

ocean layers. The analog outputs will be digitized to show time, depth, speed, and direction at uniform depth increments.

24. Salinity and temperature versus depth at manned camps

Standard STD measurements were made twice a day at each manned camp during the main AIDJEX experiment.